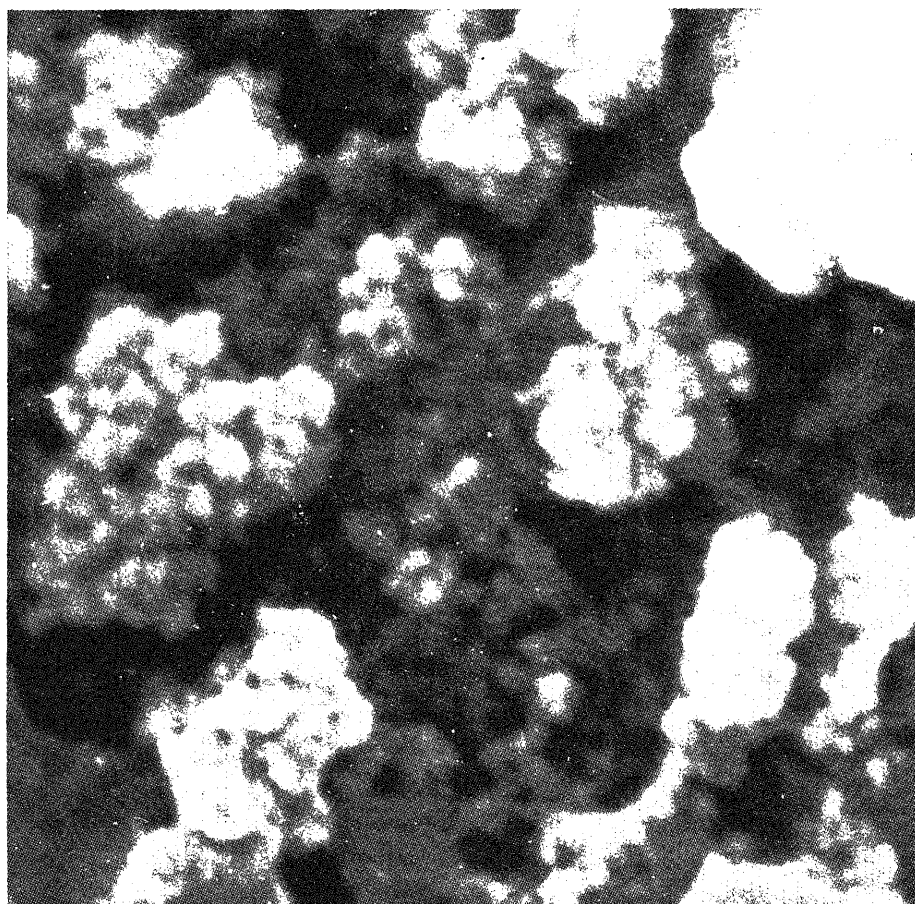


Bulletin of Materials Science

Volume 21

Number 1

February 1998



Published by

INDIAN ACADEMY OF SCIENCES

in collaboration with

**MATERIALS RESEARCH SOCIETY OF INDIA and
INDIAN NATIONAL SCIENCE ACADEMY**

International Advisory Editorial Board

M A Alario-Franco

Departamento de Química
Inorgánica
Universidad Complutense
28040-Madrid, SPAIN

B Cantor

Department of Materials
University of Oxford
Oxford OX1 3PH, UK

A K Cheetam

Materials Department
University of California
CA 93106-5130, USA

L E Cross

Materials Research Laboratory
The Pennsylvania State University
PA 16802-4800, USA

P Day

The Royal Institution of
Great Britain
London W1X 4BS, UK

J Etourneau

Institut de chimie de la
matière condensée
de Bordeaux
33608 Pessac cedex, FRANCE

A H Heuer

Materials Science and Engineering
Case Western Reserve University
Cleveland, Ohio 44106, USA

T Inoue

Dept. of Energy Conversion Science
Kyoto University
Sakyo-ku 606-01, Kyoto
JAPAN

F A Kuznetsov

J Livage

Chimie de la matière condensée
Université Pierre et Marie Curie
Paris 75252, FRANCE

S Nagakura

Kanagawa Academy of Science
and Technology
Kawasaki, Kanagawa 213
JAPAN

A E Owen

Department of Electrical Engineering
The University of Edinburgh
Edinburgh EH9 3JL
Scotland, UK

P Rama Rao

Atomic Energy Regulatory Board
MUMBAI 400 094
INDIA

A K Ramdas

Department of Physics
Purdue University
Indiana 47907, USA

C N R Rao

J N Centre for Advanced
Scientific Research
Bangalore 560 012, INDIA

B B Rath

Naval Research Laboratory
Washington DC 20375-5320
USA

M Rühle

Max Planck Institut für Metallforschung
D-70174, Stuttgart
GERMANY

E C Subbarao

Bulletin of Materials Science

Vol. 21, No. 1, February 1998

CONTENTS

SEM photograph of powders of ZrO_2 showing agglomeration of particles. For details, see p. 84.

ial

Article

ques and applications of electron spin resonance

C S Sunandana

Research Articles

ible crystallographic explanation for the five-fold diffraction symmetry in icosahedral phases

T R Anantharaman

ation of superconducting-grade copper from commercial grade copper salt

P Pramanik, A K Adak and A Pathak

ation of tetragonal zirconia powders by a solid state reaction: Kinetics, phases and morphology

V V Mishra, A K Garg and D C Agrawal

l and structural characteristics of strontium doped calcium tartrate crystals

K Suryanarayana, S M Dharmaprakash and K Sooryanarayana

of fillers on acousto ultrasonic response in GRP composites

Pravesh Kumar

Communication

oxide equilibria in the system Pt-Rh-O

K T Jacob, Shashank Priya and Yoshio Waseda

Review

d in

- CURRENT CONTENTS

CONTENTS - 1998

torial

rs may notice that there is a change in the format of issue of **Bulletin of Materials Science**. Sometime in 1997, the Editor of Publications of the journals Academy suggested that we consider adoption of a new dimension of the journal and format of the journal. The suggested format is easily adaptable for fully automated processing of the journal. The contributors are easily persuaded to send their manuscripts on time. The suggestions were considered in detail at the meeting of the Editorial Committee which was held in November 1997 at IICT, Hyderabad. Upon the recommendations of the Editorial Committee, the **Bulletin of Materials Science** will hereafter be printed in a two column format and would continue to retain the present size of the cover page. The journal itself will however be slightly bigger. This will also enable an increase in printed matter for the same number of pages. I am sure the changes will be welcomed by readers of the **Bulletin of Materials Science**.

It is opportune to remind the readers about publication options available with the journal. BMS publishes **Communications**. This will enable publishing

your research results of importance within two weeks of communication. These papers are given very fast refereeing. BMS publishes **Review Articles**—both invited and contributed. These reviews have to be on specific subjects. **Book Reviews** are also published. Authors are encouraged to send copies of their published books for reviewing. We are striving hard to reduce the time between the receipt of paper and its final publication to a minimum. The delays are often attributable to multiple revisions which some papers require. In this context, I express my sincerest thanks to the referees who have spared their most valuable time for the betterment of the journal.

The journal also publishes Proceedings of National and International Meetings on Materials Science. Although we receive a number of requests in this category every year, we have to be selective in view of the rising costs of journal production. However, the journal promises to accommodate as many such requests as possible.

I trust that the community of materials scientists will continue to offer their best cooperation in maintaining the good standards of the journal.

Techniques and applications of electron spin resonance*

C S SUNANDANA

School of Physics, University of Hyderabad, Hyderabad 500 046, India

MS received 27 January 1996

Abstract. A broad-spectrum review of the applications of electron spin resonance to advanced materials is presented. Starting with basic concepts the reader is taken through a quick tour of techniques in continuous-wave and pulse ESR, microscopy and imaging, as well as a few emerging techniques. Applications of spin identification, spin counting, spin mapping and spin imaging of a variety of advanced solid materials including metals and alloys, semiconductors, inorganics, electroceramics, catalysts, intercalated polymers, glasses, and organic charge-transfer complexes besides superionic conductors and high-temperature superconductors are included. It is thus demonstrated that the technique is at once specific, sensitive to composition, phase and texture yet accurate enough to be a quantitative but non-invasive tool that proves to be useful in the study of newer and newer materials including multilayers, ferrofluids and nanomaterials.

Keywords. Electron spin resonance; advanced materials; ESR microscopy and imaging; semiconductors; polymers; glasses; superionic; superconductors.

1. Introduction

The existence of magnetic moment of an unpaired electron — a fundamental particle with an intrinsic property of 'spin' (1/2) that is naturally found (or artificially created) in materials as an essential part of their unique crystal structures, and dictating their electrical, optical and magnetic behaviour — as a microscopic, resonance spectroscopic method of characterization is the basis of electron spin resonance (ESR) or more generally speaking electron paramagnetic resonance (EPR). It is the hierarchy of interactions between the magnetic moment with its neighbouring and the distant material environment that is exploited in this technique to learn more about either the materials processing or the induced process(es) that take place within the material. It could be said that the EPR technique and advanced materials are 'made for each other'.

Starting with a brief historical perspective, this article aims to provide a brief account of the methods and applications of this technique. The spectrum of the materials covered include semiconducting materials, polymer materials, ceramics and glasses, and superionic and superconductive materials. ESR imaging

2. A brief historical perspective

Electron spin resonance (ESR) or more generally speaking electron paramagnetic resonance (EPR), discovered by Zavoiskii (1944) in MnSO_4 employing a 47 kG magnetic field and a 133 MHz rf magnetic field, is an extension of the original Stern–Gerlach experiment (1921; Gerlach and Stern 1924), on atomic beams, which demonstrated the space quantization of atomic magnetic moments. In between, Rabi (1939a, b) had performed the 'nuclear Zeeman effect' experiment by using a microwave frequency electromagnetic field perpendicular to a homogeneous dc magnetic field. Theoretically, the possibility of quantum transitions between magnetic sublevels of atoms under the influence of an external magnetic field was suggested by Einstein and Ehrenfest (1922).

The earliest applications of microwave resonance spectroscopic technique were on (i) $\text{CuSO}_4 \cdot 5\text{H}_2\text{O}$ in which 'exchange narrowing' was discovered (Bleaney and Griffiths 1950), (ii) F-centres in alkali halides in which structural information was obtained (Kip

Table 1. Properties of fundamental particles relevant for magnetic resonance spectroscopy.

Property	Electron	Proton	Neutron
Charge (C)	$-1.602192 \times 10^{-19}$		0
Mass (kg)	$9.109534(47) \times 10^{-31}$	$1.6726485(86) \times 10^{-27}$	$1.6749543(86) \times 10^{-27}$
Magnetic moment (Joule/Tesla)	$9.284832(36) \times 10^{-24}$	$1.401671(51) \times 10^{-27}$ $2.7923456(11)\mu_N$ $\mu_N = 5.0505 \times 10^{-27} \text{ J/T}$	$-1.91304184(88)\mu_N$
<i>g</i> -factor (Zeeman)	2.00231929		
<i>g</i> -factor (spin-orbit)	2.00463858		

Sources:

1. Weast R C (ed.) 1988 *CRC Handbook of Physics and Chemistry* 1st Student edn.
2. Krane K S 1988 *Introduction to Nuclear Physics* (New York: Wiley).

An investigation of permeability of ferromagnetic metals Fe, Co and Ni, by Griffiths (1946) led to the discovery of ferromagnetic resonance. An examination of free radicals in leaves, seeds and tissue preparation saw the first biological application (Commoner *et al* 1954). McConnell pioneered the use of 'spin labels' or free radical substituents in biological systems (Stone *et al* 1965), while Sands (1955) pioneered a continuing structural investigation on transition metal ion-doped glasses. Weeks (1956) applied the technique for studying radiation-induced centres in crystalline quartz, and, Yasaitis and Smaller (1953) investigated the paramagnetic centres in irradiated borate glasses. The studies on mechanically produced free radicals in polymers were pioneered by Zakrevskii *et al* (1968).

The observation of electron spin echoes (Gordon and Bowers 1958; Mims *et al* 1961) ushered in the era of pulsed electron spin resonance, coming in the wake of Hahn's discovery of nuclear spin echoes (Hahn 1950). The last decade has seen the emergence of EPR imaging and microscopy (Ikeya 1991), again following the discovery of NMR imaging (Lauterbur 1973).

The bludgeoning activity in this field is evidenced by the very recent appearance of a number of comprehensive monographs and workshop proceedings (Pilbrow 1990; Yordanov 1991; Mabbs and Collison 1992; Ikeya 1993), besides the existing classics (Wertz and Bolton 1972; Atherton 1973; Abragam and Bleaney 1989).

motion of these moments and an understanding of the motion thereof; (iii) quantization of these moments and I for electron and nuclei, respectively; (iv) the magnetic energy levels created by a static magnetic field and a separation of these energy levels; (v) a substantial number of 'allowed' energy states at ambient temperature following the Boltzmann distribution law, according to which the population difference between two energy levels is proportional to the negative exponential of the difference between concerned energy levels divided by the energy $k_B T$, where k_B is the Boltzmann constant; finally, (vi) the natural precession frequency or Larmor frequency for the spin system. The Larmor frequency for the spin system depends on the electronic moment depends on the static magnetic field and for the nuclear moment on the static magnetic field which may be approached either by increasing the frequency of the alternating field at a constant static magnetic field or by scanning the static magnetic field at a constant frequency.

3.1 Classical picture

A planetary model of an atom with a nucleus of charge $(\mu_1 \neq 0)$ and an unpaired electron ($\mu_2 \neq 0$) has an intrinsic property of 'spin' in a classical sense. An electron of spin S with a magnetic moment μ experiences — much like a tiny bar magnet — a torque $\mu \times H_0$ in an external magnetic field.

γ_e = electron magnetogyric ratio = $-ge/2mc$, with g the spectroscopic splitting factor, e the electron charge, m the electron mass (see table 2) and c the velocity of light. For the electron, the dipole moment is the angular momentum so that

$$\boldsymbol{\mu} = -\gamma \hbar \mathbf{S}. \quad (3)$$

The magnetic component of the electromagnetic field lies in microwave region for ESR and radio-frequency region for nuclear magnetic resonance or NMR. \mathbf{H}_1 ($\ll H_0$) also rotates with microwave frequency and exerts a torque $\boldsymbol{\mu} \times \mathbf{H}_1$ on $\boldsymbol{\mu}$. As long as $\omega \neq \omega_0$, the torque is zero on the average but when $\omega = \omega_0$, $\boldsymbol{\mu}$ precesses around \mathbf{H}_1 with a frequency $\omega_1 = \gamma_e H_1$ besides its usual precession around H_0 with frequency ω_0 . Consequently, $\boldsymbol{\mu}$ slowly changes its direction going down and eventually reaching a position opposite to its original orientation (figure 2). In the flipping process, work is done on the dipole moment by the microwave magnetic field. In other words, the system absorbs energy from the microwave field H_1 during the process. At resonance the oscillatory magnetic moment, $\boldsymbol{\mu}_1$, to H , produced by Larmor precession interacts with the small oscillatory magnetic field $H_1 \cos \omega t$, also perpendicular to H , and changes the direction of component μ_z along H by 180° , and thus changes the energy of the electronic dipole, causing ESR absorption. Thus at resonance,

$$\begin{aligned} \nu_0 &= g(e/2m) H \quad (2\pi) \\ &= 139.96(gH) \quad (\nu \text{ in Hz, } H \text{ in T}). \end{aligned} \quad (4)$$

It can also be expressed in Oersted and gauss, with 10,000 Oersted units to a Tesla.

Quantum picture

Classically, the phenomenon of electron spin magnetic resonance is described as the magnetic transitions brought about by the interaction of the magnetic field of the microwave radiation with a magnetic dipole in the absorbing system. Quantum mechanics helps in understanding the probability of these transitions and shows that the probability has a sharp maximum when $\hbar\omega = E_+ - E_- = 2\mu H$, where μ is the Bohr magneton.

when the total magnetic field acting on the spin is the vector sum

$$\mathbf{H} = H_1(i \cos \omega t + j \sin \omega t) + H_0 k,$$

and g_e is assumed to be 2. The resonance condition can be arrived by considering the allowed energies of the electron magnetic dipole

$$\mu [|\boldsymbol{\mu}| = \gamma \hbar S(S+1)^{1/2}],$$

in the field H_0 , using the energy operator

$$\mathcal{H} = -\boldsymbol{\mu} \cdot \mathbf{H}_0 = \gamma \hbar \mathbf{S} \cdot \mathbf{H}_0.$$

Taking H_0 along +z axis (figure 2) the allowed energies are

$$E_{M_s} = \gamma \hbar H_0 M_s,$$

where the quantum number M_s specifies the values of the z-components of \mathbf{S} viz. $-S, -S+1, \dots, S-1, S$. For $S = 1/2$, $M_s = \pm 1/2$ and the energies are

$$E \pm \frac{1}{2} = \pm \gamma_e \hbar H_0.$$

Transitions between these levels (figure 3) caused by magnetic dipole radiation require that $\Delta M_s = \pm 1$ the resonance condition that the energy quantum $\hbar\omega$ must satisfy is

$$\hbar\omega = E \pm \frac{1}{2} - E - \frac{1}{2} = \gamma_e \hbar H_0,$$

which coincides with the classical picture $\omega = \gamma H$. The basic gyromagnetic ratio for the free electron

$$\gamma_e = 2\pi(28.0246 \text{ GHz/T}).$$

3.3 Spin relaxation

The above pictures are valid for the hypothetical case of a single isolated spin or a paramagnet. In the real world materials contain a large number of spins, and the concept of a 'reservoir' or a 'bath' or the concept of a 'thermal equilibrium' comes into the picture. A reservoir (a crystal lattice or a glass/polymer)

magnetic nuclei and hyperfine coupling constants from electron spin resonance studies.

	Nuclear dipole magnetic moment (μ_N)	$ \psi_{na}(0) ^2$ (a.u.)	$\langle r^{-3} \rangle$ (a.u.)	Isotropic coupling A_{iso} (G)	Anisotropic coupling (B_0)	g_N	Electric quadrupole moment ($1e1 \times 10^{-24} \text{ cm}^{-2}$)	Most stable paramagnetic form (S)	λ (cm^{-1})
2	+ 2.79284	0.314 (0.318) ^s		508 (1430) ^s		5.586912	-	H ⁻	
	+ 0.85743			78		0.8574376	0.002875		
2	- 2.12762	(1.867)		(-6357)		-4.255248			
	+ 0.822056			39		0.8220514	-0.000644		
2	+ 3.25644	0.1673 (0.2101)		105 (364.9)		2Å170961	-0.040	Li ⁰	0.2
	- 1.1776	0.5704 (0.7188)		130 (-451.6)		-0.7850	0.053		1
	+ 1.8007	1.408	0.775	242					
2	+ 2.6886	(1.775)	(0.9293) ^s	725 (2547)	t8	0Å600216	0.08608		11
	+ 0.70241	2.767 (3.358)	1.692 (2.002)	1130 (3777)	66	1.792424	0.040		29
	+ 0.40376	4.770 (5.599)	3.101 (3.599)	552 (1811)	34	2.0382	0.01932		76
2	- 0.28319			775	48	0.4037607			
2	- 1.89379	7.638 (8.669)	4.974 (5.820)	1660 (-5263)	104	-0.757516	-0.026		151
	+ 2.62887	11.966 (12.53)	7.546 (8.766)	17200 (52870)	1.084	5.257934			270
2	+ 2.21752	(0.7797)		317 (927.1)		1.478391	0.108	Na ⁰	11
2	- 0.85545	(1.763)		(-485.9)		-0.34218	0.22		20
2	+ 3.64150	2.358 (3.327)	1.055 (1.493)	985 (3911)	42	1.456601	0.150		75
2	- 0.5553	3.807 (5.115)	2.041 (2.691)	1220 (-4594)	62	-1.1106			149

Techniques and applications of electron spin resonance

nuclear dipole magnetic moment (μ_N)	$ \psi_{na}(o) ^2$ (a.u.)	$\langle r^{-3} \rangle$ (a.u.)	isotropic coupling A_{iso} (G)	Anisotropic coupling (B_0)	g_N	electric quadrupole moment ($1e \times 10^{-24} \text{ cm}^{-2}$)	most stable paramagnetic form (S)	λ (cm^{-1})
+ 0.68412			1395	84	2.3006	- 0.06493		
+ 0.39146	(1.066)		83 (228.5)		0.2609909	0.054		38
- 1.298						- 0.067		
+ 0.21487			45		0.1432542	0.060		
- 1.3173	(2.063)			(- 640.7)	- 0.376414	< 0.23		
+ 4.756	(2.506)	(1.851)	(2823)		1.35906	- 0.22		
- 0.7885	(2.975)	(2.444)	(- 7820)		- 0.31539	0.29	Ti ³⁺	154
- 0.10417					- 0.315477	0.24		
+ 3.34745					0.556593	0.209		
+ 5.1514	(3.378)	(3.114)	(4165)		1.46836	- 0.0515	V ⁴⁺ , V ³⁺ V ²⁺	104 55
- 0.47454	(2.811)	(3.414)	(- 748.2)		- 0.3147	- 0.0285/ + 0.022	Cr ²⁺ Cr ³⁺	57 87
+ 3.4687	(4.300)	(4.721)	(5036)		1.3819	0.33	Mn ²⁺ Mn ³⁺	- 85
+ 0.09044	(4.832)	(5.659)	(747.20)		0.1816		Fe ³⁺ Fe ²⁺	- 100 - 180
+ 4.627	(5.233)	(6.710)	(5947)		1.318	0.42	Co ²⁺	
- 0.75002	(5.755)	(7.864)	(- 2499)		- 0.50001	0.162	Ni ²⁺ Ni ³⁺	- 335
+ 2.2233	(4.617)	(8.455)	(5995)		1.484	- 0.222	Cu ²⁺	- 852
+ 2.3817					1.588	- 0.195		
+ 0.8755	4.5222 (6.379)	(10.52)	376 (2087)		0.350312	0.150		386
+ 2.01659	6.9493 (10.18)	2.8665 (3.973)	2675 (12210)		1.34439	0.168		551
+ 2.56227			3400		1.70818	0.168		

Nuclear dipole magnetic moment (μ_N)	$ \Psi_{na}(0) ^2$ (a.u.)	$\langle r^{-3} \rangle$ (a.u.)	Isotropic coupling A_{iso} (G)	Anisotropic coupling (B_0)	g_N	Electric quadrupole moment ($1e \times 10^{-24} \text{ cm}^{-2}$)	Most stable paramagnetic form (S)	λ (cm^{-1})
+ 1.43947	12.5606 (16.75)	6.9871 (9.102)	3430 (14660)		0.959647	0.29		1550
0.53506	15.7791 (20.41)	9.2284 (12.05)	4840 (20120)		1.0693			1688
+ 2.1064	19.4127 (24.47)	11.8758 (15.25)	7810 (32070)		1.404266	0.293		2460
2.2706			8400		1.513706	0.27		
- 0.9767	(29.12)	(18.76)	(- 5937)		- 0.215704	0.26		
+ 1.35302	(2.000)		(1037)		0.541253	0.273		
+ 2.7512					1.83427	0.130		
- 1.693	(3.617)		(- 853.6)		- 0.24291	0.15		
- 0.1373	(4.616)	(2.373)	(- 1250)		- 0.274836			
- 1.3036	(5.283)	(3.126)	(- 2753)		- 0.521448			
+ 6.1705	(4.736)	(3.494)	(6590)		1.3712	- 0.28		
- 0.9133	(5.264)	(4.318)	(- 1984)		- 0.3656	- 0.019		
- 0.9335					- 0.3734	0.2		
- 0.6413					- 0.279	0.076		
- 0.7188	(6.085)	(6.145)	(- 1764)		- 0.279	0.44		
- 0.0884	(6.414)	(7.179)	(- 1229)		- 0.1768	-		

Techniques and applications of electron spin resonance

	nuclear spin moment (μ_N)	$ \psi_{na}(0) ^2$ (a.u.)	$\langle r^{-3} \rangle$ (a.u.)	anisotropic coupling (A_{iso}) (G)	Anisotropic coupling (B_0)	g_N	quadrupole moment (10^{-24} cm ²)	paramagnetic form (S)	λ (cm ⁻¹)
	-0.6217					+1.2454			
	+5.523					1.22864	0.846		
	-0.918					-1.8377			
	-1.000					-2.00208			
	-1.046	(17.46)	(9.160)	(-43920)		-2.09456			
	+3.359	(21.51)	(12.25)	(351000)		1.3455	-0.33		
	+2.547					0.72876	-0.68		
	-0.7359					-1.4736			
	-0.8871					-1.7766	-		
	+2.808	(25.29)	(15.47)	(-55590)		1.12530	-0.789		
	-0.7768	(29.27)	(18.92)	(41600)		-1.55595	-		
	?	(33.79)	(22.57)	(-67790)		0.461240	-0.120		
	+2.579	(2.538)		(2467)		0.7378477	-0.003		
	+0.8365					0.55884	0.20		
	+0.9357	(4.722)		(3971)		0.62515	0.34		
	2.778	(5.492)	(3.127)	(6007)		0.79520	6.22		
	+3.707	(4.950)	(4.953)	-		0.74238	0.51		
	4.25	(5.208)	(5.565)	(12490)		-11.87375	-0.041		800
	-1.08	(5.309)	(6.201)	(-2399)		-0.3076	-0.56		900
	-0.66					+64.60	-0.29		
	-0.813					-58.7543	-0.18		1200

Nuclear dipole magnetic moment (μ_N)	$ \psi_{na}(0) ^2$ (a.u.)	$\langle r^{-3} \rangle$ (a.u.)	Isotropic coupling A_{iso} (G)	Anisotropic coupling (B_0)	g_N	Electric quadrupole moment ($1e \times 10^{-24} \text{ cm}^{-2}$)	Most stable paramagnetic form (S)	λ (cm^{-1})
+ 3.464					1.389	1.53		1416
+ 1.530				0.6134	3.92			
- 0.27	(5.952)	(8.261)	(5722)		- 0.1723	1.30		1540
- 0.36	(6.970)	(3.993)	(- 2546)		- 0.2253	1.34		
+ 1.95	(6.971)	(3.993)	(- 2546)		1.342	1.34		- 1770
- 0.48	(6.142)	(9.783)	(13630)			- 0.189	2.47	- 1860
+ 0.673	(- 0.71415)				0.266	2.51		
	(6.459)	(10.59)	(2963) (6)					
+ 4.173	(6.624)	(11.43)	(13560)		1.192	2.73		- 2000
- 0.5665	(3.739)	(12.31)	(- 1934)		- 0.1618	2.827		- 2350
- 0.2316	(6.919)	(13.26)	-					
+ 0.4919	(- 3.6302) (4)	(13.26)	(- 5835)		0.9885			- 2940
- 0.6776	(7.245)	(14.19)	(- 3670)		- 0.27185	2.8		
+ 2.2327	(8.700)	(4.588)	(10630)		0.63943	5.68		
+ 3.19					0.454	8.0		
+ 0.7935	(9.942)	(5.756)	(4410)		0.2267	4.5		
- 0.6409					- 0.1424	5.1		

Nuclear dipole magnetic moment (μ_N)	$ \psi_{na}(0) ^2$ (a.u.)	$\langle r^{-3} \rangle$ (a.u.)	Isotropic coupling A_{iso} (G)	Anisotropic coupling (B_0)	g_N	Electric quadrupole moment ($1 e 1 \times 10^{-24} \text{ cm}^{-2}$)	Most stable paramagnetic form (S)	λ (cm^{-1})
+ 3.2197	(13.09)	(9.454)	(35490)		1.2878	2.22		
+ 0.0646					0.1311			
0.6599	(13.90)	(10.79)	(13200)		0.488	0.8		
+ 0.1461					0.097	0.78		
+ 0.1591	(14.87)	(12.19)	(3493)		0.107	0.70		
+ 0.6095	(12.53)	(12.81)	(34410)		1.2190			
+ 0.1457	(12.86)	(14.31)	(2876)		0.097968	0.594		
+ 0.5059	(17.37)	(16.78)	(41880)		1.011770			
- 0.5602					- 0.373483	0.42		
+ 1.6222					3.244514			
+ 1.6382	(22.97)	(10.13)	(183800)		3.2754			
+ 0.5926	(27.96)	(14.72)	(81510)		1.1748			
+ 4.110	(33.09)	(19.15)	(77530)		0.938	- 0.46		
- 0.35					- 0.10	4.3		

) 1988 *CRC handbook of physics and chemistry*, 1st student edn

P W and Symons M C R 1967 *The structure of inorganic radicals* (Amsterdam: Elsevier)

ic (1993)

mic parameters from Hermann-Skillman wavefunction. Weltner Jr W 1983 *Magnetic atoms and molecules* (New York: Dover)

Equation (11) ensures that there is always an excess spin population in the ground state ready to undergo transitions. More significantly, since the $N^- \rightarrow N^+$ energy absorption would occur until $N^- = N^+$, when the spin system would become saturated and no resonance would be detectable. In fact, there are two mechanisms acting within the material by which energy is effectively transferred by the spin system to the surroundings. The spin-lattice relaxation, characterized by time T_1 and exponential in time, results from interactions of the electronic magnetic moments with each other and with the other electrons of the host material, or the 'lattice'. This 'longitudinal' relaxation causes changes in the component of μ parallel to H_0 . A short T_1 affects the linewidth of the resonance through the energy-time uncertainty relation $\Delta E \Delta \tau \geq \hbar$, ΔE being the uncertainty of an energy level and $\Delta \tau$ being the lifetime of that state, i.e. T_1 . A very short T_1 would thus imply a large ΔE and a broadened ESR line at ambient. ESR lines can be broadened by magnetic interaction among the spins themselves, as a result of which the different spins would experience slightly different local fields in the z-axis, leading to a spread in the Larmor precession frequencies. Eventually the spins would not precess in phase at all, and there would be a gradual dephasing, exponential in time, the process being characterized by a transverse or a spin-spin relaxation time T_2 . Spin-spin relaxation processes are adiabatic because there is no exchange of energy between the spin system and the reservoir.

Thus the spin relaxation mechanisms are crucial to the observation of electron spin resonance spectra. Aspects of lineshape and linewidth are considered in § 6.

4. ESR and allied phenomena

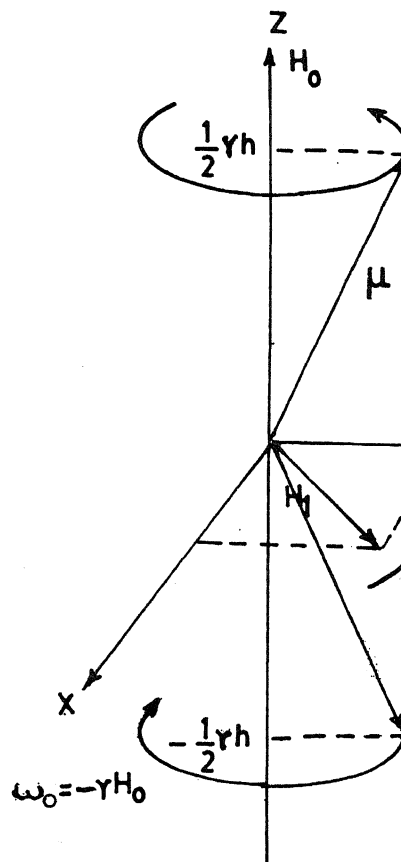
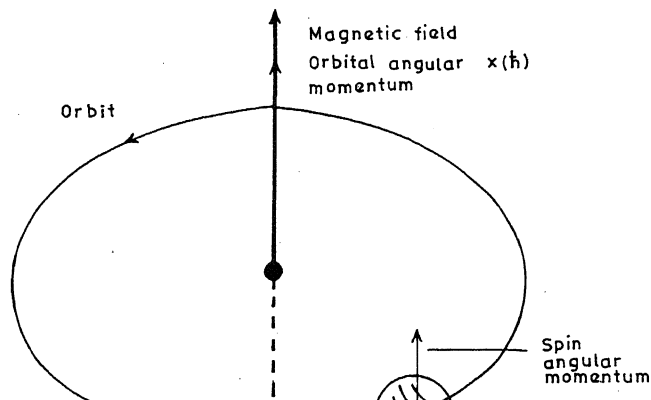
4.1 Electron spin resonance

When a material containing electrons is placed in a static magnetic field and subjected to electromagnetic radiation, absorption of energy occurs through magnetic dipole transitions occurring at characteristic frequencies in the microwave region of the electromagnetic spectrum.

For a system with electron spin $S = 1/2$ (as in silicon) there are $2S + 1 = 2$ energy levels in a static magnetic field H given by:

$$E = \langle \psi_i | \hat{H} | \psi_i \rangle = M_s g \mu_B H,$$

where ψ_i is a characteristic wave function.



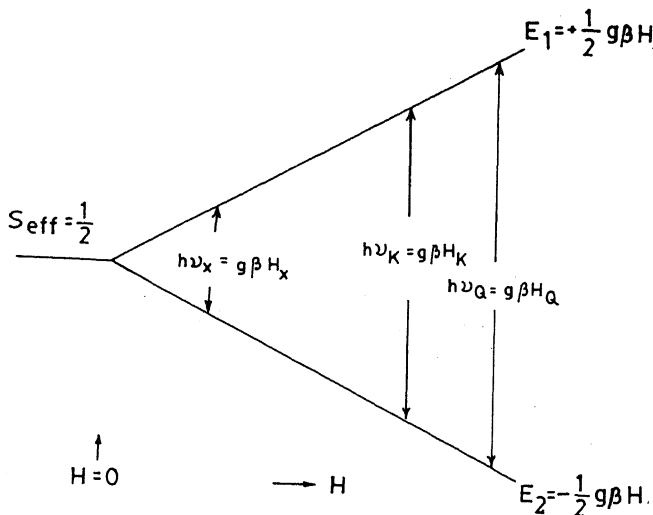
component of the spin angular momentum $S_z\hbar$, and $\hat{\mathcal{H}}$ is the spin Hamiltonian operator

$$\hat{\mathcal{H}} = g\mu_B \hat{H} \hat{S}_z, \quad (13)$$

μ_B or the Bohr magneton is a unit for the magnetic moment of the electron $\mu_e = 1/2 g_e \mu_B = 9.28485 \times 10^{-21} \text{ JT}^{-1}$ and the free electron g-value is 2.00232. The magnetic dipole transitions between the Zeeman levels (so-called because the dc magnetic field separates the levels as in Zeeman effect observed in atomic spectra) are induced by the magnetic component of the microwave electromagnetic field, when the energy of the microwave photon matches the energy level separation

$$\Delta E = h\nu = \Delta M_s g \mu_B H_r, \quad (14)$$

where $\Delta M_s = \pm 1$ is the selection rule for ESR (figure 4). Equation (14) implies a reorientation of the electron magnetic moment, or a flipping which is possible only when the electromagnetic field is polarized such that the oscillating magnetic field has a component perpendicular to the static magnetic field.

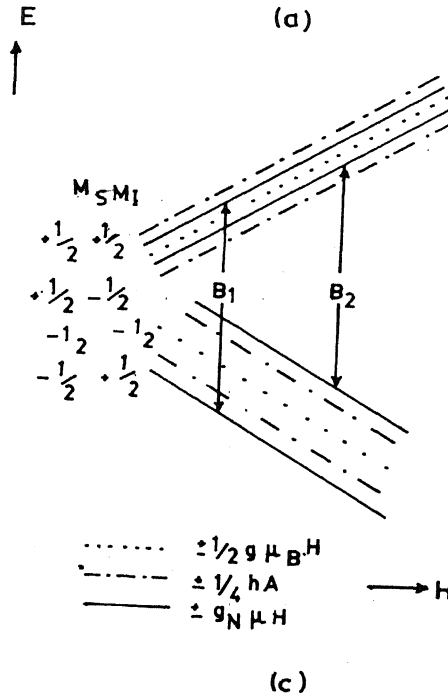


The g-factor of (13) is in general a

$$\hat{\mathcal{H}} = \mu_B \hat{S} \cdot \tilde{g} \cdot \hat{H},$$

$$\text{or } \hat{\mathcal{H}} = \mu_B (S_x S_y S_z) \begin{bmatrix} g_{xx} & g_{xy} & g_{xz} \\ g_{yx} & g_{yy} & g_{zy} \\ g_{zx} & g_{zy} & g_{zz} \end{bmatrix} \begin{bmatrix} H_x \\ H_y \\ H_z \end{bmatrix},$$

where S_x, S_y, S_z and H_x, H_y and H_z are of \hat{S} and \hat{H} , measured with respect to x, y, z of mutually orthogonal axes in the materials. The tensor components g_{ij} are along the j -axis when the magnetic field



the i-axis. Many nuclei (H through Bi in the periodic table of elements, see table 2) also possess an intrinsic spin angular momentum $I\hbar$ which produces an intrinsic magnetic field of the electron H_e that adds on to H_r so that the new resonance condition becomes

$$h\nu = (H_r + H_e) g\mu_B. \quad (14a)$$

For a nucleus such as ^1H or ^3P , $I = 1/2$ so that in the applied field H the nucleus may take up one of the two configurations $M_I = +1/2$ or $M_I = -1/2$, where M_I is the z-component of the nuclear spin quantum number. The two applied fields at which resonance will occur are:

$$H = h\nu/g\mu_B = H_0 \pm H_e = H_0 - aM_I. \quad (16)$$

Thus ESR is split into two, or, in general $(2I+1)$ line 'hyperfine structure', a being the hyperfine splitting constant. The origin of the hyperfine field H_e is traced to the nonzero probability of the unpaired electron being found at the nucleus. This probability is maximum for electrons in s-orbitals, where wave functions are isotropic. The mutual magnetic interaction between the electron and the nuclear dipoles gives rise to the anisotropy of the hyperfine interaction.

Including the hyperfine interaction, as also the nuclear Zeeman interaction and the electric quadrupole interaction, (15a) becomes

$$\hat{\mathcal{H}} = \mu_B \hat{S} \cdot \tilde{g} \hat{H} + h \hat{S} \cdot \tilde{A} \hat{I} - g_N \mu_N \hat{I} \cdot \hat{H} + h \hat{I} \cdot \tilde{Q} \hat{I}, \quad (17)$$

where I_N and μ_N are the nuclear g -factor and nuclear Bohr magneton respectively, and, \tilde{A} and \tilde{Q} are the hyperfine and quadrupolar interaction tensors, symmetric and diagonalizable. In the next section, the g - and A -tensors are related to physical quantities. Equation (17) is the spin Hamiltonian (Abragam and Bleaney 1989) — generally a polynomial in S_{eff} , the effective spin angular momentum — where $2S_{\text{eff}} + 1$ equals the total number of electronic states whose properties are being described and which may be used to determine the energy levels of the spin system and thus deduce the ESR transition frequencies. Therefore, the spin Hamiltonian such as (17) makes the contact between theory and experiment.

Considering the case of a spin-half nucleus containing

$|-\frac{1}{2}, -\frac{1}{2}\rangle$ define the four spin states given by:

$$\begin{aligned} E &= M_s, m_I | \hat{\mathcal{H}} | M_s, m_I \rangle \\ &= M_s g \mu_B H + M_s m_I h a - m_I g_N \mu_N \end{aligned}$$

Figure 4 shows these levels as a function of the applied field H . The ESR selection rule $\Delta M_s = \pm 1$ corresponds to a change in the spin angular momentum of \hbar . In the absence of hyperfine splitting, the energy levels would not change so that the total angular momentum of the system would be conserved. The presence of hyperfine splitting implies the extended selection rule $\Delta M_s = \pm 1, \Delta M_I = 0$. The resulting ESR transitions are

$$h\nu = g\mu_B H_0 \pm \frac{1}{2} ha.$$

From (16) and (14b), $A_{\text{iso}} = h a/g\mu_B$ is the isotropic hyperfine interaction (see § 5).

ESR measures ' g ' and hyperfine splitting, but does not measure g_N because the nuclear Zeeman energy does not normally affect the ESR transition. Thus the unambiguous identification of the nucleus is generally impossible. It is not possible to resolve the ambiguity by establishing ESR ($\Delta M_s = \pm 1, \Delta M_I = 0$) or magnetic resonance (NMR), (i.e. the radio frequency radiation by $\Delta M_s = 0, \Delta M_I = \pm 1$) in a technique called 'nuclear double resonance' or ENDOR. In this technique, the magnetic moment of the nucleus in the beam of hydrogen atoms has been measured (Winkler *et al* 1972).

4.2 Electron nuclear double resonance

Electron nuclear double resonance is a technique in which the conditions for ESR and NMR are established simultaneously. It can be easily seen from figure 4. To observe ESR, the magnetic field is set at one of the resonance fields (H_1) and the microwave power level is adjusted so that the transition is partially saturated. Then a second magnetic field at high power is applied and

R selection rule is the opposite of the ESR selection rule ($M_s = \pm 1$, $\Delta m_l = 0$).

$$\nu_1 = -\frac{ha}{2} + g_N \mu_N H_0, \\ \nu_2 = \frac{ha}{2} + g_N \mu_N H_0. \quad (20)$$

It is important to note from (20) that while the difference frequency measures a directly, the mean frequency $(\nu_1 + \nu_2)/2$ measures g_N and unambiguously identifies the interacting nucleus. (See table 2 for g_N values of magnetic nuclei). The principal advantage of the basic ENDOR technique is that it combines the resolution of ESR with the sensitivity of NMR. The precise determination of the spin Hamiltonian parameters, due to the greater rate of energy transition at microwave frequency and the greater energy differences involved in the ENDOR levels. Furthermore, ENDOR spectra are simpler than the corresponding ESR spectra. If several nuclei with the same or similar interactions are coupled to the unpaired electron, the ESR pattern becomes complicated and the 'hyperfine' structure is not usually resolved. But in ENDOR, all nuclei with the same interaction can give rise to only two ($S = 1/2$) ENDOR lines which greatly improve the resolution.

In semiconducting materials containing impurities, as discussed later, as in X-irradiated alkali halides, alkaline-earth halides and oxides (Henderson and Onyon 1973; Spaeth and Koschnick 1991), the ENDOR spectra are markedly dependent on the orientation of the impurity line solid in the applied field, so that the Hamiltonian of (17) is now anisotropic. The point symmetry of the defect (e.g. tetrahedral for Si and octahedral for Mg^{2+} site) helps to determine at least one principal axis of the defect so that the latter can be described. In diagonal form (17) is

$$H = g_N \mu_N H_0 \hat{S}_z + g_N \mu_N H \cdot \hat{I} + h \sum A_{ii} \hat{S}_i I_i + h \sum Q_{ii} \hat{I}_i^2, \quad (21)$$

where \hat{H} , \hat{S} and \hat{I} are written in the principal axis system of the A , and Q tensors.

At generally the electron interacts with n -shells of the impurity (substituted by first ($n=1$), second ($n=2$) etc nearest neighbours in the crystal structure) of equivalent nuclei

which has eigenvalues

$$E = M_s g_{\text{eff}} \mu_B H + \sum_n \left\{ -m_l(n) g_n \mu_N H + h M_s m_l(n) \right. \\ \times [A(n) + B(n)] \left\{ 3 \cos^2 \theta + \frac{1}{2} h P_n [3 \cos^2 \theta_n - 1] \right. \\ \left. \left. \times \left[m_l^2(n) - \frac{I(I+1)}{3} \right] \right\} \right\},$$

where g_{eff} is the effective g value, $A_0(n)$ and $B(n)$ are the isotropic and anisotropic hyperfine structure parameters corresponding to the n th nucleus ($A_0 = 1/3(A_{xx} + A_{yy} + A_{zz})$ and $B = 1/6(-A_{zz} - A_{xx} - A_{yy})$), θ_n is the angle between the symmetry (Z) axis of the paramagnetic complex and the n th nucleus, with the principal axis of the complex.

And the total nucleus spin quantum number n for the n th shell is given by

$$m_l(n) = \sum_k m_l(k) \\ = kI, kI-1, \dots, -(kI-1), k\delta.$$

The intensity of each hyperfine components depends on (i) the number of ways in which $m_l(n)$ is composed and (ii) the abundance of isotopic species (table 1).

The case of ENDOR of transition metal ion, such as interstitial Cr^+ in Si due to Si ligands, illustrates a complex case with $S > 1/2$ and $I = 1/2$. The effective spin Hamiltonian for this system with $S = 1/2$ is

$$\hat{H} = g \mu_B H \cdot S + 1/6a [S_x^4 + S_y^4 - S_z^4 - 1/5 S(S+1) \\ \times (3S^2 + 3S - 1)] + \sum_i (S \cdot \tilde{A}_i I_i - g_N \mu_N H \cdot I_i).$$

Here, the first term describes the impurity electron-magnetic field interaction, the second term represents the cubic field splitting i.e. the splitting of the ground state multiplet of Cr^+ by a crystalline electric field. In the case of cubic symmetry, the third term is the interaction between the impurity electron and a ^{29}Si nucleus, and the fourth term represents the nuclear Zeeman interaction.

The NMR transitions for this system occur on

4.3 Electron spin echo technique

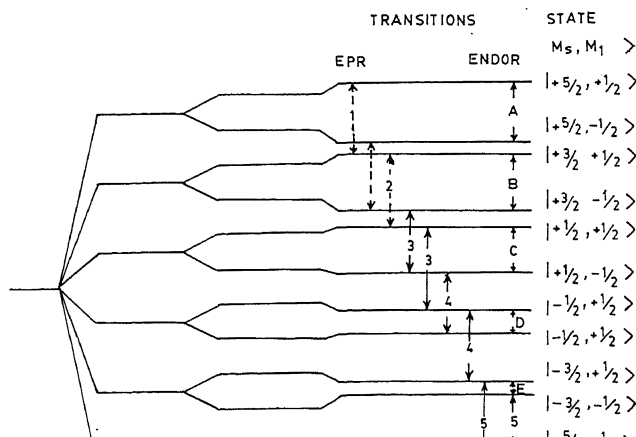
Advanced materials are not often available in single crystal form but are readily obtainable as ceramics and glasses, and they often give broad EPR spectra (linewidth ~ 1 mT, even at low temperature) due to strains and unresolved magnetic interactions due to nearby nuclei as seen by ENDOR in favourable cases. But in cases where this broadening is not resolved, one needs a technique to overcome this problem. This is possible through the electron spin echo technique that utilizes the programmed pulsed excitation of the sample through the inherently coherent, high power microwave radiation and detects the 'echo' signals that the sample 'emits' which may be observed in the time domain to obtain 'phase memory' or 'spin coherence times' of the spin system. Let us illustrate the principle of two-pulse spin-echo formation (Slichter 1978). Let at time $t < 0$ or O^- (figure 6a) the equilibrium magnetization (M_0) of the spin system point along z-axis of an orthogonal co-ordinate system. Then at $t=0$, upon application of a $\pi/2$ or 90° pulse of microwaves, M_0 would be tilted by 90° away from its equilibrium position (figure 6b) parallel to the microwave magnetic field H_1 along x-axis in time $t_w = \pi/2 |\gamma| H_1$, where γ is the gyromagnetic ratio. Left to itself, the pulse will decay, usually exponentially, producing transient or free induction decay of the mag-

netization (figure 6c). This is due to the precession frequencies of inhomogeneous fields of electrons in the sample. A pulse of π applied at $t=\tau$ reverses the direction of electron magnetization vector. Now the vectors are not equilibrium ones and they will return to equilibrium at a definite time. This is used to determine the relaxation time T_2 . The echo is formed 2τ seconds later. This is a refocusing of all the elements of the magnetization reconstruction of the original magnetization.

The so-called phase memory of the spin system, decay of transverse magnetization (in the xy-plane) created by the $\pi/2$ pulse, is governed by relaxation time (T_1) governs the decay of longitudinal magnetization (i.e. M along z-axis). In fact, T_1 is a measure of the time for the magnetization energy to be transferred to the dynamic levels of the lattice, and T_2 is less for electrons.

In a given material containing paramagnetic ions, the dependence of the echo signal on the time interval τ , which is usually recorded in experiments, is governed by: (i) the relaxation process (T_1 and T_2^*) that is perturbed by microwave pulse to the system and (ii) the frequently observed interaction between electrons with magnetic nuclei that causes the echo signal decay or 'electron spin modulation'.

These two processes are statistical in nature, thus one observes a product of random and oscillating functions that give rise to the nuclear environment around the spin system (Dikanev and Ashtashkin 1989; M



5. The ESR spectrometer

5.1 The continuous wave ESR spectrometer

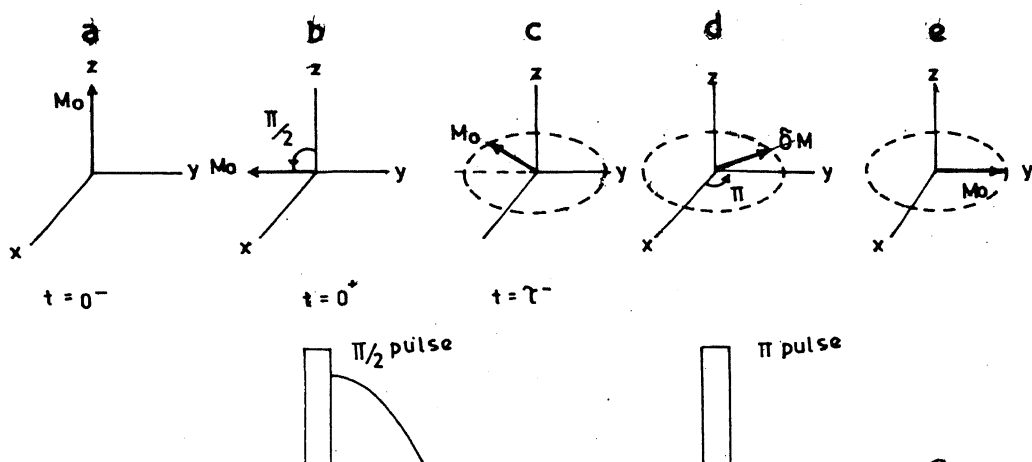
The continuous wave (CW) ESR spectrometer is distinguished from the pulsed ESR experiment. It is a steady-state experiment, where the system of the unpaired electron spin system is kept in equilibrium with the environment.

and measured by comparison with a quartz standard in the frequency counter. A linearly static magnetic field derived from an electromagnet with the pole pieces symmetrically flanking the cavity, a superconducting magnet separates the Kramers' doublets (i.e. two energy levels that differ only in spin projection) and prepares the sample for the resonance experiment. The typical spectrometer for X-band ESR is shown in schematic in figure 7. The typical cavities used and the magnetic field patterns inside them are shown (figure 8). These cavities which may be designed to the incoming microwaves concentrates the magnetic field in its standing wave pattern. The sample is placed in the region corresponding to the maximum of the standing wave magnetic field. The level of power in the cavity may be ascertained by tapping a fraction of it to a crystal (Si-rectifier) detector which converts the microwave radiation into a dc signal.

A small alternating magnetic field modulation (figure 8) is super-imposed on the static field, enables the field to be swept through resonance twice during each cycle. The output signal from crystal detector will be modulated at the frequency of modulation. For high sensitivity modulation frequency should be high compared to the Larmor frequency. Of course there is a trade off between modulation frequency and the excess noise produced by the modulation system. There is a broad minimum around 100 kHz, which corresponds to the maximum sensitivity, and the excess crystal noise ($1/f$ noise) at 100 KHz is

very small. This fact coupled with the simplicity of the design has made 100 KHz as the standard modulation frequency of most commercial spectrometers. Usually a pair of modulation coils are embedded in the walls of the cavity whose walls are thin enough to let the microwave field pass through the modulation coils without attenuation but thick enough to provide a short for microwave frequencies. The static magnetic field strength required depends on the microwave frequency employed. X-band (3.2 cm) work requires up to 0.3 T while for Q-band (~ 8 mm) work fields ~ 1.3 T are required. Work at shorter wavelengths (higher frequencies) such as 4 mm and 2 mm requires superconducting magnets which produce fields ~ 5 T. The magnetic field must be uniform over the volume of the specimen, to the extent of 0.1 ppm to resolve spectra to better than 25 mG ($2.5 \mu\text{T}$). Therefore it has to be stabilized and controlled by a Hall-effect probe located in the magnetic field. A nuclear magnetic resonance fluxmeter (Gaussmeter) is employed to measure the magnetic field and modulation. It can be used for stabilization. Resonance field position can be usually accurate to 5 significant figures.

The usual method of detection is based on the 'heterodyne' principle of mixing the signal reflected from the cavity with the output of a local oscillator (Klystron) operating at 39 MHz above or below signal frequency. This produces an intermediate frequency, which is then amplified and detected. (Note that 30 MHz as measured before corresponds to maximum sensitivity). For detection, 100 KHz signal is sent to a narrow



amplifier and then on to a phase sensitive detector. The operation of the latter is as follows: The amplified signal is mixed with the output of the modulating 100 KHz oscillator. If the two signals are in phase opposition, the output of the system is minimum, if the two phases coincide exactly, the output is maximum. The composite signal is rectified, filtered and recorded. The output signal, i.e. the final ESR spectrum naturally depends markedly on the relative phase and amplitude of the signal and reference voltages. The signal shapes before and after phase sensitive detection are shown in figure 9b.

The actual signal from the spectrometer is proportional to the first derivative of the absorption line contour. If signal dispersion is to be avoided, the amplitude of modulation sweep must be less than half the linewidth of the spectral line (figure 9a). The sensitivity of detection and display system depends only on the bandwidth of the actual recording equipment.

The voltage output of the phase-sensitive detector may be changed to a pulse train by a voltage-to-frequency counter and these pulses are counted and stored in the channels of the signal averager, which enables repetitive scans to be made through the spectrum to improve signal to noise ratio. Finally the output may be plotted as a curve or digitized using an analog-to-digital converter and computer-interfacing electronics.

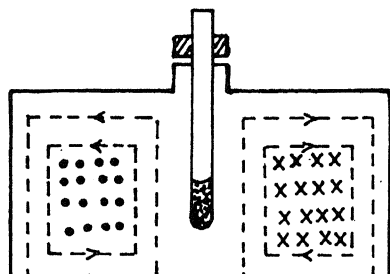
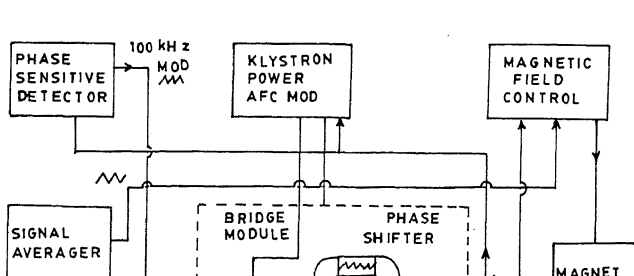
5.2 The pulsed ESR spectrometer

The pulsed or the Fourier transform ESR spectrometer system (figure 10) detects the resonance in the time domain by observing the recovery of the magnetization of the spin system from a condition of extreme non-equilibrium to which it was deliberately driven previously.

In a simplified version of a pulsed-ESR spectrometer, the microwave radiation, from a high power ($\sim 1-2$ kW)

Klystron is converted into microwave by a pulse gate. These pulses are travelling wave tube (TWT) amplified and the resonant cavity situated between the electromagnet. The in-phase components of the magnetization recover simultaneously with separate detection. These two signals are combined as the Fourier transform output.

A general time-domain spectrometer used for relaxation experiments (i) relaxation times could be measured or (ii) time-dependence of ESR signal excitation of the sample could be made as a block diagram (figure 11). The type of pulse sequence necessary. The pulse programmer generates the pulse. The computer also controls the delay after amplification the ESR signal is sent to a bridge, and starts digitizing the signal of the excitation pulse. After recording the digitizer transfers the digitized signal which in turn process it and output. The computer also controls the magnetic scan the magnetic field (for CW) at a desired value (for time-domain) sensor gives the magnitude of the main modules of this spectrometer based microwave set up, (ii) the control (AFC) of Klystron-based frequency oscillator, and (iii) the arrangement based on an electronic phase shifter to correct phase relationship between ESR signal, for any length of time.



number of special purpose continuous wave and ESR spectrometers have been built. Salient features of these are summarized in table 3.

ENDOR spectrometer

ENDOR spectrometer monitors and detects changes in electron spin populations in a sample subjected to simultaneous irradiation at microwave and nuclear magnetic resonance frequencies, at a dc magnetic field corresponding to an ESR transition which is partially saturated. This is done by choosing the microwave power high enough such that the transition probability for the microwave transition far exceeds the spin lattice relaxation when the spin levels connected by the microwave transition become equally populated. This results in a decrease and an eventual disappearance of the observed microwave absorption because microwave emission and absorption probabilities are equal. But the levels not connected by the microwave transitions are not affected. Thus an ENDOR spectrum would be a record of the changes in the ESR signal as the NMR frequency is

The major problem in the ENDOR spectrometer is to get sufficient r.f. power to the sample. There are two solutions to this problem: (i) placing an r.f. coil inside the cavity, either split the cavity to allow r.f. field (Holton and Blum 1962) or use a silvered glass cavity. This method preserves the Q of the cavity (i.e. sensitivity) but is extravagant in the use of r.f. power, and (ii) the r.f. coil is placed inside the cavity so that less r.f. power is required. In any case the r.f. coil is driven by a power amplifier fed by an external tunable oscillator. The details of the ENDOR experiment are as follows. The ESR superheterodyne spectrometer (figure 7) is used for the observation of dispersion or absorption derivative and the magnetic field is set to the centre of the ESR signal. This line is partially power saturated, while ensuring that the magnetic field stays on resonance. Then by varying the r.f. oscillator the nuclear transition is observed as a return of the unsaturated ESR signal. This procedure gives rise to baseline problems because the detection of a small change due to ENDOR in

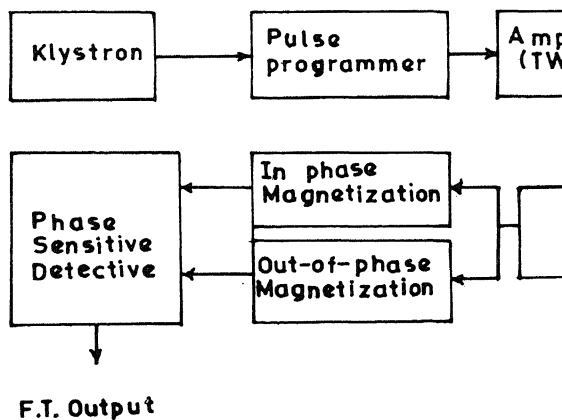
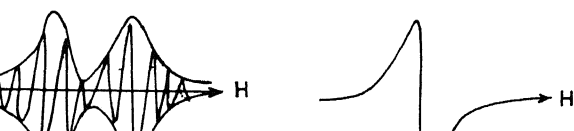
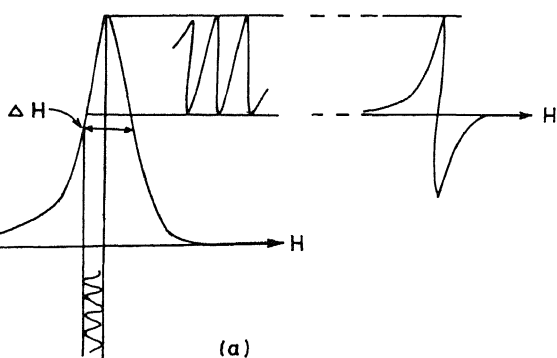
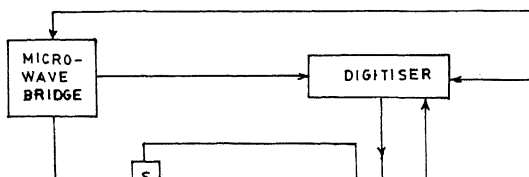


Figure 10. Block diagram of a pulsed ESR spectrometer.



ESR absorption signal. The use of dispersion mode of recording also leads to electronic noise and baseline problems. However, using absorption mode with the r.f. power amplitude modulated at an audio frequency followed by lock-in detection of the ENDOR signal overcomes these problems. In the lock-in detection technique the signal input does not vary in phase relative to the reference signal. Thus the detector output is proportional to the absorption. An output proportional

to the first derivative of the absorption is obtained by frequency modulation of r.f. at an audio frequency ν_m and using a phase-sensitive reference signal set at ν_m . This method is most convenient for investigating hyperfine interactions in materials. Signal averaging is used in the ENDOR spectrometer (Reid 1993). Commercial spectrometers are now available (Bruker Almanac 1993).

Table 3. ESR spectrometers.

Type	Frequency	Main components and characteristics	
1. Continuous wave (CW), portable	9.1–9.6 GHz	Nd–Fe–B permanent magnet (1.3 T) 275 Hz modulation Volume: $0.33 \times 0.12 \times 0.25 \text{ m}^3$	Radiationless ESR
2. CW	300 MHz	Loop gap resonator: 10.2 cm outer diameter, 15.0 cm long with 1.55 cm gap separation Unloaded Q: 5000. Automatic tuning, coupling and phase control circuits. Magnetic field gradient coils	<i>In vivo</i> ESR; biological applications
3. CW	250 MHz	Strip-line type resonator	<i>In vivo</i> ESR
4. CW microstrip induction spectrometer	X-band	Microstrip bimodal square patch resonator Superheterodyne detection	Thin film ESR
5. Pulsed	X-band	Klystron, Waveguide-based diode switches, Boxcar integrator	Measurement of lattice relaxation times, echo lifetime
6. CW/pulsed	X-band	Computer-controlled magnetic field-microwave frequency interlock saturation recovery	Spin relaxation of radicals, with transition
7. CW/pulsed		High power (1 kW) TWT amplifier. Low power (20 w) CW TWT amplifier	
8. Spin-echo		Pulsed Travelling Wave Tube (TWT) 'pulse former'. Low noise TWT-based homodyne detection	
9. Pulsed/CW (Transmission)	140 GHz	Pulsed: Extended interaction Klystron (300 w). 3.0 T field; Fabry–Perot resonator; signal averaging CW: phase locked 139.5 GHz Gunn oscillator; 500 Hz modulation and phase detection; digital oscilloscope	Dynamic ESR of electrons; high sensitivity; time scale; spectral resolution
10. Magnetic resonance force microscopy		Detection of ESR through periodic saturation of electron spin magnetization; Force between field gradient and spin moments measured with a microcantilever	Imaging

The ESR spectrum and its analysis

The ESR spectrum

The ESR spectrum is generally a plot of the first derivative of the imaginary part of the complex magnetic susceptibility of the paramagnetic system with respect to the applied dc magnetic field. The spectrum may consist of a single line or a group of lines, and could change with changes in temperature or the orientation of the specimen (e.g. a stretched polymer or a Si single crystal) relative to the magnetic field. Four basic quantities obtainable from the spectrum are: (i) g -factor or g -tensor, (ii) hyperfine splitting parameter or A -tensor, (iii) line position and line width, and (iv) double integrated intensity. Analysis of these four quantities reveal the following information about the system: (i) the nature of the paramagnetic centre or complex, i.e. electron or 'hole'-type, (ii) the precise identity of the complex/centre in terms of its nearest neighbours and symmetry, (iii) the distribution of unpaired spin density over the neighbours, and (iv) the number of paramagnetic centres per unit volume, and thus the bulk paramagnetic susceptibility of the material.

The g -factor: In the simplest of cases—that of a spin system $S = 1/2$ with a single line spectrum arising from the transition from $M_s = -1/2$ to $M_s = +1/2$ —the resonance condition $h\nu = g\mu_B H_r$, where h is Planck's constant and μ_B the Bohr magneton gives the g -factor, the frequency ν is accurately known and H_r is measured accurately from the spectrum. For example, $g = 21.4198\bar{\nu}/H_r$ ($\bar{\nu}$ in cm^{-1} , H_r in deca Tesla or 1557×10^{-6} (ν in Hz, H_r in mT)). However, it is not possible to determine g accurately using standard samples along with the test samples. A selection of these standard samples are given in table 4.

In general, neither is $g = 2.0023$, the free electron g -factor, nor is it a single number, i.e. isotropic with respect to sample rotation within the magnetic field. The

anisotropic g (particularly in materials with transition metal ions as impurities) arises from the coupling of the orbital angular momentum to the spin angular momentum via spin-orbit interaction. The effective Zeeman interaction responsible for the ESR spectrum is represented as the leading term in the spin Hamiltonian

$$\mathcal{H}_Z = \mu_B \hat{S} \tilde{g} \hat{H},$$

where \tilde{g} is a second-rank symmetric tensor and \hat{S} is the effective spin operator. With reference to a Cartesian coordinate frame x, y, z in which the electron magnetization is parallel to the applied magnetic field when the latter has components along x, y and z , \mathcal{H}_Z becomes

$$\mathcal{H}_Z = \mu_B (g_{xx} S_x H_x + g_{yy} S_y H_y + g_{zz} S_z H_z).$$

A study of a monocrystalline material (e.g. BaTiO_3) or a glassy material (e.g. photochromic glass) is a first step at obtaining g_{xx} , g_{yy} and g_{zz} and their direction relative to x, y and z through angular variation of the ESR spectrum or computer simulation of observed spectrum—a first step in the analysis of the spectrum from which further details are available. In general, a value of $g_{av} = (g_{xx} + g_{yy} + g_{zz})/3 > 2.0036$, is referred to as a 'hole centre' (e.g. V centre in X-irradiated alkali halides) while a centre with $g_{av} \leq 2.0036$ is called an 'electron excess centre' (F-centre in alkali halides) (Hershen and Garrison 1973).

In case of paramagnetic systems, in which the ground and excited states are mixed by spin (S)–orbit (L) interaction ($\lambda L \cdot S$), the elements of the g -tensor are given by

$$g_{ij} = 2\delta_{ij} - 2\lambda \frac{\langle nl L_i | 0 \rangle \langle 0 | L_j | n \rangle}{E_n - E_0},$$

where $\delta_{ij} = 1$ if $i = j$ or 0 otherwise, $|0\rangle$ is the singlet ground state of energy E_0 , $|n\rangle$ is the excited state of energy E_n and λ is the spin–orbit coupling constant.

Table 4. Standards for calibration of g -values.

Standard	g -value	ΔH_{pp} (mT)	Spin concentration (cm^{-3})
DMF (Di phenyl picryl hydrazyl)	2.0037(2)	0.28	1.5×10^2

(see table 2 for numerical values of λ). The larger the λ , the larger is the deviation of g from 2.0023, the 'free spin' value.

6.1b *The hyperfine coupling constant (A):* Just as the quantization of electron spin produces the simple ESR spectrum, quantization of the nuclear spin ($I, (2I+1)m_I$) of the magnetic nucleus associated with the unpaired electron (e.g. H atom, $S=1/2, I=1/2$) gives rise to additional splitting of levels ($\Delta M_s = \pm 1, \Delta m_I = 0$) due to the interaction between the electronic magnetic dipole and nuclear magnetic dipole.

In terms of the spin operators S and I ,

$$\mathcal{H}_{\text{hf}} = S \cdot A \cdot I, \quad (28)$$

where A is a symmetric second-rank tensor like g . In a reference frame xyz where A is diagonal,

$$\mathcal{H}_{\text{hf}} = A_{xx} S_x I_x + A_{yy} S_y I_y + A_{zz} S_z I_z. \quad (29)$$

In a majority of cases, however, the A -tensor is axially symmetric, so that

$$\mathcal{H}_{\text{hf}} (\text{axial}) = A_{\parallel} S_z I_z + A_{\perp} (S_x I_x + S_y I_y), \quad (30)$$

where z -axis being the axis of symmetry of the complex containing the unpaired electron. The A -tensor contains information about (i) isotropic contribution (A_{iso}), due to s -electron density at the magnetic nucleus and (ii) the anisotropic contribution due to the spin and orbital dipole-dipole interactions with the nuclei. The so-called Fermi-constant interaction is the origin of $A_{\text{iso}} = (A_{\parallel} + 2A_{\perp})/3$. This interaction is given by

$$\mathcal{H}_{\text{contact}} = \frac{8\pi}{3} g \cdot \mu_B g_N \mu_N |\psi(0)|^2 \text{ S.I.}, \quad (31)$$

from which

$$\begin{aligned} A_{\text{iso}} &= \left(\frac{8\pi}{3} \right) g \mu_B g_N \mu_N |\psi(0)|^2 \\ &= 4.24 g_N |\psi(0)|^2 \text{ (mT)} \text{ using } \mu_N = \mu_B/1836, \end{aligned} \quad (32)$$

where g and g_N are electron and nuclear g factors and μ_B and μ_N are Bohr and nuclear magnetons, and $|\psi(0)|^2$ (in cm^{-3}) is the unpaired electron density at the

A_{iso} (theory) has been computed for atoms from H to Bi (McMillan 1974). In the case of paramagnetic ions such as Cu^{2+} , Fe^{3+} , etc., the $3d$ orbitals give a large value of A_{iso} , despite the low s -electron density at the nucleus, Fermi contact interaction account for A_{iso} . In such cases the $3d$ orbitals have a sizeable spin density at the nucleus, and these 'core' electrons give a large A_{iso} given by:

$$A_{\text{iso}} (\text{core polarization}) =$$

$$\frac{8\pi}{3} g_p \mu_B g_N \mu_N \sum_{ns} \{ |\psi_{ns}(0)|^2 \uparrow \}$$

where arrow ' \uparrow ' indicates the spin of the unpaired electron (McMillan 1974).

The anisotropic part of the A_{aniso} is due to the dipole-dipole interaction between electron and nuclear dipoles.

$$\mathcal{H}_{\text{dipolar}} = g_e g_N \mu_B \mu_N \left[\frac{S \cdot I}{r^3} - \frac{3(S \cdot r)(I \cdot r)}{r^5} \right]$$

which may be written in terms of the vector (r) joining electron and nucleus and the magnetic field

$$\mathcal{H}_{\text{dipolar}} = g_e g_N \mu_B \mu_N \left(\frac{3 \cos^2 \theta - 1}{r^3} \right) I_z$$

In terms of equivalent magnetic field H_{eq} , the dipole-dipole interaction gives rise to the anisotropic hyperfine interaction

$$A_{\text{aniso}} = \mu_N g_N \left\langle \frac{3 \cos^2 \theta - 1}{r^3} \right\rangle I_z,$$

spatially averaged over all of the orientations of the vector r . A_{aniso} is thus proportional to I_z .

A typical polycrystalline ESR spectrum of Cu^{2+} in KHSO_4 (Ramasastry and Sunandana 1974) in an environment of rhombic symmetry is shown in figure 12.

larly for transition metal ion ESR. If $\Delta t = T_1$, the lattice relaxation time, then the magnitude of T_1 decide the 'lifetime' broadening and linewidth. Linewidth is related to the intensity through the Lorentzian function because the computation of the intensity depends on the lineshape function.

Individual ESR signals usually have two familiar shapes (Fessenden and Schuler, 1983) — the Lorentzian and Gaussian shapes — the former is due to a homogeneous broadening mechanism in which all dipoles experience the same static magnetic field but different instantaneous magnetic fields. The latter corresponds to the inhomogeneous broadening in which the dipoles are subjected to slightly different effective magnetic fields. At a given time only a small fraction of the dipoles is in resonance as the external magnetic field is swept through the line. Thus the observed signal is a superposition of a large number of slightly staggered Lorentzian 'spin packets' or an envelope. An inhomogeneous magnetic field or anisotropic interactions (g-factor hyperfine structure) in materials like glasses and polymers or unresolved hyperfine structure results in complex line shapes. Metal clusters and conduction electrons in semiconductors give Lorentzian and the Dysonian ESR lines respectively, while defects and free radicals in insulators give Gaussian lines. Normalized plots of Lorentzian and Gaussian lineshapes are shown in figure 13 (Sunandana and Srinivasan, 1983) while the mathematical expressions for possible line shapes are given in table 5. Lorentzian lines are broader than those broadened by T_1 . A relaxation time T_2 could be related to the width of the normalized line, in the absence of saturation, as

$$\left\{ \begin{array}{l} \text{shape} \\ \text{constant} \end{array} \right\} \left\{ \begin{array}{l} \text{gyromagnetic} \\ \text{ratio} \end{array} \right\} \left\{ \begin{array}{l} \text{linewidth at} \\ \text{half height} \end{array} \right\}, \quad (39)$$

where the shape constant is unity for Lorentzian and $\sqrt{2}$ for Gaussian lines. $1/T_2$ being a linear function of linewidth, includes 'lifetime' or T_1 broadening and other homogeneous mechanisms characterized by T_2' so

$$= \frac{1}{T_2'} + \frac{1}{2T_1}, \quad (40)$$

where T_1 is the spin-spin relaxation time, usually $\ll T_1$ for free

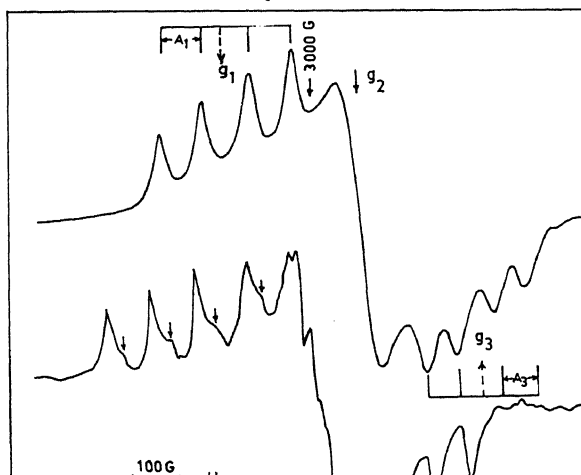
sample and to the net paramagnetic susceptibility of the sample.

Assuming that (a) ESR lineshape is Lorentzian, (b) the Curie law (i.e. $\chi \propto 1/T$) is applicable, (c) the microwave power applied to the sample does not saturate the resonance, and (d) the signal-to-noise ratio is unity, if the ESR cavity is unity, the ESR detection sensitivity is the minimum number of paramagnetic centres detectable in ESR (N_{\min}) Feher (1959) is given by

$$N_{\min} = \frac{3 V_c k T_s \Gamma}{2 \pi g^2 \mu_B^2 S(S+1) H_1 Q_u'} \left(\frac{F k t_d b}{P_0} \right)^{1/2},$$

where V_c is the volume of the rectangular cavity operating in the TE_{102} mode; k the Boltzmann constant; T_s the sample temperature; Γ the half width at half maximum (Gauss) of the absorption line; H_1 the magnetic field at the centre of the absorption line; Q_u' the effective unloaded Q factor of the cavity $= Q_e Q_u / (Q_e + Q_u)$ (Q_e the dielectric Q , Q_u = unloaded Q); T_d the detector temperature; b the bandwidth (Hz) of the entire detecting and amplifying system; P_0 the microwave power (erg/s) incident on the cavity; F the noise figure (due to sources other than the thermal detector) = 1 for an ideal spectrometer.

Typically, $Q_u' = 5000$, $T_s = T_d = 300$ K, $H_1 = 0.1$ mT, $g = 2.00$, $S = 1/2$, $V_c = 11$ cc (X-band cavity); $F = 100$; $b = 1$ Hz; $P_0 = 10^6$ erg/s = 100 mW, that $N_{\min} \approx 10^{11}$ ('Worst case sensitivity') (Went and Bolton 1972).



The absolute intensity of the observed ESR signal is determined by: (i) the area under the absorption curve or the double integrated first derivative curve (A), (ii) modulation amplitude (M), (iii) amplitude of the magnetic component of microwave field (H_1) at the sample. H_1 is a function of P_0 , Q'_0 and its own distribution within the cavity, (iv) the receiver gain of the spectrometer (G), (v) sample temperature, (vi) g -factor, (vii) microwave frequency, and (viii) filling factor (η). $\eta \sim 2V_s/V_c$, where V_s is the sample volume and V_c the cavity volume.

Assuming that the geometry of the cells are the same, so that H_1 is the same for neither the standard nor sample cells. If the concentration $[x]$ of the paramagnetic species in the sample is given, relative to that of the standard, by

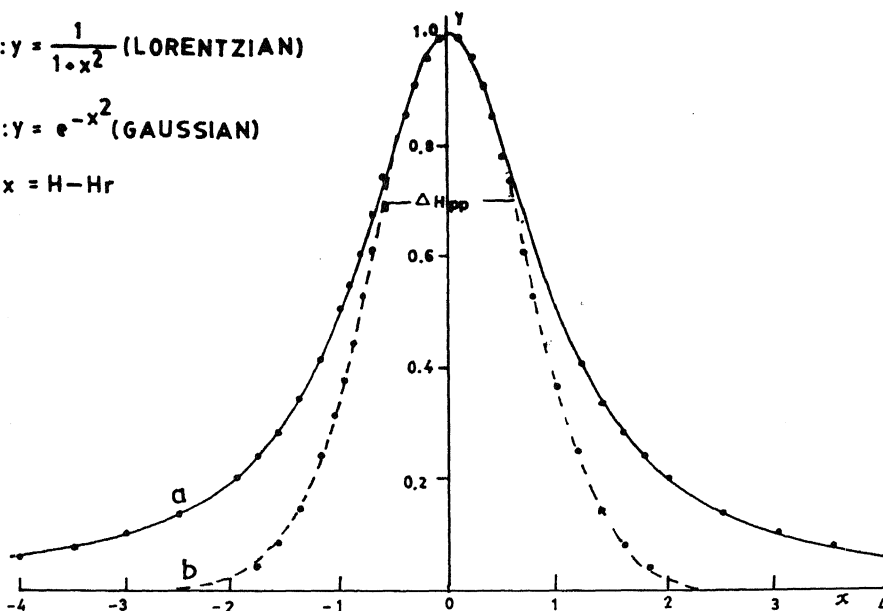
$$[x] = \frac{[\text{std}] A_x G_s M_s g_s^2 [S(S+1)]_{\text{std}}}{A_s G_x M_x (g_x)^2 [S(S+1)]_x},$$

provided the scanning of the magnetic field is the same for both.

$$a: y = \frac{1}{1+x^2} \text{ (LORENTZIAN)}$$

$$b: y = e^{-x^2} \text{ (GAUSSIAN)}$$

$$x = H - H_r$$



$$c: \frac{dy}{dx} = \frac{-2x}{1+x^2}$$

$$d: \frac{dy}{dx} = -2xe^{-x^2}$$

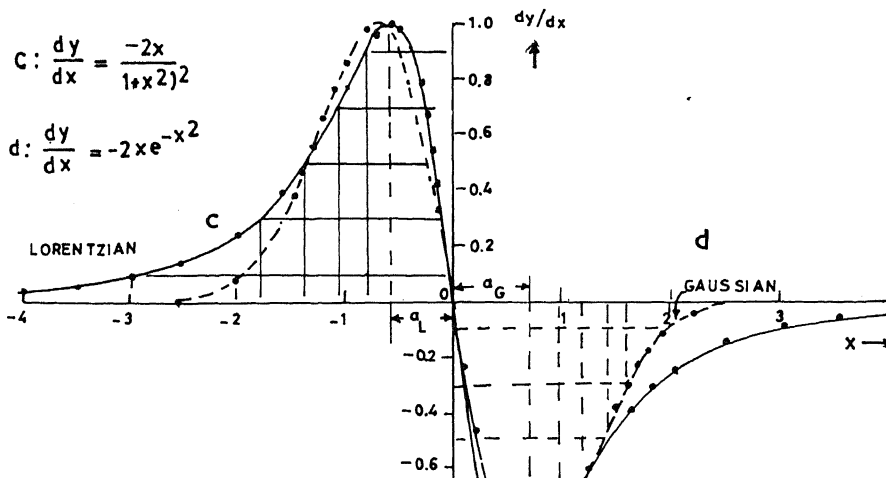


Table 5. ESR lineshapes.

Absorption lineshape and linewidth	First derivative absorption		Area
	Lineshape	Linewidth (fullwidth at half maximum) $\Delta H_{1/2}$	
<p>Lorentzian</p> $Y = \frac{y_m}{1 + \frac{1}{2} \Delta H_{1/2}^2 \frac{(H - H_r)^2}{\Delta H_{pp}^2}}$ <p>y_m = maximum amplitude $\Delta H_{1/2}$ = half-amplitude linewidth</p>	$\frac{dY^L}{dH} = \frac{16y_m \frac{(H - H_r)}{\frac{1}{2} \Delta H_{pp}}}{3 + \left[\frac{(H - H_r)^2}{\frac{1}{2} \Delta H_{pp}^2} \right]}$ <p>y_m = total vertical height H_r = resonance field ΔH_{pp} = peak-to-peak width</p>	$\sqrt{3} \Delta H_{pp}$	$\frac{2\pi}{\sqrt{3}} Y_m (\Delta H_{pp})$
<p>Gaussian</p> $Y = Y_m \exp \left[-0.693 \left[\frac{H - H_r}{\frac{1}{2} \Delta H_{1/2}} \right]^2 \right]$	$\frac{dY^G}{dH} = y_m \left[\frac{H - H_r}{\frac{1}{2} \Delta H_{pp}} \right]$ $\exp \left[-\frac{1}{2} \left\{ \left(\frac{H - H_r}{\frac{1}{2} \Delta H_{pp}} \right)^2 - 1 \right\} \right]$	$\sqrt{2 \ln 2} \cdot \Delta H_{pp}$	$(2\pi e) Y_m \left(\frac{1}{2} \Delta H_{pp} \right)$
<p>Integrated</p> $= \frac{\sqrt{\ln 2}}{\pi} \left(\frac{\Delta H_{1/2}^L}{\Delta H_{1/2}^G} \right) x$ $e^{-x^2} dx$ $\left(\frac{\Delta H_{1/2}^L}{\Delta H_{1/2}^G} \right)^2 \ln 2 + \left(2 \sqrt{\ln 2} \left[\frac{H - H_r}{\Delta H_{1/2}^G} - x \right] \right)$			
<p>Δ_{pp}^V (observed) = $\frac{\Delta_G^2 + 0.9085 \Delta_G \Delta_L + 0.4621 \Delta_L^2}{\Delta_G + 0.4621 \Delta_L}$</p> <p>$\Delta_G$ = Assumed Lorentzian and Gaussian half-widths</p>			
<p>Derivative Lorentzian</p> $= - \left[\frac{\omega H_1^2 R^2 \omega_0 x_0 T_1 A \delta}{8} \right] F_D(R, x, \chi, \eta)^*$			

$$F_D(R, x, \chi, \eta) = \left\{ \frac{R^4(x^2 - 1) + 1 - 2R^2}{2} \left[\frac{2\chi}{2 - \chi^2 + 4} + R^2(x + 1) - 3 \right] + \frac{2R^2(1 - R^2x)}{2 - \chi^2 + 4} \left[\frac{2\eta}{2 - \chi^2 + 4} + R^2(x - 1) - 3 \right] \right\}$$

the same way for standard and sample. If the lineshape of the ESR signal is accurately known (to be Lorentzian or Gaussian) then an estimate of the number of spins per unit volume (N_s) may be made using the formula

$$N_s = I_{pp} \Delta H_{pp}^2, \quad (43)$$

where I_{pp} is the peak-to-peak amplitude (intensity) and ΔH_{pp} the peak-to-peak width of the resonance line. Kwan and Yen (1979) have given the modified, easy to apply, but exact formula

$$N_s = 0.285 I_{pp} \Delta H_{10}^2, \quad (44)$$

where ΔH_{10} is the width at the position 1/10 of the peak-to-peak height of the first derivative curve.

The high frequency magnetic susceptibility involved in ESR is $\chi^* = \chi'(\omega) - i\chi''(\omega)$, where $\chi'(\omega)$ is the real part or the dispersion component, and $\chi''(\omega)$ is the imaginary or absorption component (strictly speaking χ'' is also a function of magnetic field which considerably alters the description of ESR spectra (Zhong and Pilbrow 1991)). The measurement of the usually processed ESR absorption signal, proportional to $\chi''H_1$ or the derivative proportional to $d(\chi''H_1)/dH_1$, where H_1 is the strength of the microwave magnetic field, leads to the paramagnetic susceptibility of the sample. But unlike in the conventional measurement of χ using Faraday or Guoy balance or vibrating sample magnetometer there is no need to correct for the diamagnetic contribution to χ in the ESR measurement.

The absorption susceptibility is given by

$$\chi'' = P_0 (2\omega H_1^2)^{-1}, \quad (45)$$

where P_0 is the power absorbed by the spin system when the microwave field H_1 is perpendicular to static field H and $\omega = 2\pi\nu$, ν being the microwave frequency. For an unpaired spin system $S = 1/2$ with isotropic g

$$\chi'' = \delta N \frac{1}{4} \pi g^2 \beta^2 \frac{f(\nu - \nu_0)}{h}, \quad (46)$$

where $\delta N = N(+1/2) - N(-1/2)$, the population difference between states with $M_s = +1/2$ and $M_s = -1/2$ and

of the population difference. For an unpaired spin broadened ESR signal i.e. one due to a distribution of whose resonance fields form a Gaussian distribution due to unresolved hyperfine interactions of the spin with nearby magnetic nuclei, the steady state

$$\frac{d}{dt}(\delta N) = 0 = \frac{1}{T_1} [(\delta N)_0 - \delta N] - 2\delta N W$$

where W is probability for the $M_s = +1/2 \rightarrow -1/2$ transition, given by $\pi^2 (g^2 \mu_B H_1)^2 f(0)/h$

$$\delta N = (\delta N)_0 \left[\frac{1 + 2\pi^2 (g\mu_B H_1)^2 T_1 f(0)}{h^2} \right]^{-1}$$

and finally

$$\chi''(\nu_0) = (\delta N)_0 \frac{1/4 \pi (g\mu_B)^2 f(0)}{h} \times \left[\frac{1 + 2\pi^2 (g\mu_B H_1)^2 T_1 f(0)}{h^2} \right]^{-1}$$

Thus for small H_1 , the ESR absorption is proportional to H_1 while for large H_1 it is proportional to H_1^{-1} (figure 14) (Sunandana 1991). For measurements of spin concentration N_s it is important to avoid saturation of the ESR signal. Measurements are made on saturated ESR

6.2 Analysis of ESR spectra

Advanced materials may be single crystalline or microcrystalline or glassy, and, thus, ESR spectra may be rich and well-resolved or poorly resolved. Single crystal ESR spectra contain maximum information in the way of well-resolved and narrow lines. In polycrystalline or glassy materials, the magnetic centre trapped at several symmetry inequivalent crystallographically distinct sites in the crystal lattice often having magnetic neighbours that interact with the unpaired electron. However, in polycrystalline or glassy materials, the ESR spectra often contain poorly resolved/unresolved features from which it is difficult to extract spin Hamiltonian parameters.

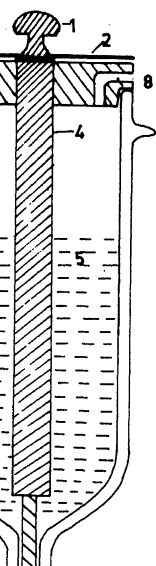
Techniques and applications of electron spin resonance

s and sometimes from the neighbouring magnetic as in silicon alkali halides.

task of deducing the principal g - and A -values two tensors begins with the identification of three mutually perpendicular directions in the crystals (e.g. [1010] and [001] axes of an orthorhombic crystal). These need not always correspond to the crystallographic axes. Then ESR spectra are recorded for rotations of the crystal mounted on a specially designed goniometer (Fig. 15), about each of the three orthogonal axes, say x , y and z -axes. The rotations about a given axis, say x , i.e. in a given plane yz are affected every 5° or depending on the magnitude of the anisotropy. From three sets of spectra arising from rotations about the three axes, 'isofrequency plots' are generated, plotting the resonance magnetic field of each observed line against the orientation θ of the crystal (in a given plane) relative to the dc magnetic field. After identifying groups of lines corresponding to either chemically distinct centres or physically distinct but chemically equivalent centres, isofrequency plots of g_{ij}^2 or $(g^4 A^2)_{ij}$ ($ij = xy, yz, zx$) vs θ are generated. Thereafter each of the observed plots are fitted, by the method of least squares to the expression

$$(\theta) = U + V \cos 2\theta + W \sin 2\theta, \quad (49)$$

a similar equation for $g^4 A^2$, where



1. Rotation head (aluminium)
2. Cursor on perspex disc
3. Perspex disc graduated in degrees
4. Perspex rod
5. Liquid nitrogen
6. Teflon crystal holder
7. Crystal stuck by silicone grease
8. Escape for nitrogen vapours

$$U = \frac{g_{ii}^2 + g_{jj}^2}{2}, \quad V = \frac{g_{ii}^2 - g_{jj}^2}{2} \quad \text{and} \quad W = g_{ij}^2.$$

Then the elements of the g^2 or hyperfine tensors are found and the matrix formed is symmetrized and diagonalized either directly, or using the Schorr (1959) method. This latter method consists in accurately locating the maxima and minima, using the relation $\tan 2\theta = W/V$ and forming the matrix elements as follows:

$$\{g^2\} = G = \begin{bmatrix} G_{xx} & G_{xy} & G_{xz} \\ G_{yx} & G_{yy} & G_{yz} \\ G_{zx} & G_{zy} & G_{zz} \end{bmatrix},$$

where

$$G_{xx} = \alpha_y + \alpha_z - \alpha_x, \quad G_{yy} = \alpha_z + \alpha_x - \alpha_y,$$

$$G_{zz} = \alpha_x + \alpha_y - \alpha_z,$$

$$G_{yz} = \pm \sqrt{(\delta_x + \alpha_y - \alpha_z)(\delta_x - \alpha_y + \alpha_z)},$$

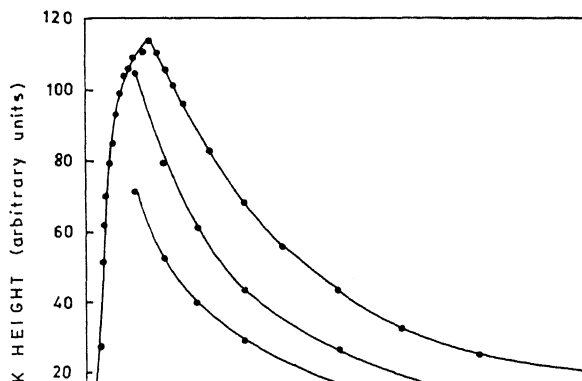
$$G_{zx} = \pm \sqrt{(\delta_y + \alpha_z - \alpha_x)(\delta_y - \alpha_z + \alpha_x)}, \quad \text{and}$$

$$G_{xy} = \pm \sqrt{(\delta_z - \alpha_x + \alpha_y)(\delta_z - \alpha_x + \alpha_y)}.$$

α 's and δ 's are determined by the accurately measured g_{\max}^2 and g_{\min}^2 for each of the three rotations and given by

$$\alpha_i = \frac{g_{\max}^2(i) + g_{\min}^2(i)}{2} \quad \text{and} \quad \delta_i = \frac{g_{\max}^2(i) - g_{\min}^2(i)}{2}$$

$i = x, y \text{ or } z.$



If the paramagnetic centre is found at n_1 sites for rotations about x-axis, n_2 sites for rotations about y-axis and n_3 sites for rotations about z-axis, then one has to sort out the correct matrix elements and matrix out of a possible n_1, n_2 and n_3 combinations of maxima and minima. The choice can be narrowed down by seeking coincidences in the g_{ij}^2 values (for example, g_{xx}^2 occurs twice, once each for rotations about y and z-axes) (Sunandana 1975). Finally, the diagonalization of the matrix is effected (using Jacobi method for instance) so that

$$\begin{bmatrix} l_{xx} & l_{xy} & l_{xz} \\ l_{xy} & l_{yy} & l_{yz} \\ l_{xz} & l_{yz} & l_{zz} \end{bmatrix} \begin{bmatrix} g_{xx}^2 & g_{xy}^2 & g_{xz}^2 \\ g_{xy}^2 & g_{yy}^2 & g_{yz}^2 \\ g_{xz}^2 & g_{yz}^2 & g_{zz}^2 \end{bmatrix} \begin{bmatrix} l_{xx} & l_{xy} & l_{xz} \\ l_{xy} & l_{yy} & l_{yz} \\ l_{xz} & l_{yz} & l_{zz} \end{bmatrix}^{-1} \\ = \begin{bmatrix} g_{xx}^2 & 0 & 0 \\ 0 & g_{yy}^2 & 0 \\ 0 & 0 & g_{zz}^2 \end{bmatrix}. \quad (54)$$

Taking the square root of the elements of the diagonal matrix gives the principal values of g-tensor. The direction cosine matrix gives the directions of $g_{xx}(l_{xx}, l_{xy}, l_{xz})$, $g_{yy}(l_{xy}, l_{yy}, l_{yz})$ and $g_{zz}(l_{xz}, l_{yz}, l_{zz})$. Once the principal g- and A-values and their direction cosines are known, the ESR centre can be located in the crystal (Atherton 1973).

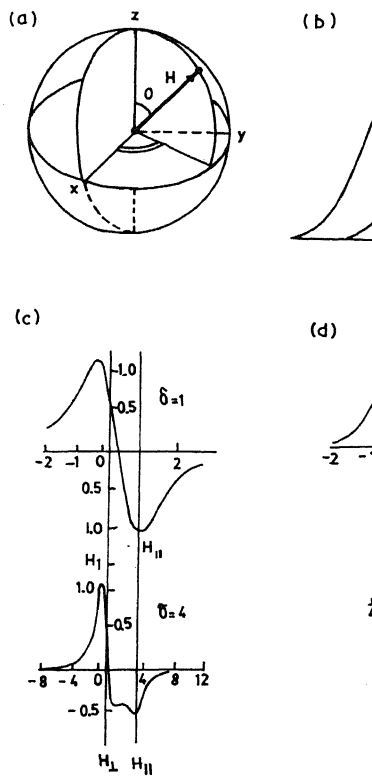
Single crystal EPR spectra of transition metal compounds occasionally consist of a single structureless, perfect Lorentzian line, for certain orientation of the crystal that indicate exchange averaging of g- and A-anisotropy and local dipolar fields. Such anomalous angular variation observed in (2,2'-bipyridine-3,3'-dicarboxylic acid) dichloro copper (II) monohydrate, in which long-range exchange interaction via lattice water was observed, has been analysed for the molecular g-tensor using a decoupling procedure that uses a molecular coordinate system and relates it to the crystal axes system through a coordinate transformation, in order to overcome the effect of incomplete averaging of g-anisotropy (Balagopala Krishna and Rajasekharan 1990).

6.2b Polycrystalline ESR spectra: Almost all varieties of advanced materials including electro-ceramics, optical materials, catalysts, polymers and glasses are composed of randomly oriented, small crystallites. The ESR spectra

equally probable. The number of field orientation between θ and $\theta + \Delta\theta$ and $\phi + \Delta\phi$ are given by the solid angle

$$\Delta\Omega = \sin\theta \Delta\theta \Delta\phi.$$

But only a fraction of these rays contribute to microwave energy absorption between H and $H + dH$, this fraction is dH/H for an individual linewidth ΔH and the total absorption is $\int_{H_r-H}^{H_r+H} f(H_r-H, \Delta H) dH$ where H_r the resonance field of the crystal is itself a function of orientation, θ and ϕ . The aim is to determine the total absorption at the magnetic field H . The intensity of the ESR signal at a given magnetic field is the derivative of the defined above and the element of solid angle $d\Omega$ over all solid angles, because all orientations contribute to the absorption, in principle:



$$\begin{aligned}
 &= 1/4 \pi \sum f(H_r - H, \Delta H) \Delta \Omega_i \\
 &= 1/4 \pi \sum_{j=0}^{2\pi} \sum_{i=0}^{\pi} f(H_r - H, \Delta H) \sin \theta_i \Delta \theta_i \Delta \theta_j \\
 &= 1/4 \pi \int_0^{2\pi} \int_0^{\pi} f(H_r - H, \Delta H) \sin \theta d\theta d\phi, \quad (56)
 \end{aligned}$$

integral sign has replaced summation and $1/4\pi$ normalized factor.

the derivative absorption is usually measured

$$\frac{I}{H} = 1/4 \pi \int_0^{2\pi} \int_0^{\pi} f'(H_r - H, \Delta H) \sin \theta d\theta d\phi.$$

specific form of the function $f'(H_r - H, \Delta H)$ depends the shape of the individual derivative curves. For Lorentzian absorption curve,

$$\begin{aligned}
 f(H_r - H, \Delta H) &= \frac{16}{\pi(\sqrt{3} \Delta H)^3} (H_r - H) \\
 &\times \left[i + 4/3 \left(\frac{H_r - H}{\Delta H} \right)^2 \right]^{-2}, \quad (57)
 \end{aligned}$$

H is the swept magnetic field and ΔH the magnetic field separation between the maximum and the minimum of the derivative curve, assumed to be constant, although it may be orientation dependent.

The spin Hamiltonian for the given situation decides the form taken by H_r . If the paramagnetic centre experiences only the Zeeman interaction, and has only one symmetry axis along z-axis, then

$$g_{xx} = g_{yy} = g_{\perp} \text{ and } g_{zz} = g_{\parallel}.$$

$$\nu_0 = (h\nu_0/\mu_B) (g_{\parallel}^2 \cos^2 \theta + g_{\perp}^2 \sin^2 \theta)^{-1/2}, \quad (58)$$

ν_0 is the experimental microwave frequency. Trivial consequences of the above equations occur when θ is $\pi/2$ or 0 , respectively, when

$$\nu_0 = \frac{h\nu_0}{\mu_B} \quad \text{and} \quad \nu_0 = \frac{h\nu_0}{\mu_B} \quad (59)$$

glasses is quite general as there is a distribution of anisotropic g -values due to random local structural fluctuations, which gives

$$g^2 = g_{xx}^2 \sin^2 \theta \cos^2 \phi + g_{yy}^2 \sin^2 \theta \sin^2 \phi + g_{zz}^2 \cos^2 \theta$$

where θ and ϕ relates as usual the resonance field with the principal axes of the g -tensor. The anisotropic linewidth that occurs in the lineshape function is expressed by a similar function

$$\begin{aligned}
 \Delta H^{-2} &= \Delta H_{xx}^{-2} \sin^2 \theta \cos^2 \phi + \Delta H_{yy}^{-2} \sin^2 \theta \sin^2 \phi \\
 &+ \Delta H_{zz}^{-2} \cos^2 \theta,
 \end{aligned}$$

where ΔH_1 , ΔH_2 and ΔH_3 are the half widths along the principal directions collinear with the corresponding principal axes of the g -tensor. Thus the simulated first derivative ESR spectrum has the general form

$$\iint f \left(\frac{H - H_r}{\Delta H} \right) \sin \theta d\theta d\phi.$$

The ESR spectrum of amorphous MoS_3 has been simulated to obtain reasonably accurate g -values for the sulphur hole centre and Mo(V) ions surrounded by sulphur and oxygen atoms (Berger and Haddad 1991). Taylor and co-workers (1975) have given an exhaustive account of the simulation of ESR spectra of polycrystalline solids. They have treated three cases of usually encountered powder spectra: (I) the most simple case of only the electron Zeeman term i.e. the first term in the general spin Hamiltonian

$$\mathcal{H} = \mu_B S \cdot g \cdot H + S \cdot A \cdot I + S \cdot D \cdot S + I \cdot Q \cdot I - \mu_N I \cdot$$

being dominant while the four other terms — hyperfine interaction, fine structure (that occurs for paramagnetic ions with $S > 1/2$, e.g. Mn ($S = 5/2$) and triplet state organic radicals ($S = 1$)) and the much smaller quadrupole and nuclear Zeeman — are neglected, with two cases (i) axial symmetry — ($g_{xx} = g_{yy} = g_{\perp}$, $g_{zz} = g_{\parallel}$, $g_{\perp} > g_{\parallel}$) — corresponding to a shoulder and a divergence, and (b) the completely anisotropic (rhombic case) $g_x > g_y > g_z$. (II) the

There exists an important relation between the ESR spectra of powders and those of single crystals: the turning points in the angular dependence of resonance fields of the single crystal determine the peak positions in this spectrum of the corresponding powder. Exploiting this relationship, Van Veen (1978) has shown that the derivatives of the resonant positions with respect to the spin Hamiltonian parameters, including the orientation of magnetic fields, can be used to calculate the peak position and intensities without the need to calculate the powder spectrum completely. He has presented a calculation scheme to simulate a complete powder spectra for spins upto $5/2$ (Mn^{2+}) and applied it to the case of Fe^{2+} substituted AlOOH (diaspore).

7. Advanced materials and EPR

The EPR technique has been applied for spin identification, spin counting, spin mapping, spin motion and spin imaging of a variety of advanced materials in their solid state including metals and alloys, elemental and compound semiconductors (crystalline and amorphous), alkali and silver halides, transition metal, rare earth and actinide compounds, electroceramics, catalysts, intercalation compounds, polymers, glasses and organic charge transfer complexes, besides superionic conductors and high temperature superconductors. The technique has

proved to be specific (local probe, dynamic environment), sensitive (conditions sufficient) to composition (accurate enough to a quantitative level) (nonperturbing or nondestructive) of the specific classes of materials. This has been applied and the information obtained.

The subsequent sections of this chapter discuss the following classes of materials: semiconducting materials, polymer materials, glasses and ceramics, and superionic materials. A section on electron microscopy discusses the basic principles of electron microscopy with certain examples. This is followed by a brief review of the emerging techniques, which could be routinely applied to selected materials. 'Spin labels' and biological materials (proteins (Hagen 1992) have not been discussed in this article although they are of immense importance. 'Spin label' ESR has been established as a physical technique (Humphries and

8. Semiconducting materials

8.1 General considerations

Characterization of point defects in semiconductors and those induced by plastic deformation.

Table 6. Basic expressions for generating EPR absorption spectra of powdered materials[†].

Type of spectrum	Expressions
(a) Axially symmetric g -tensor, $g_{\perp} > g_{\parallel}$ ($g_1 = g_2 = g_{\perp}$, $g_3 = g_{\parallel}$) Features: Divergence at $H_{\perp} = h\nu_0/g_{\perp}\mu_B$ shoulder at $H_{\parallel} = h\nu_0/g_{\parallel}\mu_B$ ν_0 = microwave frequency	$S(H) = \frac{(h\nu_0)^2}{\mu_B^2 g_{\perp} \sqrt{g_{\perp}^2 - g_{\parallel}^2} \cdot H^2 \sqrt{H^2 - (h\nu_0/g_{\perp})^2}}$ <p>for $h\nu_0/g_{\perp}\mu_B \leq H \leq h\nu_0/g_{\parallel}\mu_B$</p> $S(H) = 0 \text{ elsewhere}$
(b) Rhombically symmetric g -tensor, $g_1 > g_2 > g_3$. Features: Divergence at $H_2 = h\nu_0/g_2\mu_B$ Shoulders at $H_1 = h\nu_0/g_1\mu_B$ and $H_3 = h\nu_0/g_3\mu_B$	$S(H) = \frac{2}{\pi} \frac{H_1 H_2 H_3}{\sqrt{H^2 - H_1^2} \cdot \sqrt{H_3^2 - H^2} \cdot H_2} \cdot K(H)$ <p>($H_3 \geq H \geq H_2$)</p> $S(H) = \frac{2}{\pi} \frac{H_1 H_2 H_3}{\sqrt{H_2^2 - H^2} \cdot \sqrt{H_3^2 - H^2} \cdot H_2} \cdot K(H)$ <p>($H > H_3 > H_1$)</p>

cal doping and thermal treatment during various stages of synthesis—is an important first step in the production of semiconducting materials for applications such as integrated circuits, infrared photodiodes and solar cells. More specifically, the characterization of electronic states in a given semiconductor involves three steps: (i) the number density of various defects (e.g., dangling bonds in crystalline Si or dangling bonds in amorphous Si), (ii) the energy position of defect levels relative to the conduction band/valence band edge, or the energy level which governs the macroscopic properties of the semiconductor, and (iii) defect wave function which describes the microscopic structure of the electronic defect, which enables assessment of (a) cross-sections for

7. Principal types of advanced materials studied by EPR.

Material	Information sought
Metals and metallic materials	
ferromagnetic metals and alloys	Magnetic phase identification, magnetization, damping and magnetostriction parameters
crystalline glassy	
superconductors	Metal-insulator transitions, phase purity in ceramics, microwave impedance and penetration depth
semiconductors	
crystalline	Defect type location, concentration and geometry
amorphous	Annealing behaviour under plastic deformation, irradiation and implantation
Insulators	
organic	
monocrystalline polycrystalline glassy	Microscopic structure and electronic information
inorganic	
monocrystalline polycrystalline	Free radical production, identification and detection, kinetics, motion of spin labels
Polymers	
conducting	Behaviour under stress, irradiation and chemical doping. Defect

optical transitions, (b) electron correlation effect (c) metastability of defect densities and sample growth conditions.

In the testing of semiconductors ESR and EPR techniques are particularly valuable as they are sensitive to the short-range order of defect states, i.e. the local environment of the defect in the crystal lattice/amorphous network and its neighbourhood.

Unpaired electrons in semiconductors — both elements (Si, Ge) and compound (III–V's: InSb, GaAs and I–II: ZnS, CdS) — exist as: (i) electrons localized at isoelectronic defects (impurity atoms), (ii) electrons in a partly filled band, and (iii) electrons in broken bonds (like carbon/organic free radicals).

Physically, semiconductors are attractive materials for ESR investigations because: (i) they are intrinsically diamagnetic so that any impurity (H to Ag across the periodic table) could be studied without any interference from host lattice; (ii) these magnetically active impurities have limited solubility and give rise to narrow resonance lines; (iii) they have highly symmetric crystal structures (cubic/hexagonal) with very few atoms per unit cell (typically 2) with tetrahedral symmetry about each point so that theoretical modelling is relatively straightforward; (iv) they are tetrahedrally bonded (involving hybrid atomic *s*- and *p*-orbitals) and this covalency is manifested as (a) a reduction in the hyperfine interaction with the host ion, (b) an additional hyperfine structure with the host ion, and (c) a reduction in orbital contribution to *g*-factor; and (v) the rather small spin orbit interaction (especially in Si) and long spin-lattice relaxation time make resonance signals in doped semiconductors easily saturable and thus ideal for ENDOR studies and 'spin mapping'.

Beginning with crystalline silicon-doped with to the present day porous silicon and low-temp GaAs, the ESR characterization continues unabated follows is a brief, material-by-material description. experimental data is compiled in table 8.

8.2 Silicon

8.2a Donors, acceptors and impurities in crystal

Studies on crystalline silicon doped with shallow donor (P, Ag, Sb and Bi) and shallow acceptor (B, Al and In) impurities. 3d-transition elements (V, Cr

in semiconductors and related materials.

<i>g</i> -value(s)	Hyperfine coupling constant*	Location and origin	Remarks	Ref.
2.001(1)			[P] $\sim 2 \times 10^8/\text{cc}$ Linewidth T-independent, $4 < T < 300 \text{ K}$	a
0.34, \perp : 1.094 0.73, \perp : 1.89		As donor dislocation dangling bond (db)	Upon optical (Hg lamp) pumping	**
0.85, \perp : 1.91		Molecular donor	[0]: $\sim 10^{14}/\text{cc}$ Dynamic tunneling system	***
2.019		Midgap db		b
2.012		Conduction band, Ge-Ge antibonding		—
2.053		Valence band Ge-Ge bonding		—
1.10(5)		Isolated substitutional <i>N</i> at a trigonal symmetric site		c
2.006		Surface paramagnetic centre	$\Delta H = 0.4\text{--}0.75 \text{ mT}$ Relaxation time = $10^{-6}\text{--}10^{-7} \text{ s}$ at 300 K — stable — Lorentzian $\sim 10^{14} \text{ spins/cm}^2$	****
2.0055 \pm 0.0002				
2.00069	^{75}As : 7.3 mT ^{31}P : 4.2 mT H_2 : \parallel : 217.8 MHz \perp : 128.2 MHz	Label: Si-NL52	Plastic deformation by (compression) at 1000°C and spectra at 4 K 23.200480 GHz	†
2.00951	H^1 : \parallel 4.81 \perp 1.5 MHz H^2 : \parallel 12.1 \perp -5.0 MHz	Interstitial site	$\sim 4.2 \text{ K}$	†† d
g'_2 + 0.002 - 0.031(1)				e

g -value(s)	constant*	Location and origin	Remarks	Ref.
2.0028	^{107}Ag : 9.0, 3.9 ^{109}Ag : 10.5, 4.5 $D = 86 \text{ MHz}$ $A_{\text{iso}} = 7.3 \pm 0.3 \text{ mT}$ $A_{\text{aniso}} = 1.8 \pm 0.3 \text{ mT}$ $\text{SHF} = 2.3 \text{ mT}$	Silver impurity (X) pair		-
3.9846				
2.0004				
1.9999				
2.004		Neutral Fe^0 (?)	Xe-Light illumination	+
2.0065		Si-db at surface/ c -Si-SiO ₂ interface		
2.0022				
2.0078				
2.0055		midgap db		
2.0044		conduction band		
		Si-Si antibonding		
		valence band		
		Si-Si bonding		
2.01		Si-db		
2.004				++
2.008				
2.0055		db	$g_{\parallel} \perp$: (111)	
2.0012		Si \equiv Si		
2.0081		Pb centre	ace \parallel (111) axes	
		Si \equiv Si (G8)	$g_1 \parallel$ (111) axes	
2.0005				
2.0112		Si \equiv Si at divacancy (G7)		
2.0096				
2.0012		Si \equiv Si at pentavacancy (P-1)		
2.0135				-
2.0150				
2.0023				
2.0117				
2.0106				
2.0151		Si-Si bent bond over vacancy (G2)	$g_1 \parallel$ (011) axes	
2.0028				
2.0038				
2.0092		Si-Si bent bond, vacancy with 0 (B1)		
2.0026				
2.0033				

g-value(s)	Hyperfine coupling constant*	Location and origin	Remarks	Ref.
2.0087		Si-Si bent bond over vacancy	$g_1 \parallel (100)$ axes	
1.9989				
1.9989				
2.0018		$O_3 \equiv Si \dots Si \equiv O_3$ at 0 vacancy	E' centre	
2.0005				
2.0003				
2.0026		Si-O	HC_1 centre	
2.0090		Hole on non-bridging O		
2.0210				
2.0007	$A_{ }/g\mu_B = 12$ mT	Atomic Cl	upon 100 keV X-irradiation observed at 77 K	f
2.027	$A_{\perp}/g\mu_B = 6$ mT			
2.0018		E'_a		
2.0013				
1.9998				
2.0018		E'_γ		
2.0006				
2.0003		E'_δ		
2.0018				
2.0021				
2.0021				
2.002		Bi-radical $S=1$	$ D /g\mu_B = 13.4$ mT low OH	
4		Triplet state ($S=1$) defect	γ -irradiated O-deficient sample	g
2.0004	$I\parallel: 68 \times 10^{-4} \text{ cm}^{-1}$	G6 centre	V_2^+	
2.0030	$I\perp: 40 \times 10^{-4} \text{ cm}^{-1}$		V_2^-	
2.0012	79	G7		
2.0142	50			
2.0007	120			

g-value(s)	Hyperfine coupling constant*	Location and origin	Remarks	Ref.
2.0018 2.0006 0.28-0.50	424 362	E' conduction electron	O-vacancy in α -SiO ₂ $m^*/m = 0.015$	i
2.04 ± 0.01	(866 ± 10) × 10 ⁻⁴ cm ⁻¹	As-related antisite defect		@
2.003	(890 ± 10) × 10 ⁻⁴ cm ⁻¹ 5.7 mT	As Ga ⁰ EL2 centre		j
1.993	Fine structure = 1.55 mT		20 K	
2.046	-			i
2.106	Fine structure = 37.4 mT			
8.1		Bound hole detected by uniaxial stress		
6.7		Bound hole detected by uniaxial stress		
2.04 2.0032(4)	A/h = 2700 MHz	Antisite defect ⁷⁵ As ⁷⁵ As ₄ Dangling bonds in disordered layer	Hole configuration $\Delta H \sim 0.6$ mT, $T = 77$ K N -implantation $\geq 5 \times 10^{15}/\text{cc}$ ESR intensity is proportional to no. of defects produced by implantation	k l
2.002	60.5 ($S = 5/2?$)			i
2.023	Fine structure = 42.9 mT			

g-value(s)	Hyperfine coupling constant*	Location and origin	Remarks	Ref.
	SHF ^3P : $A_{\parallel}/h = 314 \text{ MHz}$ $A_{\perp}/h = 179 \text{ MHz}$	$^{31}\text{P}^{31}\text{P}_4$	$p\text{-GaP}$	
2.013	SHF $A_{\parallel}/h = 310 \text{ MHz}$ $A_{\perp}/h = 124 \text{ MHz}$	Isolated Ga vacancy		
2.089	SHF $A_{\parallel}/h = 112 \text{ MHz}$ $A_{\perp}/h = 55 \text{ MHz}$		35 GHz, 20 K SHF by ENDOR at $\sim 4 \text{ K}$	
2.0934				
2.1974	Fine structure = 0.031 cm^{-1}			
2.1997	$D = -1.860 \text{ cm}^{-1}$			
1.999				
1.986		$\text{Cr}^{4+}?$		
50.7-48.8		Conduction electrons	g-values, linewidth conc. dependent	i
3 line spectrum		Fe^{3+} in cubic symmetry	$T = 10 \text{ K}$, $\Delta H = 12 \text{ mT}$	n

Hz and cm^{-1} . $1 \text{ mT} = 10 \text{ gauss} = 28.02 \text{ MHz} = 9.346 \times 10^{-4} \text{ cm}^{-1}$.
expressed as $A/g\mu_B (\text{cm}^{-1})$ in spectroscopy.

structure.

Rev. **90** 988

D K 1988 *Amorphous silicon and related materials* (ed.) H Fritzsche (Singapore: World Scientific) p. 557

Conf. Series No 59 p. 81

in. *Solids* **24** 1467

as *Solids* **B86** 269

J 1986 *Phys. Rev.* **B34** 7524

Rev. **B41** 7158

Let. **50** 1450

ctors and semimetals (New York: Academic) Vol. 2, Chap 8

Res. Soc. Symp. Proc. Vol. 241, p. 69

Commun. **36** 15

Accordingly the ESR spectrum changes from a 2-line ($I = 1/2$) hyperfine pattern to a g -shifted and broadened pattern as P concentration is increased (Slichter 1971).

Three general conclusions emerge from these studies on doped Si:

(I) The hydrogen-like energy states available to an isolated impurity atom provide a set of localized atomic states capable of producing deep levels in the band gap of the semiconducting host.

(II) The interaction of the atomic states of an impurity at an interstitial site with the host bunches these deep levels and confines them within the gap. Thus the interstitial site 'attracts' deep levels.

(III) The substitutional site, however, 'rejects' deep levels, and is thus not favoured.

Local interatomic distances between Si and an s - p bonded impurity can be very accurately determined using EPR hyperfine structure from magnetic ligands as has been demonstrated by Scheffler (1987) for the case of Cu^{2+} in Si. Comparing the ratio of the experimentally determined Fermi contact parameter and the dipole parameter (b) to the same ratios calculated as a function of local geometry (i.e. different S-Si bond lengths), the equilibrium geometry of the Si-S complex is established. The S-Si bond length thus determined is 2.345 Å, practically identical with the 2.35 Å determined from extended X-ray absorption fine structure (EXAFS) measurements.

The role of the interstitial hydrogen impurity in semiconductors (especially Si) as a passivator of deep and shallow can never be over-emphasized. It is the most fundamental and one of the most challenging issues in the materials science of silicon. Hydrogen can diffuse through Si rapidly at room temperature (unlike in metals where they can be stored). While it causes embrittlement of Si at low temperatures, it aids dislocation motion in Si at high temperatures. It can exist in Si as a centre with positive (H^+), neutral (H^0) and negative (H^-) states (Myers *et al* 1992). EPR of the apparently isolated neutral hydrogen (H^0) has been observed (Gorelinskii and Nevinnyi 1987a, b) for Si after proton irradiation at 100 K. Two paramagnetic centres AA9 and AA10—both positively charged—have been identified. AA9 shows hyperfine splitting due to H atoms. Both centres anneal at 180 K.

Silver—an important 4d transition metal impurity in

stitial position and Ag in a substitutional position (17), and (iii) an Ag-transition metal pair.

In briefly annealed (250°C, 15 min) Si samples implanted with 30 MeV hydrogen and (to $\sim 10^{17}/\text{cm}^2$) an EPR spectrum attributed to a molecule oriented along $\langle 111 \rangle$ direction in the crystal has been detected, in experiments performed at K-band frequencies, at liquid He temperatures (L52' spectrum is described by the spin Hamiltonian

$$\mathcal{H} = \mu_B H \cdot g \cdot S + S \cdot A_{\text{H}_2} \cdot H_{\text{H}_2} + S \cdot A_{\text{H}^1} \cdot I_{\text{H}^1} + S \cdot A_{\text{H}^2} \cdot I_{\text{H}^2}$$

where $S = 1/2$, $I_{\text{H}_2} = 1$ for the triplet spectrum, $I_{\text{H}_2} = 0$ for the singlet spectrum and $I_{\text{H}^1} = I_{\text{H}^2} = t_{\text{H}}$. H^1 and H^2 are the orthohydrogen molecule, while H^1 and H^2 are the hydrogens. The g and A parameters are included in the spectrum. The capture of mobile H^- at the interstitial site of H^0 is proposed as the probable mechanism of formation of H_2 .

The nonobservation of Au^0 in semiconductors by EPR had been as intriguing as the nonobservation of Cu^{2+} EPR in high T_c superconductors (Miyazaki and Anderson 1988). But from Zeeman effect measurements at 1.9 K, Watkins *et al* (1991) have established that the single donor and the single acceptor levels in Si arise from isolated substitutional neutral atoms. The ground state is paramagnetic $S = 1/2$ and is tetragonally distorted with $g_{\parallel} \approx 2.8$ and $g_{\perp} \approx 0$, unlike the isoelectronic Pt^+ , for which $S = 1/2$, $g_{\parallel} \approx 2.1$ and $g_{\perp} = 1.4$. The observation of Au^0 EPR in Si is thus a direct consequence of $g_{\perp} = 0$, which implies that M_s values for the ground state quantize along the defect tetragonal axis independent of the orientation of the magnetic field. Thus the magnetic field dependent off-diagonal terms in the spin Hamiltonian, and no $\Delta M_s = \pm 1$ transitions are induced by a microwave field.

An interesting EPR and ENDOR study by Watkins *et al* (1987) of interstitial Cr^+ centres in Si, was carried out to illustrate the application of the latter, as well as to demonstrate the success of the model developed by Ludwig and Woodbury (1962) to account for the effective spin and g -values of the 3d-transition metal impurity in Si. According to their model, the interstitial

existence of a donor level in $\text{Cr}_i^{n/+}$ was established, from EPR to be 0.22 eV below the conduction level. Intriguingly, the observed hyperfine interaction between 3d electrons and the impurity nucleus is smaller than that

calculated for the free Cr_i^+ ion with rather large delocalization of the 3d orbitals leading to a large hyperfine interaction with ligands. But these interactions were small (figure 19a). ENDOR experiments (figure 19b), that in $\text{Si}:\text{Cr}_i^+$, the impurity electron is shared by one hundred and two (102) Si atoms in the shells surrounding the Cr impurity. A conclusion that emerges from this study is that the spin density is transferred from the impurity to the crystal. This has resolved the controversy about the 52% delocalization of the impurity wavefunction on the basis of EPR data, and the small hyperfine interaction due to Si ligands.

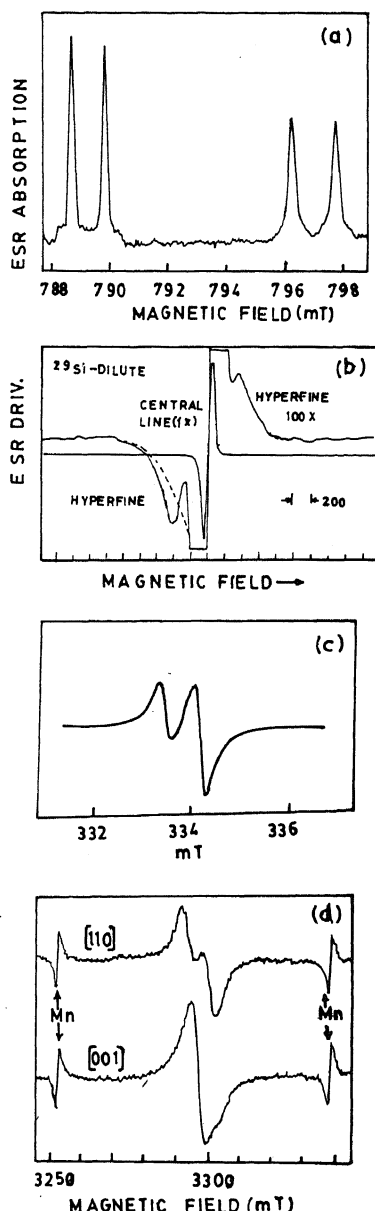
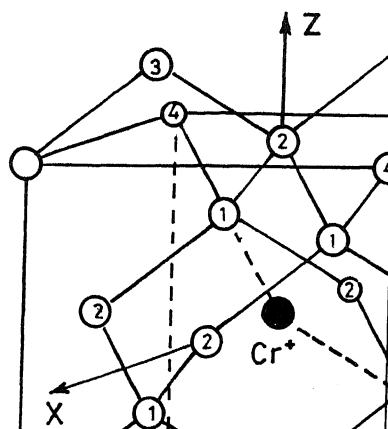


Figure 17. Typical ESR spectra of transition metal impurities and structural defects in different types of silicon. **a.** Spectrum

8.2b Deformed and implanted Si: Si gives rich EPR spectra due to various types of defects, such as vacancy type, produced during deformation, and those induced by radiation damage, and the dangling bond type — almost all of which are $g_{\perp} - g_{\parallel} > 0$ and $g_{\parallel} \approx g_c$. These centres are often graphically equivalent orientationally, but differ in intensity (Webb and Alexander 1991).

Ion implantation, an important process in semiconductor fabrication, is a process in which ions (e.g. ^{75}As or ^{76}As) are introduced in, and diffuse through, the substrate, and, occur at relatively low temperatures as room temperature substrate. Heavy ion implantation leads to the formation of layers in semiconductors (Masuda et al. 1985) which are annealed at low temperatures. It is



pic Lorentzian-shaped ESR signal with $g = 2.006$ and $\Delta H_{\text{max, slope}} = 0.48\text{--}0.6\text{ mT}$ which when annealed at 0°C yields the ideal amorphous state. Annealing at $500\text{--}550^\circ\text{C}$ produces ESR due to conduction bands with $g = 1.998\text{--}1.999$ and complete recovery of charge carriers. The important result is that the structure of voids in the amorphous layer produced by ion implantation has inhomogeneous characteristics in the void, in contrast to that in clean surfaces produced in ultra-high vacuum.

heavily P-doped ($7 \times 10^{17}\text{ atoms/cm}^3$) Si, upon 1 MeV electron irradiation at room temperature, two-phosphorus defect complexes are detected in EPR spectra (Barts and Ammerlaan 1977) whose formation is caused by a slow diffusion of the phosphorus-vacancy or E centres during irradiation at 60°C and subsequent trapping by other phosphorus atoms. An irradiation-induced diffusion mechanism is found to be essential for this process.

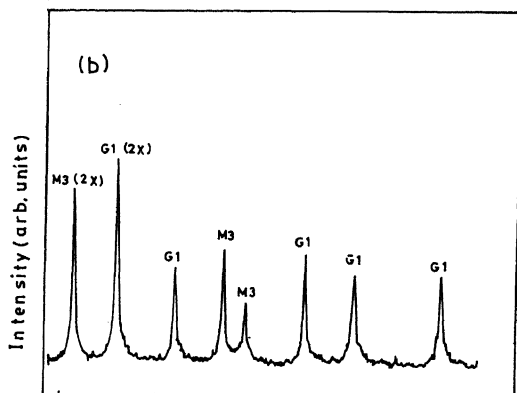
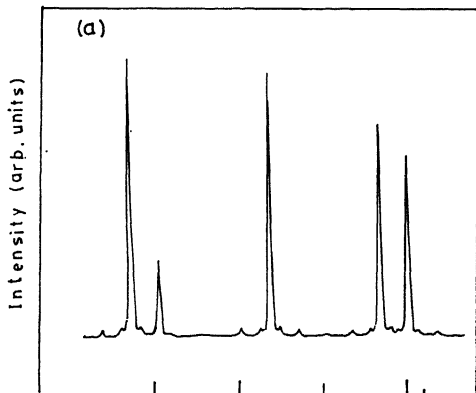
Amorphous silicon (*a*-Si) and hydrogenated amorphous silicon (*a*-Si:H): The main difference between crystalline and amorphous silicon is that in the amorphous state the edges of the valence and conduction bands are not well defined, so that the 'tails' of these two bands consist of states that exhibit a certain degree of localization. Thus these 'localized states' occur in the band gap and give rise to characteristic EPR signals, attributed to point defects.

The most widely investigated centre in undoped *a*-Si (*a*-Si:H) is the so-called D centre due to Si dangling

bonds, which are actually unbonded orbitals on the under-coordinated (instead of the usual 4-coordinated) silicon atom (Si_3^0) in the disordered network. Due to the lack of bonding partners, the fourth atomic sp^3 hybrid orbital is unbonded and thus the electronic defect is called a 'dangling band', analogous to similar defect states at the surfaces/grain boundaries of crystalline silicon. The fingerprint of this electronic defect, which, in undoped *a*-Si:H essentially determines the lifetime of charge carriers and thus limits the performance of *a*-Si:H thin films for many applications, is a characteristic ESR signal with $g = 2.0055$ whose intensity is a convenient measure of the quality of a given specimen.

The attempts to describe the macroscopic properties of device grade *a*-Si:H within the framework of microscopic structural models namely, (i) the nearest neighbour correlation energy (U) model U being the effective energy required to place a second electron in a singly occupied defect level, (ii) the thermal equilibration model and (iii) the dangling-band conversion model all of which are based on the hypothesis that the dominant structural defect in *a*-Si:H is definitely the Si dangling bond.

Pantelides (1988) has proposed a floating bond model in which 'floating bond' is likely to be more important than the dangling bond. He argues that a mobile radical centre is essential in accounting for the diverse and fascinating phenomena observed in *a*-Si. The crystalline analog of a floating band is an Si interstitial, while the analog of a dangling bond is a Si vacancy. The floating bond ($\text{Si}_{1/2}^0$) is an over-coordinated Si atom as much



dangling bond $\text{Si}_{(3)}^0$ is an under-coordinated Si atom, and is characterized by a molecular orbital vis-a-vis the atomic orbital ($\text{Si}-\text{Sp}^3$) of the dangling bond. The advantage with the floating bond is that 'bond switching' rather than 'bond breaking' results in high mobility needed for electrical transport. Self annihilation of the bond is possible and a 'kick-out' mechanism of diffusion of hydrogen is postulated wherein the stationary $\text{Si}-\text{H}$ bond is attacked by the mobile migrating floating bond, releasing or 'kicking out' a H into an interstitial. In this picture, the doping phenomenon in a semiconductor is conceived as a change in the coordination mediated by a mobile intrinsic defect, without the need for any electronic transition. Thus a 3-coordinated P defect would combine with a floating bond to yield a P_4 . P_4^0 or the neutral donor observed in the EPR, if P-doped $\alpha\text{-Si}:\text{H}$ and $\alpha\text{-Ge}:\text{H}$ through well resolved ^{31}P and ^{75}As hyperfine structures provides some support for the floating bond model, although the question whether D-centres are mobile, still needs to be answered comprehensively. This pioneering ESR study of Stutzmann and Street (1985) has shown further that disorder-induced localization of states in $\alpha\text{-Si}:\text{H}$ makes the donor hyperfine structure (^{31}P or ^{75}As) greater than that in crystalline Si and broadens the distribution of states with similar electronic character.

The observation by Stutzmann and Biegelsen (1989) of hyperfine structure ^{29}Si of the $g=2.0055$ ESR in undoped $\alpha\text{-Si}:\text{H}$ containing the natural abundance of the ^{29}Si isotope (figure 17b, table 8) has allowed quantitative modelling of the underlying hyperfine and g -tensors. The structural parameters deduced for the $g=2.0055$ defect agrees very well with those of Si dangling bonds at the Si/SiO_2 interface. Significantly the ^{29}Si hyperfine structure observed by Stutzmann and Biegelsen (1989) appears to be incompatible with the floating bond model because the floating bond wave function would leave a much less weight on any Si atom than a dangling bond state.

ENDOR studies of $\alpha\text{-Si}:\text{H}$ (made by reactive sputtering (RS) and glow-discharge (GD) decomposition) have shown (Yokomichi and Morigaki 1987; Morigaki 1988) the existence of at least two different types of dangling bonds: (i) normal dangling bonds and (ii) dangling bonds having a hydrogen as their neighbour. These experiments carried out at 7 K, 9.0 GHz and rf current in the 1–150 mA

constant of 6 MHz was deduced. Concentrations estimated from ESR measurements are $1.6 \times 10^{18} \text{ cm}^{-3}$ for GD and exposure (~ 5 h) of Gd sample. The concentration from Xenon lamp increased the concentration to $1.8 \times 10^{18} \text{ /cc}$.

There is a recent ENDOR study of normal and hydrogen dangling bonds (Yokomichi and Morigaki 1987) in $\alpha\text{-Si}:\text{H}$ of a rather large hyperfine splitting of ^{29}Si in unannealed and annealed samples at 70°C by glow discharge. This study shows that the bond is more delocalized and has a different character than those of isolated, normal dangling bonds.

8.2d Porous silicon: Crystalline silicon is a direct band gap material, unlike the light emitting diode (LED) which is an indirect band gap material. As a result of efforts to 'engineer' silicon so that it could emit light like a light emitting diode, prepared this material by etching silicon into pores into a Si wafer by applying an electrochemical process is accelerated by a small amount of light. It is possible to etch away silicon leaving an array of tiny 'dots' or 'quantum dots'. ESR studies on porous silicon by electrochemical anodization of Si (Kubo *et al* 1992; Yokomichi *et al* 1992) show that the main defect in porous silicon is a dangling bond located at the surface or at the interface. It has trigonal symmetry with a g -factor of $g_{\parallel}=2.0022$ along the $\langle 111 \rangle$ axis, with $g_{\perp}=2.0022$. The anisotropy of the defect implies that the defect retains the crystallinity of the substrate. Xe arc lamp light increases the concentration of the defects which are partially recovered on thermal annealing (figure 17d), unlike in $\alpha\text{-Si}:\text{H}$. This observation suggests that the light-emitting region of $p\text{-Si}:\text{H}$ is a crystal phase. This study has opened up new lines of investigation into the nature of hyperfine interaction, to be compared with $\alpha\text{-Si}:\text{H}$ and $\alpha\text{-Ge}:\text{H}$ as well as light-emitting diodes both photo and electroluminescence.

8.3 Germanium

In contrast to the extensively studied silicon, germanium is a

novel technique (Rodriguez 1987) called electric spin resonance has been applied to study spin-orbit coupling strength in the conduction band of zinc blende semiconductors — InSb and $\text{Cd}_{1-x}\text{Mn}_x\text{Se}$ in particular. A parity violating spin-orbit coupling mixes states with opposite spin orientations and parities. This allows electric dipole transitions between states which, in the absence of spin-orbit coupling, have equal and opposite spins. This interaction is given by

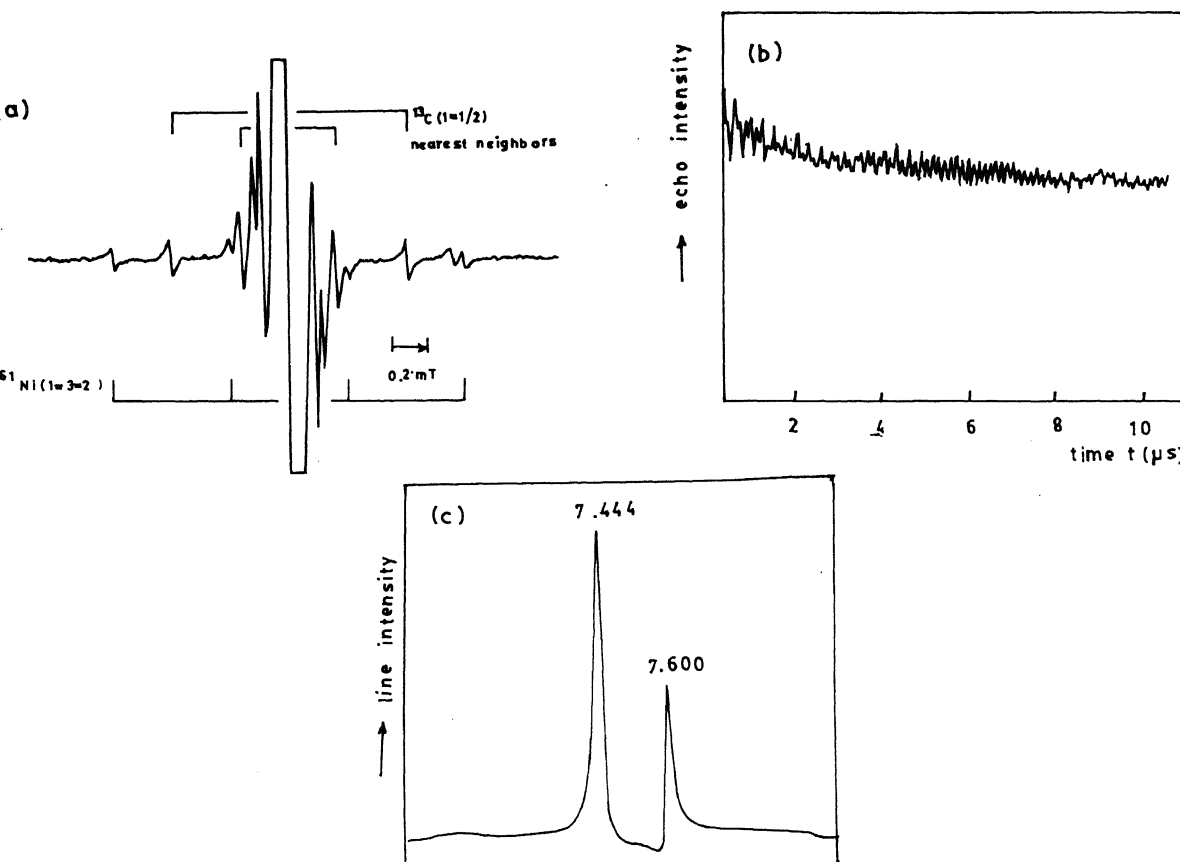
$$H = 1/2 g_0 \mu_B \sqrt{\epsilon} \mathcal{E} (\hat{n} \times \hat{\epsilon}) \cdot \sigma,$$

where g_0 is the g factor of electrons for small fields, \mathcal{E} the electric field of the wave, ϵ the dielectric constant of the material and σ the Pauli spin matrix. In InSb, $g_H - g_I = -0.428$ where g_I is the orbital g -factor

which agrees very well with the theoretical value of -0.42 .

8.6 Synthetic diamond

Synthetic diamond (carbon) ($\geq 1.0 \text{ cm}^3$) single crystals have been grown at a high temperature and under high pressure. It has application in electronic devices. Diamond, like silicon, lies directly above silicon in the periodic table and is isostructural with silicon. But unlike Si, it can only be doped with Ni among the 3d-group metals, which gives an ESR line at $g = 2.0310 \pm 0.0005$ in polycrystalline diamond grown from a metal melt containing Ni (Loubser and Van Rynweld 1966). This signal is isotropic down to 4 K, suggesting a high symmetry site for Ni in the diamond lattice without any charge compensation.



A comprehensive pulsed, Fourier transform and continuous wave (CW) EPR study has been carried out (Isoya *et al* 1990) on the Ni impurity in synthetic diamond, characterized by the $g=2.0319$ signal, whose linewidth is temperature dependent above 150 K due to strong spin-lattice relaxation. Figure 21 shows the CW spectrum, three-pulse echo modulation (In the 3-pulse echo technique, unlike in the 2-pulse spin echo technique discussed earlier, a third pulse applied whose distance from the first pulse is varied while the distance between first and second is fixed), and frequency domain spectrum for Ni. CW spectra (at 77 K) give an isotropic hyperfine splitting A (^{61}Ni , $I=3/2$) of 0.65 mT and two sets of nearly isotropic splittings due to hyperfine interaction with nearest and next-nearest neighbours ^{13}C atoms (the substitutional site in diamond has 12 'next-nearest' neighbours whereas the interstitial site has only six next-nearest neighbours). The CW EPR fails to resolve all the sets of super hyperfine lines due to interaction of unpaired electron of Ni with ^{13}C nuclei, which produce a 'modulation' of the spin echo which is detected in the time-domain. Accurate measurement of the super hyperfine coupling constant is possible for recording the frequency domain spectrum in an experiment akin to ENDOR. The effective spin of Ni has been determined to be $S=3/2$ (i.e. Ni is in -1 state at a substitutional site of tetragonal symmetry) $3d^7$ from (i) the nutation of the magnetization by the microwave magnetic field (H_1) and (ii) ^{13}C nuclear frequencies. This pioneering study has opened up new possibilities for the characterization of synthetic diamonds.

In a recent study, the ESR of diamond-like nuclei produced in a Si surface layer by high-dose C-ion doping has been measured (Izumi *et al* 1993).

The distribution of substitutional nitrogen centres (with resolved hyperfine structural from ^{14}N) and Ni impurities has been determined by ESR imaging (Furusawa and Ikeya 1990) (see § 12).

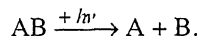
9. Polymeric materials

9.1 General considerations

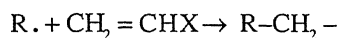
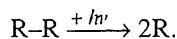
Polymers have been extensively investigated from the points of view of local structural confirmation, degrada-

tion to the propagation of one kinetic free radical chain reaction requiring a step in which a radical species reacts with the reaction mixture. Two processes

(1) Homolytic cleavage



(2) Unpaired electron transfer from monomer fragments formed by dissociation



where R is an alkyl group and dots denote unpaired electrons.

An example of an ESR study of the tunneling of methyl groups formed by γ -irradiation of polyethylene (Iwasaki *et al* 1971). Other radicals include $\text{CH}_3\text{OOC} \cdot$ or $\text{HOOC} \cdot$ and $\text{OHC} \cdot$ which gives a doublet (singlet) course $\cdot\text{CH}_3$ which gives a quartet with ratio 1:3:3:1 and a spacing due to interaction of unpaired spin with nuclei. Generally the ESR spectrum due to irradiation may be characterized

$$H_{\text{res}} = \frac{h\nu}{g\beta} - \sum_{i=1}^{\infty} (A_i + B_i) m I_i,$$

where A_i is the isotropic hyperfine interaction of the radical and nucleus i , and B_i is the anisotropic part of this interaction depending on the orientation of the radical. The singlet ESR referred to as $A=B=0$. For most hydrocarbon radicals α -protons i.e. H nuclei directly bonded to the radical atom. In highly-oriented polymers these radicals have a strongly resolved hyperfine structure. In general, for a spectrum with $(n+1)$ lines with equal intensities the coefficients of binomial distribution are observed. Thus for $\cdot\text{CH}_3$ ($n=3$),

Highly-oriented polyethylene irradiated with γ rays produces a

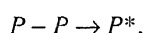
protons have different hyperfine splittings so that a quartet of lines due to four equivalent β protons, with a quintet split into a doublet by the α proton are observed. The intensity ratio of the overall spectrum is 4:4:4:6:6:4:4:1:1. The primary radicals produced by irradiation or milling are usually detected at temperatures in most of the common degraded polymers. Table 9 presents the radicals thus produced in selected polymers. An exhaustive list is given by Bors (1978). ESR affords a direct study of bond scission (and formation of 'mechano radicals') in highly stressed fibres and films of polyethylene, propylene, PMMA, polystyrene, polyesters and polyamides. The fracture of rubber has also been studied (Bors and Rabek 1977). Free radicals formed and trapped in polymer matrices under certain conditions can initiate graft polymerization. The grafting reaction depends on (i) the physical state of the polymer, and (ii) the properties of free radicals formed in the polymer. An example of electron or γ -irradiated polymer brought into contact with a monomer can diffuse into the polymer matrix and thus reach the trapped radical site. The case of styrene diffusion in polyvinyl chloride has been studied (Hamanone *et al* 1974). The use of a 'dynamic probe' (e.g. the nitroxide $\text{O}=\text{N}-\text{O}$, dissolved in the polymer) has helped probe glass transition behaviour of polymers, chain motions on the surfaces of as-grown and annealed polyethylene single crystals in relation to crystal structure, and polymer-plasticizer interaction in plasticized PVC. Among other ESR applications are the study of acceptor polymer complexes and the reinforcing properties of carbon black in rubber vulcanization.

Recent applications include studies of (i) radiation-induced cross linking of polyethylene in the presence of acetylene, (ii) molecular motion of chain-end radicals of polyethylene molecules anchored on fresh surfaces of polyethylene and PTFE, (iii) interaction of mechanically generated polypropylene radicals with phenolic antioxidants in the presence of oxygen, (iv) thermally generated free radicals in PMR-15 polyimide resin, (v) solitons and phase transitions in conducting polymers, and (vi) photo-induced charge transfer from polymers to C_{60} superconductor.

Some of these applications are discussed in more detail below.

9.2 Mechano-radicals

9.2a Polymerization: Mechano-radicals are produced by mechanical fracture (e.g. grinding) of polymers at low temperatures. The radicals known as chain-end free-radicals are produced by the 'homolytic bond scission' of carbon-carbon bond in the polymer backbone chain. For e.g. a polymer P with a $P-P$ bond undergoes the scission:



to yield the mechano-radical P^{\bullet} . In addition, 'mechano-anions' produced by heterolytic bond scission

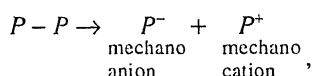


Table 9. Primary radicals in certain degraded polymers detected by ESR*†.

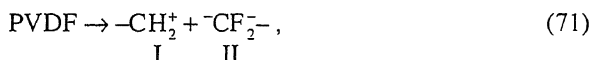
Polymer	Experimental conditions	Radical(s) found
1. Polyethylene	Milling (77, 240 K)	$-\text{CH}_2-\dot{\text{C}}\text{H}_2$
2. Polypropylene	Milling	$-\text{CH}_2-\text{CH}_3\dot{\text{C}}\text{H}$
3. Polystyrene	Milling (77 K)	$-\text{CH}_2-\text{C}_6\text{H}_5\dot{\text{C}}\text{H}$
4. PTFE	Ball mill	$-\text{CF}_2-\dot{\text{C}}\text{F}_2$
5. Polyvinyl alcohol	Grinding (80–170 K)	$\text{CH}_2-\text{OH}\dot{\text{C}}\text{H};$ $-\text{OH}\dot{\text{C}}\text{H}-\dot{\text{C}}\text{H}_2$
6. Poly(methyl methacrylate)	Milling	$\text{CH}_2(\text{COOCH}_3)\dot{\text{C}}\text{H}$

can be stabilized for instance by electron transfer due to contact in the dark e.g.

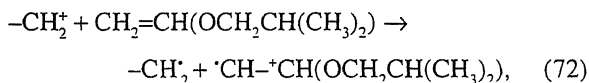


(where M = a molecule with high electron affinity like tetracyano ethylene TCNE) so that P^* may be detected by ESR spectroscopy. It is significant that these mechano radicals initiate polymerization at low temperatures under vacuum, as has been demonstrated for methyl methacrylate and ethylene (Sakaguchi *et al* 1989).

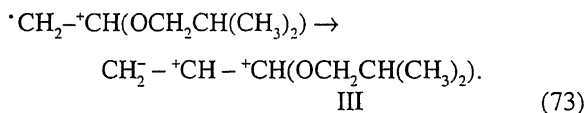
Polyvinylidenefluoride (PVDF) fractured alone and with isobutyl vinyl ether (IBVE) as well as TCNE (Sakaguchi *et al* 1988, 1989) by using a vibration ball mill (in the dark and at 77 K under vacuum) to produce dramatic changes in the ESR spectra (figure 22) show that (i) mechanical fracture of TVDF alone induces a heterocyclic bond scission in the main chain,



producing mechano cation $-\text{CH}_2^+$ and (ii) a cationic polymerization of IBVE is initiated by this mechano cation

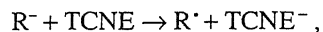
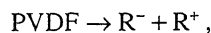
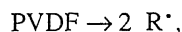


eventually producing the PVIBE homopolymer through the propagation reaction.

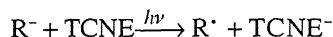


A superposition of the spectra of radicals I, II and III

is seen in the ESR spectra (not formed by the abstraction of electron from the anion that is produced by scission of C-C bonds in the polymer) in the following reactions.



(iv) photo irradiation of a fractured polymer



and increase the yields of total radicals.

9.2b Radical motion: Molecular motion of polymer chains seems to be restricted by the presence of the chains with matrix molecules and/or the intermolecular forces in the matrix. The study of such motion is an interesting looking — for instance — at the ESR spectra of blends (Shimada *et al* 1988). Sakaguchi *et al* have made a comprehensive ESR study of the radical motion of polyethylene radicals on the surfaces of polyethylene (PE) and polytetrafluoroethylene (PTFE). This radical, produced by fracture of the polymer (under vacuum at 77 K), can initiate the polymerization of ethylene monomer and other monomers on the chains which are bound to the fresh surface of the polymer. The study of this radical anchored on fresh surfaces is of interest even at 77 K because the weak interaction between radical and PTFE molecules tends to protrude from the PTFE surface in an isolated system. But the same chain



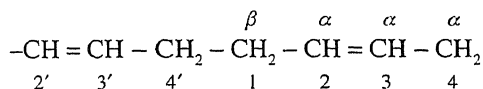
fresh surface of PE is held more strongly to the molecule and exchange motion takes place in this isolated system at 77 K. These conclusions are based on computer simulations of observed sextet and quintet spectra of radical for the case of PE and PTFE surfaces respectively. The simulation was done assuming Gaussian line shape function and spin exchange rate.

Charge generation mechanism in polymers: Static electricity in polymers arises when there is a transfer of charge between two insulating polymers or between a metal and a polymer when they are brought into contact and then separated. This phenomenon, which has applications in electrophotography and dry-ink electrophotography and is also the cause of troublesome static electricity, is a century-old problem (Harper 1964). In a recent quantitative model of contact electrification between polymers (Duke and Fabysh 1978), it has been shown that the steady-state-exchanged charge resides in intrinsic molecular ion states and the sign and order of magnitude of measured contact charge exchange between polystyrene and copolymer of styrene and methyl methacrylate have been correctly predicted.

A novel charge generation mechanism for the reaction of mechano anions and mechano radicals produced by mechanical fracture of a polymer main chain, based on studies has been reported in an attempt to deal with triboelectricity as a phenomenon involving the mechanical fracture of a polymer chain on the friction process. By measuring the yield of the ESR active mechano radicals produced under milling of PMMA, PP, PE, and PTFE with TCNE in the dark at 77 K, Kouchi *et al* (1990) have shown that (i) an electron transfer occurs from the mechano-anions to the mechano radicals produced by mechanical fracture of polymer chains via friction: $A^- + B^* \rightarrow A^* + B^-$, where A and B are the two polymers involved, (ii) the sign of the charge induced by friction can be estimated from the electron release potential of A and electron affinity of B and (iii) the triboelectric series exist: $A - PP - PE - PVDF - PTFE$, based on the reaction of polymers with TCNE, varying from high to low from left to right, a significant conclusion obtained. The ESR spectra of photo-irradiated with filtered infrared radiation, are identical to the triboelectric series of polymers (Harper 1962).

studies could also concentrate on (i) the nature of active centres involved and (ii) the structure of inclusion compounds. ESR could answer questions regarding the host-guest and guest-guest interactions at an intermediate level between the presence of monomers and the polymer.

Sozzani *et al* (1986) have sought to establish the results of a comparative study of a number of homogeneous polymers the structure of the propagating chain ends derived from diene monomers, (butadiene, 1,3-pentadiene, isoprene, 2,3-dimethyl butadiene, 2-methyl pentadiene, 2,4-hexadiene), the structure of the propagating chain ends derived from diene monomers, in particular the prevailing direction of propagating monomer units and the strict relationship between the last and the previous monomer. During polymerization, ESR spectra attributed to allyl-type propagating radicals, e.g.



in polybutadiene, characterized by a 6-line spectrum spaced 1.4 mT, and an intensity ratio 1:5:10:10:5:1 (figure 23) were observed. Except for this radical in polymer, all other radicals are stable over long periods of time, in the range -150° to $+60^\circ\text{C}$. Thus, the in methyl polybutalines are conformationally fixed.

The ESR spectrum of allyl radical in polybutadiene included in PHTP is temperature-dependent (figure 24) and rotates around the C_1-C_2 bond even at room temperature, i.e. it is mobile even at ambient temperature. The five α_1 and βH nuclei of the above radical are coupled to the unpaired electron by about the same constant, while the α_2 hydrogen is coupled to it by a much smaller coupling constant. The $\beta\text{-H}$ constant is given by

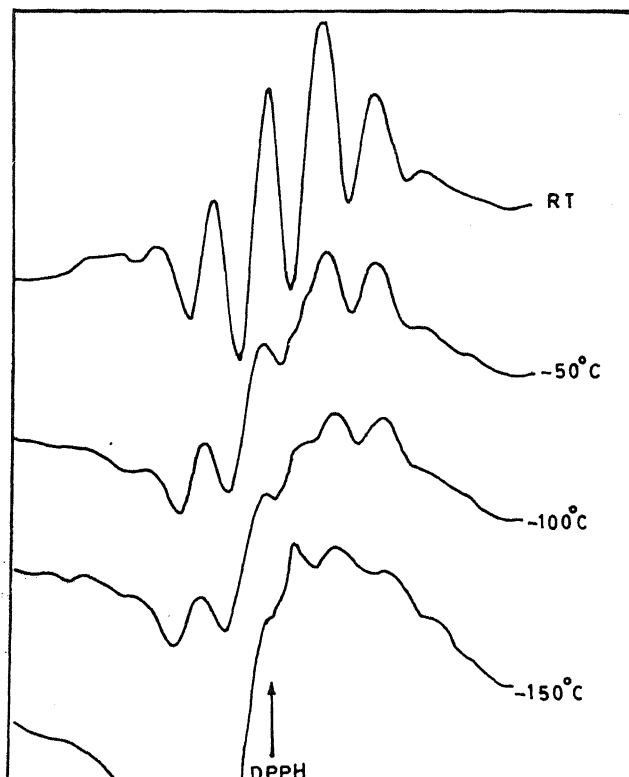
$$a_\beta = B^0 \rho_\pi \cos^2 \theta,$$

where θ is the angle between the p_z orbital axis of the allyl system and the projection of the $C_1\text{-H}$ bond on the plane perpendicular to the C_1-C_2 bond, B^0 is the constant (5.88 mT) and ρ the spin density on the carbon (assumed 0.58 for the allyl radical). The

9.4 Undoped and doped polyacetylene

Ever since Shirakawa and Ikeda (1971) prepared polycrystalline polyacetylene, $(\text{CH})_x$, a conjugated polymer, there has been an explosion of literature in the so-called 'synthetic metals', as the highly conducting, quasi one-dimensional polymeric materials are called. ESR has been a natural choice for the study of these systems in which intrinsic paramagnetic centres—to the extent of one spin per ~ 1500 carbon atoms—are present in *trans*- $(\text{CH})_x$ with an order of magnitude less in *cis*- $(\text{CH})_x$. While the spins are mobile in pure *trans*- $(\text{CH})_x$, they are fixed in *cis*-rich- $(\text{CH})_x$.

Undoped polyacetylene can be regarded as a Peierls-distorted linear chain (Rice 1979) involving π electrons at the half-filled band, with an energy of formation E_π and length l , which may be related to π -electron energy gap, 2Δ and bandwidth, W . Numerical values of E_π , Δ and W are calculated to be 0.4, 10 and 1 eV, respectively. Using a harmonic potential $1/2 au^2$ ($u =$



displacement) in which the electron is shown that $l/a \approx W/\Delta$ so that l/a is highly doped with electrons/holes can be accommodated in the form of solitons or soliton distortions rather than in the electron band states. These distortions of the polyacetylene chain generate a length l , a 180° variation in the band alternation, separating a charge change segment in which spins are shifted by one C-C length. These are charged domain walls. Thus, what would represent the dilute limit of spins stored in the form of spinless solitons doped (< 6 mol%) would create a phase which move to conduct electric current with alkali metals, AsF_5 etc.), leading to a soliton to metal phase transition. It is to be a first-order phase transition. Studies of electrochemically Na-doped polyacetylene show that the ESR linewidth exhibits a hysteresis, as functions of chemical

A thorough analysis of the ESR spectra in undoped $(\text{CH})_x$ (Holczer *et al.* 1983), has established that the signal is extremely sensitive to ambient conditions (not increase spin susceptibility) and on sample preparation. By taking measurements at various stages of material preparation, a ΔH_{pp} of 0.044 mT, while a soliton model (Holczer *et al.* 1985) has yielded a very narrow line. This narrow line, representing one-dimensional transport of mobile spins, whereas the fixed spins of *cis*-rich- $(\text{CH})_x$ broaden the line considerably. The soliton may be trapped to diffusive states, giving rise to a broad line.

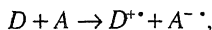
The first-order transition to the metallic state in polyacetylene, when it is heavily doped (Kivelson and Heeger 1985) in terms of a polymer model illustrated in figure 1.

An abrupt crossover from a localized state to a regular array of polaron-like states for this phase transition. In this state, a 'dirty metal' in which there is a gradual evolution of finite density of states. While the mid-gap band is

solid to give strong ESR signals. For instance, stretching of nylon under vacuum, directly in the ESR spectrometer, gives well-defined, structured spectra, similar to those obtained upon γ -irradiation are obtained (Campbell and Sariffici 1992). In conducting polymers, such as 'new' polyacetylene (prepared by nonsolvent polymerization followed by thermal treatment of catalyst solution at room temperature), stretching (say by a factor of five) is an important means of increasing the probability of carrier hopping and enhancing electrical conductivity by 5–6 orders of magnitude, because it is through stretching that a parallel arrangement of polyacetylene chains is achieved. The basic question in conducting polymer research is: What molecular and morphological changes produce a high conductivity ($\sim 10^5 \text{ S cm}^{-1}$) upon stretching? In highly oriented polymers the ESR linewidth shows a dependence on the angle Θ between the direction of stretching and the orientation of the polymer chains in the sample and the direction of the magnetic field of the ESR spectrometer. Thus, the degree of stretching is easily correlated with molecular weight of the polyacetylene chain (Bartl *et al* 1993). The degree of stretching $d_s = l/l_0$ (l = length after stretching, l_0 = initial length) while the ESR linewidth-related parameter $\delta = (\Delta H_{\parallel} \cdot \Delta H_{\perp}) / \Delta H_{\parallel}$ (ΔH_{\parallel} and ΔH_{\perp} are linewidths at $\Theta = 0$ and 90° , respectively), while d_s changes from 1 to 5, δ varies from 0.22 to 0.34. δ increases drastically with degree of stretching, while at high orientation, it shows a small effect. These behaviours correlate with the increase of electrical conductivity as a function of stretching.

'probes' for these studies, of structural and orientational aspects are the so-called neutral solitons which are paramagnetic species with spin but without charge (Bartl *et al* 1992). The mobile spins move along the stretched chain segments obtained by 'doping' to promote optically narrowed ESR lines through exchange interaction of electron spins with proton spins. Thus the length of the undisturbed conjugate chain segments defines the ESR linewidth. Short segments show broad ESR lines while long segments produce narrow ESR lines. As already stated, ESR linewidth shows a characteristic dependence with respect to the orientation of the polymer chain relative to the magnetic field.

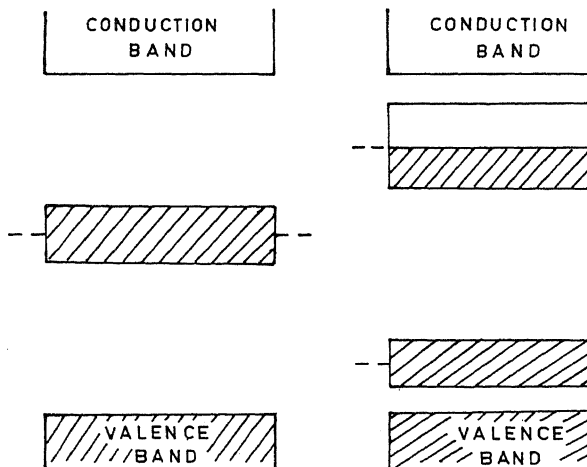
carbon superconductor or Buckminsterfullerene (C_{60}) have been investigated (Sariffici 1992). In this light-induced ESR or LESR experiment, ion radicals originating from charge separation



where D is the electron donor (MEH-PPV) and A is the electron acceptor (C_{60}), are photo-generated and detected *in situ*. Upon irradiation at 80 K with an argon-ion laser beam (2.14 eV : 150 mW) two photo-induced signals were observed at $g \sim 2.0000$ with $\Delta H_{pp} = 0.72 \text{ mT}$, and (ii) at $g \sim 1.9955$ with $\Delta H_{pp} = 0.6 \text{ mT}$, due to $(MEH-PPV)^{+\bullet}$ and $C_{60}^{-\bullet}$ were observed (figure 25). At 80 K, the ESR signal intensity increases during light ON-OFF-ON cycles, indicating the accumulation of photo-generated spins associated with $D^{+\bullet}$ and $A^{-\bullet}$ species. At 200 K, the LESR signal nearly vanishes, demonstrating the reversibility of the process, ruling out any residual species due to photo chemical reaction products. The potential applications of this prototypical reaction are in molecular optoelectronics, nonlinear optics and photovoltaics.

9.7 Polymer imaging

The fact that ESR signals can be enhanced and controlled by adding dopants to polymers has been exploited

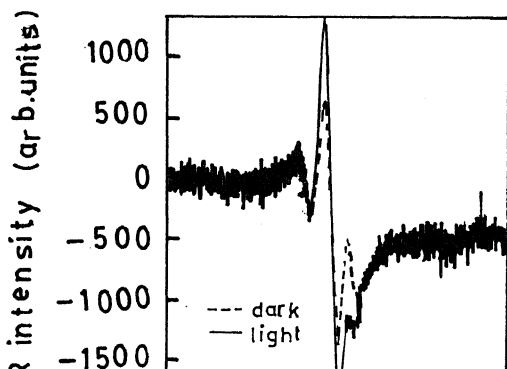


the nondestructive testing of polymer-based composite materials (Green 1990). When such materials are damaged by impact the existence and extent of damage cannot often be accessed and assessed by mere examination of the outer surface. However, by doping each layer of the polymer-based composite with a different dopant prior to lay-up, subsequent damage can be quantitatively determined as a function of depth into the composite by means of scanning EPR (figure 26). Thus both the spatial position of the dopant as well as its quantity are located (see § 12).

10. Glasses and ceramics

10.1 Glasses

Glasses form an expansive family of advanced materials which can be characterized by means of EPR. There are three groups of interest: (i) metallic glasses such as $\text{Fe}_{80}\text{B}_{20}$ and its ternary variants, which are soft amorphous ferromagnets (Bhagat 1973), (ii) semiconducting glasses such as $\text{V}_2\text{O}_5\text{--TeO}_2$ which are hopping ($\text{V}^{4+} \rightarrow \text{V}^{5+}$) electronic conductors or chalcogenide glasses (e.g. Se , As_2S_3) (Bishop *et al* 1977), and (iii) insulating glasses such as (a) soda-lime silicate glasses, containing paramagnetic impurities (e.g. Fe^{3+}) in trace quantities (Griscom 1980; Rao and Rao 1985) or else radiation induced paramagnetic centres (Griscom 1973/74), (b) soda-borate glasses of variable composition with a substitutional amount of a third component such as MoO_3 (up to 25 mol%), Mo^{4+} being an excellent sensor for the structure of borate glasses (Simon and Nicula 1983).



10.1.1 Metallic glasses

Metallic glasses are structurally obtained by rapid quenching of melts as wires and ribbons. They are amorphous soft ferromagnetic materials that differ from crystalline transformers in transformer cores. A ferromagnetic material can be crystalline or glassy, unlike a paramagnet. The presence of a net nonzero internal magnetic field leads to (i) spontaneous magnetization, (ii) crystalline anisotropy, (iii) intrinsic stress, (iv) extrinsic elastic stresses on the material. The effect. The presence of magnetostriction leads to the orientation of the spontaneous magnetization dependent on the magnitude and direction of the external elastic stresses. From a practical point of view, metallic glasses form a class of materials with strongly interacting electrons, compared to the (static) interaction which gives rise to the magnetic field mentioned above. This is a necessary condition for ferromagnetic samples.

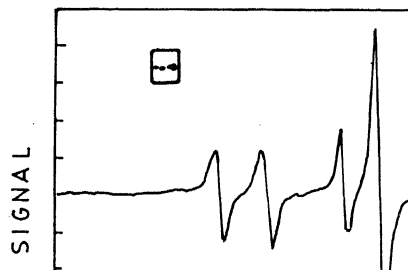
$$\hbar \omega = g \mu_B H_{\text{eff}},$$

where H_{eff} is the effective field acting on the magnetic moments and $\omega = 2\pi\nu$. The magnitude of the field and the intrinsic linewidth—both of which are experimental quantities—depend on the material to a greater extent. In fact

$$H_{\text{eff}} = H_{\text{app}} - H_{\text{dem}} + H_{\text{ani}},$$

where, H_{app} is the applied dc magnetic field, H_{dem} is the demagnetizing field, a function of the sample geometry,

$$= 8 M_s \cot^{-1} [(a^2 + b^2 + c^2)^{1/2} c / ab],$$



Using the intrinsic V^{4+} ($3d^1$) as the paramagnetic probe the ESR spectra of 55 mol% V_2O_5 –45 mol% MO_2 ($M = \text{Ge, Se, Te}$) have been examined in the temperature range 298–498 K (Sunandana and Bhatnagar 1984). The three spectra at 298 K (figure 28) are characterized by a typical axially symmetric profile due to $3d^1$ ($S = 1/2$) electron interacting with a ^{51}V ($I = 7/2$) nucleus giving rise to a well-resolved (for $M = \text{Ge}$) to poorly-resolved ($M = \text{Se}$) pattern of 8 ‘parallel’ and 8 ‘perpendicular’. The ESR parameters of selected semiconducting glasses are given in table 11. These differences are attributed to a monotonic increase in the covalency of the V–O bond on going from GeO_2 to TeO_2 to SeO_2 . All the three compositions show dramatic but reversible temperature dependence by way of progressive broadening and eventual disappearance of the vanadium hyperfine

structure. This behaviour has been attributed to thermally-activated delocalization of V^{4+} electrons leading to hopping V^{4+} electron transport. At low temperatures the hopping rate of V^{4+} is much smaller than the order as the hyperfine frequency.

A comprehensive ESR investigation of a ternary glass system $(\text{CuO})_x(\text{V}_2\text{O}_5)_{1-x}$ with $x = 0.005, 0.01, 0.05, 0.1, 0.2$ and 0.5 has been reported (Sunandana and Bhatnagar 1984). It has revealed that (i) addition of CuO (0.5 mol%) of CuO has the effect of suppressing V^{5+} and thus suppressing the V^{4+} ESR signal, (ii) large concentration of CuO produces exchange effects of the V^{4+} ESR signal and g -shift of Cu^{2+} ESR, with the

Table 10. Characteristic parameters for certain amorphous ferromagnetic materials determined from ESR

Material	T_c (K)	g	M_s (mT)	λ (10^8 s^{-1})	
				300 K	77 K
$\text{Fe}_{90}\text{Zr}_{10}^a$	240 ± 1	2.07 ± 0.02	90 ± 1	5.18	—
$\text{Fe}_{91}\text{Zr}_9^a$	212 ± 1	2.07 ± 0.02	89 ± 1	5.07	—
$\text{Co}_{90}\text{Zr}_{10}$	00	2.09 ± 0.02	—	—	—
$\text{Fe}_{75-x}\text{Ni}_x\text{B}_{25}^b$					
$x = 35$	637 ± 10		76 ± 1	1.17(8)	1.3
$x = 45$	539 ± 10		72 ± 0.5	0.80(7)	0.9
$x = 55$	373 ± 10		51.5 ± 0.5	0.42(3)	0.7
$\text{Fe}_{83-y}\text{WyB}_{17}^b$					
$y = 5$	450 ± 10		106.6 ± 0.4	1.28(20)	1.7
$y = 9$	354 ± 10			1.36(14)	2.4
$\text{Fe}_{20}\text{Ni}_{60}\text{B}_{20}^c$					
	93 GHz	420 ± 5	2.1	500.8	1.3
$(\text{Fe}_x\text{Ni}_{1-x})_{75}\text{P}_{16}\text{B}_6\text{Al}_3^d$					
$x = 0.2$	92	—	26.3	—	—
$x = 0.25$	154	2.08	38.2	—	—
$x = 0.30$	221	2.08	43.0	—	—
$x = 0.35$	280	2.06	47.7	—	—
$x = 0.50$	440	2.08	66.0	—	—
$(\text{Co}_x\text{Ni}_{1-x})_{75}\text{P}_{16}\text{B}_6\text{Al}_3^d$					
$x = 0.40$	88	—	15.9	—	—

detectable at 289 K for a CuO content of 25 mol%. Structural model, showing probable path of hopping shown in figure 29. While the hopping could be from V^{5+} to V^{3+} , the interactions between Cu^{2+} and V^{4+} and probably be mediated by $Cu^{2+} \cdots O^{2-} \cdots V^{4+}$ exchange mechanism.

Investigation of pseudobinary glass (0.5 MO (V_2O_5), (0.45 TeO_2), (MO = TiO_2 , Cr_2O_3 , MnO_2 , and Co_2O_3), with the 3d-transition metal ion par-substituting V-ion has shown (Sunandana 1987) while Ti^{3+} , Cr^{3+} and Co^{3+} modify the geometry of paramagnetic complex and thus control the electron hopping process, introduction of Mn^{2+} and Fe^{3+} leads to formation of paramagnetic clusters.

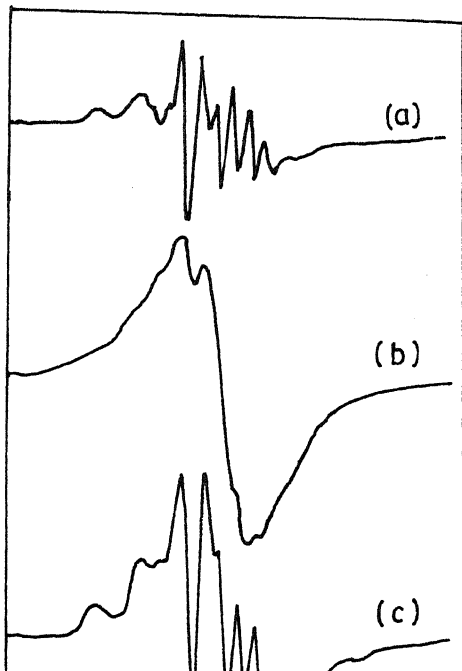
2b Chalcogenide glasses: ESR signals in pure chalcogenide glasses (Bishop *et al* 1977) are generally observed only upon optical excitation. The ground electronic states of these materials are invariably diamagnetic ($S=0$). Amorphous Se, As and Ge chalcogenide glasses all exhibit a broad (≈ 50 mT wide) resonance with $g=2$ due to unpaired spin localized on

a single chalcogen atom. Amorphous As and Se containing glasses exhibit an additional, much broader ($\Delta H \sim 150$ mT) resonance that could arise from unpaired electron localized on a predominantly p -orbital of As (remnescent of the P_4^0 centre in amorphous Si), interacting with the ^{75}As ($I=3/2$). This unresolved hyperfine interaction could be resolved through ENDOR studies to obtain the exact neighbourhood of this centre.

Structural imperfections or any deviation from the random network structure or from chemically random bonding expected from chemical composition in chalcogenide glasses play a significant role in their useful electrical and optical properties. These imperfections usually involve a pair of positively and negatively charged defects. Direct experimental evidence for the presence of these defects help to understand their role in the context of their electrical and optical properties.

Kawazoe *et al* (1987) investigated, through ESR, the type of defects in chalcogenide liquids S and As-Ge-S at a particular temperature, and the manner in which these defects combine to form normal bonds during the cooling process. In liquid S, an asymmetric Lorentzian, singlet homogeneously broadened absorption with $g=2.02$ is observed for temperatures above $160^\circ C$, the temperatures at which S_8 ring molecules begin to break to form long linear chains. This resonance is thus attributed to the formation of dangling bonds in the liquid. The width of the line increases markedly with temperature due to a decrease in the lifetime of the radical. Likewise, liquid As_2S_3 gives a broad absorption at temperature greater than $360^\circ C$ with lineshape changing from Lorentzian to Gaussian at $500^\circ C$. The concentration of these broken bonds during cooling the melts to form glass is determined by the chemical equilibrium between normal bonding ($As-S$), broken bonds (As and S) and homobonds ($As-As$ and $S-S$). The concentration of these 'chain end radicals' (somewhat like in fractured polymers) increases markedly reaching ~ 10 mol% at $700^\circ C$.

The enthalpy difference between normal bonding and homobonds is usually small. Upon cooling the radicals disappear while the radical species disappear in the case of $As-S$, a fraction of the neutral defects or E' centres ($A \sim 2.01$, $A \sim 24$ mT) remains in Ge-S, implying that the rate of ^{73}Ge recombination of radical species in



highlighted the crucial role of hierarchy of chemical bond strengths in determining the structure of glass forming chalcogenide liquids.

ESR studies on transition-metal-ion-doped Ge chalcogenide glasses have focused on aspects of local structure and bonding. In $\text{Ge}_x\text{Se}_{1-x}$ ($0 \leq x \leq 0.42$), containing 0.01 at.% Mn (Durny 1980), two characteristic resonances, one at $g=4.3$ with resolved hyperfine structure due to ^{55}Mn ($I=5/2$) and the other at $g=2.0$ with hyperfine structure (A) rarely resolved are found. In this case $A = (51 \pm 5) \times 10^{-4} \text{ cm}^{-1}$, which is correlated to the structure through the Hannay-Smith relation which relates the degree of covalency of the Mn complex (C) with the electronegativity difference between the Mn impurity and the chalcogen neighbours (L), $x_L - x_{\text{Mn}}$

$$C = 1 - 0.16(x_L - x_{\text{Mn}}) - 0.35(x_L - x_{\text{Mn}})^2. \quad (85)$$

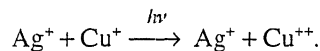
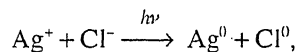
To get the number of nearest neighbours around (n), Pauling covalency c/n is plotted against A . The above-mentioned A value is compatible with $n=4$ so that Mn sites occupy Ge sites in the Ge-Se network with four Se neighbours. Mn^{2+} in $\text{Ge}_{100-x}\text{Sn}$ ($x=50, 54, 58, 62, 66.7$) gives rich ESR spectra (Watanabe *et al* 1978) with the composition $x=58$ and 66.7 giving as many as four times at $g=2.0, 2.8, 4.3$ and 6.0 , suggesting a large variety of internal electric fields of distinct symmetry in these glass compositions, while the $x=50$ composition gives only the $g=2.0$ line, corresponding to Mn^{2+} , in nearly cubic symmetry. The two other compositions $x=54$ and 62 give two resonances at $g=4.3$ and $g=2.0$ with the latter exhibiting a hyperfine structure of magnitude $(65 \pm 5) \times 10^{-4} \text{ cm}^{-1}$.

$\text{Ge}_x\text{Se}_{1-x}$ ($23 \leq x \leq 44$) glasses containing 0.5 at.% Ti (Zhilinskaya *et al* 1991) give, when n lies between 32.5 and 41, a line with $g_{\text{av}}=1.982$, due to Ti^{3+} ($3d^1$) in a tetragonally-compressed octahedral environment. The

concentration of this centre increases with increasing x . For $x \leq 33.3$, an intrinsic paramagnetic centre I and I' with principal g values 2.051, 2.025, 2.0036, corresponding to different configurations of S in the Ge-S group. While doping with Ti or/and Cu, the g -parameters, Ti doping decreases the intensity, Cu doping affects the intensity depending on the concentration. Cu-doping decreases the concentration of this centre.

10.1.3 Insulating glasses

10.1.3a Photochromic glasses have the characteristic property of optical absorption. They are prepared by the introduction of Cu(I)-doped (0.01%) (Ag-halide microcrystals ($\sim 100 \text{ \AA}$) in a borosilicate glass matrix. The process is due to photolysis of silver halide particles, which is akin to photographic latent image formation (Khan 1992), is enhanced by Cu, a well-known catalyst. It exists as optically inactive but ESR active in the glass matrix and as optically active in the form of Cu^+ in Ag-halide particles. The darkening mechanism are:



The glass matrix does not allow the reaction to proceed so that the darkening is reversible. The absorption of colloidal silver ($\sim 400 \text{ nm}$) is due to Ag^0 aggregates on silver halide particles. Darkening i.e. brown colouration is due to the formation of photoproducts are expected to exist in the glass matrix.

Table 11. ESR parameters for $\text{V}_2\text{O}_5\text{-MO}_2$ glasses[#].

Second component	g_{\parallel} (± 0.005)	g_{\perp} (0.005)	A_{\parallel} (mT ± 0.1)	A_{\perp} (mT ± 0.1)
GeO_2 950°C	1.908	1.984	17.9	6.7
750°C	1.915	1.966	17.5	6.9
SeO_2	1.974	1.993	15.6 ± 1	7.5 ± 1
TeO_2	1.921	1.990	17.7	6.5
SrO	1.993	1.982	17.6	5.7

quardt (1976) detected the ESR of photo-induced ions distributed among 16 distorted randomly-oriented, approximately axial cation sites in the silver phase. These Cu^{2+} centres, resembling those in AgCl crystals doped with Cu^{2+} , are characterized by $g_1 = 2.05(2)$, $g_2 = 2.11(5)$ and $g_3 = 2.22(5)$, $A_1 \leq 2$ mT, $A_2 = 7.8$ (0.5) mT and $A_3 = 9$ (0.5) mT obtained by computer simulation and are to be distinguished from matrix-glass-like Cu^{2+} . A dual-cavity method together with microwave saturation of Cu^{2+} was employed to enhance the ESR signal.

Recent ESR studies (Caurant *et al* 1992) on photochromic glasses containing 0.175 wt.% Ag, 0.204 wt.% Br and 0.007 wt.% Cu have used a simple method which selectively eliminates the signal of matrix Cu^{2+} (figure 30). Keeping the dc magnetic field fixed, the intensity of Cu^{2+} resonance is monitored as a function of irradiation time (mercury lamp light focused through optical fibre). The role of the hole trapped by copper is demonstrated to be both to stabilize such holes and to generate the interstitial silver ions which trap the electrons.

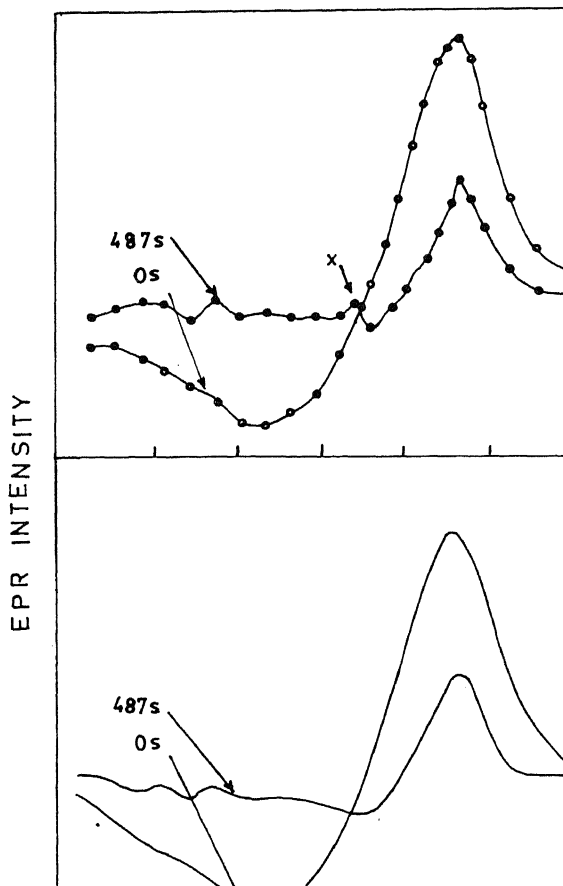
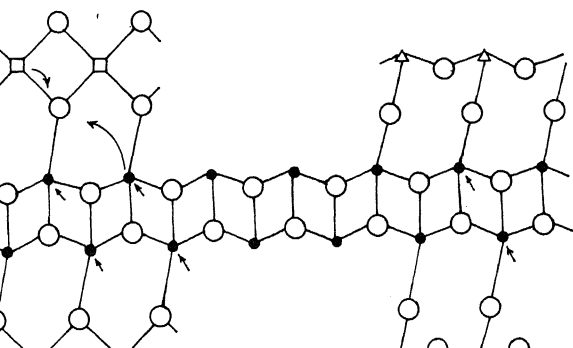
ESR studies of time evolution of photo-induced Cu^{2+} in thermally-bleached silver halide photochromic glasses (Caurant *et al* 1993) have shown that during exposure to light, only one stable Cu^{2+} species — a Cu^{2+} -Ag vacancy complex with silver in a nearest neighbour position ($\text{Cu}^{2+}-\text{V}_{\text{Ag}})_A$ — is formed. It is characterized by $g_x = 2.116$, $g_y = 2.244$, $g_z = 2.076$ and $A_x = 6.8$, $A_y = 7.0$, $A_z = 3$ mT. This centre decays rapidly in the dark, through two parallel mechanisms:

(i) Dislocation of the complex ($\text{Cu}^{2+} + e^- \rightarrow \text{Cu}^+$) by

displacement of vacancy along a (Chen *et al* 1985) direction in the fcc lattice of $\text{AgCl}_x\text{Br}_{1-x}$, with an activation energy of 0.44 eV and a frequency factor of $3.4 \times 10^5 \text{ s}^{-1}$.

(ii) Conversion of $(\text{Cu}^{2+}\text{V}_{\text{Ag}})_A$ to $(\text{Cu}^{2+}\text{Cl}^-\text{V}_{\text{Ag}})_B$ if the silver vacancy is in the next nearest neighbour position along (Chen *et al* 1985) direction, with the same activation energy as A but with a slightly different frequency factor of $3.1 \times 10^5 \text{ s}^{-1}$. The $(\text{Cu}^{2+}\text{Cl}^-\text{V}_{\text{Ag}})_B$ centre with $g_x = 2.066$, $g_y = 2.077$, $g_z = 6.5$ mT, decays slowly by a vacancy hopping mechanism ($B \rightarrow \text{Cu}^{2+}$) with an activation energy 0.22 eV and a frequency factor of 4.6 s^{-1} .

Annihilation of A and B centres via the formation of a Cu^+ ion and a neutral complex $(\text{Ag}^{++}\text{V}_{\text{Ag}})_C$ which migrates to the surface of the silver halide particle.



where electron-hole recombination occurs) explain these two decay channels. This study convincingly demonstrates that the $\text{Cu}^{++}(\text{A})$ centre is the one detected at equilibrium darkening while $\text{Cu}^{++}(\text{B})$ is the one found at the end of thermal bleaching.

10.1.3b Fluoride glasses: Halide glasses in general and fluoride glasses in particular, are an important class of optical materials. Water-free BeF_2 glass for instance, is a laser host and a UV window material besides being a core material for ultra-low loss optical fibres. Structurally, BeF_2 glass is akin to fused silica so that a study of impurity ESR spectra would offer important clues to local structure. An ESR study of 'distilled' BeF_2 glasses containing traces of Mn^{++} (13 ppm), Ni (<1.9 ppm) and Fe (20 ppm) have revealed (Griscom *et al* 1986) two resonances: (i) Mn^{++} resonance at $g=2.0$ of six primary hyperfine lines with each line showing a clear $^{19}\text{F}(I=1/2)$. Super hyperfine splitting of at least six components due to F -neighbours, when studied at 35 GHz (figure 31) and (ii) an FMR signal due to precipitated heterogeneous magnetite-like phases similar to NiFe_2O_4 .

A computer simulation of the Mn^{++} spectrum based on an isotropic ^{19}F splitting of 15 G and assuming an octahedral surroundings for Mn^{++} reproduces fairly well the experimental spectrum, leading to the conclusion that the predominant coordination state on Mn^{++} in BeF_2 glass is six-fold.

10.2 Ceramics

Ceramics are ubiquitous materials with uses ranging from capacitors and support for catalysts to devices based on high temperature superconductors. Paramagnetic centres occur in these materials as trace impurities or as deliberately doped additives or else as defects created as a

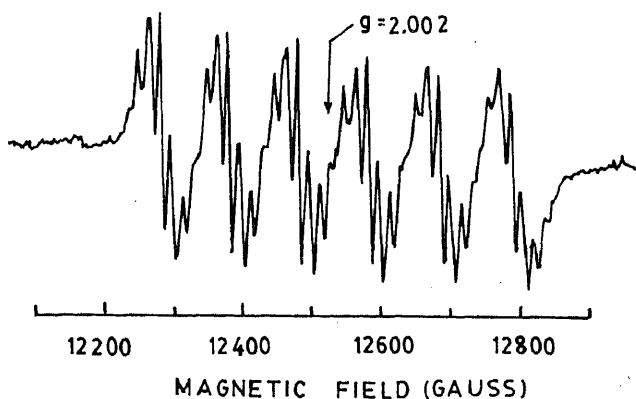


Figure 31. A 35 GHz ESR spectrum of Mn^{++} in distilled BeF_2 glasses, showing the six $^{55}\text{Mn}(I=5/2)$ primary hyperfine lines and the superhyperfine splitting of at least six components due to F neighbours in the glass network.

result of the processing employed to synthesize or modify them. EPR could be used to monitor either the process itself or to characterize the processed materials.

10.2.1 Catalytic ceramics

10.2.1a Shock-modified rutile: High pressure (4.5–27 GPa) shock-modified rutile is found to exhibit enhanced catalytic activity (Graham *et al* 1986). Shock compression does not introduce any structural changes but creates anisotropic residual strain leading to the formation of paramagnetic defects. These defects are stable even at 450°C where catalytic activity is monitored. ESR studies at liquid helium temperatures reveal unique features of these defects and their relation to enhanced catalytic activity. While the starting powder is white and exhibits no ESR, it turns dark grey upon shock compression, the darkness being a function of shock conditions. When the dark grey powder is annealed in air around $500\text{--}600^\circ\text{C}$, the original whiteness is restored.

Two intense resonances are produced due to shock compression: an isotropic one with $g=2.0029(3)$ and an axially symmetric defect with $g_{\parallel}=1.969(5)$, $g_{\perp}=1.937(3)$ for 20 GPa shock. The first one, due to free electrons trapped at a vacancy is less intense (concentration: 3×10^{16}) than the second one, due to a reduction in valence of interstitial Ti from +4 to +3. Higher shock pressures do not alter the concentration of the axial defects but introduce a strong dispersion in the lineshape.

10.2.1b Vanadia catalysts: The study of the mechanism of heterogeneous catalysis requires in-depth studies of the active intermediates formed by transition metal ions interacting with various molecules on the surface of a supported oxide catalyst. ESR offers a powerful and sensitive technique with which to determine (i) oxidation states, (ii) surface and bulk coordination, and (iii) the physical form of a transition metal oxide on a diamagnetic support (Kazanskii 1976). This technique has been applied to V_2O_5 catalysts supported on SiO_2 , Al_2O_3 , MgO as well as MoO_3 and TiO_2 to obtain specific information about (i) the local structure around the paramagnetic $\text{V}^{4+}(3d^1)$, (ii) the differences in the microstructure arising from the distinct nature of the support and (iii) the so-called 'carrier effect' involving the support and active sites. Results of such investigations allow definite conclusions to be drawn about the reactivity of V^{4+} with gaseous oxygen formed on the supported catalysts, which is the theme of heterogeneous catalysis.

Vanadia catalysis supported on alumina has been used in a number of oxidation and ammoxidation reactions involving aromatic hydrocarbons and also for reduction of NO with NH_3 . ESR characterization of the catalyst with respect to the amount of transition metal oxide and

conditions of reduction is an important first step towards optimization, for end use in an actual reaction.

In a typical study (Chary *et al* 1984), 3.41–20.11 wt% V_2O_5 prepared by decomposition of NH_4VO_3 , impregnated on 60–70 mesh $\gamma-Al_2O_3$ support with a pore volume of 0.45 cm³/g and surface area 188 m²/g and reduced by flowing hydrogen (500°C), was investigated by ESR. While the colour of the catalysts ranged from light green to dark yellow as V_2O_5 content was increased, none of the catalysts exhibited any ESR at 300 K, unlike the unsupported V_2O_5 which shows a symmetric singlet ESR at 300 K with $g = 2.000$, $\Delta H_{pp} = 17$ mT which reduces to 2 mT at 109 K. The ESR spectra of the catalysts obtained at 109 K (figure 32a) are characteristic of isolated $(V \dots O)^{2+}$ species in a ligand field of axial symmetry produced by a distorted octahedron of oxygen atoms (table 12). For V_2O_5 content equal to or in excess of 9.84%, the low-field parallel ^{51}V ($I = 7/2$) hyperfine components (figure 32b) of the axial ESR spectra show a doublet structure, characteristic of two chemically distinct

V^{4+} species. The concentration of the second component attains a maximum when the V_2O_5 content in the catalyst is 20.11%. The second, weaker set of parallel components, also due to V^{4+} could arise from a relatively unstable intermediate whose ligands consist of adsorbed oxygen atoms. An examination of the crystal structures of the orthorhombic V_2O_5 (figure 32c) and cubic $\gamma-Al_2O_3$ reveals that the two distinct set of hyperfine peaks arise from V^{4+} occupying octahedral and tetrahedral vacant sites surrounded by oxygens in the $\gamma-Al_2O_3$ lattice. Thus on the surface of $\gamma-Al_2O_3$ one could have V^{4+} dispersed uniformly as active sites with tetrahedral or square pyramidal surroundings, with dynamic equilibrium between the two and with the number of sites available for occupation depending on the concentration of V_2O_5 in the catalyst.

10.2.1c *Molybdenum sulphide catalysts:* Heteroccracking—an important catalytic process in the conversion of crude petroleum to gasoline—uses molybdenum

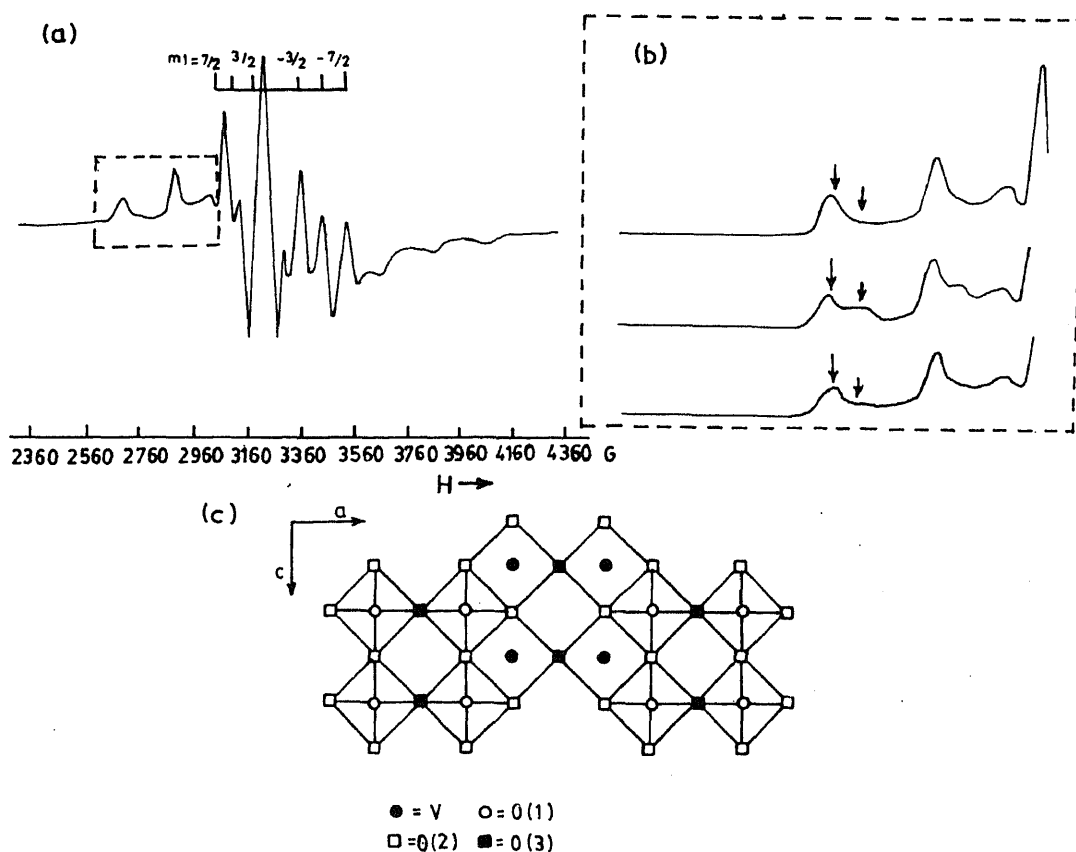


Figure 32. a. ESR spectra of a reduced 3.41% vanadia catalyst supported on γ -alumina, at 109 K. The parallel and perpendicular hyperfine structures of ^{51}V ($I = 7/2$) are clearly resolved, b. evolution of the low field parallel ESR peaks (marked area in (a)) as a function of V_2O_5 content. Top: 6.96%, middle: 9.84%, bottom: 11.89%. The lengths of arrows indicate relative peak heights of the main and subsidiary V^{4+} centres and c. schematic structure of V_2O_5 in the crystallographic ac plane with VO_5 polyhedra idealized to tetragonal pyramids. The $O(1)$ oxygens forming the strongest bonds with V are shown as open circles (Chary *et al* 1984).

sulphide as a catalyst. The catalyst is prepared from Mo-oxides sulphurized either before melting with petroleum or directly *in situ*. Usually sulphurization is never complete, and thus the catalytically active compounds are Mo sulphides in which oxygen remains. The electron configuration of the catalyst determines the catalytic process.

ESR measurements of amorphous MoS_{2+x} ($0 \leq x \leq 1$) and their compounds Mo_yO_z obtained by oxygen exposure at 130°C have revealed the nature and concentration of active sites (Bensimon *et al* 1992). The ESR spectrum is always the sum of three elementary signals arising from (i) unsaturated sulphur atoms and characterized by $g = 2.027 \pm 0.001, 2.038$ and 2.034 for MoS_2 , $\text{MoS}_{2.6}$ and MoS_3 , respectively, and (ii) Mo^{5+} ($4d^1$) found in two different surroundings, as reflected by the g -tensors: A : $0.02, 1.99$ and 1.97 and B : $1.94, 1.92$ and 1.89 . As the evolution from MoS_3 to MoS_2 proceeds, the spectra show a drastic modification around the composition $\text{MoS}_{2.6}$ by way of a 'pseudo-transition' in which a change in the short-range structural order of the amorphous solid occurs. This is confirmed by the influence of oxygen exposure which leads to an increasing number of paramagnetic defects in accordance with catalytic properties.

10.2.2 Cuprate ceramics

CuO and its binary and ternary compounds with MO ($M = \text{Mg, Sr, Ca, Ba}$) and R_2O_3 ($R = \text{Y, La, Gd, Nd, Bi, Tl}$) form an extensive class of magnetic (e.g. Bi_2CuO_4 antiferromagnetic, $T_N = 42 \text{ K}$) and superconducting

ceramics (e.g. $\text{YBa}_2\text{Cu}_3\text{O}_7$ with $T_c \sim 90 \text{ K}$, $\text{Bi}_2\text{Sr}_2\text{CaCu}_2\text{O}_8$ with $T_c = 120 \text{ K}$) whose study is crucial to a basic understanding of magnetism and superconductivity, and, eventual applications to high-field magnets and magnetic levitation. Zero-field and low-field microwave absorption and ESR have played a significant role in the characterization of superconducting ceramics.

10.2.2a Cupric oxide: Cupric oxide, the precursor to high- T_c superconductors of the La-, Y-, Bi-, Tl-, and Hg-families, is a monoclinic-structured anti-ferromagnetic insulator, with a Neel temperature T_N of 230 K . A recent ESR study at 45 GHz (Kindo *et al* 1990), using pulsed magnetic field and a reflection cavity has detected a 1.6 T wide resonance line at room temperature, with a slight temperature dependence of $g \approx 2.0$ and a lineshape between Lorentzian and Gaussian, and arises from anisotropic exchange interaction between Cu^{++} spins. The linewidth decreases as the temperature is decreased and the line broadens near T_N due to critical slowing down. One-dimensional spin correlation is seen in the ESR line-profile.

The antiferromagnetic coupling between Cu spins via oxygen atoms is believed to be important for the mechanism of superconductivity in cuprate superconductors.

10.2.2b Ternary cuprates: Compared to CuO , ternary cuprates SrCuO_2 , Sr_2CuO_3 , Ca_2CuO_3 , Li_2CuO_2 , and Bi_2CuO_4 have very small net magnetic susceptibilities and a few of these have very low T_N values. Li_2CuO_2 , with $T_N = 9.3 \text{ K}$ and Bi_2CuO_4 , are both three-dimensional antiferromagnets. Bi_2CuO_4 , which has a simple anti-ferromagnetic order consisting of magnetic moments

Table 12. Spin Hamiltonian parameters of V^{4+} in $\text{V}_2\text{O}_5/\gamma\text{-Al}_2\text{O}_3$.

V_2O_5 content (wt %)	Colour of catalyst	g_{\parallel}	g_{\perp}	A_{\parallel} (mT)	A_{\perp} (mT)
3.41	light green	1.940	2.000	19.4	7.1
6.96	light green	1.939	1.997	19.4	7.3
9.84	dark green	M 1.942 S 1.983	2.000	19.4 17.5	7.0
11.89	light yellow	M 1.942 S 1.983	1.999	19.2 17.0	7.0
13.64	dark yellow	M 1.938 S 1.971	1.995	19.4 17.4	7.1
14.76	dark yellow	M 1.939	1.998	19.2	7.2
16.37	dark yellow	M 1.941 S 1.977	1.999	19.2 17.5	7.1
18.46	dark yellow	M 1.939 S 1.966	1.999	19.3 18.0	7.1
20.11	dark yellow	M 1.939 S 1.960	1.997	19.2 18.0	7.1

[#]Chary *et al* (1984); M: Main centre; S: additional centre.

igned ferromagnetically along c-axis and antiferromagnetically between spins at the corner and body-centre sites of the orthorhombic crystal lattice. ESR of the powder at $T > T_N$ at X-band gives a resonance at $g_{\parallel} = 2.09$, while for a single crystal at 370.4 K and 265 K (Bhat *et al* 1992), an axial spectrum is obtained with $g_{\parallel} = 2.26 \pm 0.01$ and $g_{\perp} = 2.04 \pm 0.01$ for H_{\parallel} c-axis and H_{\perp} c-axis, suggesting Cu^{++} situated at an pseudo octahedral site, even though there are only four oxygen ligands for Cu^{++} . The line is Lorentzian and exchange-narrowed and the linewidth (0.37 ± 0.03 T) is almost field independent. An antiferromagnetic resonance mode of the planar type in an antiferromagnet has been observed below T_N .

2.2c Cuprate superconductors: Nonresonant microwave absorption in small magnetic fields is one of the most sensitive techniques for observing small amounts

of superconducting phase in an otherwise nonsuperconducting environment (Muller *et al* 1980; Bhat *et al* 1987) or small amount of nonsuperconducting impurity in an otherwise superconducting sample, by way of Cu^{++} ESR with $g_{\parallel} = 2.117$, $g_{\perp} = 2.120$ for BaCuO_2 (Jones *et al* 1990). In this simple technique the sample is placed in a microwave cavity at ~ 9 GHz which is connected to a standard ESR spectrometer. A small magnetic field (± 10 mT) and a modulation field parallel to the external field are applied to the sample. The change in the microwave absorption is detected via lock-in amplifier when varying the external field.

The shape of the signal (figure 33a) is characteristic of a granular superconductor in the superconducting state. This frequency independent signal which vanishes above T_c is caused by weak links or Josephson junctions connecting large superconducting areas, and represents the change of the superconducting surface impedance as a function of the applied magnetic field. This technique has been applied (Mehring *et al* 1993) to the study of the topology of superconducting phase changes in La_2CuO_4 :Sr processing parameters especially the rate of cooling, which decides the size and shape of superconducting region. The low-field microwave absorption (figure 33b), shows a maximum at a field which is recognized as the lower critical field, H_{c1} , of the superconductor. For $H > H_{c1}$ the superconductor enters the 'mixed state' which persists until the upper critical field, H_{c2} , ($H_{c2} \gg H_{c1}$) (Tinkham 1980). For $0 < H < H_{c1}$, the microwaves penetrate only the sample surface, while for

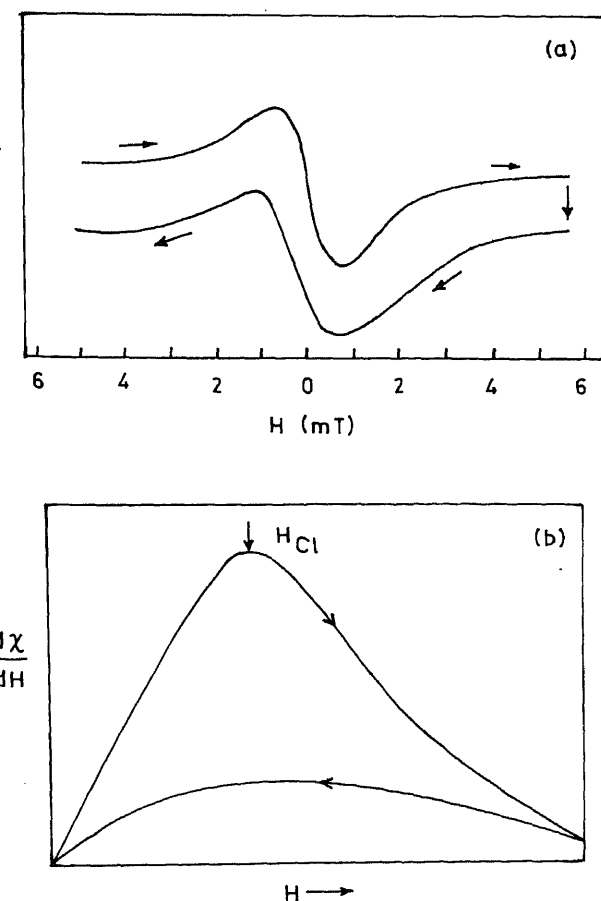


Figure 33. Zero-field and low-field microwave absorption in high temperature cuprate ceramic superconductors (schematic). The frequency-independent, reversible, absorption as the dc magnetic field is scanned from negative through zero to positive. **(b)** the low-field microwave absorption showing hysteresis. The turning point obtained upon increasing magnetic field from negative to positive corresponds to the lower critical field (H_{c1}) which characterizes these granular, type II superconductors.

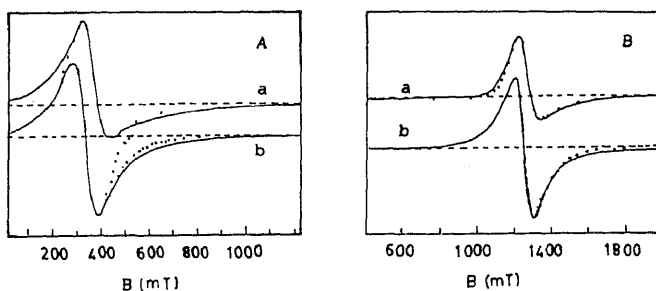


Figure 34. ESR spectra of superconducting, orthorhombic $\text{GdBa}_2\text{Cu}_3\text{O}_7$ (with $T_c \sim 90$ K), at 300 K. **A.** (a) X-band ($\nu = 9.384$ GHz) spectrum of single crystal at 20 mW power and modulation of 2 mT peak-to-peak: $g_{\text{eff}} = 1.82$, $\Delta H_{\text{pp}} = 128 \pm 6$ mT static field parallel to c-axis. The line has been fitted (*) to a Dysonian shape and (b) powder spectrum at 9.380 GHz $g = 2.02$ $\Delta H_{\text{pp}} = 112 \pm 6$ mT, fitted to Lorentzian (*) and Gaussian (.) shapes. **B.** (a) Q-band (34.982 GHz) spectrum of single crystal at 5 mW power and 4 mT modulation amplitude. $g_{\text{eff}} = 1.96$ and $\Delta H_{\text{pp}} = 124 \pm 8$ mT, fitted to a Dysonian shape (*) and (b) powder spectrum at 35.001 GHz and 5 mW. $g = 2.004$ and $\Delta H_{\text{pp}} = 108 \pm 4$ mT fitted to Lorentzian (*) and Gaussian (.) shapes. In (A) and (B) the ESR intensity of same sample increased by factors of 7 and 20 respectively upon grinding (Deville *et al* 1993).

$H > H_{c1}$ microwaves penetrate into the core of the superconductor. Thus we have a quick and convenient method of determining H_{c1} of high T_c (type II) superconductor using a conventional EPR spectrometer after compensating for remnant field of the electromagnet (Janes *et al* 1991).

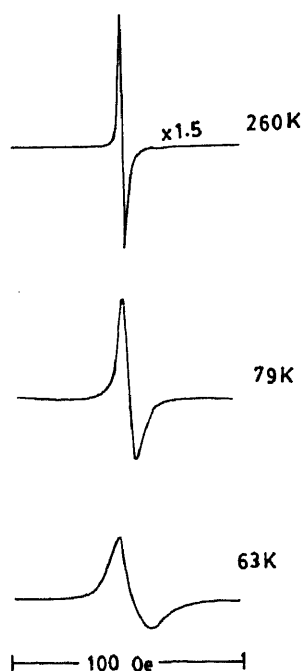
ESR has been applied to (i) look at the pinning centres for the flux motion in the $\text{YBa}_2\text{Cu}_3\text{O}_7$ superconductor (Baranov and Badalyan 1993), (ii) the nature of the paramagnetic systems in the normal state ($T > T_c$) of $\text{GdBa}_2\text{Cu}_3\text{O}_7$ (Deville *et al* 1993) (figure 34) and (iii) the study of flux line lattice through measurement of the magnetic penetration depth (λ) in ceramic $\text{YBa}_2\text{Cu}_3\text{O}_7$, $\text{Bi}_2\text{Sr}_2\text{CaCu}_2\text{O}_8$ (Rakvin *et al* 1990), and $\text{Tl}_2\text{Ba}_2\text{Ca}_2\text{Cu}_3\text{O}_{10}$ (figure 35) and single crystals of $\text{YB}_2\text{Cu}_3\text{O}_7$ (Koshta *et al* 1993), with the surfaces coated (decorated) by organic radical of DPPH (the calibration standard for g -factor). In the superconducting state, there is observed an inhomogeneously broadened ESR signal from DPPH due to the so-called flux-line lattice formation. From the temperature-dependent linewidth the magnetic penetration depth at 0°K (λ_0) is calculated. The variation of λ follows the law

$$[1 - (T/T_c)^4]^{-1/2}.$$

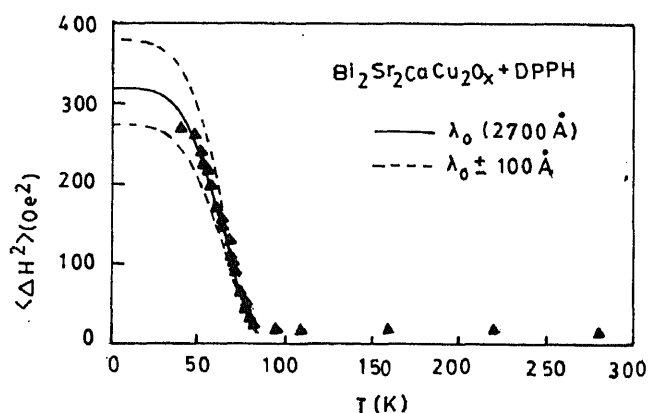
Experiments on single crystal samples show that the main contribution to inhomogeneous broadening comes from the flux lattice and not from granularity and screening effects.

10.2.3 Fullerenes: Superconductors based on the C_{60} or Buckminsterfullerene or fullerene, with soccerball structure and unusual electronic structure that makes it accept up to 6 electrons obtained by intercalating it with alkali metals K (Hebard *et al* 1991) and Rb (K_3C_{60} : $T_c = 18$ K; Rb_3C_{60} : $T_c = 28$ K), exhibit well-defined ESR spectra in their normal and superconducting states. A precise ESR study of K_xC_{60} (Kosaka *et al* 1993) ($x=3$, face centred cubic (fcc); $x=4$, body centred tetragonal (bct); $x=6$, body centred cubic (bcc)) has clearly identified resonances at g 's = 2.0014, 2.0004 and 1.9952 (figure 36) as arising from the fcc, bct and bcc phases, respectively. In another interesting application to Rb_xC_{60} compounds (Byszewski *et al* 1992), thermally-treated samples (diffusion of Rb into C_{60} powder at

$\text{Bi}_2\text{Sr}_2\text{CaCu}_2\text{O}_x + \text{DPPH}$



(a)



(b)

Figure 35. ESR spectra of DPPH absorbed on $\text{Bi}_2\text{Sr}_2\text{CaCu}_2\text{O}_x$ superconductor, in order to determine microwave penetration depth. **a.** Temperature dependence through the superconducting transition temperature ($T_c = 82$ K). Note the significant line broadening below T_c and **b.** temperature dependence of second moment or linewidth of DPPH ESR signal. The solid line is a theoretical fit (see text) which yields zero temperature penetration depth (λ_0) of 2700 Å with $T_c = 84$. The dashed lines correspond to fits with 2700 ± 100 Å which shows that the λ_0 deduced is accurate to better than 3.7% (Rakvin *et al* 1990).

0–450°C and subsequent homogenization at 200–300°C) exhibited ESR signals due to an on-molecule electronic state. Thus clear differences exist in the ESR spectrum at the transition from normal to superconducting state, by way of a decrease in ESR signal amplitude at the superconducting to normal state transition. Thus it appears that carriers partially localized on the C_{60} molecules due to the Coulomb repulsion energy form superconducting states by intermolecular coupling.

Optoelectronic and superionic materials

1 Optoelectronic materials

Optoelectronic phenomena rely on the ability of certain materials (e.g. $BaTiO_3$, $Bi_4Ge_3O_{12}$) to exhibit photoconductive and photorefractive effects. These materials respond to light-induced space-charges by large changes in the refractive index (Gunter and Heiguard 1988, 1989). These effects arise from the UV/visible light sensitivity of transition metal impurities doped in these materials. EPR is thus a natural technique to apply to these materials to learn about the valence state of the doping ions, changes in the valence state under illumination, and the physical location of the impurity in the crystal lattice. This basic characterization is crucial for all applications including optical memory and information storage, frequency doubling and parametric oscillation, as an important first step towards optimization of device performance.

11.1a Barium titanate: Barium titanate — the well known ferroelectric material — when doped with transition metal ions of iron group and suitably poled to give wide (~10 K) thermal hysteresis for the cubic-to-tetragonal phase transitions at nearly 130°C on cooling, exhibits high photorefractive gain and is thus of interest for many applications that involve optical phase conjugation and signal processing. The origin of its photorefractive properties i.e. the exact nature of the microscopic centres responsible for the large changes in refractive index light-induced space is linked with (i) control of doping level of single crystals, (ii) discrimination between dopant-related charge-compensation-related effects, and (iii) the oxygen vacancies created by thermal treatments (e.g. in oxidizing/reducing atmospheres).

EPR experiments with transition-metal-doped $BaTiO_3$ powder treated under a wide range of oxygen partial pressures revealed valence state changes in Co, Cr and Mn-doped material whereas for the dopants Fe, Ni and Cu such changes were absent, which suggest that the former group of ions are likely to show better photorefractive effect than the latter. Of Co, Cr and Mn, Mn has a smaller optical absorption while Cr-doped crystals of optical quality are difficult to obtain. Thus Co-doped $BaTiO_3$ emerges as the most promising candidate for photorefraction.

The EPR spectrum of powdered single crystal of 50 ppm Co-doped $BaTiO_3$ processed in a reducing atmosphere at 18 K (Rytz *et al* 1990) is shown in figure 37. It exhibits the extended hyperfine structure (by way of two overlapping octets) that arise from the

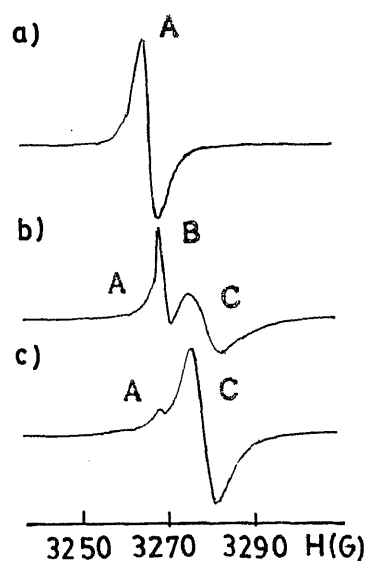


Figure 36. ESR spectra, at 5 K, of K-intercalated C_{60} (a) K_3C_{60} , (b) K_4C_{60} and (c) K_6C_{60} . The signals A, B and C correspond to fcc, bct and bcc phases of these fullerenes (Kosaka *et al* 1990).

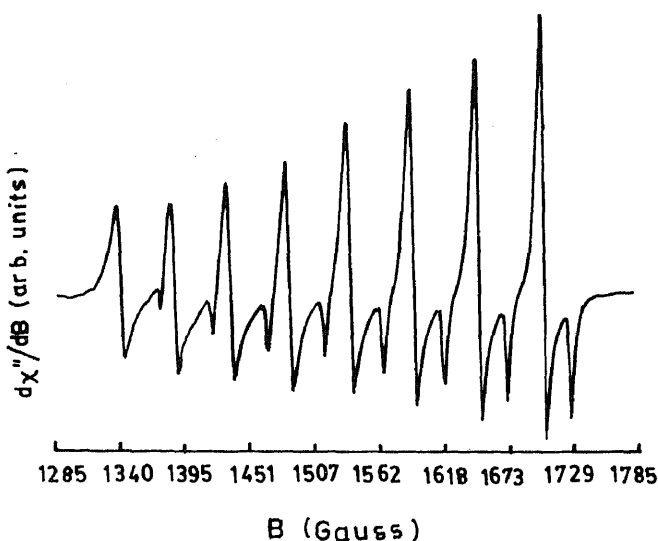


Figure 37. X-band EPR spectrum of powdered single crystal of $BaTiO_3:Co$ at 18 K, recorded at 1 mW power, and 9.26569 GHz, with a field modulation of 0.2 mT. The octet is assigned to Co^{2+} with $S = 3/2$, $I = 7/2$, with $g_{||} = g_{\perp} = 4.341$ and $|A| = 5.16$ mT (Rytz *et al* 1990).

100% abundant ^{59}Co ($I=7/2$). For the intense octet, $g_{\parallel} = g_{\perp} = 4.341$ with hyperfine constant $|A| = 5.16$ mT. The octet is assigned to high spin Co^{2+} with $S=3/2$. A spin Hamiltonian with isotropic g and moderate zero field splitting accounts for the spectrum. Besides this, an intense feature with $g=2.004$ due to high spin Fe^{3+} ($S=5/2$) is also present. This high spin Co^{2+} not associated with an oxygen vacancy is EPR active, while Co^{2+} , (low spin $S=1/2$) — oxygen vacancy, complex a product of reduction diamagnetic Co^{3+} (low spin) — oxygen vacancy complex — though EPR active is not detected at X-band frequencies.

11.1b Lead-zirconate-titanate: Ferroelectric lead-zirconate-titanate (PZT) thin films find use in nonvolatile memories and optical information storage devices. Defects and optically-induced metastable trapping centres in PZT control the electrical and optical behaviour. It is thus necessary to understand the nature of these trapping centres.

Warren *et al* (1993) have identified, through EPR, a positively charged Pb^{3+} defect centre in PZT ($\text{Zr/Ti}=53/47$) ceramics. The charged traps were generated by ultraviolet illumination in the band gap region (3.4 eV). The EPR spectrum of the centre, recorded using high power microwave quanta of 0.314652 cm^{-1} and second harmonic detection, consists of an intense peak with $g=1.995$ at 0.5530 T arising from non-magnetic Pb nuclei, a weaker line 1.145 T, caused by a very large hyperfine ($A_{\text{isotropic}} = 1.0803\text{ cm}^{-1}$ or 1.1599 T, $A_{\text{aniso}} = 0.00233\text{ cm}^{-1}$ or 2.5 mT) with a less abundant ^{207}Pb nucleus with $I=1/2$, on the basis of which the centre is assigned to Pb^{3+} which has valence-shell configuration of $6s^1$. Pb^{3+} could arise from some of the Pb^{2+} corner-sites in the perovskite PZT lattice, by capturing a hole and becoming paramagnetic. The centre is further characterized through its wave function with 40% 6s-character and at the most 8% 6p-character so that there is 48% localization of unpaired electron on Pb atom, with the rest of $\approx 52\%$ unpaired spin density being spread over the 12 oxygen neighbours in the perovskite.

11.1c Bismuth germanate: $\text{Bi}_4\text{Ge}_3\text{O}_{12}$ has a crystal structure made up of a cubic arrangement of distorted oxygen octahedra surrounding each Bi^{3+} ion and oxygen tetrahedra around each Ge^{4+} . Thus it offers two sites — Bi^{3+} and Ge^{4+} — for occupation by a transition metal rare earth impurity ion (Bravo *et al* 1993). EPR studies have established that Gd^{3+} impurities occupy Bi^{3+} sites, while Cr ions, detected as Cr^{4+} occupy Ge^{4+} , and Cr^{3+} occupy Bi^{3+} sites. Mn^{2+} ions are found to occupy Bi^{3+} sites without charge compensation, and undergo change of valence under UV illumination. Co^{2+} ions, likewise, are found to occupy Bi^{3+} probably without charge compensation.

11.1d Lithium vanadate and lithium borate: These are nonlinear optical materials employed for doubling of optical frequencies e.g. to obtain blue/green light from an infrared laser beam. These materials need to be thoroughly characterized for trace chemical impurities and for irradiation-induced defects because their optical and electrical properties are strongly influenced by defects and impurities.

Lithium vanadate (Li_3VO_4) when prepared in β -II phase, has a second harmonic generation behaviour comparable to that of LiNbO_3 (Sakita and Fujii 1991). Two ESR active, trapped hole centres are formed when Li_3VO_4 is exposed to X-rays at 77 K (Murata and Miki 1993): (i) CO_3^- , stable at ambient, with $g_1 = 2.021$, $g_2 = 2.011$ and $g_3 = 2.0057$, coming from Li_2CO_3 used in sample preparation, and (ii) an intrinsic O^- type centre with one neighbouring vanadium ion, with $g_{xx} = g_{yy} = 2.026$, $g_{zz} = 2.028$ and $A_{xx} = A_{yy} = 2.05$ mT, $A_{zz} = 3.075$ mT due to ^{51}V ($I=7/2$) nucleus. This second centre is unstable above 150 K and is completely annealed at room temperature. Two significant features of this centre viz. poor thermal stability and no coloration at ambient temperature favour the use of Li_3VO_4 as a frequency doubler.

LiB_3O_5 is a common second-harmonic generator material, involving a fundamental wave, around $1.06\text{ }\mu\text{m}$, with a phase-matching angle along a crystallographic axis. Two unique properties: (i) temperature dependent refractive indices, and (ii) wide (160–1300 nm) range of optical transmission make this an ideal nonlinear material.

Two prominent point defects: (i) a trapped hole centre localized on an oxygen ion near a ^{11}B nucleus (with a smaller ^{11}B hyperfine structure), and (ii) a trapped electron centre — also localized on a ^{11}B but with a larger hyperfine structure — have been observed in the ESR and ENDOR of this biaxial crystal irradiated with γ -rays near 77 K (Scripsick 1993). The significant findings are: (i) the lack of ESR spectra due to transition metal impurities Fe^{3+} , Cr^{3+} and Mn^{2+} present at < 100 ppb level in LiB_2O_5 rather than at ppm level in other SHG materials LiNbO_3 and KTiOPO_4 , and (ii) both the irradiation-induced centres thermally anneal in the 120–130 K range.

11.1e Other materials: A recent EPR study has demonstrated (Whitmore 1993) that tetrahedral Cr^{4+} is responsible for the near-infrared laser activity in Cr-doped Forsterite (Mg_2SiO_4). Fe^{3+} , Fe^{3+} -oxygen vacancy, Co^{2+} , Co^{2+} -oxygen vacancy and Ir^{4+} have been identified in photorefractive KNbO_3 in its rhombohedral and orthorhombic phases (Possenriede 1989).

11.2 Superionic materials

Superionic conductors are ionic solids whose conductivities at ambient temperatures are of the order of molten salt electrolytes and thus they are also called solid

electrolytes. Thus any application of ESR to such systems must aim at elucidating the effects of ionic motion and determine site symmetries of defects that block preferred hopping paths in the superionic conductor.

Four such studies are noteworthy: (1) Mn^{2+} in PbF_2 , (2) Cu^{2+} in β -sodium gallate, (3) Ag^{2+} in β -alumina and (4) Ag^{2+} in $\text{AgI-Ag}_2\text{O-B}_2\text{O}_3$ glass.

(a) Mn-doped lead fluoride: PbF_2 is an F^- ion conductor at high temperatures where the high mobility of F^- ions is expected to affect the EPR of Mn^{2+} ions by effects of line narrowing, line broadening and disappearance of additional structure in each of the Mn^{2+} ($I = 5/2$) hyperfine components (Evora and Jaccorino 1977) due to ^{19}F nuclei observed at low temperatures (figure 38). Indeed, at the temperatures of onset of motional narrowing (100°C (^{19}F hf frequency)) $\tau_{\text{conductivity}} \sim 1$. Above 400°C , the lines start to broaden due to a fluctuating crystal field. The linewidth increases as m_i^2 , where m_i is the nuclear magnetic quantum number, which is interpreted as a phonon enhanced spectral density of the fluctuating crystal field. F^- sublattice melting enhances hyperfine interaction. This phonon coupling is greatly enhanced by rapid ionic diffusion, giving lines as narrow as 0.1 mT.

(b) Copper-doped β -sodium gallate: In a study of copper-doped single crystal β -sodium gallate isostructural with β -alumina, and with nearly same Na^+ conductivity, it was found that at room temperature, the anisotropic hyperfine structure of $^{63,65}\text{Cu}$ ($I = 3/2$) and the g -anisotropy of Cu^{2+} resonance is washed out/averaged out due to symmetry fluctuations through Cu^{2+} /ligand motion

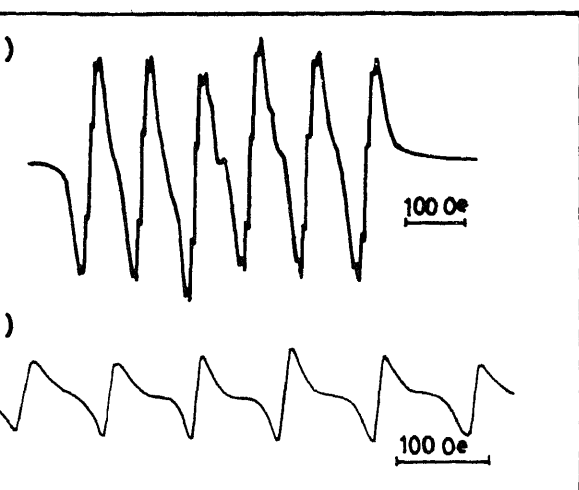


Figure 38. EPR spectra of Mn^{2+} in PbF_2 at (a) 77 K and (b) 460 K. Note the line broadening and absence of additional structure in (b) when PbF_2 is in the disordered superionic phase (Evora and Jaccorino 1977).

(Title and Chandrasekhar 1976). A correlation time (for the $\text{Cu}^{2+}/\text{Cu-O}$ complex) of 10^{-11} sec, two orders faster than Na^+ hopping time (10^{-9} sec) was deduced. A motional effect correlating with ionic diffusion is involved, whereby rapid fluctuations of bridging O^{2-} ions with respect to Cu^{2+} triggered by rapid Na^+ diffusion could give rise to the isotropic, structureless ESR line observed.

11.2c Ag centres in β -alumina: Atomic Ag^0 centres and hole Ag^{2+} centres were detected in X-irradiated (77 K) β -alumina crystals (Badalyan and Zhitnikov 1985). Ag was incorporated by immersing Na^+ β -alumina crystals in molten AgNO_3 at 350°C . Orientation dependence of g -factor revealed that Ag^{2+} becomes stabilized at 77 K in a position between two oxygen ions as a minor plane. It is this minor plane that separates the four alternate spinel blocks (containing Ag and O ions) of the β -alumina ($11\text{Al}_2\text{O}_3 \cdot \text{Na}_2\text{O}$) structure, and that contains the mobile Na^+ ions besides O ions, and it is these Na^+ ions that are replaced by Ag^+ ions. Two environments for Ag^{2+} are indicated, with the same axial g but with two different sets of planar g 's. The $^{107,109}\text{Ag}$ hyperfine interaction constants are low, suggestive of a strong delocalization of the hole from Ag^{2+} ion to two oxygen ions on the axis of the centre. A model for Ag^{2+} based on these results is shown in figure 39.

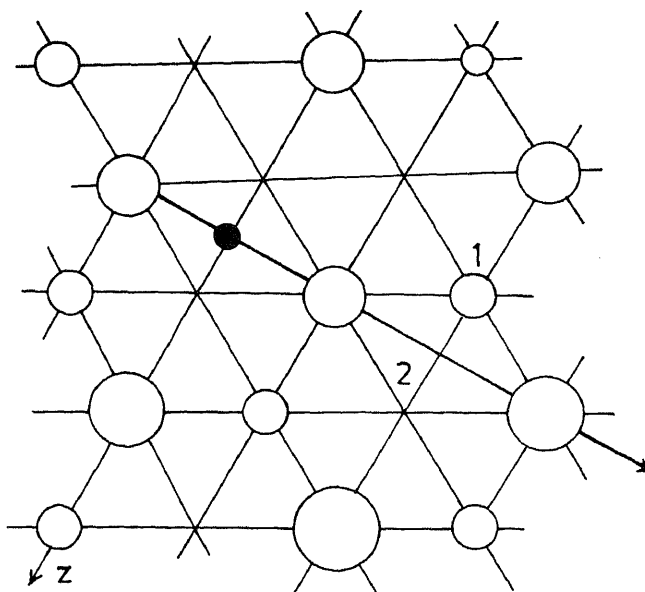


Figure 39. Schematic representation of a reflection plane in the hexagonal β -alumina ($\text{Na}_2\text{O} \cdot 11\text{Al}_2\text{O}_3$) crystal containing Ag^+ ions showing the position occupied by Ag^{2+} centre formed by X-irradiation (dark circle). Large circles are O^{2-} and small ones Ag^+/Na^+ ions. 1 and 2 are the occupied and vacant cation sites called Beavers-Ross and anti-Beavers-Ross sites. In the superionic state, Ag^+/Na^+ ions spend some time at 2 (Badalyan and Zhitnikov 1985).

11.2d Ag^{2+} in $\text{AgI-Ag}_2\text{O-B}_2\text{O}_3$ glass: ESR-active Ag^{2+} ions, stabilized during melt-quenching, in the optimum conductivity 60 AgI-30 Ag_2O -10 B_2O_3 glass have been used to probe the glass structure and Ag^+ conduction mechanism (Balaya and Sunandana 1990). Two clearly distinguishable Ag^{2+} ESR species with different thermal stabilities were identified (figure 40, table 13) and attributed Ag^{2+} in different chemical surroundings. The ESR data neatly correlate with Minami's structural model (Minami *et al* 1982) for this glass and Ag^+ conductivity. The centre I, with a smaller A_{\perp} due to ($I = 1/2$ of Ag) is due to less mobile Ag^{2+} bonded covalently to non-bridging oxygens of BO_3 , and thus thermally more stable, and not involved in conduction. While the centre II with a larger A_{\perp} , should arise from Ag^+ ion ionically bonded to bridging oxygens of BO_4 groups in the borate glass network, are more mobile and contribute to Ag^+ conduction. Ag^{2+} ESR has also been observed in $\text{Ag}_2\text{O-TeO}_2$ (Balaya and Sunandana 1992) glasses where the large covalency of Te-O bond in the glass structure leads to washing out of Ag-hyperfine structure in the ESR spectra.

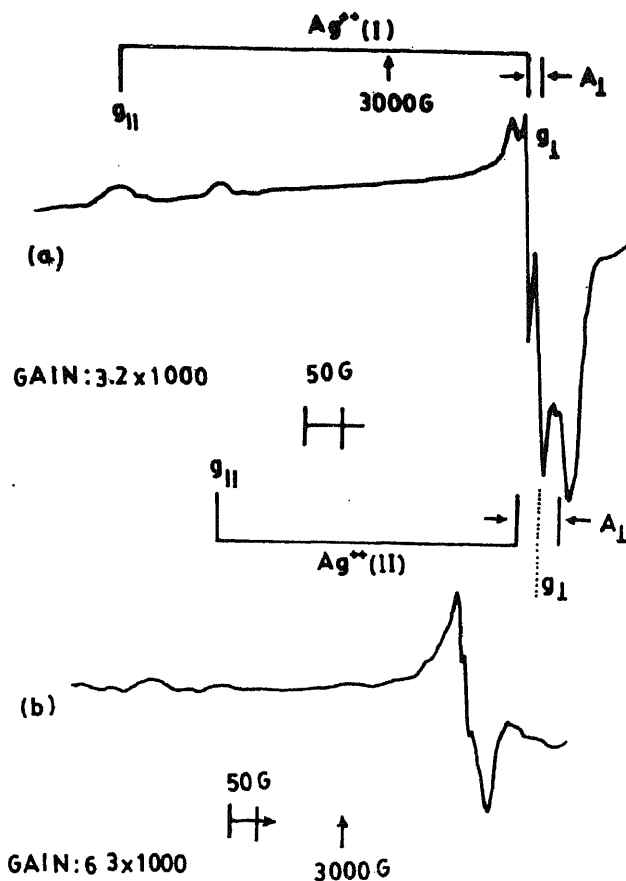


Figure 40. EPR spectra of Ag^{2+} in the superionic conducting 60 AgI-30 Ag_2O -10 B_2O_3 glass at (a) 303 K and (b) 413 K. Note that of the two centres Ag^{2+} (I) and Ag^{2+} (II), the first one is thermally more stable, and is thus less mobile, while the second one contributes significantly to conductivity (see text) (Balaya and Sunandana 1990).

11.2e *Other materials:* ESR of CO_3^- radical formed by X-irradiation in CO_3^{2-} doped $\text{Li}_2\text{SO}_4 \cdot \text{H}_2\text{O}$ single crystal (monoclinic) and cubic (fcc) Li_2SO_4 stabilized at ambient by programmed quenching from the melt aided by a few mole% Li_2CO_3 has been used as a structure sensitive probe (Balaya and Sunandana 1990). The high conducting cubic phase is characterized by a nearly isotropic ESR signal with $g = 2.0094$ and $\Delta H_{pp} = 0.6$ mT resulting from motional averaging of CO_3^- ions. ESR of DPPH adsorbed on AgI has been used to probe the hexagonal-cubic phase transition (147°C) in AgI (Murthy and Sunandana 1992).

12. ESR imaging and microscopy

12.1 ESR imaging

Imaging of the spatial distribution of the properties of advanced materials, especially on a microscopic scale enables a deeper insight into their (physico-chemical) nature to be obtained. ESR imaging (Ikeya 1991) allows for an accurate mapping of the spatially distributed paramagnetic species in the sample. In a typical continuous-wave magnetic resonance imaging experiment, the material is initially placed in a highly uniform dc magnetic field and its ESR spectrum measured (Lauterbur 1973). Then a small magnetic field gradient (1–10 mT/cm) is applied external to the microwave carrier (or inside it) and the broadened, convoluted ESR spectra is recorded. Deconvolution, with the original ESR spectral lineshape gives the spatial distribution of spins because the magnetic field intensity corresponds to the position under a linear magnetic field gradient.

Suppose small magnetic field gradients $\partial H/\partial x$, $\partial H/\partial y$ and $\partial H/\partial z$ are applied, through properly positioned field coils, along x , y and z directions with the uniform field (H_0) along z -direction (H_0). Then the field at the spatial site (x, y, z) is given by

$$H(x, y, z) = H_0 + (\partial H/\partial x)x + (\partial H/\partial y)y + (\partial H/\partial z)z. \quad (88)$$

Resonance occurs at the magnetic field H_r , for the microwave frequency ν , when $h\nu = g\mu_B H_r$. Thus the field intensity obtained by sweeping H_0 is indicative of the positions.

The spatial distribution function of the spins being imaged, $f(z)$ can be expressed as a function $f(H)$ of the magnetic field H because

$$H = H_0 + (\partial H/\partial z)z = H_0 + bz. \quad (89)$$

The ESR spectrum under the field gradient, $g(H)$ is then expressed as a convolution of $f(H)$ and the signal shape function $r(H)$ in the uniform magnetic field as:

$$g(H) = \int_0^\infty r(H - H')f(H')dH'. \quad (90)$$

then the Fourier transform (FT) of the above integral obtained as

$$G(\omega) = R(\omega) F(\omega), \quad (91)$$

where $G(\omega)$, $R(\omega)$ and $F(\omega)$ are the FT's of $g(H)$, $r(H)$ and $f(H)$, respectively. Finally the distribution function $g(H)$ may be obtained by deconvolution using the inverse FT of $F(\omega) = G(\omega)/R(\omega)$ with same filter function as $r(H)$. $F(\omega)^{-1}$ diverges.

There are advantages of modulating the field gradient. The resolution of ESR imaging is limited by the bandwidth of the resonance signals and the available field gradients.

1a Use of a linear field gradient: By using a straight four-wire configuration inside a cavity, Furusawa and Ikeya (1991) have imaged an irradiated teflon tube. The four-wire gradient coil system in a TE_{011} cavity is shown in figure 41. The four copper wires connected to each other and to current sources constitute four independent current loops, the current magnitude and direction of each of which is controlled to produce the linear gradient. Thus the current through the wire located at (y, θ) in the y - z plane is controlled by the equation

$$I(\theta) = I_{\max} \cos(\theta - \phi), \quad (92)$$

where r is the radius of the cylinder, θ the angle from the y -axis, I_{\max} the maximum current per wire, ϕ the direction of the linear field gradient produced. The magnetic field around the centre of the four-wire line on gradient axis is

$$B_z(y, z) = \frac{4\mu_0 I_{\max}}{\pi r^2} (y \cos \phi + z \sin \phi), \quad (93)$$

(where μ_0 is the magnetic permeability of the free space) which implies that the field gradient makes an angle ϕ with y -axis and has a magnitude $8\mu_0 I_{\max}/\pi r^2$ (Furusawa and Ikeya 1991). The deconvolution process, the important intermediate step to imaging is shown in figure 42 for the case of a γ -irradiated teflon tube. The ESR spectrum of this sample, without a field gradient (figure 42a) is used as an instrumental function to obtain the deconvoluted spectrum (figure 42c) of the ESR spectrum recorded with field gradient of 1 T/m (figure 42b). The ESR image is finally obtained using the filtered back projection technique (Ohno 1982).

12.1b Use of two-dimensional wire arrays: Using an ordinary commercial ESR spectrometer, Ikeya *et al* (1991) have used two-dimensional wire arrays ($i \times j$) for scanning the local static (DC) field and the modulation (100 kHz AC) field (figure 43a). These two fields — DC and AC — are electronically scanned by switching the current through the array. The spectra for the AC and DC currents at various locations of the $i \times j$ array are shown schematically in figure 43b. When the test sample (DPPH) is outside the loop current from i th to $(i+1)$ th wires, an out-of-phase derivative signal is obtained. This is an example of a two-dimensional imaging which when obtained as a plot of signal intensities gives the distribution of spins on the sample surface.

A spectral-spatial two-dimensional imaging of E' defects in X-irradiated SiO_2 has been performed by Sukei *et al* (1993) using a Varian E.9 X-band spectrometer and an additional set of coils which give a gradient of 10 mT/cm/amp along the main magnetic field and a computer for data collection and iterative image reconstruction with filtered back projection.

Table 13. Ag^{2+} ESR parameters in silver iodo-borate and related glasses*.

Sample	g		A	
	g_{\parallel}	g_{\perp}	A_{\parallel} (mT)	A_{\perp} (mT)
60AgI-30Ag ₂ O-10B ₂ O ₃				
Centre I	2.495(2)	2.060(2)	not resolved	1.8(0.3)
Centre II	2.373(2)	2.054(2)	not resolved	5.6(0.3)
30Ag ₂ O-70B ₂ O ₃				
Centre I	2.503(2)	2.065(2)	not resolved	2.0(3.0)
Centre II	2.388(2)	2.059(2)	not resolved	6.5(0.3)
30Ag ₂ O-70TeO ₂				
Centre I	2.493(2)		not resolved	not resolved
Centre II	2.389(2)	2.070	not resolved	not resolved
Ag ₂ O-B ₂ O ₃	2.310	2.040		
X-irradiated				
Silver activated phosphate glass	2.350	2.050	not resolved	not resolved
X-irradiated at 300 K				

*Adapted from Balaya P 1992 *Electrical, thermal and spectroscopic studies on disordered superionic conductors*, Ph.D. thesis, University of Hyderabad, Hyderabad.

12.2 ESR microscopy

A one-dimensional scanning ESR microscope based on a microwire array has been built by Miyamura and Ikeya (1993) to obtain ESR images of fossils. This instrument (figure 44a) involves scanning of the localized magnetic field moderation (instead of the static magnetic field) which is facilitated by placing the microwire array on the sample holder. The modulated ESR signals are detected by lock-in-amplifier, ensuring high-sensitive signal detection.

The images of a 'point' DPPH powder (figure 44b) and a naturally irradiated fossil shark tooth, containing

CO_2^- radical detected at $g=2.0025$ and $g=1.998$. The signal intensities is high at the enamel point of the tooth at both edges (figure 44c).

Important emerging applications of ESR microscopy include the following (Ikeya 1991):

- (I) Monitoring of distribution of active species during catalytic reactions to clarify mechanisms and to design large catalytic reactors.
- (II) Evaluation of crystal perfection using anisotropic ESR signals.
- (III) Information on crystal growth and inner mantle of the earth, using images of synthetic ruby/sapphire and natural diamonds, respectively.

13. Emerging techniques

Apart from the techniques discussed in § 4, which are routinely employed for the characterization of advanced materials, several new innovative techniques have been developed during the last decade. In what follows a few of these are briefly discussed and possible application areas mentioned.

13.1 Loop gap resonators and multi frequency EPR

The cavity resonators employed in EPR spectrometers (e.g. TE_{011} cylindrical cavity) are distributed circuits, and

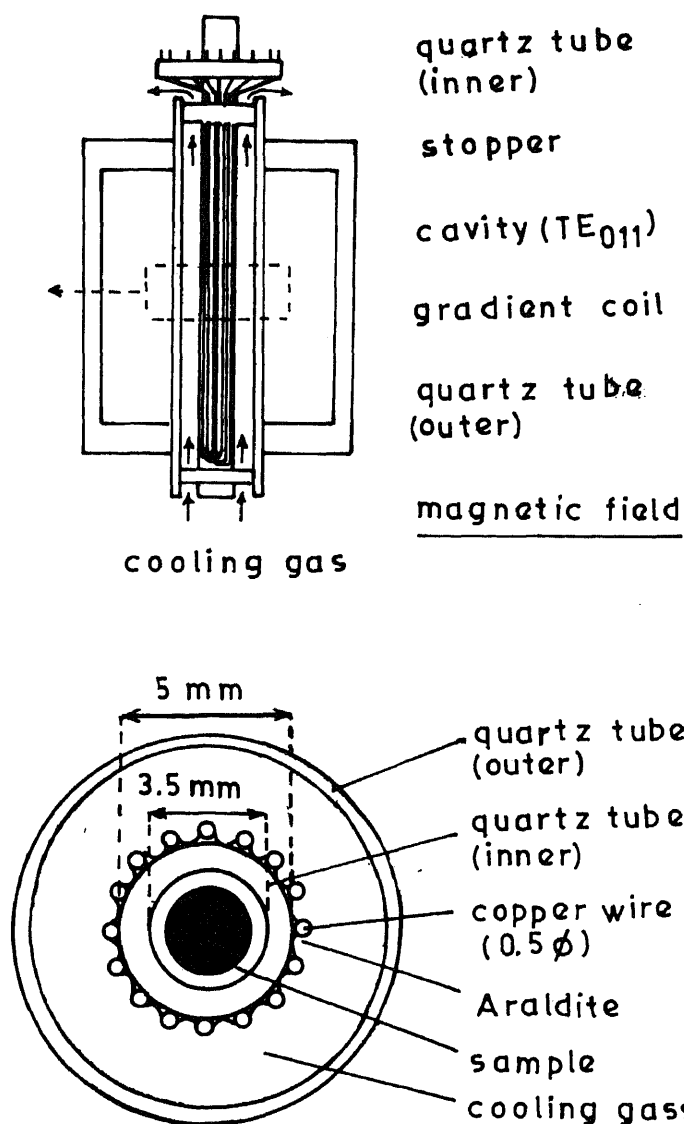


Figure 41. The use of a linear field gradient in ESR imaging. **a.** Field gradient coil in TE_{011} cylindrical cavity and **b.** cross section of the central portion of the gradient coil in the y - z plane (Furusawa and Ikeya 1991).

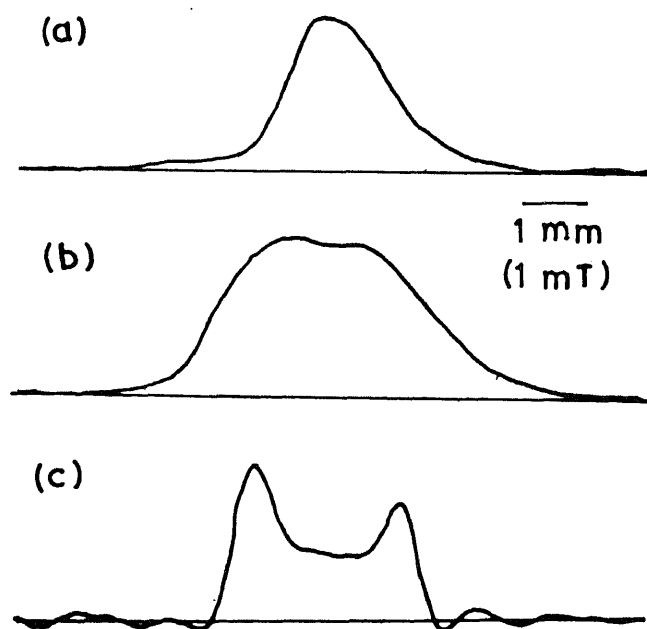


Figure 42. ESR spectrum of a γ -irradiated teflon tube. **a.** Without a magnetic field gradient, **b.** with a field gradient of 1 T/m and **c.** after deconvolution of **b** using spectrum **a** as an instrumental function (Furusawa and Ikeya 1991).

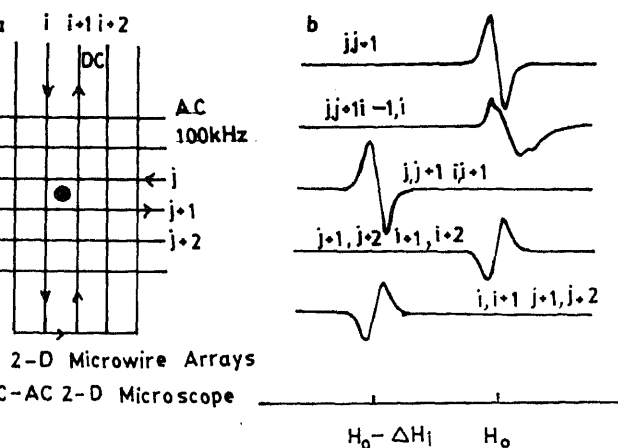


Figure 43. Two-dimensional ESR imaging. a. Wire arrays (i, j) for scanning the static (dc) field and the modulation (ac) field and b. spectra for ac and dc currents at selected locations of the wire array with ac current at j th and $(j+1)$ th wires and current at j th wires as indicated (Ikeya *et al* 1991).

the dimensions of these cavities are of the order as the wavelength of the microwave radiation. The electric and magnetic field vectors are interdependent and related by Maxwell's equations. The loop gap resonator or LGR, on the other hand, is based on the lumped circuit concept, with the circuit elements R , L and C are clearly defined, the circuit dimensions being small compared to the wavelength by typically $1/10$ to $1/3$. Most importantly, the electric and magnetic fields are independent of each other in the lumped circuit limit.

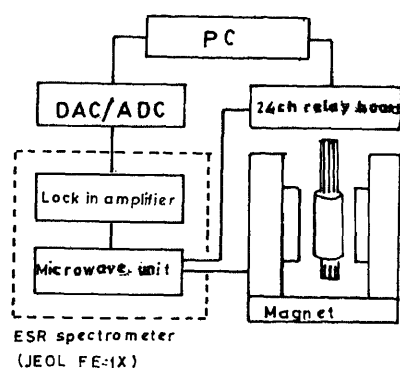
For a simple loop of radius r with n gaps, each of width W , separated by t units, the inductance is given by ($n = 1, 2, 4$)

$$L = \frac{\mu_0 \pi r^2}{Z}, \quad (94)$$

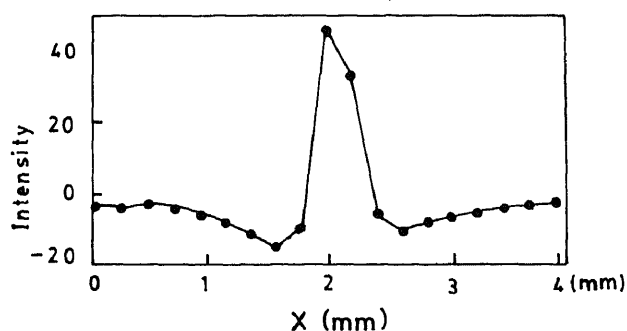
and the capacitance by

$$C = \frac{\epsilon W Z}{m}, \quad (95)$$

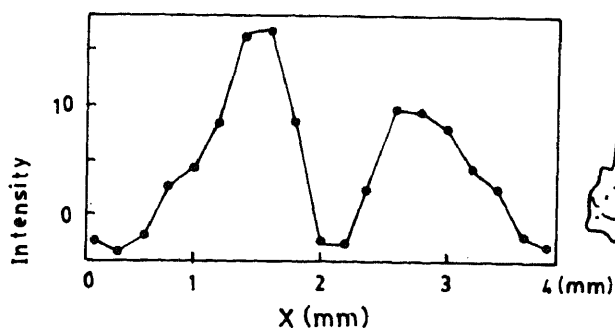
where μ_0 and ϵ are free space permittivity and dielectric



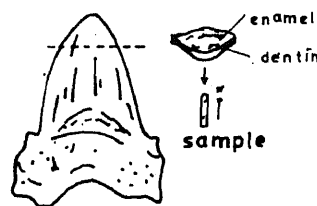
(a)



(b)



(c)



(d)

Figure 44. The scanning ESR microscope with micro-wire array and its applications. a. Block diagram. b. ESR intensity distribution for a DPPH point sample (powder), $200 \mu\text{m}$ diameter and c. one-dimensional ESR image of a fossil shark tooth, cut and scanned as illustrated (Miyamura and Ikeya 1993).

constant and Z the impedance of the circuit. The resonance frequency is

$$\nu_r = \frac{1}{2\pi\sqrt{LC}}. \quad (96)$$

An X-band LGR has a central loop 1–3 cm in diameter, which contains the sample whose EPR spectrum is required. The structure is shielded by a ~2 cm diameter radiation shield. The filling factor is nearly 1 for a sample in such a loop. Generally, LGR's have been constructed from low frequencies (10 MHz, for magnetic resonance imaging) to 35 GHz and Q 's of 500–2000 have been realized.

An important technical advantage of LGR is the possibility of doing multifrequency EPR i.e. the capability of examining the same sample over a range of frequencies say from 0.5 to 1 and from 4 to 8 GHz (Hyde and Froncisz 1989). For pulsed EPR investigation at X-band frequencies a bridged LGR (BLGR) has been designed (Pfenninger *et al* 1988). With its high rf transparency BLGR is suitable for a variety of multi-frequency experiments including pulsed and hyperfine-selective ENDOR, and, Fourier transform EPR (Schweiger 1989).

13.2 Millimeter wave EPR

Synthesis and processing of signals in the far-infrared and millimeter wave regions for applications in radar, communications and radio astronomy, have stimulated the efforts towards high frequency and high field EPR spectroscopy. Specific advantages of this technique are increased spectral resolution, permitting very accurate determination of g -tensor principal values, and increased sensitivity to molecular motions besides increased absolute sensitivity for detection (number of electron spins/unit field). Freed and coworkers (1989) have built an 1 mm wave EPR spectrometer that operates at 249.9 GHz generated by a solid state (an InP Gunn Oscillator) and 8.9 T (generated by a superconducting magnet) for $g \sim 2$, with a sensitivity comparable to that of a 9 GHz EPR spectrometer. Their design is based on far-infrared technology that uses the principles of Gaussian optics to propagate the millimeter waves, 'feed-horns' being used for launching the beam and to convert it into a Gaussian beam, and couple it back to the Fabry–Perot cavity resonator housing the sample in a teflon holder. The detector is a Schottky diode coupled to a low-noise video amplifier, whose response is amplified by a lock-in-amplifier, to be digitized and fed to a personal computer.

An important application of this spectrometer is based on its ability to resolve g -anisotropy of nitroxide spin labels and organic free radicals such as DPPH.

13.3 Reaction yield detected magnetic resonance (RYDMR)

Many photophysical processes, such as the rate of recombinations of excess carriers in semiconductors, involve the formation of very short-lived (\leq ten nanosec) paramagnetic states, which are not detectable either by continuous wave EPR (~microsecond time scale) or pulsed EPR/spin echo techniques (tens of nanosecond resolution). The RYDMR experiment on the other hand, monitors the product that is usually much longer lived than the paramagnetic precursor state but detects it through an easily measured property e.g. its optical absorption. The experiment (Lersch and Michel-Beyerle 1989), as in time-resolved EPR, consists in irradiating resonant microwaves on to the sample during the lifetime of the paramagnetic state of interest. The effect of microwave irradiation is detected as a change of the product yield of some spin-selective reaction of the spin-correlated pairs. The virtue of the RYDMR technique is the effective decoupling of the stages of inducing microwave transitions and detecting the effect of microwaves.

This technique has been applied to: (i) semiconductors (Cavenett 1981), where it was found that the recombination rate of excess carriers can be influenced by changing their spin orientation (or that of paramagnetic recombination centre in a resonant microwave field) and (ii) polymers, to investigate the conductivity mechanism of weakly doped polyacetylene (Frankevich *et al* 1985).

14. Concluding remarks

It is hoped that this article has given a 'working knowledge' of the technique of electron paramagnetic resonance as applicable to advanced materials in their solid state. It is apparent that EPR is the 'method of choice' for the range of materials discussed—semiconductors to insulating and conducting polymers to ferroelectric and superconducting ceramics, and structural and optical glasses to optoelectronic and superionic materials—and more, to obtain information about an unpaired electron and its neighbourhood, and to relate it to the macroscopic behaviour. In the future the use of EPR technique for newer materials like multilayer, Langmuir–Blodgett films, ferrofluids to name a few, is being investigated, pushing the 'frontier' of technical parameters—frequency and magnetic field—to unbelievable limits in the quest for accuracy and detail in characterization.

Acknowledgements

I thank all my colleagues and students whose work has figured in this article. I particularly recall the Late Dr

S Subrahmanyam for many years of collaborative analytic activity.

List of Symbols

Isotropic hyperfine constant;
hyperfine structure tensor;
anisotropic hyperfine constant, sometimes dc magnetic field intensity;
Fine structure constant tensor;
energy, energy level;
line shape function, function in general;
 g -factor, g -tensor;
Gauss, g^2 -tensor;
component of g -tensor;
nuclear g -factor;
spin Hamiltonian;
dc magnetic field expressed as milli Tesla (mT) or Oersted or Gauss (10 Gauss = 1 mT);
microwave magnetic field;
anisotropy field of ferromagnet;
demagnetization field of non-spherical ferromagnetic sample;
magnetic field at resonance, centre of ESR line;
nuclear spin operator, nuclear spin, intensity of ESR spectrum, current;
uniaxial anisotropic constant for amorphous ferromagnet;
components of direction cosine matrix;
magnetization vector;
magnetization along Z-axis;
electron spin quantum number, m_1 nuclear spin quantum number;
 N^- , Boltzmann population of levels;
transition probability, microwave power;
nuclear quadrupole moment, quality factor of cavity;
position vector;
alkyl radical;
saturation factor;
electron spin, electron spin operator;
spin-lattice relaxation;
spin-spin relaxation time;
 T_2' , transverse-electric mode of rectangular cavity, numbers refer to components along cavity dimensions (a, b, c);
 W , coefficients of $g^2(\theta)$ function;
coordinate axis;
test sample, principal direction;
coordinate axis;
principal direction;
coordinate axis;

Z , circuit impedance, principal direction;
 α, β , label for protons in a polymer;
 γ , magnetogyric ratio;
 δ , skin depth;
 ΔH_{pp} , peak-to-peak width of the first derivative ESR signal;
 ϵ , dielectric constant;
 η , filling factor of cavity;
 θ , angle between two vectors;
 λ , spin-orbit coupling constant, microwave penetration depth, Gilbert damping factor in ferromagnetic resonance;
 μ_B , Bohr magneton;
 μ_e , electronic magnetic moment;
 μ_N , nuclear magneton;
 ν , microwave frequency, ENDOR transition frequency;
 χ , magnetic susceptibility.

References

- Abragam A and Bleaney B 1989 in *Electron paramagnetic resonance of transition ions* (New York: Dover)
Alger R S 1968 in *Electron paramagnetic resonance techniques and applications* (New York: Interscience)
Atherton N M 1973 in *Electron spin resonance* (Chichester: Ellis Horwood) Ch. 1
Badalyan A G and Zhitnikov R A 1985 *Sov. Phys. Solid State* **27** 1774
Bagguley D M S and Griffiths J H E 1950 *Proc. Phys. Soc.* **A201** 366
Balagopala Krishna C and Rajasekharan M V 1990 *Phys. Rev.* **B42** 7794
Balaya P and Sunandana C S 1990 *Solid State Ionics* **40/41** 770
Balaya P and Sunandana C S 1990 *Recent advances in fast ion conducting materials and devices* (eds) B V R Chowdari *et al* (Singapore: World Scientific) p. 535; 1994 *J. Phys. Chem. Solids* **55** 39
Bartl A, Frohner J, Zinzok R and Roth S 1992 *Synth. Metals* **51** 197
Bartl A, Frohner J and Roth S 1993 *Synth. Metals* **55-57** 613
Bensimon Y *et al* 1992 *J. Non-Cryst. Solids* **149** 218
Beranov P G and Badalyan A G 1993 *Solid State Commun.* **85** 987
Berger R and Haddad M 1991 *Phys. Status Solidi* **b163** 463
Bhagat S M 1973 *Resonance methods of magnetic materials, Part II* (ed.) R F Bunshah (New York: Wiley) Vol. II
Bhagat S M, Manheimer M A and Moorjani K 1987 *Key Engg. Mater.* **13-15** 641
Bhat S V, Ganguly P, Ramakrishnan T V and Rao C N R 1987 *J. Phys. C: Solid State* **20** L559
Bishop S G, Strom U and Taylor P C 1977 *Phys. Rev.* **B15** 2278
Bowman R C Jr., Venturini E L and Witt S N 1987 *J. Vac. Sci. Tech.* **A5** 3171 and references therein
Bravo D, Martin A and Lopez F J 1993 *Solid State Commun.* **86** 281 and references therein

- Bruker Almanac 1993 *Bruker spectrospin*, Zurich
- Byszewski P, Jablonski R and Kolesnik S 1992 *Solid State Commun.* **84** 1111
- Campbell D and Peterlin A 1968 *Polym. Letts* **6** 481
- Canham L T 1990 *Appl. Phys. Lett.* **57** 1046
- Caplan P I, Poindexter E H, Deal B E and Razouk R R 1977 *J. Appl. Phys.* **50** 5847
- Carter F L (ed.) 1982/1987 *Molecular electronic devices I, II* (New York: Dekker)
- Caurant D, Gourier D, Vivien D and Prasson M 1993 *J. Appl. Phys.* **73** 1657
- Cavenett B C 1981 *Adv. Phys.* **30** 475
- Chary K V R, Mahipal Reddy B, Nag N K, Subramanyam V S and Sunandana C S 1984 *J. Phys. Chem.* **88** 2622
- Chen J, Chung T C, Moras F and Heeger A J 1985 *Solid State Commun.* **53** 757
- Commoner B, Townsend J and Pake G E 1954 *Nature* **174** 689
- Das R *et al* 1986 *Pramana-J. Phys.* **27** 661
- Deville A *et al* 1993 *Phys. Rev.* **B47** 2840
- Duke C B and Fabysh T T 1978 *J. Appl. Phys.* **49** 315
- Dikanav S A and Ashtashkin A V 1978 in *Principles of magnetic resonance* (ed.) A J Hoff (Amsterdam: Elsevier) Ch. 2, p. 59
- Doyle W T 1962 *Rev. Sci. Instrum.* **33** 118
- Durny R 1980 *J. Non-Cryst. Solids* **41** 273
- Einstein A and Ehrenfest P 1922 *Z. Phys.* **11** 31
- Evora C and Jaccorino V 1977 *Phys. Rev. Lett.* **39** 1554
- Feher G 1959a *Phys. Rev.* **114** 1219
- Feher G 1959b *Bell. Syst. Tech. J.* **36** 449
- Frankevich E L *et al* 1985 *Phys. Status Solidi* **B132** 283
- Freed J H, Budil D K, Earle K A and Lynch W B 1989 *Advanced EPR* (ed.) A J Hott (Amsterdam: Elsevier) Ch. 8, p. 307
- Furusawa M and Ikeya M 1990 *J. Phys. Soc. Jap.* **59** 2340
- Fletcher R C, Yager W A, Pearson G L and Merrit F R 1954 *Phys. Rev.* **95** 844
- Frait Z and Fraitova D 1988 *Spin waves and magnetic excitations* (eds) A S Borovik-Romonov and S K Sinha (Amsterdam: Elsevier) Ch. 1, p. 1
- Furusawa M and Ikeya M 1991 *Jpn J. Appl. Phys.* **60** L1687
- Gerlach W and Stern O 1924 *Ann. Phys. Leipzig* **74** 673
- Gordon J P and Bowers K D 1958 *Phys. Rev. Lett.* **1** 301
- Gorelkinskii Yu V and Nevinnyi N N 1987a *Pisma Zh. Tekh. Fiz.* **13** 105
- Gorelkinskii Yu V and Nevinnyi N N 1987b *Sov. Tech. Phys. Lett.* **13** 45
- Graham R A, Morosin B, Venturini E L and Carr M J 1986 *Ann. Rev. Mater. Sci.* **16** 315
- Green R E Jr 1990 *Ann. Rev. Mater. Sci.* **20** 197
- Griffiths J H E 1946 *Nature* **158** 67
- Griscom D L 1973/74 *J. Non-Cryst. Solids* **13** 251
- Griscom D L 1980 *J. Non-Cryst. Solids* **40** 211
- Griscom D L, Stapelbroek M and Webb M J 1986 *J. Non-Cryst. Solids* **41** 329
- Gunter P and Heiguard J P 1988/1989 *Photorefractive materials and their applications*, in *Topics 61 and 62 in applied physics* (Berlin: Springer Verlag) Vols I and II
- Hagen W R 1992 *Adv. Inorg. Chem.* **38** 165
- Hahn E L 1950 *Phys. Rev.* **80** 580
- Haller E E and Falicov L M 1978 *Phys. Rev. Lett.* **41** 192
- Hamanone K *et al* 1974 *J. Polymer Sci.* **A12** 1189
- Harper W R 1964 *Contact and frictional electrification* (Oxford: Clarendon)
- Hebard A *et al* 1991 *Nature* **350** 600
- Henderson B and Gorrison A K 1973 *Adv. Phys.* **22** 423
- Heniker J 1962 *Nature* **196** 474
- Holczer K, Boucher J P, Devreux F and Nechtschien M 1981 *Phys. Rev.* **B23** 1051
- Holton W C and Blum M 1962 *Phys. Rev.* **125** 89
- Humphries G M K and McConnell H M 1982 *Methods of experimental physics* (eds) G Ehrenstein and H O Lccar (New York: Academic) Vol. 20, Ch. 2, p. 53
- Hyde J S and Froncisz W 1989 *Advanced EPR, applications in biology and biochemistry* (ed.) A J Hott (Elsend) Ch. 7, p. 227
- Ikeya M 1991 *Annu. Rev. Mater. Sci.* **21** 45
- Ikeya M 1993 in *New applications of electron spin resonance, dating, dosimetry and microscopy* (Singapore: World Scientific Pub.)
- Ikeya M, Megvo K, Miyamaru H and Ishii H 1991 *Appl. Mag. Res.* **2** 663
- Isoya J *et al* 1990 *Phys. Rev.* **B41** 3905
- Iwasaki M *et al* 1971 *J. Chem. Phys.* **54** 1839
- Izumi T *et al* 1993 *Thin Solid Films* **228** 285
- Janes R, Liu R-S, Edwards P P, Stevens A D and Symons M C R 1991 *J. Chem. Soc. Faraday Trans.* **87** 1209
- Jones R, Janes R, Armstromy R, Pyper N C, Edward P P, Keeble D J and Harrison M R 1990 *J. Chem. Soc. Faraday Trans.* **86** 675
- Kaul S N and Babu P D 1992 *Phys. Rev.* **B45** 295
- Kaul S N and Siriguri V 1992 *J. Phys. Condens. Matter* **4** 505
- Kausch H H 1978 *Polymer fracture* (Berlin: Springer Verlag) p. 119
- Kawazo H, Watanabe Y and Yamane M 1987 *Diffusion Defect Data* **53-54** 189
- Kazanskii V B 1976 *Proc. 6th int. congress on catalysis* (London: Chemical Society) Vol. 1, p. 50
- Kindo K, Honda M, Kohashi T and Date M 1990 *J. Phys. Soc. Jap.* **59** 2332
- Kip A F, Kittel C, Levy D H and Portis A M 1953 *Phys. Rev.* **91** 1066
- Kiss E and Szorenyi T 1977 *Amorphous semiconductors* (ed.) I K Somogyi (Budapest: Akademiai Kiado) p. 25
- Kittel C 1947 *Phys. Rev.* **71** 270
- Kivelson S and Heeger A J 1985 *Phys. Rev. Lett.* **55** 3118
- Kosaka M *et al* 1993 *Chem. Phys. Lett.* **203** 429
- Koschnick F K, Rai M, Spaeth J M and Eachus R S 1993 *J. Phys. Condens. Matter* **5** 733
- Koshta A A, Shvachko Yu N, Romanyukha A A and Ustinov V V 1993 *Zh. Eksp. Teor. Fiz.* **6** 629
- Kubo N O *et al* 1992 *Appl. Phys. Lett.* **61** 940
- Kwan C L and Yen T F 1979 *Anal. Chem.* **51** 1225
- Lauterbur P C 1973 *Nature* **242** 190
- Lebedev Ya S 1963 *J. Struct. Chem. (USSR)* **4** 22
- Lersch W and Michel-Beyerle M E 1989 *Advanced EPR* (ed.) A J Hoff (Amsterdam: Elsevier) Ch. 19, p. 685
- Loubser J H N and Van Ryneweld W P 1966 *Nature* **211** 517
- Ludwig G W and Woodbury H H 1962 *Solid state physics* (eds) F Seitz and D Turnbull (New York: Academic) Vol. 13, p. 223
- Mabbs F A and Collison D 1992 *Electron paramagnetic resonance*

- of *d* transition metal compounds, in *Studies in inorganic chemistry* (New York: Elsevier) Vol. 16
- Arquardt C I 1976 *Appl. Phys. Lett.* **28** 209
- Asada K 1977 *Inst. Phys. Conf. Ser.* No. 31, (Bristol: Inst. Phys.) Ch. 2, p. 174
- Millan J A 1974 in *Systematic materials analysis* (ed.) N L Peterson (New York: Academic Press) Ch. 7, Vol. 1, p. 193
- Millan J A and Halpern T 1971 Argonne Natl. Lab. Rep. Phys.) ANL-7784
- Enrnan F and Anderson P W 1988 *Solid State Commun.* **67** 187
- Enring M *et al* 1993 *Proc. workshop on phase separation in superate superconductors, Erice, Italy* (eds) K A Muller and C Benedek (Singapore: World Scientific) p. 67
- Enns W B 1989 in *Advanced EPR* (ed.) A J Hoff (Amsterdam: Elsevier) Ch. 1, p. 1 and references therein
- Enns W B, Nassau K and McGee J D 1961 *Phys. Rev.* **123** 1059
- Enami T, Ikeda Y and Tanaka M 1982 *J. Non-Cryst. Solids* **2** 15
- Enamura H and Ikeya M 1993 *Appl. Radiat. & Isotopes* **44** 79
- Enigaki K 1988 *Amorphous silicon and related materials* (ed.) Fritzsche (Singapore: World Scientific)
- Enst N F 1968 *J. Non-Cryst. Solids* **1** 1
- Enst N F 1971 *Adv. Phys.* **21** 785
- Ensky M H and Tittle R S 1961 *Phys. Rev. Lett.* **23** 581
- Enler K A *et al* 1980 *Phys. Rev. Lett.* **45** 832
- Enata T and Miki T 1993 *J. Appl. Phys.* **73** 1110
- Enthy N R K and Sunandana C S 1992 *Solid state ionics: Materials and applications* (eds) B V R Chowdari *et al* (Singapore: World Scientific) p. 357
- Enrs S M *et al* 1992 *Rev. Mod. Phys.* **64** 559
- Enrschien M, Devreux F, Genoud F, Gugleelumi M and Enolezer K 1983 *Phys. Rev.* **B27** 61
- Eno K 1982 *J. Magn. Reson.* **50** 145
- En H *et al* 1992 *J. Phys. Soc. Jap.* **61** 2921
- Enlis E J and Jeffries C D 1981 *Phys. Rev. Lett.* **45** 1859
- Enelides S T 1988 *Amorphous silicon and related materials* (ed.) H Fritzsche (Singapore: World Scientific) p. 541
- Enninger S, Forrer J, Schweiger A and Weiland Th 1988 *Rev. Sci. Instrum.* **59** 752
- Enow J R 1990 *Transition ion electron paramagnetic resonance* (Oxford, London, New York: Clarendon Press)
- Enne C P 1983 in *Electron spin resonance, A comprehensive treatise on experimental techniques* (New York: Interscience) 2nd ed.
- Enriede E 1989 *J. Phys. Condens. Matter* **1** 7267
- En I I *et al* 1939a *Phys. Rev.* **55** 526
- En I I *et al* 1939b *Phys. Rev.* **56** 728
- Envin B *et al* 1990 *Phys. Rev.* **B41** 769
- Enasastry C and Sunandana C S 1976 *J. Magn. Res.* **23** 87
- Enoy B and Rabek J F 1977 *ESR spectroscopy in polymer research* (Berlin: Springer Verlag)
- Enoy B and Rabek J F 1977 *ESR spectroscopy in polymer research* (Berlin: Springer Verlag) Ch. VIII
- En K J and Rao B G 1985 *Proc. Indian Acad. Sci. (Chem. Sci.)* **95** 169
- Enhart J F and Pereli J 1966 *Rev. Sci. Instrum.* **37** 426
- En M J 1979 *Phys. Lett.* **A71** 152
- Rodriguez S 1987 *Physica* **B146** 212
- Roitsin A B and Maevskii V M 1989 *Sov. Phys. Usp.* **32** 891
- Roth L M, Lax B and Zwerdling S 1959 *Phys. Rev.* **114** 90
- Rytz D *et al* 1990 *J. Opt. Soc. Am.* **B7** 2245
- Sahyun M R V 1992 *Chemtech* 418
- Sakaguchi M *et al* 1988 *J. Polym. Sci. Part B, Polym. Phys.* **26** 1307
- Sakaguchi M *et al* 1989 *Macromolecules* **22** 1277 and references therein
- Sakaguchi M, Shimada M and Kashiwabara H 1990 *Macromolecules* **23** 5038
- Sakaguchi M, Yamakuchi T, Shimada S and Hon Y 1993 *Macromolecules* **26** 2612
- Sakita S and Fujii I 1991 *Jpn J. Appl. Phys.* **30** L1489
- Sands R H 1955 *Phys. Rev.* **99** 1222
- Sariffici N S, Smilowitz L, Heeger A J and Wudl F 1992 *Science* **258** 1474
- Schonland D S 1959 *Proc. Phys. Soc.* **73** 788
- Scheffler M 1987 *Lattice relaxations at substitutional impurities in shallow impurity centre in semiconductors* (eds) A Boulder and R Resta (Amsterdam: North Holland) p. 171
- Schweiger A 1989 *Advanced EPR* (ed.) A J Hoff (Amsterdam: Elsevier) Ch. 6, p. 243
- Scripsick M P 1993 *J. Appl. Phys.* **73** 1114
- Shimada H, Hon Y and Kashiwabara H 1988 *Macromolecules* **21** 2107
- Shirakawa H and Ikeda S 1971 *Polym. J.* **2** 231
- Sieverts E G and Ammerlaan C A J 1977 *Inst. Phys. Conf. Ser.* No. 31, Ch. 2, p. 213
- Simon S and Al Nicula 1983 *J. Non-Cryst. Solids* **57** 23
- Slichter C P 1955 *Phys. Rev.* **99** 479
- Slichter C P 1978 in *Principles of magnetic resonance* (Berlin: Springer Verlag) 2nd ed., p. 38
- Sozzani F, Di Silvestro G and Gervasini A 1986 *J. Polym. Sci. Part A: Polym. Chem.* **24** 815
- Son N T, Kustov V E, Gregorkiewicz T and Ammerlaan C A J 1992 *Phys. Rev.* **B46** 4544
- Spaeth J M and Koschnick F K 1991 *J. Phys. Chem. Solids* **52** 1
- Spano M L and Bhagat S M 1981 *J. Magn. Magn. Mater.* **24** 143 and references therein
- Stallinga P, Gregorkiewicz T, Ammerlaan C A J and Gorelkinskii Yu V 1993 *Phys. Rev. Lett.* **71** 117
- Stern O 1921 *Z. Phys.* **7** 249
- Stone T J, Buckman T, Nordio P L and McConnell H M 1965 *Proc. Natl. Acad. Sci. USA* **54** 1010
- Stutzmann M and Street R A 1985 *Phys. Rev. Lett.* **54** 1836
- Stutzmann M and Biegelson D K 1989 *Phys. Rev.* **B40** 9834
- Stutzmann M, Biegelson D K and Street R A 1987 *Phys. Rev.* **B35** 5666
- Sukei M, Eaton S S and Eaton G R 1993 *Appl. Radiat. & Isotopes* **44** 377
- Sunandana C S 1975 in *ESR studies on some X-irradiated and doped sulphates*, Ph.D. Thesis, Indian Institute of Technology, Madras
- Sunandana C S 1978 *Phys. Status Solidi* **A48** K19
- Sunandana C S 1987 *Key Engg. Mater.* **13-15** 623
- Sunandana C S and Bhatnagar A K 1984 *J. Phys. C: Solid State Phys.* **17** 467
- Sunandana C S and Rao K S 1985 *Phys. Status Solidi* **A90** 681

- Taylor P C, Baugher J F and Kriz H M 1975 *Chem. Rev.* **75** 203
- Tinkham M 1996 *Introduction to superconductivity* (New York: McGraw Hill) 2nd ed.
- Title R S and Chandrasekhar G V 1976 *Solid State Commun.* **20** 405
- Vanheusden K and Stesmans A 1993 *Appl. Phys. Lett.* **22** 2405
- Van Kemp R, Sieverts E G and Ammerlaan C A J 1987 *Phys. Rev.* **B36** 3528
- Van Veen G 1978 *J. Magn. Reson.* **30** 91
- Venugopal Rao G, Sunandana C S and Bhatnagar Anil K 1992 *J. Phys. Condens. Matter* **4** 1373
- Von Bardeleben H J *et al* 1992 *Mater. Res. Symp. Proc.* (eds) G L Witt, R Calavu, U Mishra and U Weber (Philadelphia: Mater. Res. Soc.) Vol. 241, p. 69
- Warren W L *et al* 1993 *Appl. Phys. Lett.* **62** 482 and references therein
- Watanabe I, Inakagi Y and Shimizu T 1978 *J. Non-Cryst. Solids* **27** 295
- Watkins G D, Kleverman M, Thilderkvist A and Grimmeiss H G 1991 *Phys. Rev. Lett.* **67** 1149
- Webb E and Alexander H 1977 *Inst. Phys. Conf. Ser.* No. 31, Ch. 2, p. 266
- Weeks R A 1956 *J. Appl. Phys.* **27** 1376
- Wertz J E and Bolton J R 1972 in *Electron spin resonance, elementary theory and practical applications* (New York: McGraw Hill)
- Whitmore M H 1993 *J. Chem. Phys.* **98** 3656
- Wilmshurst T H 1967 in *Electron spin resonance spectrometer* (London: Hilger)
- Winkler P F, Kleppner D, Myint T and Walther F G 1972 *Phys. Rev.* **A5** 83
- Yasaitis E L and Smaller B 1953 *Phys. Rev.* **92** 1068
- Yokomichi H and Morigaki K 1987 *Solid State Commun.* **63** 629
- Yokomichi H and Morigaki K 1993 *Solid State Commun.* **85** 759
- Yokomichi H, Takakuki H and Kondo M 1993 *Jap J. Appl. Phys.* **32** L365
- Yordanov N D (ed.) 1991 in *Electron magnetic resonance of disordered systems (EMARDIS 91)* (Singapore: World Scientific)
- Zakrevskii V A *et al* 1968 *Sov. Phys. Solid State* **10** 1341
- Zavoiskii E K 1944 *Phys. Inst. Acad. Sci., Moscow*
- Zhilinskaya E A, Valeev N K H and Oblasoe A K 1991 *J. Non-Cryst. Solids* **136** 76
- Zhong Y C and Pilbrow J R 1991 *J. Magn. Res.* **93** 447
- Zunger A 1986 *Solid state physics* (eds) F Seitz, D Turnbull and H Ehrenreich Vol. 39, p. 275

Note added in proof: The following developments have been most noteworthy — ever since this article was submitted. Among the techniques, electrical detection of EPR (B Stich *et al* 1995 *J. Appl. Phys.* **77** 1546), that measures the microwave/rf induced change of conductivity of semiconductors containing shallow and deep defects, offers new possibilities for the study of point defects. Such a study on a Si diode (Z Xiang and D J Miller 1995 *J. Appl. Phys.* **78** 4895) has identified broken bonds in a vacancy cluster acting as recombination centres. Bhat *et al* (S V Bhat, A Anand and Rajiv Bhat 1997 *Solid State Physics (India)* **40C** 62) have developed a spectrometer for unmodulated high-power rf absorption studies in high-temperature superconductors. Exciting applications include: study of spin-Peierls transitions in $\text{Cu}_{1-x}\text{Zn}_x\text{GeO}_3$ (P Fronzes *et al* 1997 *Phys. Rev.* **B56** 7827), low-temperature phase transitions in CuO by a DPPH probe (A M Suvarna and C S Sunandana 1997 *Physica* **C276** 65), defects in diamond films (A K Sikder *et al* 1997 *Solid State Physics (India)* **40C** 435), Ni^+ in AgGaSe_2 (L E Halliburton *et al* 1996 *J. Appl. Phys.* **79** 556), Cr-doped fluorochloro- and fluorobromozirconate glasses (J L Martinez *et al* 1997 *J. Phys. Cond. Matt.* **9** 9175) and studies of dangling bonds in porous silicon (Y Xiao *et al* 1994 *J. Appl. Phys.* **76** 1759; R Laiho and L S Vlasenko 1995 *J. Appl. Phys.* **78** 2857), besides a very interesting study of an oxygen defect centre associated with red photoluminescence from freshly etched and oxidized porous silicon (S M Prokos and W E Carlos 1995 *J. Appl. Phys.* **78** 2671). A comprehensive review of EPR in semiconductors has appeared (W Gehlhoff, M Hohne and J Schmidt 1992 in *Hyperfine interaction of defects in semiconductors* (ed.) G Langouche (Amsterdam: Elsevier) Chap. 5, p. 217).

possible crystallographic explanation for the five-fold diffraction symmetry in icosahedral phases

T R ANANTHARAMAN

Metals and Alloys Group, National Physical Laboratory, Dr K S Krishnan Road, New Delhi 110 012, India

MS received 16 December 1997

Abstract. X-ray and electron diffraction data from the Al–Cu–Fe icosahedral phase are compared and analysed on the basis of the microcrystalline and multi-domain model developed by the author. It is shown that a crystallographic explanation is now possible for both the enigmatic five-fold symmetry and non-periodicity of reflections observed in electron diffraction patterns of icosahedral phases.

Keywords. Crystallography; diffraction symmetry; icosahedral phases.

Introduction

The discovery of quasicrystalline alloy phases (Schechtman *et al* 1984) displaying crystallographically disallowed five-fold diffraction symmetry has generated a great deal of excitement, as also some confusion and controversy, in scientific circles (Kelton 1993). One of the fundamental questions raised by intensive researches on icosahedral and decagonal quasicrystals relates to the limits of our ability to distinguish through experiment between true quasicrystals and multi-twinned or multi-domain crystals with large unit cells (Goldman and Kelton 1993). A further important recent development in this regard has been the discovery of many so-called crystalline or rational approximants (see, for example, Liu 1993), which seem to have atomic arrangements in their rather large unit cells closely resembling the local atomic structure in quasicrystals.

Starting with Field and Fraser (1985), many investigators (Carr 1986; Pauling 1985, 1987, 1988, 1990; Schio and Williams 1988; Anantharaman 1989, 1990, 1994a) have sought a conventional crystallographic explanation for the quasicrystal phenomenon in terms of large unit cells or multi-twinned crystals. Interest in multi-twinned or multi-domain crystalline aggregates has been revived in recent years by reports in their favour based on high-resolution single crystal synchrotron X-ray studies of two thermodynamically stable and 'perfect' quasicrystals, e.g. Al–Cu–Fe icosahedral phase (Schischke *et al* 1992) and Al–Cu–Co(–Si) decagonal phase (Weis *et al* 1993, 1994). As pointed out by Steurer (1995) in his most recent review, practically all quasicrystals transform to crystalline phases at lower temperatures or under high pressure, running through intermediate phases with rather complicated and/or nanoscale structures.

In this paper, X-ray and electron diffraction data from Al–Cu–Fe icosahedral phase is presented and analysed on the basis of the microcrystalline and multi-domain model developed by the author for both icosahedral and decagonal phases (Anantharaman 1993). A crystallographic explanation is thereby sought for the unusual five-fold symmetry and nonperiodicity of reflections observed in electron diffraction patterns of all icosahedral phases.

2. Experimental

Alloys with the nominal composition $\text{Al}_{65}\text{Cu}_{20}\text{Fe}_{15}$ were prepared by arc melting in purified argon atmosphere and then rapidly solidified by planar flow casting. The resulting ribbons (20–30 μm thick) were examined before and after annealing at 1073 K for 8 h in a Siemens Rotating Anode X-ray Diffractometer, using CuK_α or CoK_α monochromatic radiation. Transmission electron microscopic studies were also conducted in a JEOL JEM-200CX 200 kV Electron Microscope after thinning the ribbons by chemical means or by ion beam in a BAL-TEC RES 010 Rapid Etching System. As has been reported earlier (Ishimasa *et al* 1988; Liu 1993), the rapidly solidified ribbons were characterized by a homogenous icosahedral phase, while the annealed samples revealed also traces of the monoclinic $\text{Al}_{13}\text{Fe}_4$ phase. The two thinning techniques employed to produce specimens transparent to the electron beam did not make any difference to the electron diffraction data, as presented and analysed in this paper.

Table 1 presents results of an analysis of the first 32 Debye–Scherrer reflections with intensities of at least 1% of the strongest one from *i*-Al–Cu–Fe on the basis of the model proposed by the author (Anantharaman 1989, 1993, 1994b) for the multi-domain crystallization

of icosahedral and decagonal phases through nucleation from icosahedral atomic clusters in the concerned alloy melts. The orthorhombic unit cell built up of 96 orthorhombic basic cells with $a = 6a' = 1.4868$ nm, $b = 4b' = 1.6840$ nm and $c = 4c' = 1.6024$ nm and belonging to the space group P_{mmm} (No. 47), as assigned here to i -Al-Cu-Fe, is quite similar to the ordered orthorhombic unit cells proposed earlier for i -Al-Mn, i -Al-Mn-Si, i -Al-Cu-Mg, i -Al-Cu-Li and i -Al-Cu-Ru phases. Depending on the actual composition, method of preparation and subsequent heat treatment, the parameters of the i -Al-Cu-Fe refined basic cell have been found to vary over a small range viz. $a' = 0.248$ – 0.252 nm; $b' = 0.421$ – 0.429 nm and $c' = 0.400$ – 0.408 nm. The agreement between calculated and observed interplanar distances (d_{hkl}) is extremely satisfactory in this case, the

Table 1. Comparison of calculated and observed interplanar distances (d_{cal} and d_{obs} in nanometers) and observed relative intensities (I_{obs}) for Debye-Scherrer reflections from Al-Cu-Fe icosahedral phase.

No.	hkl	d_{cal}	d_{obs}	I_{obs}
1	020	0.842	0.833	2
2	220	0.557/		
3	202	0.545	0.551	3
4	040	0.421/		
5	004	0.401	0.415	3
6	042	0.373	0.374	13
7	420	0.340/		
8	402	0.337	0.339	15
9	224	0.325	0.324	12
10	440	0.279	0.280	3
11	600	0.248	0.245	7
12	602	0.237	0.238	3
13	444	0.229	0.229	2
14	604	0.211/		
15	080	0.211	0.211	94
16	642	0.206	0.206	2
17	624	0.204	0.204	2
18	008	0.200	0.200	100
19	644	0.189	0.188	1
20	428	0.173	0.173	3
21	448	0.163	0.162	2
22	088	0.145	0.145	13
23	0.10.6	0.143	0.142	4
24	10.44	0.132	0.133	1
25	22.12	0.130/		
26	848	0.130	0.130	1
27	12.00	0.124	0.124	36
28	12.42	0.118	0.117	2
29	12.80	0.107	0.107	20
30	12.08	0.105/		
31	0.16.0	0.105	0.105	15
32	00.16	0.100	0.100	1

Unit cell: Orthorhombic
 Space group: P_{mmm} (No. 47)
 I_{obs} : Rounded to integers
 (Weak reflections with I_{obs} less than 1.0 are not included).

$a = 1.4868$ nm
 $b = 1.6840$ nm
 $c = 1.6024$ nm

indices of all recorded reflections being significantly common to both face-centred cubic (fcc) and body-centred cubic (bcc) structures (table 1).

Table 2 contains an analysis of the selected area electron diffraction pattern of i -Al-Cu-Fe, displaying the well-publicized and much-discussed five-fold symmetry first observed in i -Al-Mn (Schechtman *et al* 1984) and subsequently in many other icosahedral phases. Among over 200 reflections or spots recorded in this pattern, it could be noted that 130 reflections are equally distributed in 10 rows, each row starting from the origin and displaying an angle of 36° to its neighbours on either side. Their interplanar distances (d_{hkl}) were calculated from several rows of reflections and from many diffraction patterns of i -Al-Cu-Fe with differing camera lengths. The reliable and reproducible averages of the observed d_{hkl} values for a row of reflections are recorded in column 2 of table 2, their relative intensities (I_{R}) being shown in column 3. The nonperiodicity of the diffraction spots in such patterns has generally been explained on the basis of the so-called Fibonacci sequence, viz. 2, 3, 5, 8, 13, 21, etc. Columns 4 and 5 of table 2 attempt an analysis of the concerned d_{hkl} values on this basis and show that there is considerable deviation between the estimated and observed values in case of the low-angle reflections.

The X-ray evidence in table 2 studied along with the proposal in the author's multi-domain model for the emergence of five-fold diffraction symmetry in icosahedral phases (see Anantharaman 1994b), as illustrated in figure 1, brings out some very significant and interesting features (see column 6 of table 2) of the five-fold electron diffraction patterns of i -Al-Cu-Fe. Based on the [110] zone for one orientation, the very strong 008 reflection along with its rather weak second order companion, i.e. 00.16 reflection, appears as expected in every one of the ten rows of reflections, but the only other reflection that can be identified from X-ray patterns is 224, along with its second order, i.e. 448. The latter pair actually comes from a crystal (or domain) with a different orientation, inclined 72° to the original crystal, and appears on this line or row only because the angle between 001 and 112 crystallographic planes in this orthorhombic phase works out to almost exactly 36° . No other reflection on this row can be identified in the concerned Debye-Scherrer patterns. Of course the observed d_{hkl} values of two electron reflections, viz. 0.144 nm and 0.123 nm, have their counterparts in the X-ray pattern, viz. 0.145 nm for 088 and 0.124 nm for 12.00, but these two reflections cannot possibly appear in the [110] zone under consideration.

As regards the 9 electron reflections in each row, that are not accounted for in the Debye-Scherrer patterns, the last column of table 2 brings out the real reason for their appearance, viz. they are all caused by dynamic

Table 2. Analysis of a representative set from the ten identical rows of reflections in the electron diffraction pattern of AlCuFe icosahedral phase.

d_{hkl} observed	I_R	hkl_F	d_{hkl} calculated	X-ray evidence	Double diffraction possibility
0.850	w	002	0.801	not observed	$0.527 + 0.324 = 0.851$
0.527	m	003	0.534	not observed	$0.324 + 0.200 = 0.524$
0.324	s	005	0.320	observed, $d_{224} = 0.324$	not called for
0.261	vw	006	0.267	not observed	$0.162 + 0.100 = 0.262$
0.234	vw	007	0.229	not observed	$0.145 + 0.090 = 0.235$
0.200	vs	008	0.200	observed, $d_{008} = 0.200$	not called for
0.162	vw	00.10	0.160	observed, $d_{448} = 0.162$	not called for
0.144	vw	00.11	0.146	not observed	$0.234 - 0.090 = 0.144$
0.123	s	00.13	0.123	not observed	$0.324 - 0.200 = 0.124$
0.100	m	00.16	0.100	observed, $d_{00.16} = 0.100$	not called for
0.090	m	00.18	0.089	no data	$0.234 - 0.145 = 0.089$
0.076	s	00.21	0.076	no data	$0.200 - 0.123 = 0.077$
0.062	s	00.26	0.062	no data	$0.162 - 0.100 = 0.062$

I_R = Relative observed intensity; vw = very weak; w = weak; m = medium; s = strong; vs = very strong, hkl_F = indices based on the Fibonacci sequence; d_{hkl} = values in nanometers).

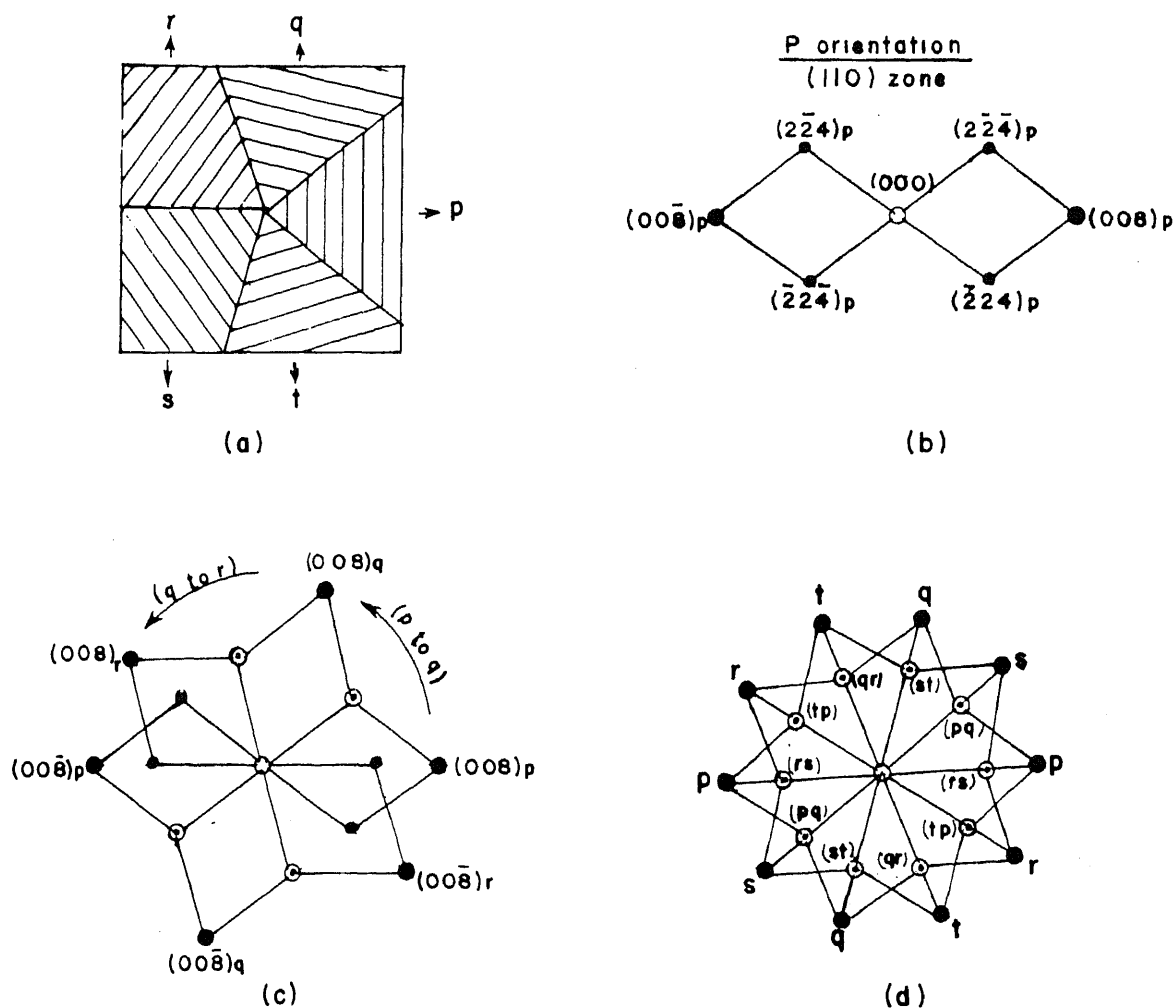


Figure 1. Emergence of the five-fold electron diffraction pattern of an icosahedral phase prior to double diffraction. (a) Five orientations of the same crystal (p , q , r , s and t) with 72° angular relationships between them, (b) single crystal diffraction pattern: $[110]$ zone, ' p ' orientation, (c) impact of two other orientations (q and r) on (b), and (d) diffraction pattern generated from all five (p , q , r , s and t) orientations before double diffraction.

double diffraction, a phenomenon known for long to cause extra spots in electron diffraction patterns. In fact, computer simulation has earlier been used to confirm the emergence of such extra reflections due to double diffraction in icosahedral phases (Field and Fraser 1985; Anantharaman 1989). It is relevant to add here that in this case actual experimental demonstration, through dark field characterization and tilting, of the occurrence of extra reflections due to double diffraction is extremely difficult, if not impossible, because of the complex multi-domain structure assigned to such phases.

3. Discussion of results

In the present work, perhaps for the first time, a careful and detailed analysis has been undertaken of both X-ray and electron diffraction patterns from the same icosahedral phase on the basis of a crystallographic model. The observed five-fold diffraction symmetry is shown to be caused by one very strong reflection (along with its second order) from a crystal of the icosahedral phase with a particular orientation and another not so strong reflection (along with its second order) from the same type of crystal, but with a 72° orientation relationship with the former. These four electron spots in each of the ten rows of spots radiating or spreading out from the origin at 36° intervals are shown to generate another nine spots by dynamic double diffraction. Thus 130 electron reflections get recorded in ten rows of the diffraction pattern through just two reflections, one each from two orientations, 72° to each other! In fact, many other reflections in the diffraction patterns can also be explained as only due to double diffraction from these four reflections.

The nonperiodicity and Fibonacci sequence, associated with the electron reflections in such patterns for nearly a decade, can thus be seen to arise out of some extraordinarily unusual circumstances related to the icosahedral phases, viz. the geometry of the unit cell leading to an angle of 36° , i.e. half of 72° , between the 001 and 112 planes, the emergence of five 72° orientations of the crystal due to random changes in direction during its growth and the fortuitous closeness between the 224 and 005 interplanar distances (0.324 nm and 0.320 nm, respectively). Further, such a five-fold pattern is not generated by the 800 and 080 reflections since the concerned crucial angular relationships viz. between 800 and 422 in the [011] zone and between 080 and 242 in the [101] zone, work out to 33° and 38° , respectively, and not 36° . Incidentally, the 800 reflection does not appear in the X-ray pattern, but 1200 does (see table 1). It is relevant to report here that the extraordinary role of unit cell geometry in causing five-fold electron diffraction has recently been highlighted in case of a well-known crystalline phase viz. orthorhombic Al_3Fe_4 (Ellner 1995).

It is appropriate to record here that the lattice parameters of $i\text{-Al-Cu-Fe}$ may well be higher than the values used in the present analysis, depending on the appearance and identification of further weak Debye-Scherrer reflections at very low Bragg angles. In fact, a much larger rhombohedral unit cell has already been proposed (Motsch *et al* 1992) for $i\text{-Al-Cu-Fe}$ with $\gamma = 3.208$ nm and $\alpha = 36^\circ$ on the basis of high resolution synchrotron X-ray studies of this phase. This unit cell can be converted to the orthorhombic system with $a = 1.983$ nm; $b = 3.434$ nm and $c = 8.978$ nm. On the basis of the author's model, these parameters work out to $8a'$, $8b'$ and $22c'$, respectively, allowing for the slight differences in chemical composition of the two alloys concerned. So long as the proposed unit cells constitute superstructures of the small basic orthorhombic cell identified in the author's model (Anantharaman 1994b), as shown in this case, the present analysis can be applied convincingly and with the same conclusions to all icosahedral phases, albeit with different and numerically higher indices for the crucial 008 and 224 reflections.

Acknowledgements

The experimental work described above was carried out during a six-week visit to the Institute for Solid State and Materials Research, Dresden, Germany. Author thanks Mr R Rennekamp of this Institute's Electron Microscopy Division, for his valuable assistance in thinning and mounting specimens, as also examining them in the electron microscope. He also thanks Prof. H Warlimount, Scientific Director, Dr H D Bauer, Head, Electron Microscopy Division, and Dr N Mattern, Head, X-ray Crystallography Division, of this Institute for their encouragement and support. He is indebted to the Director General, Council of Scientific and Industrial Research, New Delhi for nominating him on an Indo-German Exchange Programme for this Research Visit to Dresden.

References

- Anantharaman T R 1989 *Curr. Sci.* **58** 1057
- Anantharaman T R 1990 *Quasicrystals and incommensurate structures in condensed matter* (eds) M J Yacaman, D Romeu, V Castano and A Gomez (Singapore: World Scientific) p. 199
- Anantharaman T R 1993 *Scr. Met. Mater.* **28** 1555
- Anantharaman T R 1994a *Experimental methods of phase diagram determination* (eds) J E Morral, R S Schiffman and S M Merchant (USA: TMS) p. 173
- Anantharaman T R 1994b *Bull. Mater. Sci.* **17** 717
- Carr M J 1986 *J. Appl. Phys.* **59** 1063
- Ellner M 1995 *Acta Cryst.* **B51** 31
- Fettweis M, Launois P, Denoyer F, Reich R, Godard J M and Lambert M 1993 *J. Non-Cryst. Solids* **153/154** 24
- Fettweis M, Launois P, Denoyer F, Reich R and Lambert M 1994 *Phys. Rev.* **B49** 15573

- Field R D and Fraser H L 1985 *Mater. Sci. Eng.* **68** L17
- Goldman A I and Kelton K J 1993 *Rev. Mod. Phys.* **65** 213
- Imasa T, Fukano Y and Tsuchimori M 1988 *Philos. Mag. Lett.* **58** 157
- Kelton K F 1993 *Int. Mater. Rev.* **38** 105
- W 1993 *Fortschritt-Berichte VDI Reihe 5*, No. 300
- otsch T, Denoyer F, Launois P and Lambert M 1992 *J. Phys. France* **2** 861
- Pauling L 1985 *Nature* **317** 512
- Pauling L 1987 *Phys. Rev. Lett.* **58** 365
- Pauling L 1988 *Proc. Natl. Acad. Sci.* **85** 8276
- Pauling L 1990 *Proc. Natl. Acad. Sci.* **87** 7849
- Schechtman D, Blech I, Gratias D and Cahn J W 1984 *Phys. Rev. Lett.* **53** 1951
- Steurer W 1996 *Physical metallurgy* (eds) R W Cahn and P Haasen (Elsevier Science BV) 4th ed., p. 372
- Vecchio K S and Williams D B 1988 *Metall. Trans.* **A19** 2875

Preparation of superconducting-grade copper from commercial grade copper salt

P PRAMANIK*, A K ADAK and A PATHAK

Department of Chemistry, Indian Institute of Technology, Kharagpur 721 302, India

MS received 31 May 1997; revised 28 October 1997

Abstract. Fine samples with nominal composition of $\text{Bi}_{1.6}\text{Pb}_{0.4}\text{Sr}_2\text{Ca}_2\text{Cu}_3\text{O}_x$ have been produced by solid state method using various purity grades of starting copper oxide powder. Studies on T_c and high- T_c volume fraction measurements of these samples revealed that the samples produced using CuO powders obtained in laboratory after double purification of the commercially available copper salts have higher T_c (104.46 K) and increased percentage of high T_c volume fraction (58%) compared to even the samples prepared from Aldrich grade (99.99%) CuO. A simple and cost-effective chemical route for the purification of CuO from commercially available copper salts has been outlined.

Keywords. Superconductor; high purity copper; chemical purification.

Introduction

Since the discovery of superconductivity in YBCO ceramics (Bednorz and Muller 1986) and later extension of this discovery (Wu *et al* 1987), there have been large-scale research efforts in this direction the world over. The voluminous research publications in this field stand testimony to the global urge to understand and realize the potentials of these ceramic superconductors. Huge chunks of research funds worldwide are continuously being directed towards the large-scale production of ceramic superconductors having high critical current density (J_c) and transition temperature (T_c) into the superconducting phase.

Research into the basic chemistry of these materials is continuing as improvements on the superconducting properties are being sought for. However, some realizations can now be made for these materials owing to the consistent replication of findings. One such realized finding is that in all copper oxide based ceramics, the pairing of carriers in the Cu–O₂ planes is responsible for their high (T_c) superconductivity (Ascon *et al* 1987). Thus any substitution on the copper site of these materials, which alters the electronic structures of the Cu–O₂ plane, would tend to strongly suppress their (T_c) (the transition temperature into the superconducting phase or the zero resistance temperature) and the volume fraction of the high (T_c) superconducting phase (Jones *et al* 1989). Therefore, impurities, particularly the transition metals (3d), which have the requisite electronic and ionic radii would tend to replace copper in the Cu–O₂ planes and detriment the superconducting

properties (Ginsberg 1989; Maeda *et al* 1990). As a consequence, the purities of the starting materials, particularly the copper salts, used in the preparation of these ceramic superconductors, is expected to play a major role in obtaining a high T_c phase-pure product.

In this paper, we deal with the $\text{Bi}_{1.6}\text{Pb}_{0.4}\text{Sr}_2\text{Ca}_2\text{Cu}_3\text{O}_x$ ceramic superconductor system which is constituted of (2223) phase with T_c at 110 K, the (2212) phase with T_c at 80 K, and the (2201) phase with T_c at 20 K. To increase the critical current density (J_c) above liquid nitrogen temperature, it is important to increase the volume fraction of the high T_c phase (i.e. the (2223) phase with T_c at 110 K) and decrease that of the other phases. Here, we report results of the investigations on the effects of purity of the starting copper oxide on T_c and the volume fraction of the high T_c superconducting phase. We also report a cost-effective chemical route for the preparation of high purity grade ($\geq 99.99\%$) copper oxide from commercially available copper salts.

2. Experimental

Five different grades of copper oxide powders were used for the preparation of $\text{Bi}_{1.6}\text{Pb}_{0.4}\text{Sr}_2\text{Ca}_2\text{Cu}_3\text{O}_x$ samples. The copper oxide powders used were: (i) Copper oxide (98%) supplied by LOBA Chemie, India, (ii) Copper oxide (98%) supplied by S.D. Fine Chemicals, India, (iii) Laboratory (single) purified copper oxide from commercially available copper chlorides/sulphates, (iv) Laboratory (double) purified copper oxide from single purified copper and (v) Aldrich grade (99.99%) copper oxide.

The $\text{Bi}_{1.6}\text{Pb}_{0.4}\text{Sr}_2\text{Ca}_2\text{Cu}_3\text{O}_x$ samples prepared using each of the five mentioned grades of copper oxide powders

*Corresponding author

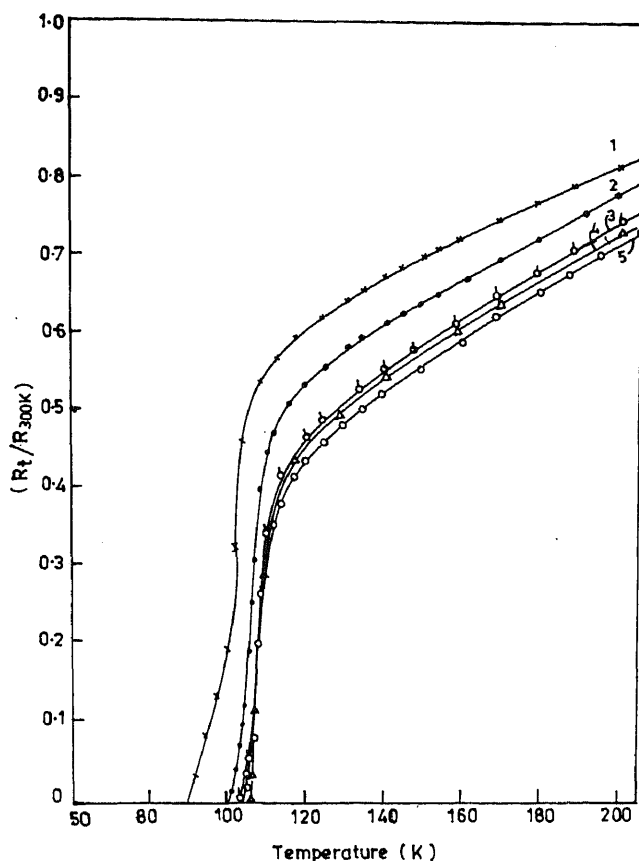


Figure 1. Resistance (R_t/R_{300K}) vs temperature (K) plots for $\text{Bi}_{1.6}\text{Pb}_{0.4}\text{Sr}_2\text{Ca}_2\text{Cu}_3\text{O}_x$ samples prepared from CuO: (1) LOBA Chemie, (2) S.D. Fine Chemicals, (3) Laboratory single purification, (4) Laboratory double purification and (5) Aldrich.

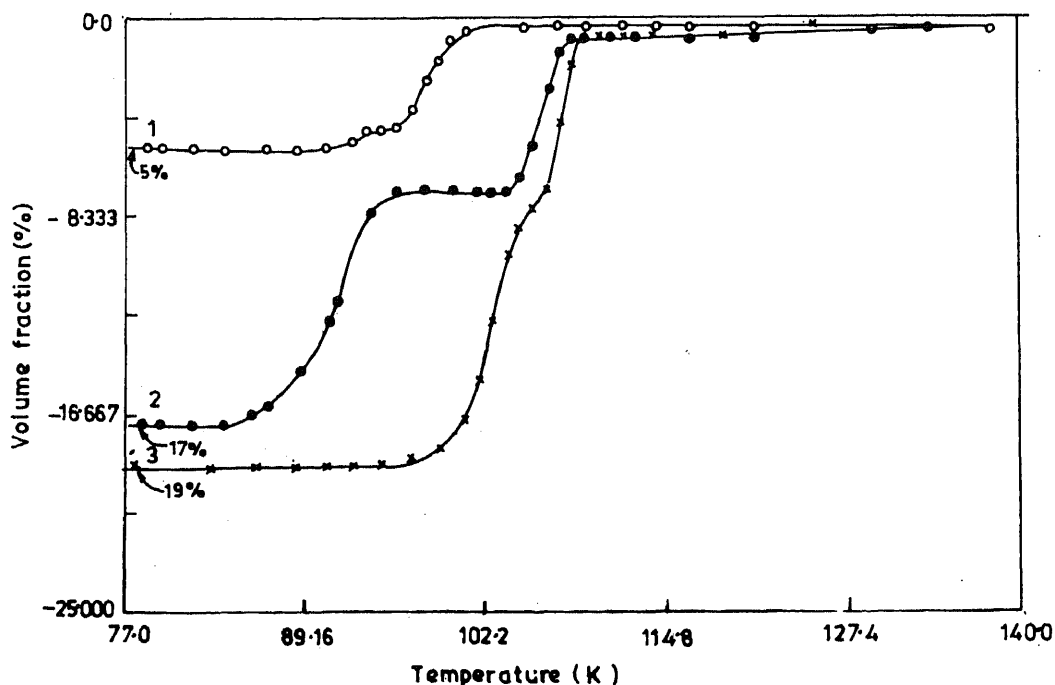


Figure 2. High T_c volume fraction (percentage) vs temperature (K) plots for $\text{Bi}_{1.6}\text{Pb}_{0.4}\text{Sr}_2\text{Ca}_2\text{Cu}_3\text{O}_x$ samples prepared from CuO: (1) LOBA Chemie, (2) S.D. Fine Chemicals and (3) Laboratory single purification.

are referred to in the text as samples 1, 2, 3, 4 and 5, respectively.

2.1 Sample preparation

Stoichiometric amounts of each of these copper oxides were separately taken and mixed with the required amounts of Bi_2O_3 , PbO , SrCO_3 and CaCO_3 . The mixed compositions were then calcined in air at 820°C for 24 h. On cooling, the powders were intimately mixed and again calcined in air at 820°C for 24 h. On cooling each of the powder compositions were pulverized and pressed into pellets. The pellets were finally sintered at 840°C for 100 h in an atmosphere of $\text{O}_2 : \text{N}_2 = 1 : 10$.

The resistance for each of the pellets were measured by a.c. method using a lock-in-amplifier by the standard four-probe contact method. The temperatures were recorded using a Cu-const thermocouple. The measurement of the (2223) phase volume fraction for each of the pellets were also carried out using a lock-in-amplifier.

2.2 Purification of copper oxide powders

To get single purified CuO, the commercially available copper sulphates (or, chlorides), with purity $< 98\%$, was dissolved in distilled water and complexed with sodium-potassium tartrate (Rochelle salt) in presence of optimum amounts of sodium hydroxide and sodium carbonate. The solution was filtered (to get rid of any turbidity or, suspended impurities) so as to get a clear blue coloured filtrate. The filtered solution then refluxed with 40%

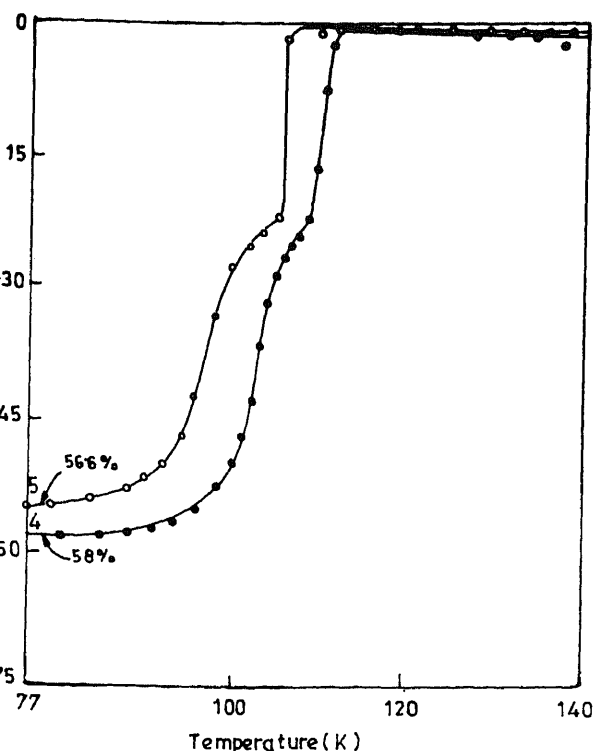


Figure 3. High T_c volume fraction (percentage) versus temperature (K) plots for $\text{Bi}_{1.6}\text{Pb}_{0.4}\text{Sr}_2\text{Ca}_2\text{Cu}_3\text{O}_x$ samples prepared from CuO: (4) Laboratory double purification and (5) Aldrich.

formaldehyde (with ratio 5 : 1) over a water bath. Reddish metallic copper precipitated within 10–15 min of refluxing. The metallic copper was then separated and dried with acetone. Calcination (in air) at 400°C for 3 h, of the metallic copper gave the single purified CuO powder.

To obtain double purified CuO, the precipitated copper mentioned above was dissolved in chlorine water and the entire process from separation of copper from the solution to calcination in air was repeated.

3. Results and discussion

The fall of resistance with temperature were recorded for each of the $\text{Bi}_{1.6}\text{Pb}_{0.4}\text{Sr}_2\text{Ca}_2\text{Cu}_3\text{O}_x$ compositions prepared from varied purity of CuO and are depicted in figure 1. From the measurements, it was observed that the sample prepared from LOBA Chemie grade CuO (i.e. sample 1) had the lowest T_c ($R=0$) while the sample from double purified CuO (i.e. sample 4) and Aldrich CuO (i.e. sample 5) had higher and comparable T_c values. The fall in resistance with temperature (figure 1) in the case of samples 1 and 2 were not very sharp, reflecting the presence of phases other than the (2223) as the major phase. On the other hand, relatively sharper fall in resistance in samples 3, 4 and 5 were indicative of the realization of the (2223) as the major phase.

The details of the volume fraction of the (2223) phase for the various $\text{Bi}_{1.6}\text{Pb}_{0.4}\text{Sr}_2\text{Ca}_2\text{Cu}_3\text{O}_x$ samples are

Table 1. T_c ($R=0$) and percentage volume-fraction of the (2223) phase for various samples of $\text{Bi}_{1.6}\text{Pb}_{0.4}\text{Sr}_2\text{Ca}_2\text{Cu}_3\text{O}_x$.

Sample	Source of CuO	T_c	Percentage volume fraction
1	LOBA Chemie, India (98%)	89.30 K	5.0%
2	S.D. Fine Chemicals (98%)	99.20 K	17.0%
3	Single purified	102.98 K	19.0%
4	Double purified	104.46 K	58.0%
5	Aldrich Grade (99.99%)	104.44 K	56.6%

Table 2. Analysis of the impurities present in the various grades of CuO powder.

Impurity	Percentage present				
	LOBA Chemie	S.D. Fine Chemicals	Single purified	Double purified	Aldrich
Fe	0.1321	0.0580	0.0120	0.0020	0.0030
Zn	1.4250	0.0355	0.0246	0.0052	0.0040
Ni	0.0525	0.0135	0.0221	0.0060	0.0060
Co	0.0932	0.0162	0.0047	0.0032	0.0030
Mn	0.0324	0.0021	————	Not detectable	————
Cr	0.0201	0.0020	————	Not detectable	————
Se	0.0943	0.0240	————	<0.001	————
Te	0.0762	————	————	<0.001	————

represented in figures 2 and 3. The formation of steps in the volume fraction versus temperature curves are manifestations of the presence of (2212) phase along with (2223) phase. From figure 2, it is conclusive that in sample 1 very little of the (2223) phase exists in the sample. The striking feature of figure 3 reveals that the sample 4, prepared from double purified CuO, has a higher percentage volume-fraction of the (2223) phase compared to that of sample 5, which was prepared from Aldrich-grade (99.99%) CuO.

The T_c ($R=0$) values and their respective percentage volume-fraction of the (2223) phase for the various samples of $\text{Bi}_{1.6}\text{Pb}_{0.4}\text{Sr}_2\text{Ca}_2\text{Cu}_3\text{O}_x$, prepared from various grades of CuO are summarized in table 1.

The atomic absorption data for the various grades of CuO powders revealed the presence of Zn, Ni, Fe and trace amounts of Co, Se and Te as trace impurities. The impurities present were the maximum for the CuO powders supplied from the LOBA Chemie, India while it was the minimum for the double purified CuO. The analysis of impurities present in double purified CuO determined by atomic absorption spectroscopy (AAS) is given in table 2. The order of increase of purity in CuO powders were as follows:

LOBA Chemie < S.D. Fine Chemicals < Single purified
 << Aldrich-Grade \leq Double purified.

Presence of impurities, such as Zn, Ni and Fe, in the starting CuO powders provided scope for their substitution

for the Cu sites. With increased levels of impurities their chances of replacing Cu in the Cu sites were increased and the electronic structure of the Cu-O₂ plane was expected to get altered. Consequently, the T_c values and the percentage volume fraction of the (2223) phase got depressed.

Supplementing with the atomic absorption data, it can be concluded that higher purity of the starting CuO leads to higher values of T_c and increased volume fractions of high T_c phase. It can also be concluded that double purification of copper oxide by simple chemical route indeed leads to a better superconducting final material. The chemical route used for single and double purification requires commonly available and less costly chemical reagents such as formaldehyde, sodium-potassium tartrate, NaOH and Na₂CO₃ thus making the route cost-effective for large scale production of high-purity copper oxide.

References

- Bednorz J G and Muller K A 1986 *Phys. B: Condens. Matter* **64** 189
- Ginsberg D M 1989 *Physical properties of high temperature superconductors 1* (Singapore: World Scientific)
- Jones T E, Thibado P M, McGinnes W C, Boss R D, Schindler J W and Oseroffs S 1989 *Physica* **C162** 25
- Maeda A, Yabe T, Tukebayashi S, Hase M and Uchinokura K 1990 *Phys. Rev.* **B41** 4112
- Tarascon J M *et al* 1987 *Phys. Rev.* **B36** 8393
- Wu M K *et al* 1987 *Phys. Rev. Lett.* **58** 908

Preparation of tetragonal zirconia powders by a solid state reaction: Kinetics, phases and morphology

V V MISHRA, A K GARG and D C AGRAWAL*

Materials Science Programme, Indian Institute of Technology, Kanpur 208 016, India

MS received 18 February 1997; revised 7 November 1997

Abstract. Powders of tetragonal (*t*)ZrO₂ have been prepared by a solid state reaction between sodium metazirconate and sodium metaphosphate. The reaction temperatures and times have been varied between 450 and 550°C and 5 and 75 h, respectively. Zirconia powder, mostly in the *t* and *t'* phases, is obtained. The yield of ZrO₂ powder increases monotonically with time at all reaction temperatures according to a phase boundary controlled kinetics. The fraction of *t* phase also increases with time at 450°C and 500°C but goes through a maximum at 550°C, the highest temperature employed. A maximum of 55% of the precursor monoclinic zirconia (used to prepare sodium meta zirconate) is converted to *t* phase at 500°C/75 h. The ZrO₂ powder consists of crystallites of size 9–25 nm agglomerated into particles having average size between 2 and 4 µm. The agglomerates have a breaking strength of 100 MPa. A hydrothermal treatment is found to break the agglomerates into smaller sizes. Grinding the powder in a mortar and pestle converts only 12% of the *t* phase into monoclinic, indicating that substantial fraction of the tetragonal phase is the non transformable variety *t'*. Heating experiments also confirm this.

Keywords. Tetragonal zirconia; powder preparation; solid state reaction.

Introduction

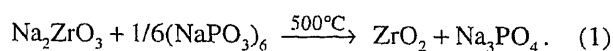
Tetragonal (*t*) to monoclinic (*m*) phase transformation of zirconia (ZrO₂), accompanied by 3–5% volume expansion and 8% shear strain, is utilized in toughening of ceramics. The stable phase of ZrO₂ at room temperature is monoclinic but the tetragonal phase can be stabilized by a very small particle size or if ZrO₂ is alloyed with Y₂O₃, CeO₂ etc. Ultrafine *t*-ZrO₂ powders have been successfully prepared by a variety of methods (Diyasni *et al* 1967; Habeko *et al* 1975; Brook *et al* 1981; Kagawa *et al* 1983; Jean 1991; Harrison *et al* 1992; Suzuki *et al* 1992; Maher *et al* 1993). Brook *et al* (1987) briefly reported some years ago a simple method for preparation of *t*-ZrO₂ powders having a crystallite size of ≈13 nm by a solid state reaction between sodium metazirconate (Na₂ZrO₃) and sodium hexa metaphosphate (NaPO₃)₆ at relatively low temperature (500°C). The method converts coarse *m*-ZrO₂ to *t*-ZrO₂ in a two-step process: first the precursor Na₂ZrO₃ is prepared from coarse *m*-ZrO₂ and subsequently a solid state reaction between Na₂ZrO₃ and (NaPO₃)₆ to obtain *t*-ZrO₂ powder is obtained. The *t*-ZrO₂ particles are expected to be agglomerated but are expected to break into smaller particles during compaction. No further study on this preparation route has been reported.

It appeared to be an attractive process for preparation

of *t*-ZrO₂. We have therefore explored it further in this work, by conducting experiments under varying preparation conditions to optimize the yield of *t*-ZrO₂ powders. Objectives of this work were to study the kinetics of the solid state reaction and to ascertain the phases and preparation of the powder. Possibility of breaking the agglomerates by hydrothermal treatment and under compaction has also been studied. A key property of *t*-ZrO₂ is its ability to undergo *t* → *m* transformation in a stress field and the extent to which it is effective in enhancing toughness. An attempt has been made to evaluate these parameters also.

2. Experimental

The preparation method used here is essentially the same as described by Harrison *et al* (1987). A solid state reaction between Na₂ZrO₃ and (NaPO₃)₆ proceeds as follows



The precursor Na₂ZrO₃ for the above reaction was prepared by calcining a pellet of an equimolar mixture of *m*-ZrO₂ (1–2 µm size, Indian Rare Earths, Kerala) and Na₂CO₃ (Laboratory grade, Glaxo Laboratories, Bombay) at 1250°C for 90 min. The equimolar quantities of Na₂ZrO₃ and (NaPO₃)₆, (predried at 150°C) were

or for correspondence

mixed and ground in an agate mortar and pestle for 30 min and held in a Pt crucible at temperatures of 450°C, 500°C and 550°C for times ranging from 5 h to 75 h. Na_3PO_4 was removed from the reaction product by leaching with dilute HNO_3 (5 N) four times. The residue was washed with triple distilled water (4 to 5 times). Some unknown intermediate phase, besides zirconia, insoluble in HNO_3 was noticed, particularly in powders prepared at lower reaction times. This phase was removed by a further leaching with 1.5% HF solution for 10 min. The residual powders were again washed by triple distilled water followed by ethyl alcohol, dried at 60°C and weighed for determining yield of reaction. The phases present in the resulting ZrO_2 powder and their respective amounts were determined by X-ray diffraction (XRD) using a diffractometer (Reich Siefert 150 Debyeflex 2002) with $\text{CuK}\alpha$ radiation. The monoclinic volume fraction (V_m) was determined by the polymorph method as modified by Toraya *et al* (1984)

$$V_m = \frac{PX_m}{1 + (P - 1)X_m} \quad (2)$$

where $P = 1.31$, a constant factor to account for non-linearity and X_m the integrated intensity ratio,

$$X_m = \frac{I_m(11\bar{1}) + I_m(111)}{I_m(11\bar{1}) + I_m(111) + I_t(111)} \quad (3)$$

$I(hkl)$ is the intensity of the (hkl) peak, given by the area under the respective (hkl) peak. The crystallite size (D_{111}) was determined by X-ray line broadening and the surface area of powders by single point BET method from which equivalent spherical diameter ($\text{esd} - D_{\text{BET}}$) was calculated. The morphology of powders was observed in a scanning electron microscope (JEOL, JSM 840A, Japan). It was noticed that the particles were agglomerated. The particle size was determined by Coulter Counter (Quantachrome, USA). The median particle size (D_{50}) corresponding to 50 wt% on the cumulative plot was used to calculate agglomeration parameter (D_{50}/D_{BET}). The nature of agglomeration of particles was studied by compaction of powders filled in a die (3 mm ϕ) under pressure up to ≈ 500 MPa, using a universal testing machine (Instron 1195). To study the possibility of breaking agglomerates to smaller aggregates by a hydrothermal treatment (HTT), the powder with calculated amount of water (to generate ≈ 2 MPa steam pressure) was sealed in a quartz tube (8 mm outer diameter, wall thickness 1.5 mm) and held at 220°C for times up to 40 h. The resulting powder was again characterized with respect to crystallite size, surface area and particle size. To obtain an indication of the $t \rightarrow m$ transformability, the powder was ground vigorously in a mortar and pestle for 45 min. High temperature stability was determined by heating the powder at 1200°C and 1400°C. The

relative amounts of m and t phases were determined in each case.

3. Results and discussion

3.1 Phases

Figure 1 shows X-ray diffractogram from one of the powders. The predominant phase is tetragonal, though some monoclinic is also present. Sometimes it is hard to distinguish between the cubic and the tetragonal phases. However, in the present case the splitting of the (200)–(002) and (131)–(113) peaks, characteristic of the t phase and absence of the 100% cubic peak at $2\theta = 30.48^\circ$ shows that it is the t phase and not the cubic phase which is forming.

A t' phase is also found to be present in the powders prepared at 450°C and 500°C (figure 2) but not in the powders prepared at 550°C. In ZrO_2 stabilized by alloying oxides such as Y_2O_3 etc, the t' phase is considered to be a variant of the t phase having a higher solute content which makes it less prone to stress induced $t \rightarrow m$ transformation. As shown later, the transformation of the powder on grinding or on heating is found to be difficult which is consistent with the presence of a t' phase.

The stability of the tetragonal phase depends on the grain size, grain shape, stabilizer content and the constraint provided by the matrix. In the absence of a matrix constraint (e.g. for free powder) and with no stabilizer, the critical size for the t phase to be stable is very low, ≈ 30 nm. The average crystallite size of ZrO_2 prepared

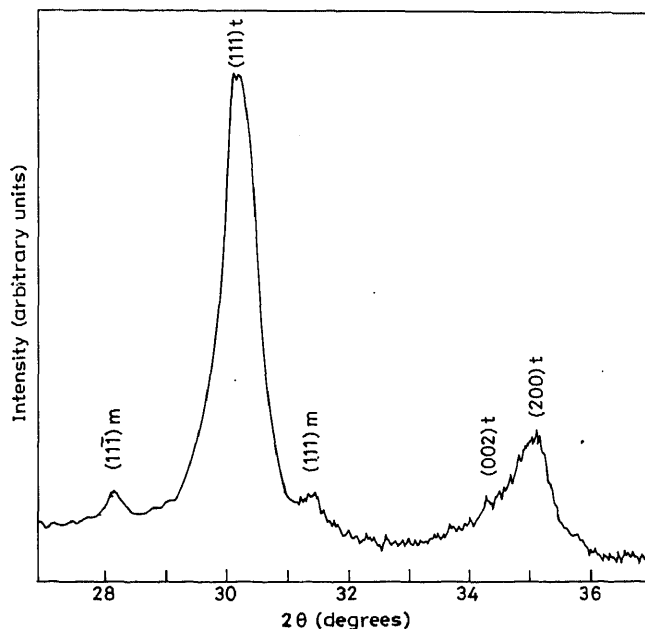


Figure 1. X-ray diffraction plot from ZrO_2 powder prepared at 500°C/75 h.

the present experiment is well within this size as shown later. Hence stability of the *t*-ZrO₂ appears to be primarily due to the small crystallite size as also proposed by Harrison *et al* (1987).

As Na is present during the solid state reaction, it is possible that the *t* phase may also be getting additionally stabilized due to oxygen vacancies and lattice strains created by dissolution of Na₂O in ZrO₂. Benedetti *et al* (1989) have shown that 3 wt% Na stabilizes the cubic phase in ZrO₂. Nishizawa and coworkers (Nishizawa *et al* 1982, 1984) have also obtained similar results. In the powders prepared in the present work, the amount of Na in the ZrO₂ powders, as determined by atomic absorption spectrophotometer, was found to be too small (0.8 wt%) to stabilize the cubic phase. However, small amount of Na may contribute to the stability of the *t* phase as reported by Sircar and Brett (1970) who found in their study of phase equilibria in the system Na₂O–ZrO₂–SiO₂, the formation of *t*-ZrO₂ and attributed to limited solution of Na₂O in ZrO₂. The role of Na₂O dissolved in ZrO₂ appears to be to increase the critical crystallite size up to which the *t* phase is stable from 10 nm for unalloyed ZrO₂ to \approx up to 50 nm as shown in the SEM results (§ 3.3).

Yield and reaction kinetics

The yield (α) of the process defined as the quantity of *t*-ZrO₂ obtained after the reaction as a fraction of the amount of ZrO₂ in the precursor (excluding unreacted monoclinic ZrO₂) is shown in figure 3. The yield increases with the reaction temperature. However the fraction of (*t*') ZrO₂ in the total powder is maximum at an intermediate temperature as shown in figure 4. The optimum temperature appears to be 500°C where the yield is 67% out of which 84% is (*t* + *t'*) phase.

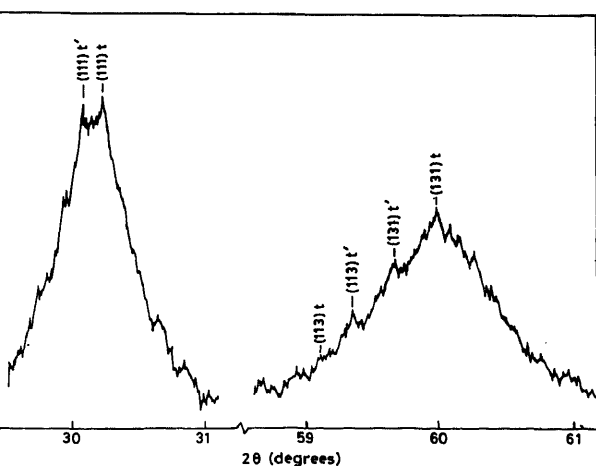


Figure 2. X-ray diffraction plots from sample prepared at 550°C/75 h showing the presence of *t'* phase.

The yield data was analyzed using the general method for the treatment of isothermal solid state reaction as proposed by Hancock and Sharp (1972). The data fitted the following equation

$$1 - (1 - \alpha)^{1/3} = kt \quad (\text{phase boundary controlled-sphere}), \quad (4)$$

with a high correlation coefficient (> 0.999 for 550°C) signifying that the reaction is most probably phase boundary controlled.

3.3 Powder morphology

The average crystallite size determined by X-ray line

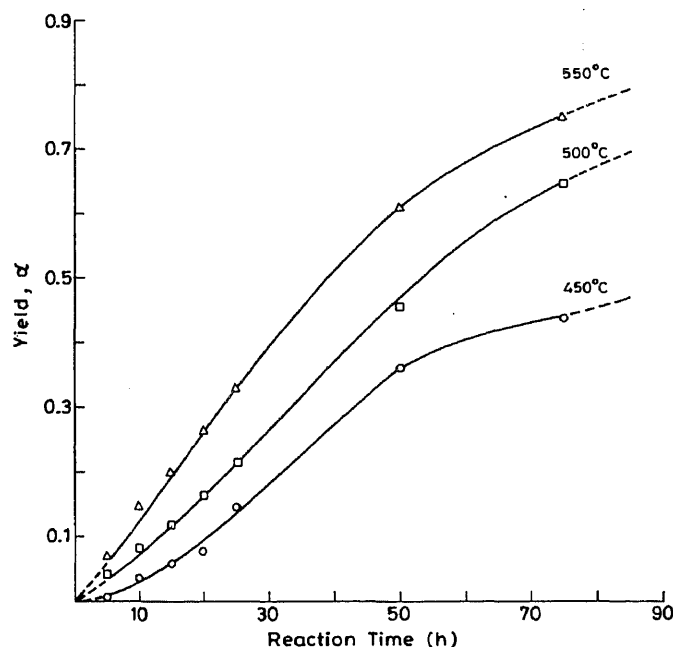


Figure 3. Yield (α) of ZrO₂ with reaction time at different temperatures.

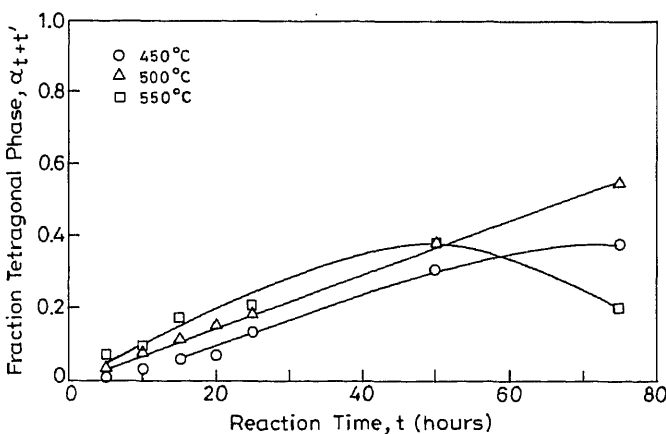
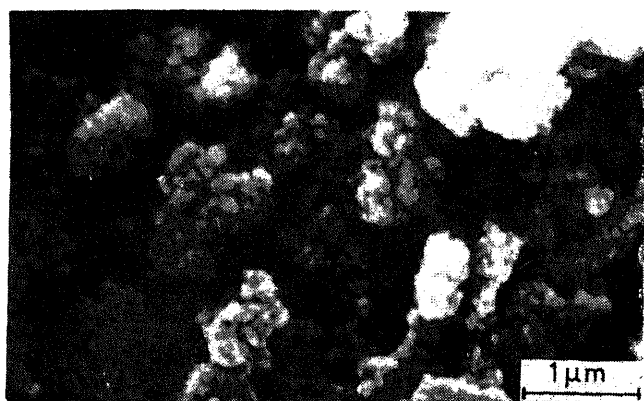


Figure 4. Yield of (*t* + *t'*) under different reaction conditions.

Table 1. Characteristics of the ZrO_2 powder obtained in the present experiments: properties of three powders from references is also given.

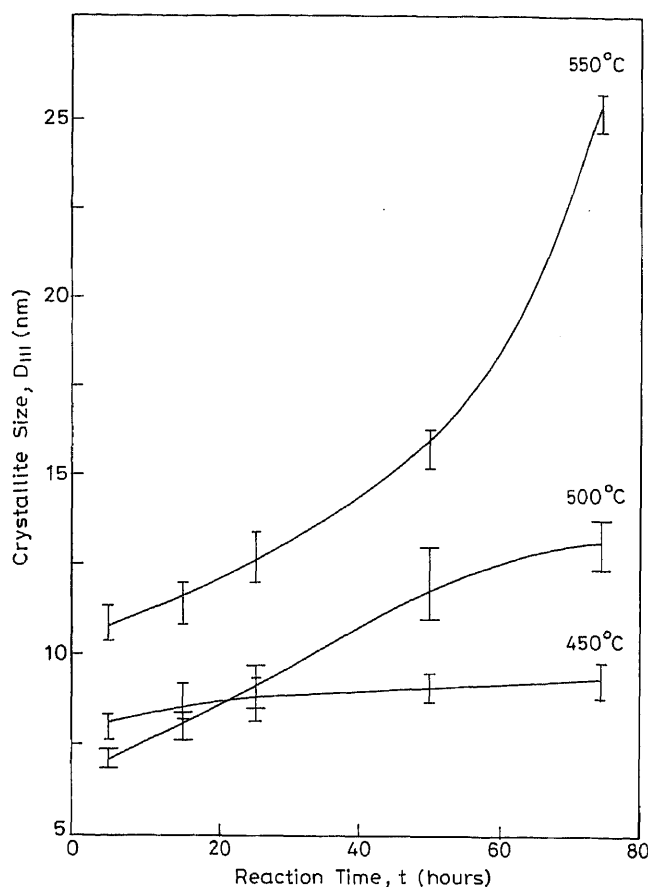
Powder characteristics	This work Reaction time (75 h)			Roosen and Hausner		Haberko and Pyda
	450°C	500°C	550°C	Coprecipitated dried at 120°C	Coprecipitated freeze dried	Coprecipitated gels
Phase composition	87% <i>t</i> + <i>m</i>	84% <i>t</i> + <i>m</i>	25% <i>t</i> + <i>m</i>	Cubic	Cubic	Cubic
Specific surface area (m^2/g)	77	53	27	68	68	101.6
BET particle size (D_{BET} (nm))	12.9	18.9	37	16	16	10.5
Crystallite size (D_{111} (nm))	9	13.1	25.4	12.2	12.2	10.5
Agglomerated particle median size (D_{50} (μm))	2.1	2.05	4.3	1.9	0.7	—
Agglomerate parameter (D_{50}/D_{BET})	162	108	116	127	44	—

**Figure 5.** SEM photograph of powders of ZrO_2 (500°C/75 h) showing agglomeration of particles.

broadening as well as by BET surface area and the particle size determined by a Coulter Counter are given in table 1. Data on some other powders reported in literature is also included. An SEM picture is shown in figure 5. It is seen that the powders consist of 10–50 nm sized crystallites agglomerated into particles of a few microns. The discrepancy in the X-ray and BET data is due to the assumption of a spherical crystallite in the latter and also due to the presence of contacts between the crystallites. The rate of increase in crystallite size during the reaction is nearly zero at 450°C (after the initial crystallites are formed, figure 6). At 550°C, the crystallite size increases with time at a nearly constant rate up to 50 h and then levels off. At 550°C, the behaviour is similar as that for 500°C up to 50 h but then there is a rapid increase in the average crystallite size. This appears to be due to the exaggerated grain growth which is found to occur during sintering of ceramics and is characterized by the growth of a few large grains to very large sizes at the expense of the smaller grains.

3.4 Agglomerate strength by compaction test

When an agglomerated powder is subjected to a uniaxial

**Figure 6.** Crystallite size (D_{111}) of powders prepared at different times and temperatures.

pressure, the agglomerates break at a pressure indicated by a break in the plot of pressure vs packing density of the powder. Such a plot for 500°C/75 h powder is shown in figure 7. For comparison, data from literature (Graff *et al* 1980; Graff and Burggraaf 1983; Haberko and Pyda 1983) for powders prepared by other methods is also included. It is seen that the powder prepared in

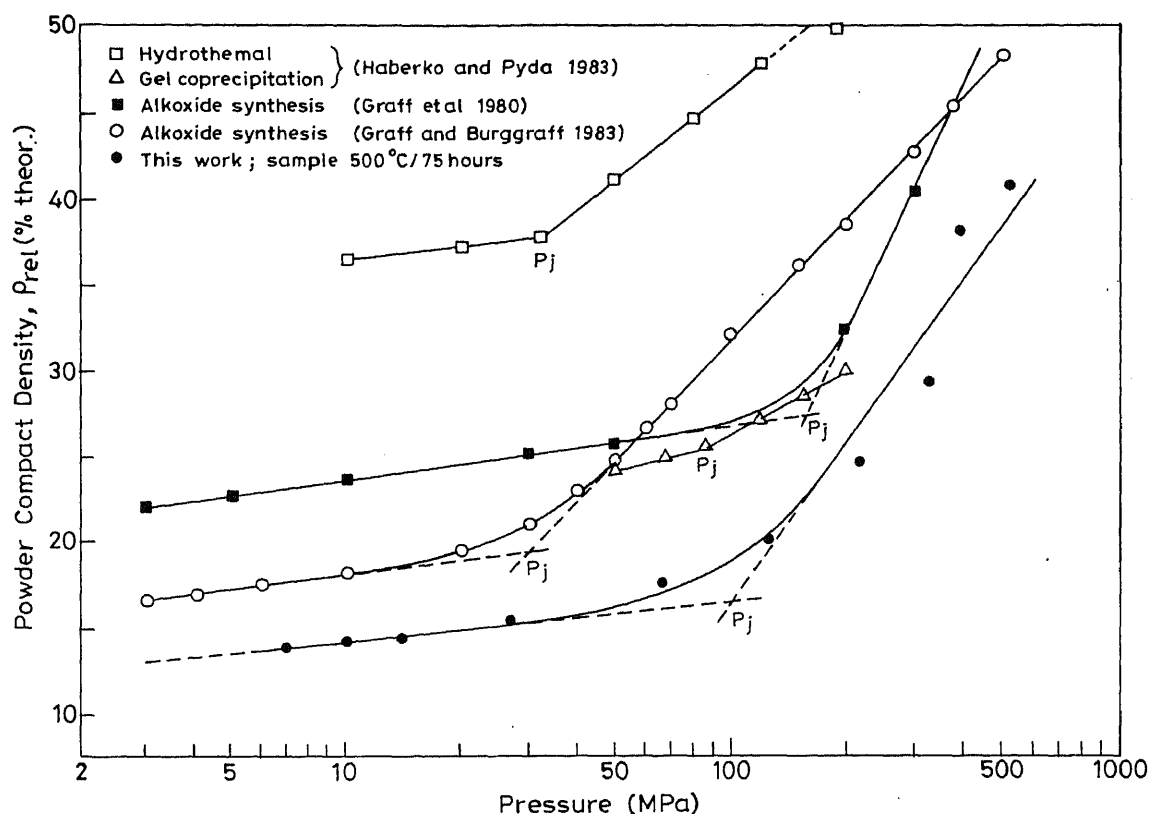


Figure 7. Powder compact density ρ_{rel} vs compaction pressure, P , of the powder prepared at 500°C/75 h, compared to data reported in literature for powders by alkoxide synthesis, hydrothermal synthesis and coprecipitation/calcination methods.

Figure 2. Effect of hydrothermal treatment on particle characteristics (500°C/75 h)

	Surface area (m^2g^{-1})	D_{III} (nm)	D_{BET} (nm)	D_{50} coulter (μm)	$\frac{D_{50}}{D_{BET}}$
Before HTT	53.2	13.1	18.9	2.1	108
After HTT (50 h)	57.0	12.9	19.6	1.6	83

The powder has a high agglomerate breaking strength (10 MPa) and a low packing density (Powder compact density $\rho_{rel} = 13\%$) at low pressure (≈ 3 MPa). The latter is due to the poor flow characteristics of the powder and may also be due to a low agglomerate density. The low agglomerate density implies that the crystallites maintain their individuality in the agglomerates to a large extent. This is supported by the earlier results that they are predominantly tetragonal and have high specific surface area. Thus these powders have strong solid bridges between crystallites and appear to be quite porous.

Effect of hydrothermal treatment

Hydrothermal treatment has been found to be quite

effective in breaking agglomerates in a TiO_2 powder by Heistand *et al* (1985). To study this effect the ZrO_2 powders obtained by reaction at 500°C/75 h were subjected to a hydrothermal treatment for 40 h in a quartz tube using 2 MPa steam at 220°C. The results are given in figure 8 and table 2. The hydrothermal treatment shifts the particle size distribution to lower sizes, with agglomerates larger than $6\mu\text{m}$ totally eliminated. The average particle size comes down to $1.6\mu\text{m}$ from $2\mu\text{m}$. There is no change in the crystallite size. However, the agglomerate parameter (agglomerate size/crystallite size) is reduced from 108 to 83 indicating that significant number of bonds between crystallites are broken under the conditions of hydrothermal treatment used. Further reduction in agglomerates may be produced by using higher pressures and temperatures during the hydrothermal treatment.

3.6 Transformability under stress and on heating

The powder (500°C/75 h) was crushed in mortar and pestle for 30 min. Only 12% of the $t\text{-ZrO}_2$ transformed to monoclinic indicating the presence of considerable amount of the t' phase. The powder was heated to different temperatures, held for 1 h and cooled to room temperature to determine the extent of $t \rightarrow m$ transfor-

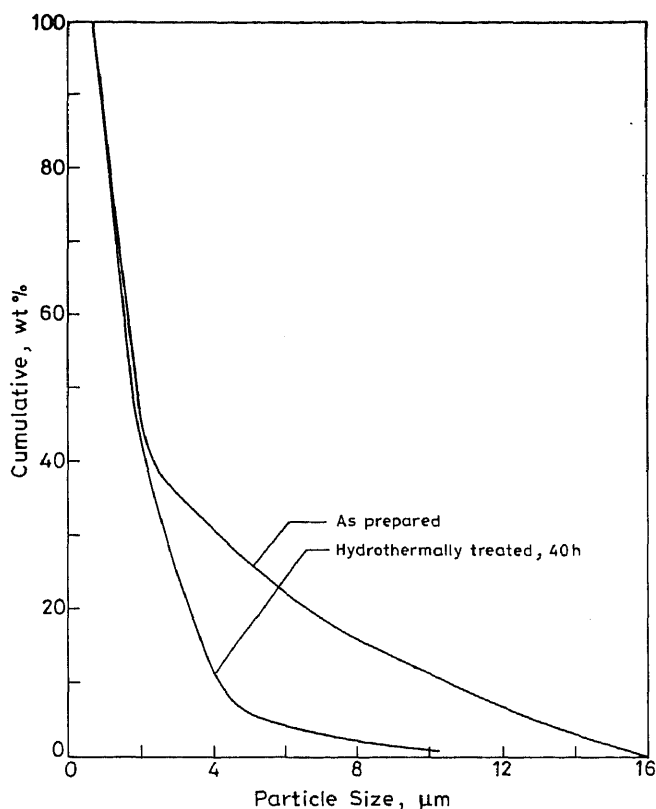


Figure 8. Particle size distribution of powder prepared at 500°C/75 h.

mation. Heating to 1200°C resulted in only slight increase in the monoclinic content while heating to 1400°C converted all the ($t+t'$) to monoclinic phase. Pellets sintered at 1550°C were also fully monoclinic. The t' phase is stable up to 1400°C. Above experiments thus show that most of powder prepared at 500°C exists as t' .

4. Summary

The solid state reaction used in the present work is successful in producing tetragonal zirconia. The kinetics of the reaction appears to be phase boundary controlled. The yield of tetragonal ZrO_2 is found to be maximum at 500°C where 84% of the powder is in the t phase. The zirconia crystallites, 9–25 nm in size, are agglomerated into particles of 2–4 μm. A substantial fraction of the powder is found to be in a nontransformable t' form. The factors which lead to this need to be understood in order to make these powders useful for toughening applications. The agglomerates have a breaking strength of 100 MPa which is well within the pressures used during dry pressing of ceramics. In order to exploit the property of the stress induced $t \rightarrow m$ transformation in t zirconia, it may be necessary to

incorporate some stabilizer (e.g. Y_2O_3 , CeO_2) in the powder and also to reduce the agglomerate size. A hydrothermal treatment is found to be useful in reducing the particle size substantially.

Acknowledgement

This work was partially supported by a grant from the Board of Research in Nuclear Sciences, Department of Atomic Energy, Government of India.

References

- Benedetti A, Fagherazzi G and Pinna F 1989 *J. Am. Ceram. Soc.* **72** 467
- Brook R J 1980 in *Advances in ceramics* (eds) A H Heuer and L W Hobbs (Columbus, Ohio: The American Ceramic Society) Vol. 3, p. 272
- Graff M A C G Van de, Keizer K and Burggraaf A J 1980 in *Science of ceramics* (ed.) H Hausner (Berlin: Deutsche Keramische Gesellschaft) Vol. 10, p. 983
- Graff M A C G Van de and Burggraaf A J 1983 in *Advances in ceramics* (eds) N Claussen, M Ruhle and A H Heuer (Columbus, Ohio: The American Ceramic Society) Vol. 12, p. 744
- Haberko K, Ciesla A and Pron A 1975 *Ceram. Int.* **1** 111
- Haberko K and Pyda W 1983 in *Advances in ceramics* (eds) N Claussen, M Ruhle and A H Heuer (Columbus, Ohio: The American Ceramic Society) Vol. 12, p. 774
- Hancock J D and Sharp J H 1972 *J. Am. Ceram. Soc.* **55** 74
- Harrison A, Stevens R and Milne S J 1987 *J. Mater. Sci. Lett.* **6** 673
- Heistand II R H, Ogure Y, Okamura H, Moffatt W C, Novich R, Barringer E A and Bowen H K 1985 in *Science of ceramic processing* (eds) C L Hench and R Ulrich Donald (New York: John Wiley and Sons) pp. 482–497
- Jean V S 1991 *Br. Ceram. Proc.* **47** 45
- Kagawa M, Honda F, Onodera H and Nagawa 1983 *Mater. Res. Bull.* **18** 1081
- Maher G H, Hutchins C E and Ross S D 1993 *Am. Ceram. Soc. Bull.* **72** 72
- Mazdiyasn K S, Lynch C T and Smith J S III 1967 *J. Am. Ceram. Soc.* **50** 532
- Mottet B, Pichvant M, Beny J M and Alary J A 1992 *J. Am. Ceram. Soc.* **75** 2515
- Nishizawa H, Yamasaki N, Matsuoka K and Mitsushio H 1982 *J. Am. Ceram. Soc.* **65** 343
- Nishizawa H, Tani T and Matsuoka K 1984 *J. Mater. Sci.* **19** 2921
- Rhodes W H 1981 *J. Am. Ceram. Soc.* **64** 19
- Roosen A and Hauser H 1983 in *Advances in ceramics* (eds) N Claussen, M Ruhle and A H Heuer (Columbus, Ohio: The American Ceramic Society) Vol. 12, p. 714
- Sirkar A and Brett N H 1970 *Trans. Br. Ceram. Soc.* **69** 131
- Suzuki M, Kagawa M, Syono Y and Hirai T 1992 *J. Mater. Sci.* **27** 679
- Toraya H, Yoshimura M and Somiya S 1984 *J. Am. Ceram. Soc.* **67** C-119

Optical and structural characteristics of strontium doped calcium tartrate crystals

K SURYANARAYANA*, S M DHARMAPRAKASH and K SOORYANARAYANA†

Department of Physics, Mangalore University, Mangalagangothri 574 199, India

†Solid State and Structural Chemistry Unit, Indian Institute of Science, Bangalore 560 012, India

MS received 17 April 1997

Abstract. We report here on the optical and structural characteristics carried out on strontium doped calcium tartrate tetrahedral single crystalline materials obtained by diffusing calcium and strontium ions through silica gel impregnated with optically active tartaric acid. Linear optical properties of this material such as refractive index, birefringence and transmission characteristics were measured in the wavelength range $200\text{ nm} < \lambda < 1500\text{ nm}$. No dispersion of the birefringence was observed within the experimental accuracy. The packing of tartrate molecules remained unaltered with 12% of the strontium doping.

Keywords. Silica gel; refractive index; crystal structure; second harmonic generation.

Introduction

Single crystals of calcium tartrate (CT) and strontium tartrate (ST) have attracted considerable attention in recent years on account of their ferroelectric, non linear optical and spectral characteristics (Medrano *et al* 1987; Kricheldorf and Wyncke 1989; Nakatani 1991; Selvarajan *et al* 1993; Rethinam *et al* 1994). CT and ST crystallize in the orthorhombic system with space group $P2_12_12_1$ containing four molecules in the elementary unit cell (Ambady *et al* 1987; Bohandy and Murphy 1968). In the course of our investigations on the physical properties of CT and ST, attention was drawn to the growth and characterization of strontium doped calcium tartrate (CST). This work was undertaken to study the optical characteristics and the effect of doping on the structural role of tartrate ion in the presence of two divalent metallic elements.

Experimental

Growth and crystal habit

Strontium doped calcium tartrate single crystals employed for optical and X-ray diffraction studies were grown by the silica gel method. The growth process involves the controlled diffusion of calcium chloride–strontium chloride solutions into gel made up of sodium silicate and tartaric acid (all AR grade) solutions at constant temperature and visible light conditions. The experiment was performed in Corning glass tubes of length 200 mm and inner dia. 25 mm. The suitable conditions for the growth of the best quality CST single

crystals were: pH 3.5–4.0, gelling time 12 days, concentration of the reactants 1.0 M and growth temperature 30°C . Growth of CST crystals (about $10 \times 6 \times 4\text{ mm}^3$ in size) was observed down the gel column in the experimental vessels within a week. During the exchange reaction HCl yielded as a byproduct. The crystal size and time of formation of ST depend on the density of the gel and concentration of the supernatant solutions. The gel grown CST single crystals were colourless and optically transparent. Qualitative chemical analyses using an energy dispersive X-ray spectrometer (EDX) confirmed that the single crystals are those of CST in which two alkaline earths form solid solution in the ratio 0.88 : 0.12. The maximum uptake of strontium in the CST crystal depends on the molarity of the mixed calcium chloride and strontium chloride solutions with different ratios. The crystals grown were confirmed to have the composition $\text{Ca}_{0.88}\text{Sr}_{0.12}\text{C}_4\text{H}_4\text{O}_6 \cdot 4\text{H}_2\text{O}$ under the above mentioned growth conditions. The single crystalline habit of CST is deviated from the habit of CT and ST single crystals (figure 1). The crystals are elongated in the b-direction and the principal faces are (110), (010) and (011) with their symmetry equivalents.

2.2 Structure

The crystal thus grown was transparent and was mounted on the X-ray diffractometer after confirming the quality by examining under a polarizing microscope. The intensity data were collected on an Enraf–Nonius CAD4 diffractometer having graphite monochromated $\text{MoK}\alpha$ radiation ($\lambda = 0.7107\text{ \AA}$) in the $\omega/2\theta$ mode. The cell parameters were obtained from the least square refinement of 25 reflections ($-2\ 3\ 1$, $-1\ 3\ 0$, $0\ 3\ -1$) after every 3600 s

*Author for correspondence

of exposure time; the orientation was checked every 400 reflections and no significant fluctuations in their intensity were observed. The data was corrected for Lorenz and polarization effects but not for absorption effect since it is negligible. The structure of strontium doped calcium tartrate tetrahydrate was solved using SHELXS 86 (Sheldrick 1985). The heavy atoms were located using Patterson method and the rest of the structure was developed using partial structure expansion technique. The structure refinement was carried out using SHELX 93 (Sheldrick 1993). Hydrogen atoms were located from the difference map. All nonhydrogen atoms were refined anisotropically. The details of crystal data and refinement results are given in table 2.

3. Results and discussion

3.1 UV-visible spectrum of CST single crystals

Optical absorption measurements for CST single crystal

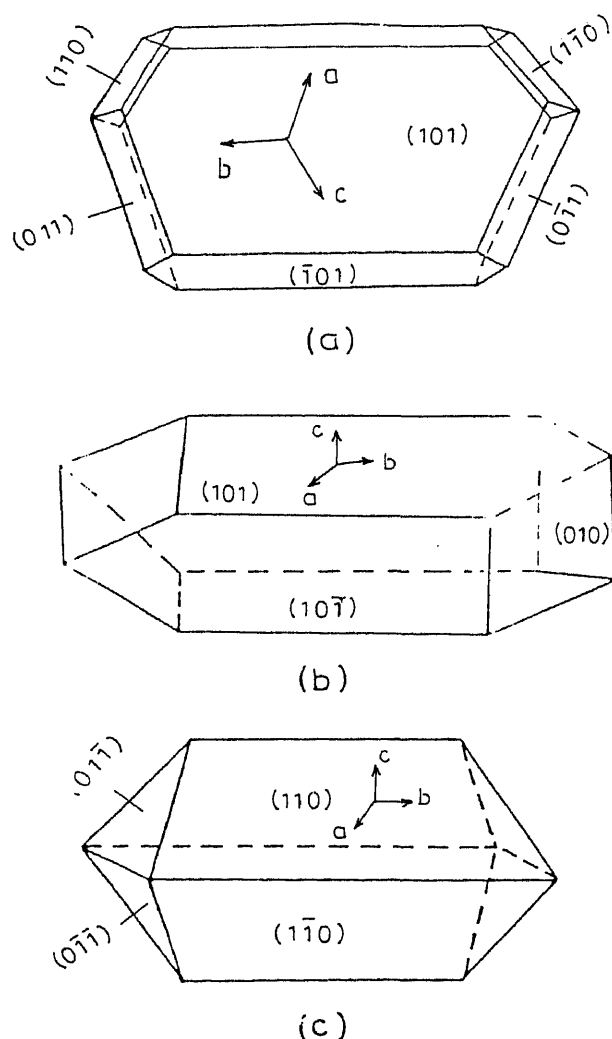


Figure 1. Habit of (a) calcium tartrate, (b) strontium tartrate and (c) strontium doped calcium tartrate single crystals.

with thickness 1.0 mm were performed with a Cary-14 spectrophotometer in the range 200–1400 nm at room temperature. No absorption decreasing film was coated on the surfaces of the crystal and the light loss caused by reflections on the surfaces was ignored. The absorption coefficient as a function of wavelength, was evaluated. Anisotropy was observed for different light directions. One can see from figure 2 that the single crystals of CST are transparent in the range 275–1325 nm and the transmittivity is greater than 85%. The optical transmission range as determined from the optical characteristics, makes the CST crystal interesting for second harmonic generation in the ultra violet region.

3.2 Linear optical properties

According to the crystal system three planes normal to the three orthorhombic unit cell axes with x, y, z parallel

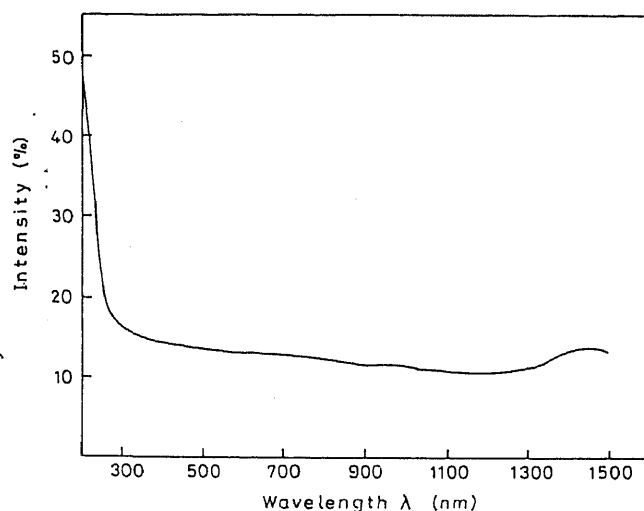


Figure 2. UV visible spectra of strontium doped calcium tartrate single crystal (thickness, 1.0 mm).

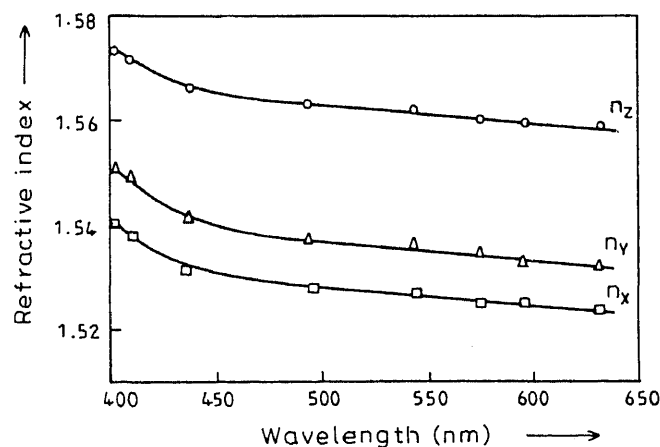


Figure 3. Dispersion of the principal refractive indices of strontium doped calcium tartrate single crystal at room temperature.

the crystallographic *a*, *b* and *c* axes, respectively, were compared to determine birefringence and refractive indices. The refractive index of the crystal within the visible light range was measured by the Brewster's angle method

Table 1. Linear optical data of CST single crystals.

λ (nm)	Refractive indices			Birefringence	
	<i>n_x</i>	<i>n_y</i>	<i>n_z</i>	Δ <i>n_x</i>	Δ <i>n_z</i>
5	1.5398	1.5514	1.5738	0.02	0.03
6	1.5383	1.5501	1.5726	0.02	0.03
7	1.5316	1.5431	1.5661	0.02	0.03
8	1.5292	1.5392	1.5639	0.02	0.03
9	1.5272	1.5378	1.5632	0.02	0.03
10	1.5255	1.5356	1.5611	0.02	0.03
11	1.5243	1.5344	1.5589	0.02	0.03
12	1.5229	1.5336	1.5567	0.02	0.03

Table 2. Crystal data and structural refinement.

Empirical formula	Ca _{0.876} Sr _{0.124} C ₄ H ₁₂ O ₁₀
Molecular weight	266.11
Crystal size (in mm)	0.41 × 0.12 × 0.18
Crystal system	Orthorhombic
Space group	<i>P</i> 2 ₁ 2 ₁ 2 ₁
Unit cell dimensions	9.231(2) Å 9.619(4) Å 10.610(5) Å
Volume	942.2(6) Å ³
Number of molecules per unit cell	4
<i>D</i> _c (calcd)	1.875 g/cm ³
Radiation used	Mo Kα (λ = 0.7107 Å)
Goniometer	Enraf-Nonius CAD4
Scanning method	ω/2θ
Reflections collected	2284
Unique reflections	2027
θ range	2.86° to 26.97°
h, k, l range	−11 ≤ <i>h</i> ≤ 11 0 ≤ <i>k</i> ≤ 12 0 ≤ <i>l</i> ≤ 13
Refinement method	Full matrix least squares on <i>F</i> ²
Goodness of fit on <i>F</i> ²	1.587
Final <i>R</i> indices	<i>R</i> = 0.087, <i>wR</i> = 0.233
<i>R</i> indices (<i>I</i> > 2σ(<i>I</i>))	
<i>R</i> indices (all data)	<i>R</i> = 0.152, <i>wR</i> = 0.268
Residual electron density	max = 0.83 e/Å ³ , min = −0.58 e/Å ³

(figure 3). The data are listed in table 1. The quality of the crystal together with the low birefringence of this material led to a precise measurement with an accuracy of ±0.005. The wavelength dependence of the birefringence was determined by using a monochromator, mercury lamp, sodium lamp and He-Ne laser as light source for the polarizing microscope. The birefringence is independent of the wavelength in the wavelength range 400–650 nm.

CST belongs to one of the four acentric orthorhombic point groups, determined by the convention that the principal refractive indices are such that *n_z* > *n_y* > *n_x*, which implies that in CST crystal the optical plane is the *x*–*z* plane. Results on the dispersion of the indices of refraction show that CST is an optically positive biaxial crystal.

3.3 Non linear optical properties

The second harmonic generation experiments were performed with an unfocussed and linearly polarized, Nd : YAG laser (λ = 1.064 μm). CST crystal exhibits small optical nonlinearity. The second harmonic generation intensity of CST is 0.1 times that of quartz. Limited by the experimental condition, the nonlinear optical coefficients of CST single crystal have not been obtained.

3.4 Structure

There is no significant structural change in the CST

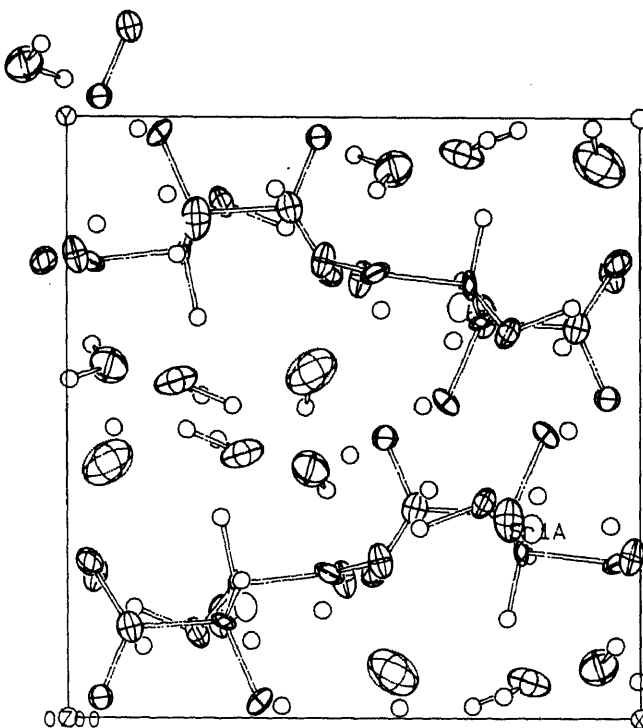


Figure 4. The structure of strontium doped calcium tartrate single crystal.

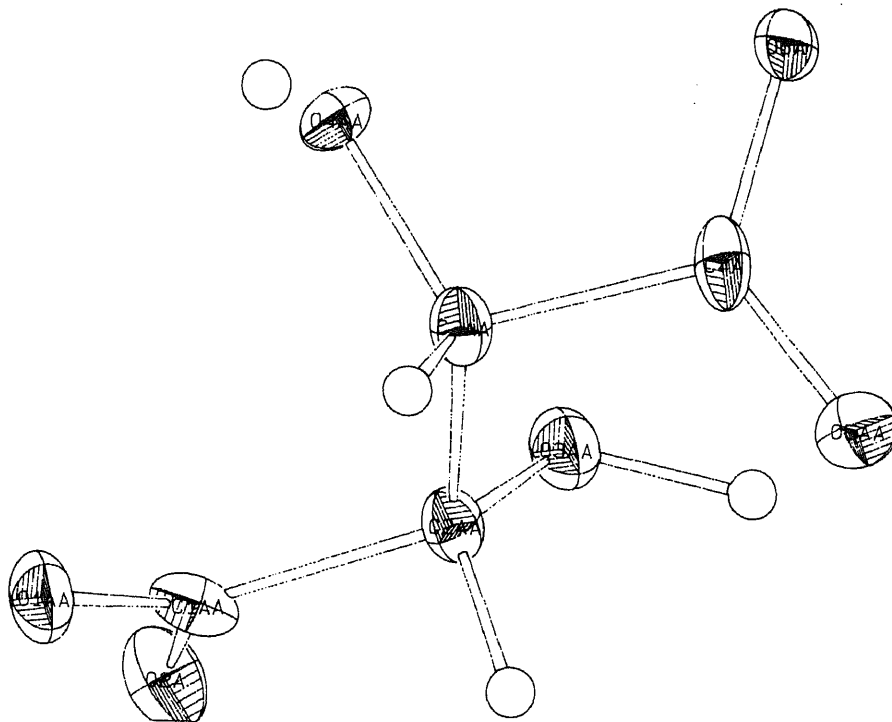


Figure 5. The details of the tartrate molecule.

Table 3. Atomic coordinates, occupancy and U_{eq} .

	x/a	y/b	z/c	Occupancy	U_{eq}
Sr	0.1864(2)	0.8160(2)	0.8218(2)	0.124	171(4)
Ca	0.1864(2)	0.8160(2)	0.8218(2)	0.876	171(4)
O1	0.4507(8)	0.7617(8)	0.8086(8)	1.000	209(1)
O2	0.0153(8)	0.7688(9)	0.9920(9)	1.000	273(6)
O3	0.7717(8)	0.6415(8)	0.9517(8)	1.000	198(6)
O4	0.6627(8)	0.5273(8)	0.7168(8)	1.000	219(0)
O5	-0.0389(8)	0.7583(9)	0.7143(8)	1.000	222(8)
O6	0.0573(8)	1.0334(7)	0.8275(9)	1.000	221(4)
O7	0.1928(12)	0.5604(9)	0.8296(13)	1.000	552(6)
O8	-0.0732(11)	1.0854(10)	1.0702(10)	1.000	404(0)
O9	0.2269(9)	0.8309(11)	0.5877(8)	1.000	329(8)
O10	0.4285(14)	0.5763(12)	0.5668(12)	1.000	624(6)
C1	0.5407(12)	0.7405(11)	0.8927(11)	1.000	200(0)
C2	0.7049(11)	0.7216(11)	0.8612(10)	1.000	172(4)
C3	0.7245(11)	0.6604(10)	0.7293(10)	1.000	119(9)
C4	0.1095(11)	1.1503(11)	0.7979(11)	1.000	177(8)
H1	0.88270	0.68360	0.95580	1.000	
H2	0.72970	0.83370	0.85550	1.000	
H3	0.69380	0.72880	0.65570	1.000	
H4	0.62410	0.52030	0.67590	1.000	
H5	0.29020	0.52030	0.86380	1.000	
H6	0.23640	0.53680	0.76380	1.000	
H7	-0.04380	1.12040	1.16000	1.000	
H8	-0.00440	1.06240	0.98000	1.000	
H9	0.17630	0.87130	0.60350	1.000	
H10	0.36640	0.88110	0.60310	1.000	
H11	0.41840	0.51760	0.48280	1.000	
H12	0.55200	0.67930	0.53880	1.000	

U_{eq} is defined as one-third of the trace of the orthogonalized U_{ij} tensor.

Table 4. Anisotropic thermal parameters ($\text{\AA}^2 \times 10^4$).

Atom	U_{11}	U_{22}	U_{33}	U_{23}	U_{13}	U_{12}
Ca	126(8)	209(9)	178(9)	0(9)	3(9)	-7(9)
Sr	126(8)	209(9)	178(9)	0(9)	3(9)	-7(9)
O1	149(35)	313(40)	166(42)	-29(36)	-2(35)	46(35)
O2	165(38)	359(53)	297(50)	21(38)	-24(36)	-60(35)
O3	160(37)	228(43)	207(42)	-62(32)	-43(32)	70(29)
O4	163(42)	167(39)	328(48)	-78(32)	-76(34)	-84(31)
O5	178(39)	197(39)	294(51)	-93(35)	-11(35)	98(50)
O6	154(36)	148(35)	362(53)	6(38)	109(40)	-1(30)
O7	529(66)	198(46)	932(92)	-55(57)	-112(79)	98(50)
O8	373(53)	334(52)	506(69)	-162(45)	40(49)	46(42)
O9	244(44)	491(57)	254(46)	-165(46)	27(35)	3(45)
O10	680(78)	557(73)	637(88)	-153(59)	-311(68)	212(61)
C1	218(57)	108(49)	274(69)	51(46)	56(52)	76(48)
C2	59(49)	218(58)	240(56)	65(40)	72(42)	-15(39)
C3	154(50)	63(50)	142(50)	61(37)	-8(38)	58(37)
C4	156(52)	257(66)	120(57)	-99(42)	-17(44)	-27(43)

The anisotropic displacement factor exponent takes the form $-2\pi^2[(ha^*)^2U_{11} + \dots + 2hka^*b^*U_{12}]$.

Table 5. Interatomic distances (\AA) in strontium doped calcium tartrate tetra hydrate.

Ca(Sr)-O6	2.407(7)
Ca(Sr)-O5	2.436(8)
Ca(Sr)-O2	2.441(9)
Ca(Sr)-O7	2.461(8)
Ca(Sr)-O4	2.498(8)
Ca(Sr)-O1	2.499(7)
Ca(Sr)-O9	2.516(9)
Ca(Sr)-O3	2.561(8)
O1-C1	1.236(14)
O2-C1	1.249(14)
O3-C2	1.377(13)
O3-Ca(Sr)	2.561(8)
O3-H1	1.103(8)
O4-C3	1.408(12)
O4-Ca(Sr)	2.498(8)
O4-H4	0.565(8)
O5-C4	1.233(13)
O6-C4	1.263(13)
O7-H5	1.044(11)
O7-H6	0.837(13)
O8-H7	1.046(10)
O8-H8	1.170(10)
O9-H9	0.630(9)
O9-H10	1.385(8)
O10-H11	1.059(11)
C1-O2	1.249(12)
C1-C2	1.563(15)
C2-C3	1.530(15)
C2-H2	1.104(10)
C3-C4	1.562(14)
C3-H3	1.060(10)
C4-O5	1.233(13)
C4-C3	1.562(14)

Table 6. Selected bond angles (degrees).

C2-O3-H1	103.8(7)
C3-O4-H4	115.8(10)
H5-O7-H6	77.0(9)
H7-O8-H8	131.7(10)
H9-O9-H10	116.2(11)
H11-O10-H12	104.2(9)
O1-C1-C2	121.1(10)
O3-C2-C1	110.5(9)
C1-C2-H2	95.7(9)
C1-C2-C3	110.8(8)
O3-C2-H2	119.5(9)
O3-C2-C3	111.7(8)
C3-C2-H2	107.5(9)
O4-C3-C2	112.9(8)
C2-C3-H3	113.8(9)
O4-C3-H3	112.8(9)
O7-H5-H6	43.6(7)
O7-H6-H5	59.4(8)

atomic distances, selected bond angles and hydrogen bond lengths are given in tables 5–7. The metal ion is coordinated by eight oxygens forming a distorted Siamese dediacahydron (Johnson 1966). The water molecule connects tartrate motifs by hydrogen bonding hence forming an infinite chain which runs along the a-axis. The adjacent chains are linked along b-axis by the metal and tartrate oxygen bonds. We conclude from this study that the packing of tartrate molecules remains unaltered with 12% of the strontium doping. Details of the tartrate molecule are shown in figure 5.

4. Conclusion

The silica gel growth system involves the use of calcium chloride and strontium chloride as the top reactants and sodium meta silicate impregnated with tartaric acid as

en compared with calcium tartrate (Hawthorne *et al* 32). The crystal structure is shown in figure 4. Atomic ordinates and anisotropic thermal displacement parameters are given in tables 3 and 4, respectively. Inter-

Table 7. Hydrogen bonds.

A-H...B	A-H	A...B	H...B	A-H...B
O4-H4...O10	0.565(8)	2.725(15)	2.211(13)	152.5(8)
O7-H5...O1	1.044(11)	3.077(13)	2.816(8)	94.4(5)
O8-H8...O2	1.170(10)	3.261(13)	2.833(9)	100.8(5)
O8-H8...O6	1.170(10)	2.887(14)	1.738(9)	166.0(6)
O9-H9...O5	0.630(9)	2.882(11)	2.551(8)	115.8(9)
O9-H10...O1	1.385(8)	3.194(11)	2.584(8)	103.0(4)
O3-H1...O2	1.103(7)	2.596(11)	1.522(8)	162.8(5)
O3-H1...O5	1.103(7)	3.266(11)	2.758(8)	107.6(5)

lower reactant results in the crystallization of calcium strontium tartrate with the molecular formula $\text{Ca}_{0.88}\text{Sr}_{0.12}\text{C}_4\text{H}_4\text{O}_6 \cdot 4\text{H}_2\text{O}$. The optical transition range has been determined from the UV-visible spectra for CST which extends from 275 nm to 1400 nm. This makes the CST material interesting for second harmonic generation in the UV region. The optical characteristics of CST crystal is found to be positive. CST exhibits optical nonlinearity. From the structural study, it is found that the packing of tartrate molecules remains unaltered with 12% of strontium doping in CST.

Acknowledgement

We thank Prof. T N Guru Row, Solid State and Structural Chemistry Unit, Indian Institute of Science, Bangalore, for providing facilities to carry out the structural work of material.

References

- Ambady G K 1968 *Acta Crystallogr.* **B24** 1548
- Bohandy J and Murphy J C 1968 *Acta Crystallogr.* **B24** 286
- Brehat F and Wyncke B 1989 *J. Phys. B: At. Mol. Opt. Phys.* **22** 1981
- Hawthorne F C, Borys I and Ferguson R B 1982 *Acta Cryst.* **B38** 2461
- Johnson N W 1966 *Canadian J. Math.* **18** 169
- Medrano C, Gunter P and Arend H 1987 *Phys. Status Solidi (b)* **14B** 749
- Nakatani N 1991 *Jap. J. Appl. Phys.* **30** 1961
- Rethinam F J, Arivuoli D, Ramasamy S and Ramasamy P 1994 *Mater. Res. Bull.* **29** 309
- Selvarajan P, Has, B N Gon and Rao K V 1993 *J. Mater. Sci. Letts* **12** 1210
- Sheldrick G M 1985 *SHELXS 86, program for the solution of crystal structures* (Germany: Univ. of Gottingen)
- Sheldrick G M 1993 *SHELXL 93, program for the refinement of crystal structures* (Germany: Univ. of Gottingen)

Effect of fillers on acousto ultrasonic response in GRP composites

PRAVESH KUMAR

MTC Division, National Metallurgical Laboratory, Jamshedpur 831 007, India

MS received 20 January 1996; revised 24 December 1996

Abstract. In recent years, there has been a wide interest in fillers which improve the quality and performance of fibre composites when mixed in a small quantity in the matrix. In the present work the effect of addition of mica and graphite powders in cross ply glass fibre reinforced plastic (GRP) composites has been studied by using acousto ultrasonic (AU) technique. The mechanical strengths of these composites were correlated with fibre volume fraction (V_f). The stress wave factor (SWF) was evaluated and correlated with tensile/flexural strengths of these composite specimens. The observations show a linear relationship between the SWF values and strength of unfilled and filled GRP composites.

Keywords. Stress wave factor; filled and unfilled GRP; acousto ultrasonic; fibre volume fraction.

Introduction

Glass fibre reinforced plastic (GRP) composites have gained acceptance by many industries because of their high strength to weight ratio, good corrosion resistance and availability of design criteria. It has been seen that fillers are used in many applications. The filled composites exhibit moderately improved mechanical properties, damping, attenuation as well as thermal stability characteristics depending on the kind of filler employed. Many cases have been discussed and illustrated where the highest concentration of filler and therefore maximum strength reduction is highly advantageous. Conversely, the limitations of filler use are also described. The filler selection is primarily determined by the particle size distribution. Average particle size is useful for evaluating specific properties of fillers. Quality control of these fillers is usually exercised by controlling the coarseness of average particle size control of coarseness is essential. However, instead of particle size, particle packing is most significant.

Errigno (1978) described and illustrated the advantages of use of fillers in fibre-reinforced composite material. Vastava *et al* (1988) used fly ash as a filler in glass fibre-reinforced plastic composites and determined the fracture toughness and fracture surface energy. Ramsteiner and Theysohn (1984) studied the tensile behaviour of filled composites. Lorne (1992) studied filled glass fibre-reinforced polyester composites in aqueous environments and reported that GRP are used extensively in replacement of underground piping and storage vessels for water and sewage applications for reasons of economy. A compromise between the cost and mechanical performance, mica and graphite powder have been used in this study. Nondestructive testing of GRP composites is

of great significance if the GRP composites are to be used with greater reliability. Therefore, the mechanical and nondestructive AU testing of fabricated GRP composites with and without fillers was extensively studied in the present paper.

2. Experimental

2.1 Preparation of samples

Cross ply composite laminates were fabricated in laboratory by hand lay-up technique. This is a conventional technique being used from the ages for its ease and low cost. In this technique *E* glass fibre (0/90°) was used as a reinforcing medium; resin (Cy205) and hardener (Hy951) were used as matrix. The resin and hardener were mixed in the ratio of 10:1 for about five min at room temperature. Thereafter, the mixture was kept at 60°C for about 30 min to avoid air bubbles, voids and to get proper mixing. The mixture of resin and hardener was poured in a mould which was coated with the releasing agent. In this mould a layer of woven glass fibre mat was laid. After evenly spreading the resin in mould another layer of woven glass fibre mat was laid and this process was repeated until the required thickness was obtained. Thereafter, a suitable dead weight was placed on the top plate of the mould for removal of excess resin and air bubbles. After curing, GRP plates were removed from the mould. Curing time at room temperature was observed to be about 24 h.

The filler chosen in the present study is graphite. It is a crystalline carbon formed by mineralogical process and is uniform and provides good acid and alkali resistance. GRP plates with muscovite mica and graphite powders as fillers were fabricated in laboratory in the same manner as described above.

The particle sizes were measured by sieving; mica powder, particle size 100μ and 5% by weight, was used and was mixed in matrix (resin : hardener :: 10 : 1). Similarly, graphite powder, particle size 100μ and 5% by weight, was mixed in matrix. The mechanical properties of these fillers are given in table 1. The composite plates were fabricated with least possible variation in fibre volume fraction (V_f) achieving a constant V_f of 50%. Also, composite sheets were fabricated with varying V_f . Variation in V_f was achieved by controlling the amount of fibre being used while making the composites. Fibre volume fraction of the sample was measured by acid digestion high temperature heating process as per BIS specification HIVID 4 (001S) P1.

The mica-powder-filled GRP composite plates and graphite-powder-filled GRP composite plates were used for comparative study of their mechanical properties vis-à-vis GRP composites.

2.2 Evaluation of tensile and flexural strengths

Thirty tensile specimens were made from the fabricated composite sheets in dog bone shape for tensile strength.

The SWF values at different locations were obtained and tensile strength was evaluated using Hounsfield tensometer.

Flexural strength of unfilled and filled composites, was obtained under three-point bending test using an universal testing machine. In three-point bending, when a force is applied at the centre of the upper surface of an end supported beam as in ASTM D-790, the upper surface is under compression and the lower surface is in tension. Maximum stress is applied only to the surface in tension. The decreasing strain through the cross section (from lower to upper surface) had the effect of providing somewhat higher flexural than tensile yield strength. This is especially pronounced for matrices having elongation greater than about 5%. Inherently tough polymers may obtain higher flexural strength with high aspect ratio fillers or solid fillers treated with coupling agents. The flexural strength (σ_m) is evaluated using the following expression:

$$\sigma_m = 3PL/2bh^2,$$

where, P is the maximum load in Kgf, b the specimen width, h the thickness of the specimen and L the distance between two spans.

Table 1. Properties of mica and graphite particles used in study.

Materials	Size	Tensile modulus (GN/m ²)	Density (g/cc)	Compressive strength (MN/m ²)	Response
Mica powder	100μ	172	2.13	72.15	Very soft/mild
Graphite powder	100μ	1250	3.20	80.60	Tough/brittle

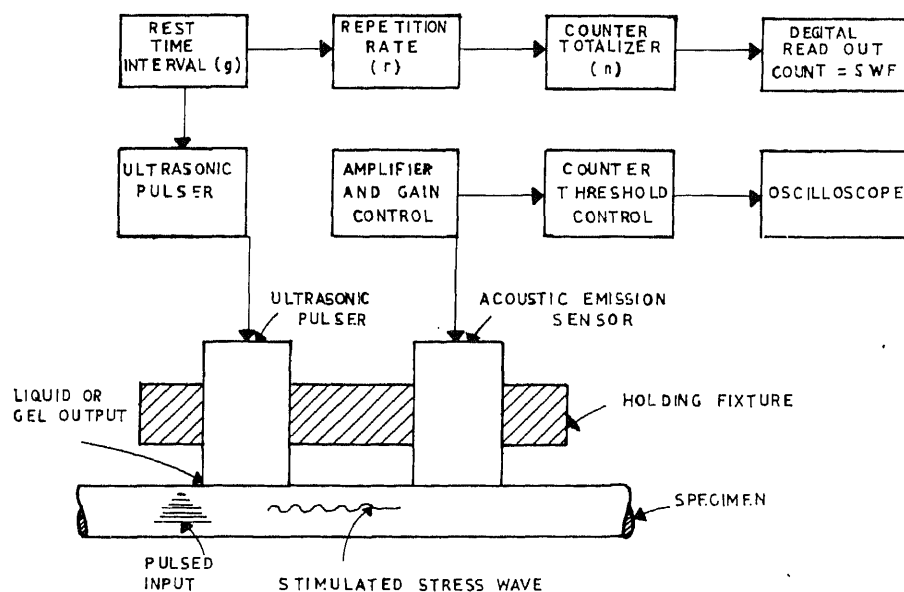


Figure 1. Block diagram for measurement of stress wave factor.

Acousto ultrasonic testing

The fabricated composites were characterized by AU technique according to ASTM standard E 1495. This is relatively a new non-destructive testing technique and is essentially an amalgamation of the two techniques: acousto-emission and ultrasonic technique, in which ultrasonic waves are induced in the material by a pulser. The induced pulses interact with voids and cracks present inside the material and the pulse thus gets modulated. The modulated signals are picked up by another piezoelectric acoustic emission sensor called receiver. These

pulses pass through a preamplifier and to an amplifier and finally to the analysing circuit. For characterization of material quality, one has to calculate stress wave factor (SWF). It was defined by Vary (1980) as:

$$SWF = grn,$$

where, g is the pulse rate (ultrasonic pulse), r the repetition rate (time) and n the number of pulses which cross a fixed threshold voltage.

In other words, multiplication of these parameters would give stress wave factor of a particular material. Therefore SWF was evaluated in the present investigation by using AET-206 AU instrument. The SWF values thus obtained at different locations on unfilled and filled GRP-composites when the noise interference was minimum. Transducers were firmly placed at a distance of 4 cm against the specimen to avoid changes in the pressure during the time when pulser was activated. The block diagram of the apparatus for measurement of SWF is shown in figure 1.

TENSILE STRENGTH (MPa)

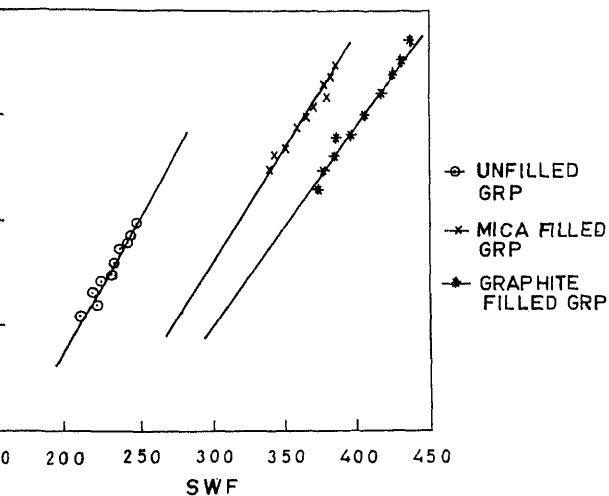


Figure 2. Variation of tensile strength with SWF of GRP composites.

FLEXURAL STRENGTH (MPa)

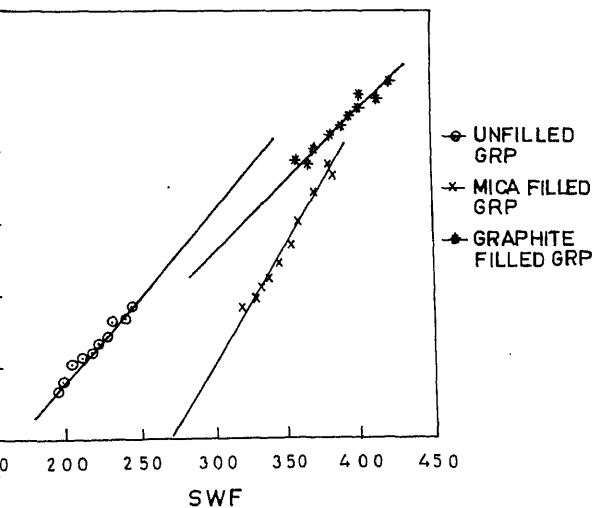


Figure 3. Variation of flexural strength with SWF of GRP composites.

3. Results and discussion

Figures 2 and 3 show the relationship between the SWF and tensile strength, and SWF and flexural strength of unfilled GRP, mica- and graphite-filled GRP composites. As far as unfilled and mica-filled composites are concerned, the SWF values were found to be lower whereas graphite filled composites showed significantly higher values. The correlation coefficient r and student t values were evaluated from the plots of SWF and tensile/flexural strengths and are listed in table 2. The results show that a good correlation exists between SWF values and the mechanical strengths in the unfilled as well as filled composites.

Figures 4-6 show and describe tensile and flexural strength with respect to fibre volume fraction. Fillers affect tensile properties according to their packing characteristics, size and interfacial bonding. The spaces between particles are assumed to be filled with matrix and no voids or air bubbles are present. Under these conditions, for a given system, the matrix volume is at a minimum and acts as individual segment or pocket to support tensile load.

Table 2. Correlation coefficient (r) values of GRP composites.

Materials	Tensile strength correlation coefficient (r)	Flexural strength correlation coefficient (r)
Unfilled GRP	0.945	0.895
Mica filled GRP	0.964	0.927
Graphite filled GRP	0.986	0.976

Flexural testing can be used for grading specimens in materials evaluation, process development and improvement and quality control. However, a true correlation

between flexural properties and other mechanical properties has never been established. There are many subtle variables affecting bending test strength so that the problem of correlating flexural data with the more basic properties can outweigh all advantages of meaningful design data.

In the present investigation, it was observed that the quality of virgin GRP composite is improved by adding graphite powder, but this is not so when mica powder was added which has been frequently used in composite development programmes. The reason being that the carbon atoms of the graphite powder easily reacted with the epoxide of epoxy resin which in turn contributed for the improved cohesive strength. In the mica powder $K_2Al_4(Al_2Si_6O_{20})(OH)_4$ having chemical composition as: SiO_2 -47.9%, Al_2O_3 -33.13%, MgO -0.69%, Fe_2O_3 -2.04%, K_2O -9.8%, Na_2O -0.8%, CaO -0.5%, TiO_2 -0.65%, Cr_2O_3 -0.65%. These do not easily dissolve in the epoxy resin and, therefore, will not help to increase strength of the composite. The higher SWF values obtained would generally provide a means of rating the efficiency of dynamic

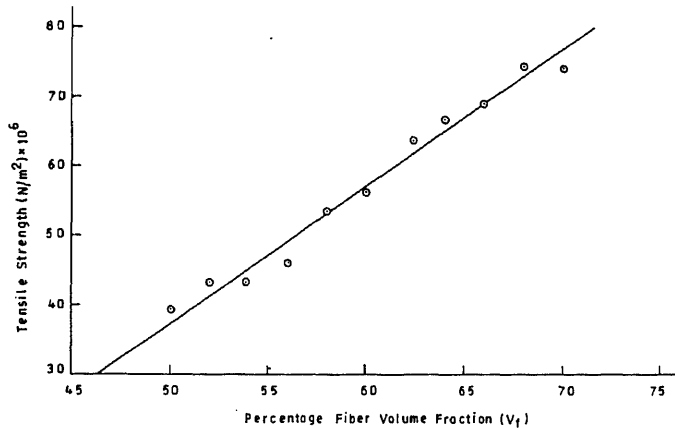


Figure 4. Variation of tensile strength with percentage V_f of unfilled GRP composite.

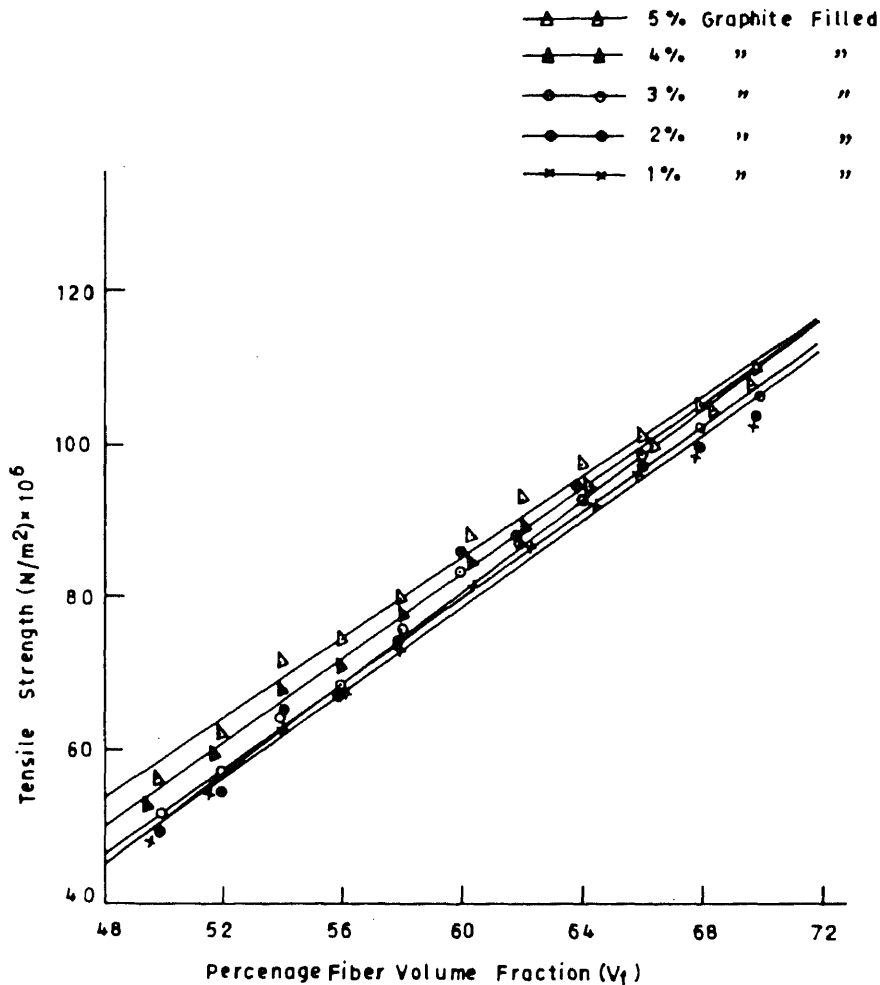


Figure 5. Variation of tensile strength with percentage V_f of graphite filled GRP composite.

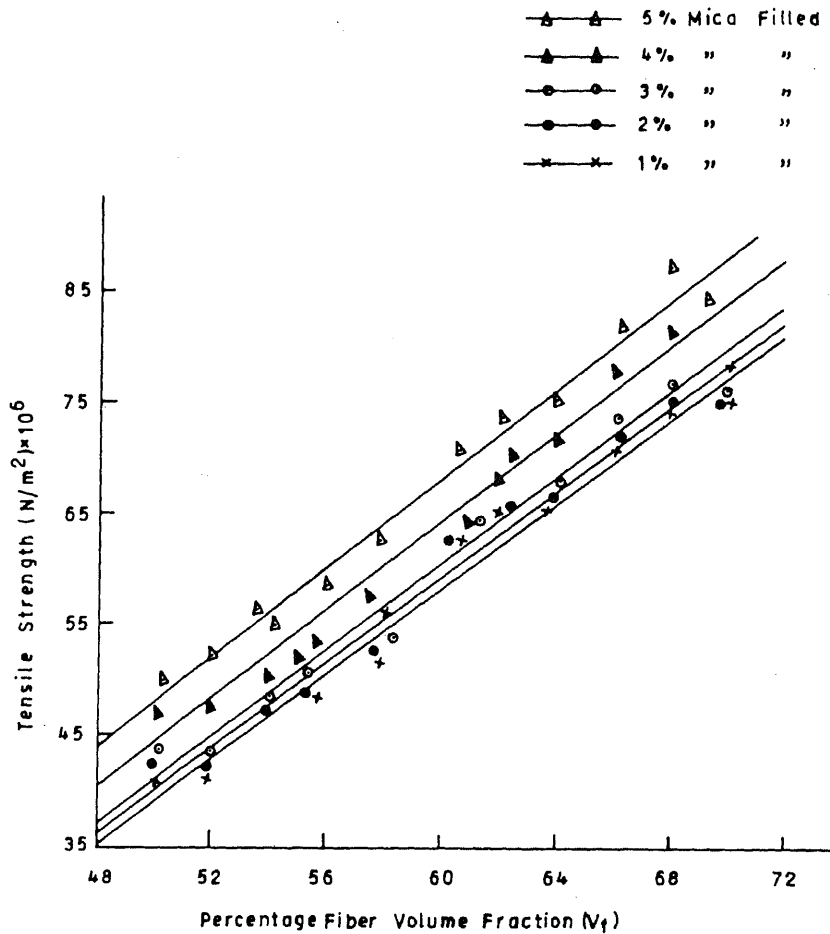


Figure 6. Variation of tensile strength with percentage V_f of mica filled GRP composite.

energy transfer in a GRP composite specimen. In turn would provide information about the quality of the material. The ultimate purpose of AU approach is to relate efficiency of stress wave energy propagation to the material.

For fibre-reinforced composite, better stress wave energy transfer means better transmission of dynamic energy, better load distribution, greater strength and better fracture resistance. However, the lower values of SWF would suggest that the material has a higher attenuation which may be due to local variations in microstructural features, porosity, bond quality, cure state and microcrack population of the composites.

It was found in the present investigation that the SWF is very much reproducible when background noise at a certain gain was deleted. This was achieved by fixing up a threshold voltage. The factors that affect the experimental results could be coupling, contact pressure, pulse gain, frequency and threshold. If all these are kept constant, then the SWF should reflect the variation in composition of the specimen under test.

4. Conclusions

Based on the present study the following conclusions can be drawn:

(I) The mechanical strengths i.e. tensile and flexural, were found to vary with SWF as well as with fibre volume fraction in the GRP composite with and without fillers.

(II) Fillers were found to be extremely useful in improving the strength SWF of the GRP composites.

(III) Out of the two fillers used in the present investigation graphite was found to improve the strength of unfilled GRP composites significantly.

References

- Ferrigno T H 1978 *Principle of filler selection and use*, in *Handbook of fillers and reinforcement for plastic* (eds) H S Katz and J V Mikwski (New York: Van Nostrand Reinhold Co.) p. 11
- Lome W D 1992 *Diss. Abstr. Int.* **52** 8
- Ramesteiner F and Theysohn R 1984 *Composites* **15** 121
- Srivastava V K, Shembekar P S and Prakash R 1988 *Comp. Struct.* **10** 271
- Vary A 1980 *J. Mater. Eval.* **40** 650

Alloy–oxide equilibria in the system Pt–Rh–O

K T JACOB*, SHASHANK PRIYA and YOSHIO WASEDA†

Department of Metallurgy, Indian Institute of Science, Bangalore 560 012, India

†Research Centre for Metallurgical Process Engineering, Institute for Advanced Materials Processing, Tohoku University, Sendai 980-77, Japan

MS received 12 January 1998

Abstract. The composition of Pt–Rh alloys that co-exist with Rh_2O_3 in air have been identified by experiment at 1273 K. The isothermal sections of the phase diagram for the ternary system Pt–Rh–O at 973 K and 1273 K have been computed based on experimentally determined phase relations and recent thermodynamic measurements on $\text{Pt}_{1-x}\text{Rh}_x$ alloys and Rh_2O_3 . The composition dependence of the oxygen partial pressure for the oxidation of $\text{Pt}_{1-x}\text{Rh}_x$ alloys at different temperatures, and temperature for the oxidation of the alloys in air are computed. The diagrams provide quantitative information for optimization of the composition of $\text{Pt}_{1-x}\text{Rh}_x$ alloys for high temperature application in oxidizing atmospheres.

Keywords. System Pt–Rh–O; phase diagram; thermodynamic properties; Pt–Rh alloys; oxidation; stability field.

Introduction

Alloys of platinum and rhodium are extensively used in thermocouples for high temperature measurement, and as clean and inert heating elements in experimental high temperature furnaces. Phase diagram of the binary system, as displayed in figure 1, shows continuous solid solubility between the end members. An important limiting factor for the use of Pt–Rh alloys is the temperature below which Rh in the alloy can be oxidized to form Rh_2O_3 . In air, pure Rh_2O_3 is stable below 1315 K (Jacob and Sriram 1994). The thermodynamic stability window for Pt–Rh alloys as function of temperature and oxygen partial pressure has not been quantitatively evaluated earlier. Recently, the standard Gibbs energy of formation of Rh_2O_3 (Jacob and Sriram 1994) and mixing properties of Pt–Rh alloys (Jacob *et al* 1998) have been determined accurately. Using these data, equilibrium conditions for the oxidation of Pt–Rh alloys can be computed. This communication presents the computed thermodynamic stability domain for Pt–Rh alloys against oxidation.

Alloy–oxide equilibrium

Platinum does not form a stable oxide at high temperature. To check if ternary oxides are stable in the system Pt–Rh–O, mixtures containing Pt–Rh alloy and Rh_2O_3 were equilibrated at 1273 K for 85 h in air. Alloys containing 10.2, 20.7, 30.5, 39.6, 48.8, 59.3, 69.5, 80.6 and 90.0 at.% Rh were used in the equilibration studies.

The alloys were made by arc melting Pt and Rh sponge of 99.9% purity on a water-cooled copper hearth. Each alloy button was remelted four times to ensure homogeneity. Alloy powders were prepared by filing. Iron particles in the powder were removed by a strong magnet. Residual iron was removed by chemical dissolution in acid. Fine powder of Rh_2O_3 used in equilibrium studies was of purity >99.99%. Equimolar mixtures of alloy and Rh_2O_3 were pelletized using a steel die before equilibration in air. After heat treatment, the pellets were examined by X-ray diffraction analysis (XRD) and optical microscopy. In pellets containing alloys with 10.2 and 20.7 at.% Rh, the oxide phase (Rh_2O_3) was found to decompose. No change was detected in the phase composition of the other pellets. There was no evidence of formation of ternary condensed phases in the system Pt–Rh–O.

3. Thermodynamic data

3.1 Pt–Rh alloys

The relative excess chemical potential ($\Delta\mu_{\text{Rh}}^{\text{E}}$) or excess partial molar free energy of mixing ($\Delta G_{\text{Rh}}^{\text{E}}$) of Rh in Pt–Rh alloys has been determined recently using an emf technique (Jacob *et al* 1998). The results at 1273 K can be expressed by the relation (Jacob *et al* 1998):

$$\Delta\mu_{\text{Rh}}^{\text{E}} = \Delta G_{\text{Rh}}^{\text{E}} = RT \ln \gamma_{\text{Rh}} = (1 - X_{\text{Rh}})^2 [-6,130 + 50 X_{\text{Rh}}] \text{ J/mol.} \quad (1)$$

From the Gibbs–Duhem equation, the relative excess

*Author for correspondence

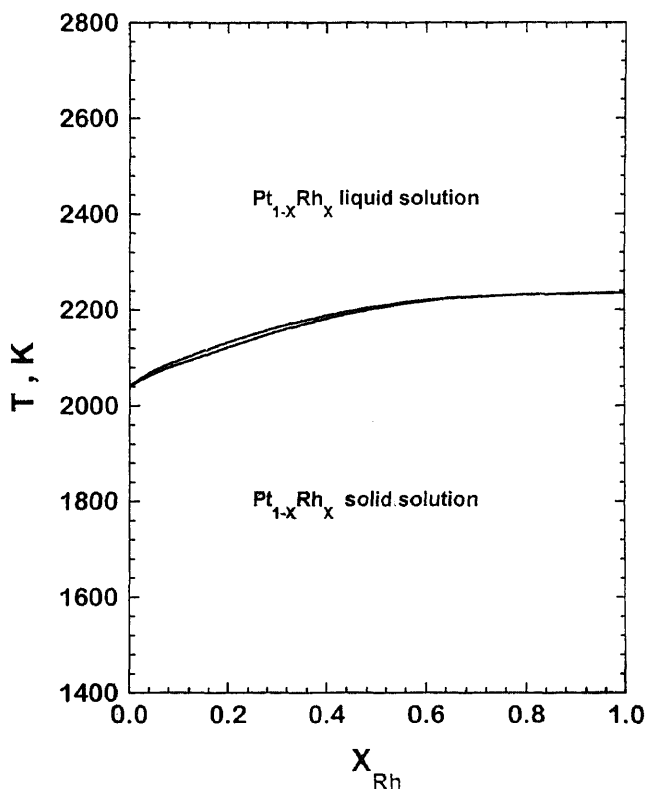


Figure 1. Phase diagram for the system Pt-Rh (Jacob *et al* 1998).

chemical potential of Pt ($\Delta\mu_{\text{Pt}}^{\text{E}}$) and integral excess free energy of mixing of solid Pt-Rh alloys (ΔG^{E}) at 1273 K were derived:

$$\Delta\mu_{\text{Pt}}^{\text{E}} = \Delta G_{\text{Pt}}^{\text{E}} = RT \ln \gamma_{\text{Pt}} = X_{\text{Rh}}^2 [-6,155 + 50 X_{\text{Rh}}] \text{ J/mol}, \quad (2)$$

$$\Delta G^{\text{E}} = X_{\text{Rh}} (1 - X_{\text{Rh}}) [-6,130 + 25 X_{\text{Rh}}] \text{ J/mol}. \quad (3)$$

The compositional dependence of excess partial entropy of mixing of Rh ($\Delta S_{\text{Rh}}^{\text{E}}$) was evaluated from the variation of emf with temperature (Jacob *et al* 1998):

$$\Delta S_{\text{Rh}}^{\text{E}} = (1 - X_{\text{Rh}})^2 [-3.80 + 0.031 X_{\text{Rh}}] \text{ J/mol}\cdot\text{K}. \quad (4)$$

By combining the partial excess free energy at 1273 K with partial excess entropy, the partial enthalpy of mixing of Rh was obtained:

$$\begin{aligned} \Delta H_{\text{Rh}} &= \Delta G_{\text{Rh}}^{\text{E}} + 1273 \cdot \Delta S_{\text{Rh}}^{\text{E}} \\ &= (1 - X_{\text{Rh}})^2 [-10,970 + 90 X_{\text{Rh}}] \text{ J/mol}. \end{aligned} \quad (5)$$

From the Gibbs–Duhem equation, partial excess properties of Pt and integral excess mixing properties were obtained:

$$\Delta S_{\text{Pt}}^{\text{E}} = X_{\text{Rh}}^2 [-3.8155 + 0.031 X_{\text{Rh}}] \text{ J/mol}\cdot\text{K}, \quad (6)$$

$$\begin{aligned} \Delta S^{\text{E}} &= X_{\text{Rh}} (1 - X_{\text{Rh}}) [-3.80 \\ &\quad + 1.55 \times 10^{-2} X_{\text{Rh}}] \text{ J/mol}\cdot\text{K}, \end{aligned} \quad (7)$$

$$\Delta H_{\text{Pt}} = X_{\text{Rh}}^2 [-11,015 + 90 X_{\text{Rh}}] \text{ J/mol}, \quad (8)$$

$$\Delta H = X_{\text{Rh}} (1 - X_{\text{Rh}}) [-10,970 + 45 X_{\text{Rh}}] \text{ J/mol}. \quad (9)$$

Activities of component elements exhibit negative deviation from Raoult's law. Recent thermodynamic measurements (Jacob *et al* 1998) disprove the existence of solid state immiscibility below ~ 1033 K shown in current phase diagram compilations (Moffatt 1976; Massalski *et al* 1990).

3.2 Rh_2O_3

The standard Gibbs free energy of formation of Rh_2O_3 (ΔG_f°) with orthorhombic structure has been measured recently using an advanced design of the solid state cell with three electrodes (Jacob and Sriram 1994). This arrangement minimizes polarization of the electrodes and gives more accurate values. The data in temperature range 850–1300 K can be represented by the relation:

$$\Delta G_f^\circ(\text{Rh}_2\text{O}_3) = -3,96,365 + 282.0 T (\pm 120) \text{ J/mol}. \quad (10)$$

4. Oxygen potentials for alloy–oxide equilibria

The oxygen chemical potential corresponding to the equilibrium between the alloy and Rh_2O_3 can be computed as a function of composition of the alloy at different temperatures using the thermodynamic data. At a temperature T ,

$$\begin{aligned} \Delta G_f^\circ(\text{Rh}_2\text{O}_3) &= -RT \ln K = -RT \ln \frac{1}{a_{\text{Rh}}^2 \cdot P_{\text{O}_2}^{3/2}} \\ RT \ln P_{\text{O}_2} &= \Delta\mu_{\text{O}_2}(\text{Pt}_{1-x}\text{Rh}_x + \text{Rh}_2\text{O}_3) \\ &= \frac{2}{3} \Delta G_f^\circ(\text{Rh}_2\text{O}_3) - \frac{4}{3} (RT \ln a_{\text{Rh}}) \\ &= \frac{2}{3} \Delta G_f^\circ(\text{Rh}_2\text{O}_3) - \frac{4}{3} [\Delta H_{\text{Rh}} + RT \ln X_{\text{Rh}} \\ &\quad - T \Delta S_{\text{Rh}}^{\text{E}}], \end{aligned} \quad (11)$$

where $\Delta\mu_{\text{O}_2}$ is the oxygen chemical potential, $\Delta G_f^\circ(\text{Rh}_2\text{O}_3)$ the standard Gibbs free energy of formation of Rh_2O_3 , P_{O_2} the oxygen partial pressure, a_{Rh} the activity of Rh, X_{Rh} the mole fraction of Rh in the alloy, and the other symbols have their usual meaning. The computed oxygen potentials are displayed in figure 2 as a function of

composition at different temperatures. Conditions for oxidation of Pt-Rh alloys at equilibrium can be readily evaluated from the diagram. At oxygen partial pressures above the curve the alloy will not oxidize. Rapid oxidation may result in depletion of Rh from the alloy surface, thus increasing the oxygen potential for further oxidation of the alloy.

Often Pt-Rh alloys are used in air and it is useful to know the temperature below which oxidation is feasible from a thermodynamic point of view for a given alloy composition. The temperature for oxidation in air can be computed from thermodynamic data for alloys and Rh_2O_3 . Setting $(P_{\text{O}_2}/P^\circ) = 0.21$ in (11) and rearranging:

$$T = \frac{\left(\frac{2}{3} \Delta H_f^\circ(\text{Rh}_2\text{O}_3) - \frac{4}{3} \Delta H_{\text{Rh}}^\circ\right)}{\left(\frac{2}{3} \Delta S_f^\circ(\text{Rh}_2\text{O}_3) - \frac{4}{3} \Delta S_{\text{Rh}}^\circ + \frac{4}{3} R \ln X_{\text{Rh}} + R \ln 0.21\right)}, \quad (12)$$

where P° is the standard atmospheric pressure (1.01×10^5 Pa). The computed curve is shown in figure 2. With increase in the concentration of Rh in the alloy,

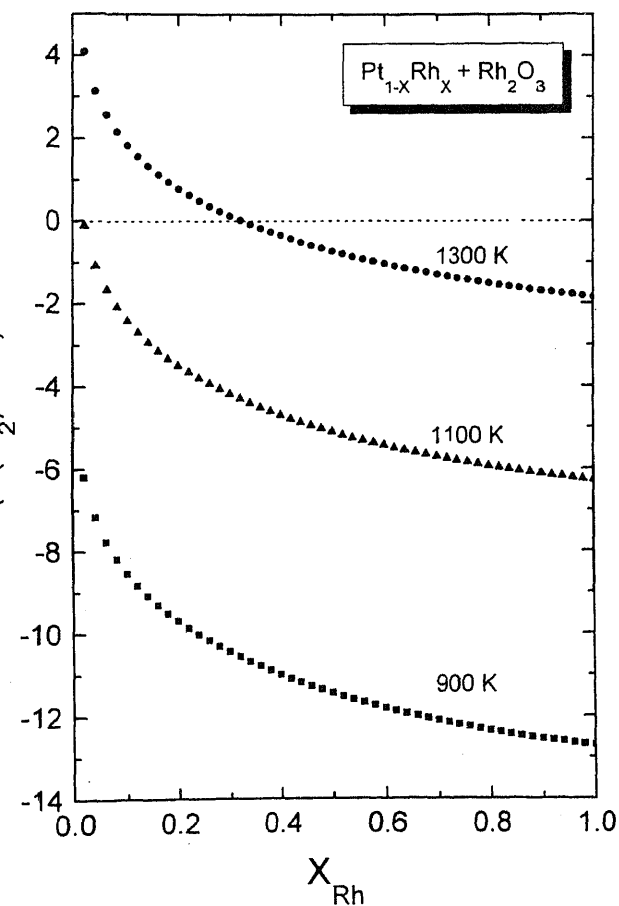


Figure 2. Variation of the equilibrium oxygen chemical potential for the formation of Rh_2O_3 as a function of composition Pt-Rh alloys at different temperatures.

the temperature for the decomposition of Rh_2O_3 in air increases rapidly at low concentrations and more gradually at higher concentrations. The safe region for the use of Pt-Rh alloys lies above the computed curve. Oxidation will not occur in this domain. Oxidation of alloys containing less than 15 at.% Rh is limited by kinetic factors at temperatures below the curve. Oxidation will become significant with increasing concentration of Rh in the alloy, especially at $T > 1200$ K.

5. Ternary phase diagram of the system Pt-Rh-O

Since the oxides of platinum are unstable in the experimental temperature range and ternary oxides do not exist in the system Pt-Rh-O, isothermal sections of the phase diagram for the ternary system Pt-Rh-O at high temperatures can be constructed from the thermodynamic data using a free energy minimization algorithm (Morris and Stephenson 1986). The computed isothermal sections at 973 and 1273 K are displayed in figures 4 and 5, respectively. Phase diagrams at other temperatures can be readily calculated from the thermodynamic data. All

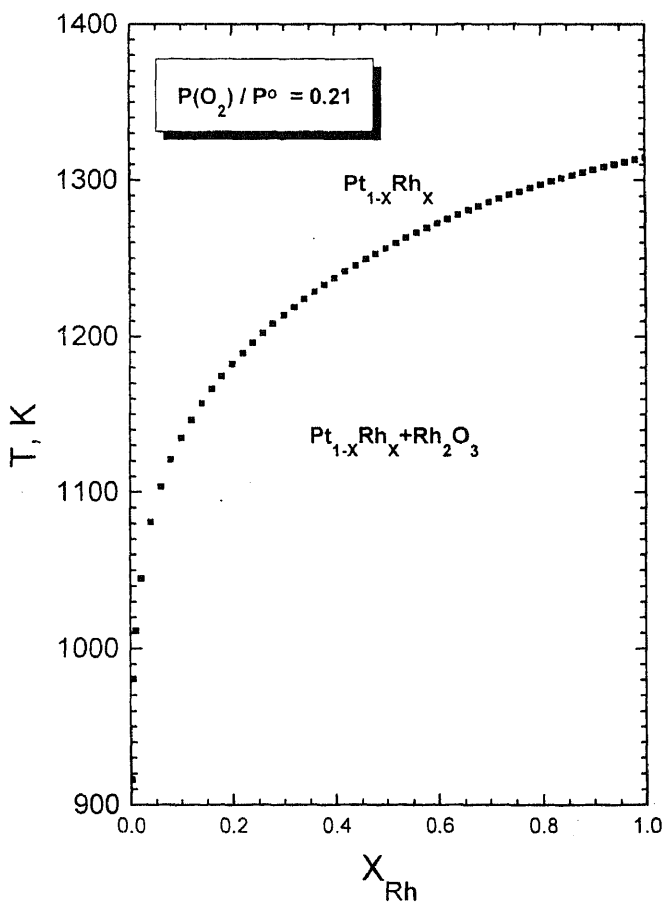


Figure 3. Variation of the equilibrium temperature for the oxidation of Pt-Rh alloys in air ($P_{\text{O}_2} = 2.12 \times 10^4$ Pa).

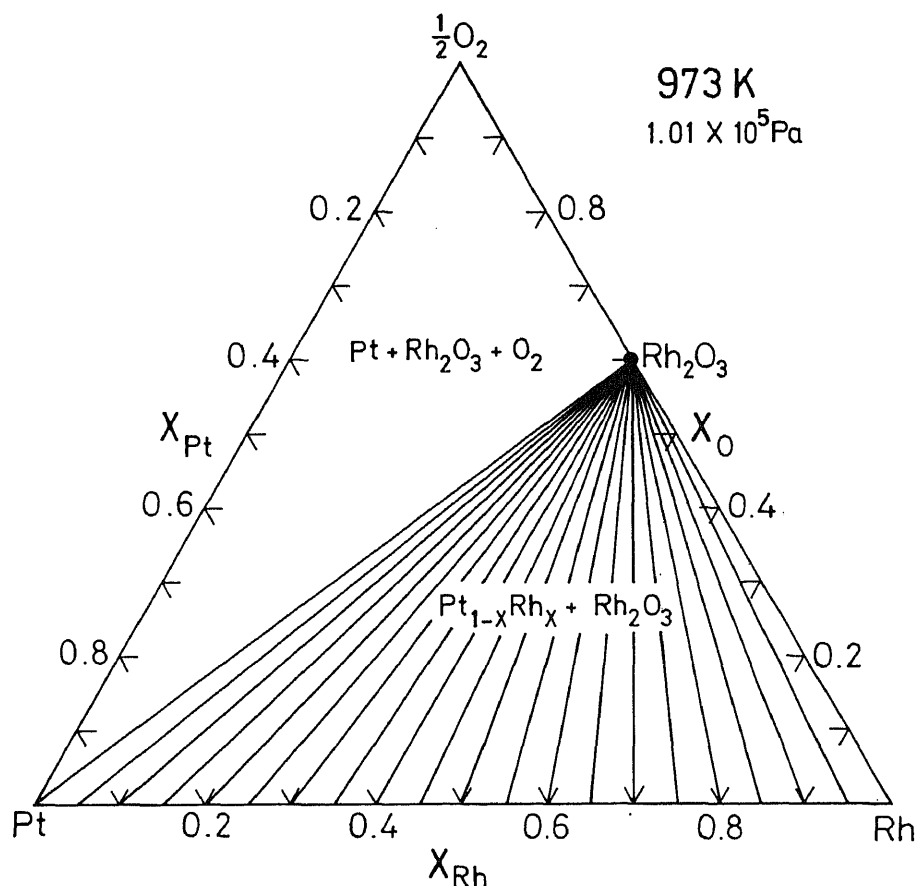


Figure 4. Isothermal section of the Pt-Rh-O system at 973 K computed from thermodynamic data.

Table 1. Temperature above which commercial $Pt_{1-x}Rh_x$ alloys will not be oxidized in air.

X_{Rh}	T, K
0.06	1104
0.13	1153
0.30	1214
0.40	1237
0.60	1272

Use of Rh-rich alloys should be limited to temperatures above the oxidation limit. Although at low temperatures where oxidation is limited by kinetic factors, alloys can degrade at moderately elevated temperatures where oxidation is thermodynamically feasible and kinetics are favourable. The computed results provide valuable information for the intelligent use of Pt-Rh alloys in various high temperature environments containing oxygen. The lower thermodynamic limits for safe use of common alloy compositions in air are listed in table 1.

6. Optimization of alloy composition

Pt-Rh alloys are used as heating elements for furnaces that operate at temperatures higher than can be reached with pure Pt. An alloy containing ~80 at.% Rh is the most suitable from the point of view of melting and recrystallization temperature. However, this composition is relatively more expensive and difficult to work mechanically. Significant improvement in melting and recrystallization temperatures can be achieved by alloying up to 40 at.% Rh. Wires of $Pt_{0.6}Rh_{0.4}$ alloy are more easy to fabricate. This composition is also characterized

the alloy compositions are in equilibrium with Rh_2O_3 at the lower temperature (973 K). There is a three-phase equilibrium involving Pt, Rh_2O_3 and O_2 gas at $P_{O_2} = 1.01 \times 10^5$ Pa. At the higher temperature (1273 K), an alloy containing 24 mol% Rh is in equilibrium with Rh_2O_3 and O_2 . The computed diagram is in agreement with phase equilibrium data obtained in the study, after correcting for the difference in the partial pressure of oxygen. Pt-rich alloys coexist with O_2 gas at 1.01×10^5 Pa at 1273 K. The alloy composition corresponding to three-phase equilibrium between the alloy, Rh_2O_3 and O_2 shifts to higher concentration of Rh with increasing temperature.

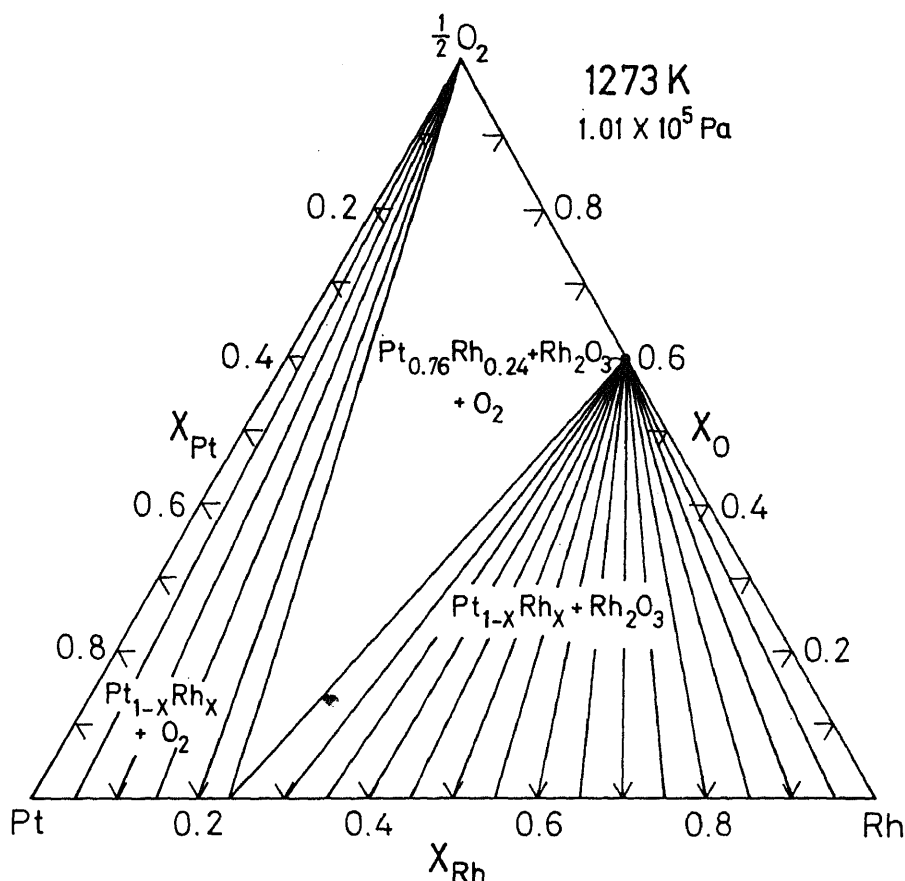


Figure 5. Isothermal section of the Pt-Rh-O system at 1273 K, computed from thermodynamic data.

high value for electrical resistivity and a relatively low value for temperature-coefficient of resistance (Jacob and Sriram 1994). However, prolonged use in air at $T/K > 1000$ is not recommended because of its susceptibility for oxidation. At temperatures below 1000 K, Pt-Rh alloys may remain untarnished for significant periods of time due to kinetic factors.

Conclusion

The thermodynamic stability domain of Pt-Rh alloys at various temperatures and in atmospheres containing oxygen has been computed using recent thermodynamic data on Pt-Rh alloys and oxides (Jacob and Sriram 1994; Jacob *et al.* 1998). The diagrams provide a quantitative guide for the selection of Pt-Rh thermocouples and heating elements

in oxidizing atmospheres. The prolonged use of Pt-40% Rh alloys in air is not recommended below 1237 K.

References

- Jacob K T and Sriram M V 1994 *Metall. Mater. Trans.* **A25** 1247
- Jacob K T, Priya S and Waseda Y 1998 *Metall. Mater. Trans.* **A29** (in press)
- Massalski T B, Subramanian P R, Okamoto H and Kacprzak L (eds) 1990 *Binary alloy phase diagrams* (Materials Park, OH, USA: ASM International) Vol. 3
- Moffatt W G 1976 and updates *Handbook of binary phase diagrams* (New York: General Electric Co.)
- Morris A E and Stephenson J 1986 *J. Metals* **38** 41
- Acken J S 1934 *J. Res. Bur. Stand.* **12** 249

BOOK REVIEW

The Metals Data Book by Alok Nayar, Tata McGraw Hill Pub. Co. Ltd., New Delhi 110 008, pp. 876 and Price: Rs 650.

The Metals Data Book contains extensive information on aspects such as classification of alloys, their composition, mechanical properties, transformation temperatures, heat treatment temperatures and typical applications of several grades of alloys including cast irons, steels, aluminium alloys, copper alloys and zinc alloys. Also provided is information on the physical properties of metals. The effect of each alloying element is described for many alloys. A chapter is exclusively devoted to powder metallurgy of some commercial alloys. This is indeed a one-stop source for all metallurgical data which are expressed in SI units. The data are compiled in the form of tables which makes reference and comparison of different alloys easy. The compilation provides Indian,

American, German, British, Japanese and ISO equivalents. The book also devotes a full chapter to Units and Measures wherein conversion factors and conversion tables are included which will be of immense help.

The author, a metallurgical engineer himself with vast experience, has painstakingly put together information from available standards, reference books and publications of technical societies. The book is really the result of a commendable effort. The author may consider extending the coverage to nickel alloys, titanium alloys, molybdenum alloys and tungsten alloys in the next edition to further enhance its usefulness.

This excellent handbook is extremely useful for engineering professionals like designers, manufacturing engineers, maintenance engineers, quality assurance engineers, purchase department staff as well as teachers and researchers in the area of metals and alloys. With 876 pages and priced modestly at Rs 650, this reference book should find a place in all technical libraries.

D H Sastry
Indian Institute of Science
Bangalore 560 012, India

Bulletin of Materials Science

Notes on the preparation of papers

Authors may communicate their research work as papers and short communications to the Bulletin of Materials Science. They may also submit topical reviews. The papers may be sent to the Editor or to one of the International Advisory Board members.

All communications should be submitted in triplicate (original and two copies).

Authors are encouraged to send electronic files prepared using plain latex or MS Word (RTF), of final accepted version of their articles. This will help hasten the process of typesetting. Line drawings also may be submitted in electronic format in some standard graphic format—TIFF, for example, and saved in EPS format. However, a hard copy with figures must also be submitted along with floppy disk of electronic files.

Submission of a script will be held to imply that it has not been previously published and is not under consideration for publication elsewhere; and further that, if accepted, it will not be published elsewhere.

Manuscript

Scripts must be typed double spaced with ample margin on all sides on one side of white bond paper of quarto size (229 × 215 mm). This also applies to the abstract, tables, figure captions and the list of references which are to be typed on separate sheets.

Page

The title of the paper must be brief but informative. Serial numbers are to be avoided.

The names with initials of authors and the name and address of the institution where the work was done must be given. An abbreviated running title of not more than 50 letters and spaces must also be given.

Authors are requested to provide e-mail and fax addresses while submitting the script.

Abstract

Scripts must have a brief abstract of the significant results stated in the paper.

Keywords

Between 3 and 6 keywords must be provided for indexing and information retrieval.

Text

The paper must be divided into sections starting preferably with 'Introduction' and ending with 'Conclusions'. The main sections should be numbered 1, 2 etc., the sub-sections 1.1, 1.2, and further sub-sections (if necessary) 1.1a, 1.1b, etc.

Tables

All tables must be numbered consecutively in arabic numerals in the order of occurrence in the text; they should be self-contained and have a descriptive title.

Figures

All figures including photographs should be numbered consecutively in arabic numerals in the order of appearance in the text. Line drawings must be in Indian ink on good quality tracing paper or Bristol board of the same size as the text paper. Lines should be sufficiently thick (axes about 0.3 mm, curves about 0.6 mm).

Units

Units and associated symbols must invariably follow SI practice.

References

References should be cited in the text by author and year, not by number. If there are more than two authors, reference should be to the first author followed by et al in the text. References at the end of the paper should be listed alphabetically by author's names, followed by initials, year of publication, name of the journal (abbreviated according to the World List of Scientific Periodicals, Butterworths, London), volume number, and number of the first page. Reference to books should include: name(s) of author(s), initials, year of publication, title of the book, edition if not the first, initials and name(s) of editor(s) if any, preceded by ed(s), place of publication, publisher and chapter or pages referred to. References to thesis must include the year, the title of the thesis, the degree for which submitted and the University.

Footnotes

Footnotes must be avoided if possible but when necessary should be numbered consecutively, and typed on a separate sheet.

Proofs

Authors are requested to prepare the manuscript carefully before submitting it for publication to minimize corrections and alterations in the proof which increase publication costs. Page-proofs sent to author together with the reprint order form must be returned to the editorial office within two days of their receipt by SPEED POST/COURIER.

Reprints

50 reprints of each article will be supplied free of charge.